REDUCTION OF THE COOLANT VOID REACTIVITY EFFECT IN A CANDU LATTICE CELL

By

JEREMY JOHN WHITLOCK, B.Sc., M.Eng.

A Thesis

Submitted to the School of Graduate Studies

in Partial Fulfilment of the Requirements

for the Degree

Doctor of Philosophy

McMaster University

REDUCTION OF THE COOLANT VOID EFFECT IN A CANDU LATTICE CELL

DOCTOR OF PHILOSOPHY (1995)
(Engineering Physics)

McMASTER UNIVERSITY
Hamilton, Ontario

TITLE: Reduction of the Coolant Void Reactivity Effect in a CANDU Lattice Cell

AUTHOR: Jeremy John Whitlock, B.Sc. (University of Waterloo)
M.Eng. (McMaster University)

SUPERVISORS: Dr. Wm. J. Garland
Dr. M.S. Milgram

NUMBER OF PAGES: xxii, 332

Abstract

A positive feedback mechanism linking reactor power and loss of coolant exists in the current configuration of the CANDU* reactor. This mechanism creates a "coolant void effect" which is accommodated in both the safety system and control system designs, although a political incentive exists to reduce the effect's magnitude. This dissertation includes a review of current methods and knowledge in the area of CANDU lattice cell analysis of the coolant void effect, presented in two parts: (1) an investigation of the methodology and modelling, and (2) an investigation of the contributing reactor physics. This study also explores several routes toward the goal of reducing the coolant void effect, drawing from both existing work and original contributions. A novel approach to CANDU fuel design is defined, combining the concepts of coolant displacement, concentric tubular fuel, and differential uranium enrichment. Several variations of the new design are discussed, as well as practical difficulties that would be associated with the realization of this design. Finally, a corrective algorithm is developed and utilized which compensates for a modelling deficiency arising in the simulation of tubular fuel.

Acknowledgements

No PhD student is an island. I am indebted to many people for guidance and support throughout this project, although I claim sole responsibility for any errors, misjudgements, or omissions found herein. The following people are thanked whole-heartedly for lending a hand, or an ear, or in some cases, an arm and a leg:

Bill Garland at McMaster and Mike Milgram at AECL shared shepherding duties as my co-supervisors. On the road to discovery, these fellows have walked ahead of me with insight, behind me with motivation, and beside me with friendship. I thank them both. (Mike, you can stop worrying now.)

Archie Harms at McMaster also provided guidance as the third member of my supervisory committee. Ray Findlay and Jim Waddington, both at McMaster, supplied many useful comments as members of my thesis examination committee.

Several people at AECL deserve mention for helping with technical input. Jack Veeder contributed one of the earliest "expert" reviews of my work, providing the impetus for much of the thermalhydraulic analysis in Chapter 5. Terry Carter, Elias Zariffeh, and De Groeneveld also shared their wisdom in this area. David Sears, Richard Verrall, and Peter Boczar shed light on the issues of fuel materials and applications. Peter Laughton, John Griffiths, and Jim Donnelly all provided assistance at various times in interpreting or managing WIMS-AECL. Diana McElroy always gave a helping hand and a cheery smile, as did Henny Hamel of the Chalk River library, who dug long and deep on my behalf to unearth literature references. Rick Jones was instrumental in arranging my attachment to Chalk River Laboratories one summer near the beginning, which introduced me to the fine people of the Reactor Physics Branch there.

Since this brings my graduate career at McMaster to a close, I must make special mention of Elaine Moore and Bobbie Kartonchik in the Department of Engineering Physics, who over the last 6½ years have flawlessly kept me administratively on track. Also contributing to my well-being were Denise Mann, Vera Iarossi, Charlene Bradt and Dreena Burrows of the Nuclear Research Building. Lastly, I can't leave McMaster without acknowledging the consistently cordial and competent treatment I received from the staff of the School of Graduate Studies over the years.

Funding for this work was partially supplied by the Natural Sciences and Engineering Research Council of Canada.

On a less tangible note, my family and friends have never failed to be pillars of support during my years in the wilderness. My parents, Ken and Verlie Whitlock, contributed to this present accomplishment of mine many years ago by having faith in me and letting me know it. They gave me the basics, and continue to give — more than can be put into words. Fred and Lois Kipfer, and the rest of my family-in-law, have been equally supportive (even if I did go 600 in the hole one day in Rummy).

Finally, my love and eternal gratitude goes to my wife, Beth, for taking this journey with me, accepting sacrifices, sharing in my joy, helping with the word processing, tolerating my occasional absenteeism from the real world, and for giving me something far more valuable than any thesis: our son. To Alexander Montgomery Whitlock I dedicate this work — the two of you gestated together and were born at the same time. May you never gather dust like this will.

Jeremy Whitlock

April 25, 1995

Table of Contents

List of Illustrations

List of Tables

Chapter 1

Introduction

This dissertation is an investigation of the CANDU* reactor's inherent response to coolant loss, embodied in a phenomenon called the *coolant void effect*. Included are a review of analysis methodology in this area, and a search for fuel modifications that minimize the effect, culminating in the definition of a new fuel design.

In this introductory chapter the foundation for the dissertation is established. Basic terminology and formulae are introduced, along with the concept of reactivity feedback which motivates the present study, and an overview of the CANDU reactor system. Goals for the present dissertation are established, and the computer codes to be used are described. The chapter ends with an outline of the work presented in the following chapters, including indications of original research contributions where they occur.

1.1 Background to the Problem

Nuclear power reactors use the heat of a controlled nuclear fission reaction to raise steam and drive a steam turbo-electric generator. The heat is generated in a vessel filled with uranium fuel, through which coolant is circulated at high temperature and pressure. The nuclear fission reaction involves the absorption of a neutron in the U-235 isotope of

uranium, causing instability in the isotope and subsequent fragmenting, or "fissioning", into a pair of lighter nuclei. At the same time about 200 MeV (8×10^{-12} cal) of energy is released, along with two or three high-energy neutrons which are added to the total neutron population of the reactor. The fission reaction is thus self-supporting, although constant control must be exercised to maintain the supply and use of neutrons in perfect balance, and the neutron population therefore constant with time.

Changes in the neutron population can be induced by perturbations in the state of materials within the reactor (for example, fuel temperature or coolant density), with a typical time-scale measured in milli-seconds. If such perturbations have an increasing effect on the neutron population, special measures must be taken to ensure that the energy production in the fuel does not reach unsafe levels (for example, the fuel's melting point) before the population increase can be terminated.

In the CANDU reactor (to be described later) a positive influence on neutron population is induced by the removal of coolant, either by boiling or leakage from the system. Hence, analysis of this phenomenon is central to the design and licensing of safety systems for this reactor, and a "runaway" response of neutron population to loss-of-coolant accidents (LOCA's) is avoided in all credible scenarios.

Nevertheless, a political incentive exists to reduce the coupling between coolant loss and neutron population, and this dissertation is concerned with methods for achieving this goal. Also examined here are current methodologies for analysing this phenomenon, and the reactor physics behind the phenomenon. First, however, it is important to establish the terminology and concepts that characterize this general area of reactor

analysis.

1.2 The Role of Reactivity in Reactor Kinetics

In the study of nuclear reactor control and safety, the fundamental parameter is the ratio of total neutron production rate to loss rate, for which a value of unity indicates steady-state core multiplication,

$$k \equiv \frac{\textit{neutron production rate}}{\textit{neutron loss rate}} \tag{1.1}$$

A related parameter is the *prompt neutron lifetime*[1,2], the average time between the production and loss of a "prompt" neutron, a neutron directly created by a fission event. This parameter is found by dividing the time-dependent total neutron population, $N(t)$, by the loss rate,

$$l = \frac{N(t)}{\textit{loss rate}} \tag{1.2}$$

By substituting k and l into a simple statement of population balance, an exponential relationship is defined,

$$\begin{aligned} \frac{dN(t)}{dt} &= \textit{source rate} - \textit{loss rate} \\ &= \frac{(k-1)}{l} N(t) \quad , \end{aligned} \tag{1.3}$$

having a period of $\tau = l/(k-1)$. In the CANDU reactor the prompt neutron lifetime is about 0.001 seconds, and since deviations from unity of 0.1% in k are not uncommon, it

is evident that Equation (1.3) defines a *prompt neutron period* much too small for effective reactor control.

For this reason the CANDU core, as all reactor cores, is designed to utilize a small fraction, β, of neutrons that are delayed in their release following a fission event. Such neutrons come from neutron-emitting fission products called *delayed neutron precursors*, having half-lives ranging from tenths of a second to over a minute. The modified rate equation taking this slower component into account is[1,2]

$$\frac{dN(t)}{dt} = \frac{(\rho - \beta)}{\Lambda} N(t) + \sum_i \lambda_i C_i(t) \quad , \tag{1.4}$$

where λ_i and $C_i(t)$ are the decay constant and concentration, respectively, of delayed precursor i, and the following substitutions have been made:

$$\rho \equiv \frac{k-1}{k} \tag{1.5}$$

is defined as the *reactivity* of the system (the fractional deviation from unity of k), and

$$\Lambda \equiv \frac{l}{k} \tag{1.6}$$

is defined as the *mean generation time* of the system (the mean time between neutron production and neutron absorption causing fission). The rate equation for each precursor concentration $C_i(t)$ is

$$\frac{dC_i}{dt} = \beta_i \frac{k}{l} N(t) - \lambda_i C_i(t) \quad . \tag{1.7}$$

Taken together, Equations (1.4) and (1.7) are known as the *point-kinetics equations*[1,2],

since they describe the kinetic behaviour of a "point", or space-independent, reactor.

The *effective* neutron lifetime that takes the decay times of these precursors into account is approximately 0.1 seconds, or about 100 times longer than the prompt neutron lifetime. This is slow enough to allow efficient control by engineered power regulation and safety systems. However, it is evident from Equation (1.4) that should a value of reactivity, ρ, exceed the delayed neutron fraction, β, then $dN(t)/dt$ will become positive based upon prompt neutron multiplication alone. This situation is termed *prompt criticality*, for which the kinetic behaviour reverts back to the simpler form of Equation (1.3) with its much shorter reactor period.

The value of $\rho=\beta$ therefore represents a general limit on the size of reactivity that can be safely introduced into a reactor core. In general, β is isotope-dependent, and thus determined by the isotopic mixture in the core at time t. For natural uranium fuels the value of β is approximately 0.7%, leading to a prompt criticality limit of 0.007. In this dissertation the units of reactivity are *mk* ("milli-*k*"), where 1 mk = 0.1% deviation in k from unity. The prompt criticality limit, therefore, is approximately 7 mk in natural uranium systems, and dependent upon irradiation time (usually termed *burnup*, and measured in units of "megawatt-days per tonne of initial uranium", MWd/Te, or "neutrons per kilobarn", n/kb).

1.3 Cross-Sections and Reaction Rates

In any fission event, prompt neutrons are emitted with kinetic energies of

approximately 1 MeV. In a thermal reactor these neutrons are slowed, or *moderated*, to energies of less than 1 eV, in order to take advantage of the higher neutron-nuclear interaction probability in this range. The energy-dependent probability, which is termed *cross-section* and is measured in units of barns (1 b = 10^{-24} cm^2), is shown[2] in Figure 1.1 for fission in both U-235 and Pu-239. The extensive resonance structure in the mid-energy, or *epithermal*, range is characteristic of absorption processes in all of the heavy fuel isotopes. However, since only absorption takes place at these energies in U-238, the most abundant fuel isotope, it is imperative that neutrons be removed from the fuel region as they are reduced in energy through this region. This concept is central both to the design of thermal reactors, and to the particular mechanism for reactivity insertion studied in this dissertation.

Knowledge of neutron-nuclear cross-section, σ(r,E), nuclear density, n(r,E), neutron population, N(r,t), and neutron velocity, v(E), leads to a statement of neutron-nuclear reaction rate per unit volume,

$$\begin{aligned} R(r,E) &= n(r,E)\sigma(r,E)N(r,E)\,v(E) \\ &= \Sigma(r,E)\phi(r,E) \quad , \end{aligned} \tag{1.8}$$

where use is made of two new parameters, *macroscopic cross-section* (in units of cm^{-1}),

$$\Sigma(r,E) \equiv n(r,E)\sigma(r,E) \quad , \tag{1.9}$$

and *neutron flux* (in units of cm^{-2}s^{-1}),

$$\phi(r,E) \equiv N(r,E)\,v(E) \quad . \tag{1.10}$$

Using this notation, Equation (1.1) for k can be stated in terms of reaction rates, switching to the conventional terminology of k_{eff} ("k-effective"), which indicates that neutron leakage

from finite reactor geometries, L(r,E), is taken into account,

$$k_{eff} = \frac{\int_V \int_E \nu \Sigma_f \phi \, dV dE}{\int_V \int_E (\Sigma_a \phi + L) \, dV dE} \quad . \tag{1.11}$$

Here, the subscripts "f" and "a" indicate fission and total absorption, respectively. In the numerical analysis of reactors, the spatial and energy dependence is usually "collapsed" into discrete mesh cells, j, and energy groups, g, for which Equation (1.11) becomes a ratio of double summations,

$$k_{eff} = \frac{\sum_{j,g} \nu_g \Sigma_{f,jg} \phi_{jg}}{\sum_{j,g} (\Sigma_{a,jg} \phi_{jg} + L_{jg})} \quad , \tag{1.12}$$

which can be substituted into Equation (1.5) to yield a new statement of the definition of reactivity,

$$\rho = \frac{\sum_{j,g} [(\nu \Sigma_{f,jg} - \Sigma_{a,jg}) \phi_{jg} - L_{jg}]}{\sum_{j,g} \nu_{jg} \Sigma_{f,jg} \phi_{jg}} \quad , \tag{1.13}$$

the ratio of *net* to *total* neutron production over all energy and space. Two points should be noted here: (1) reactivity is actually a non-linear parameter, dependent upon neutron flux, which is dependent upon reactivity, i.e., $\rho = \rho(\phi(\rho))$; and (2) both k_{eff} and ρ are global parameters; that is, a reactivity perturbation may be referred to in local terms (such as a single fuel channel refuelling), but the implication is always of a global effect.

1.4 Reactivity Feedback

In an operating reactor, changes in reactivity are introduced by engineered control systems in order to manipulate the neutron population, and thus the energy output, of the reactor. At the same time reactivity is affected by the temperature and density of every material present in the reactor core, which in turn depend upon the reactor power. It follows that routine operation of this core includes continuous compensation for the reactivity effects of these state variables.

This non-linear feedback situation is illustrated in Figure 1.2, where reactor power as the output parameter and "total" reactivity, $\rho_{tot}(t)$, is the sum of both the reactivity due to feedback, $\rho_f(t)$, and the reactivity externally applied, $\rho_{ext}(t)$. In an operating CANDU reactor, $\rho_{ext}(t)$ would be supplied by a number of light-water zone controllers and stainless-steel adjuster rods.

The sensitivity of $\rho(t)$ to state variables associated with different reactor core states is measured by the *reactivity coefficient*,

$$\alpha_x \equiv \frac{\partial \rho}{\partial x} \quad , \tag{1.14}$$

where x is the state variable. As an example, the *fuel temperature reactivity coefficient*, α_T, caused predominantly by Doppler broadening of resonance absorption cross-sections, is about -0.0135 mk/°C for fresh fuel in the CANDU core and -0.0005 mk/°C at discharge burnup[3]. This creates a component of reactivity feedback (other components such as coolant and fuel density would be taken into account simultaneously) that reactor control

systems must accommodate when changing power levels through external reactivity (ρ_{ext}) manipulation. The irradiation dependence of the fuel temperature reactivity coefficient in the example above indicates the significance of irradiation ("burnup") and the corresponding importance of accurate fuel history models.

This dissertation addresses the issue of *coolant void effect*, which is directly related to the coolant void reactivity coefficient, the system response to removal of coolant. This concept will be defined fully in Chapter 2, but it is worth noting here that two of the most important factors in assessing the usefulness of a void effect calculation is knowledge of the precise definition of void effect used and the fuel history model used. The methodology for calculating reactivity coefficients, to be described in detail in Chapter 2, starts by reducing the problem to a study of a single *lattice cell* model. A lattice cell is the smallest repeatable structure in the reactor core, usually consisting of a fuel region surrounded by coolant and/or moderator and support material, extending out to a suitable boundary condition representing the rest of the core. Chapter 2 elaborates on the ramifications of this model, and Chapter 3 describes the CANDU lattice cell.

1.5 The CANDU Design and Philosophy

The CANDU (which stands for "CANadian Deuterium Uranium") reactor is a Canadian power reactor design developed by AECL in the 1960's with evolutionary roots[4] in the large research reactor installations at Chalk River, Ontario. Figure 1.3[5], illustrates the generic CANDU steam-supply system. The core consists of pressure tubes (380 to

480, depending on the design) that penetrate a D_2O-filled moderator tank called the *calandria* and contain 12 or 13 half-meter long fuel bundles of 28 ("Pickering" design) or 37 ("Bruce" design) natural UO_2 fuel pins, as depicted in Figure 1.4[5]. Net electrical output ratings range from about 500 MWe to about 900 MWe, depending on the design. More detail, with special focus on the commercial version, CANDU 6, can be found in Reference 5.

The central philosophy of the CANDU design can be summarized with the phrase, *fiscal economy through neutron economy*. Canada originally developed a natural uranium-fuelled power reactor because this country possesses large amounts of uranium ore, and no large-scale fuel enrichment technology. This forced CANDU designers to work with a strong mindset for *neutron economy* (avoidance of neutron wastage by parasitic absorption), since this is the only way a reactor fuelled with natural uranium can be competitive[6,7,8] against other designs. They discovered, for example, that a cost advantage is gained by cooling the D_2O moderator instead of letting it run hot, because of the resulting increase in effective fuel fission cross-section[9].

An emphasis on neutron economy produces low total fuelling costs in any reactor design, but the lowest fuelling costs are achieved with natural uranium and an extreme emphasis on neutron economy[10]. As parasitic absorption increases an advantage is gained with enrichment (for example, the optimum enrichment for uranium utilization in the CANDU core is around 1.2%[11]), but fuelling costs are usually greater. Additionally, high neutron economy provides the CANDU design with the strategic benefit of being an industry leader in resource utilization, and of having available alternate fuel cycles such

as thorium fuels and recycled fuel from light water reactors[3,11,12,13].

The coupling of fiscal economy and neutron economy is not absolute, and in some cases a cost advantage is gained by accepting a certain wastage of neutrons. For example, the thermodynamic efficiency of the CANDU system is improved as coolant temperatures are increased, requiring thicker pressure tubes that increase parasitic absorption. The CANDU approach to neutron economy therefore does not preclude compromise if appropriate mitigating factors are involved.

1.6 Coolant Voiding Scenarios in the CANDU System

For reasons to be outlined in Chapter 3 the coolant void coefficient in operating CANDU reactors is positive. In compensation for this, the reactors are designed with a thoroughly distributed flux detection system, and a fast and reliable system of shutdown rods backed up by an independent secondary shutdown system (liquid poison moderator injection or moderator gravity dump, depending on the design)[5]. Large Loss-of-Coolant-Accident (LOCA) analysis in CANDU safety studies therefore deals mainly with the thermalhydraulics of a subcritical or shutdown core[14]. However, in order to assess the requirements of a safety shutdown and core cooling system in the first place it is necessary to accurately characterize both the power pulse caused by the LOCA and the resulting state of the fuel (fission product inventory, centre-line temperature, etc.) at the moment of shutdown. This requires knowing the neutronic reaction time of the fuel during the first milli-seconds of a LOCA, and hence an accurate estimate of the coolant

void reactivity coefficient is needed. One must be aware of the dependence of this coefficient, if any, on spatial distribution of voiding, and one must know the different modes with which a LOCA can occur.

The CANDU primary cooling system is divided into two parallel circuits, each servicing one horizontal half of the core[5]. This fact alone makes it very unlikely that more than half the core will experience a LOCA at one time (detailed risk analysis and system behaviour will not be part of this dissertation, however). Within either circuit is a network of piping with diameters ranging from roughly 1 cm (instrument tubing, steam generator tubing) to over 15 cm (header piping, headers), leading to a corresponding range of *pressure drop rate* and *volumetric leak rate* scenarios with leak probabilities decreasing with increasing diameter. Countering these scenarios are three coolant inventory control systems triggered by different primary pressure levels: normal D_2O feed, high-pressure H_2O injection, and low-pressure H_2O injection. Even without external control the pressure drop following a LOCA would take a finite amount of time depending on the location of the break, and the action of these control systems extends the associated time constant to several minutes (stopping at a minimum pressure level determined by the requirement for decay heat removal)[14].

The "worst-case" LOCA scenario used in CANDU safety analysis is a 100%, instantaneous break in either a reactor coolant header or a primary pump suction pipe. In contrast, the calculation of the coolant void coefficient at the lattice cell level (employing Equation (1.14)) involves an instantaneous removal of coolant inventory, as described in detail in Section 2.1. The result is a parameter for use in subsequent safety

analysis, and not, in isolation, an indication of the system reactivity response to realistic voiding scenarios. The parameter is also useful as a point of comparison in parametric studies, such as this dissertation.

1.7 AECL Programme to Lower Coolant Void Reactivity

Although in current CANDU design the complication of added reactivity at the outset of a LOCA is countered by strict shutdown requirements for speed, efficiency and reliability, a potential marketing problem exists. Non-domestic reactor licensing agencies such as the US NRC have generally not been exposed to design license applications that include positive coolant void reactivity coefficients, and their criteria reflect this[15]. More importantly, a global shift towards design simplification with less reliance on engineered safety (so-called *passive safety*) threatens the CANDU design's ability to compete in the future, if only because of this one characteristic[16]. It is important to note that large swings of reactivity in *any* direction can introduce instabilities to be designed against, and also that a negative void reactivity coefficient does not guarantee negative reactivity in all thermalhydraulic scenarios (for example, large void collapse in a BWR[17]). Furthermore, it is also noteworthy that the prompt neutron lifetime[2] in the D_2O CANDU lattice is about 30 times longer than in a typical LWR lattice[18], making the termination of neutronic excursions a comparatively easier task. This is the case not only because of the larger time constant, but also because the slope of the transient does not change appreciably upon crossing the point of prompt criticality[18]. Nevertheless, a problem of

perception does exist with the positive void reactivity coefficient of the CANDU reactor.

AECL has addressed this concern with a programme to develop Low Void Reactivity Fuel (LVRF) for the CANDU core. The chief candidate design at the moment involves the addition of burnable poison to strategic regions of the fuel bundle, combined with the use of low enrichment uranium (LEU) of varying degree throughout the bundle[19]. This approach, which will be explained from a reactor physics point of view in Chapter 4, Section 4.2.4, represents a relatively easy target for LVRF in terms of R&D commitment, and has currently reached the physical testing stage[20]. In calling for poison material to be added to the fuel, however, this approach also implies a major departure from the principle of maximum neutron economy presented in Section 1.5. Thus a penalty in uranium utilization can be expected as a compromise for satisfying client requirements with respect to void reactivity in this manner.

1.8 Goals of Present Dissertation

One of the goals of this dissertation is to pursue a "more difficult" target for LVRF in the CANDU core — observing neutron economy and thus adhering to the original CANDU design concept. As such, this work will explore the periphery of what is practically possible in the future development of CANDU fuel. The expectation of being on the "periphery" is mainly due to the added expense of fuel redevelopment and associated safety studies that will be required for implementation. Not unlike the current AECL LVRF programme, this study will seek a fuel design that is compatible with

current CANDU systems. Fuel burnup, and thus resource utilization, must not suffer significantly as a result of design modifications, for this will amplify the economic argument against any necessary fuel redevelopment. For the same reason the fuel throughput rate should not be altered significantly; that is, a fuel design with comparable burnup to the current design should also require a comparable mass of fissile material. Thermalhydraulic parameters such as channel inlet and outlet enthalpy will be maintained, as will coolant flow rate; thus, the steam supply characteristics will be unchanged. The moderator (and, in fact, everything radially outward from the pressure tube) will also be unchanged, although the effects of modifying the fuel channel and moderator materials will be examined. Keeping within the goal of neutron economy, the degrees of freedom that remain to be probed are fuel geometry and enrichment. This will be the direction of this dissertation.

Before this direction can be taken, it will be necessary to examine the reactor physics of CANDU fuel and the nature of coolant void reactivity feedback. Another goal of this dissertation is therefore to investigate the current methodology for analysing the coolant void effect in the CANDU lattice cell, in order to clearly define the technique to be used herein, and the bounds within which this technique is applicable. This technique will then be applied to investigate the causes of the coolant void effect in the CANDU lattice cell, separating the component effects into spectral, spatial, and material categories in order to determine a direction in which to seek designs with low void reactivity.

It will not be within the scope of this work to perform a full-scale LOCA calculation such as that usually carried out in CANDU analysis. A complete void

reactivity study includes a coupled thermalhydraulics and neutron kinetics calculation (using, for example, CATHENA and CERBERUS, respectively, at AECL), employing a lattice code to provide the modified material cross-sections[21]. It is within this latter category that the present work will have relevance, in accordance with the various assumptions and definitions to be described in Chapter 2.

A note should be made concerning what level of void reactivity would be considered "acceptable". While any value greater than zero contravenes policy in some jurisdictions, it is recognized that positive values have the benefit of providing a neutronic mechanism for tripping the reactor's safety system. This is a much faster mechanism than thermalhydraulic processes, although it demands high reliability and speed in the response of the safety system, such as that found in the CANDU design. Therefore, while a negative void reactivity will be sought in this dissertation, a positive value less than that inducing prompt criticality will be considered acceptable. This corresponds[2] to a maximum value equal to the delayed neutron fraction, β, which can be estimated at zero-burnup using β for U-235, and at mid-burnup using a weighted sum of the β values for U-235 and Pu-239. At zero-burnup, therefore, the limit is 7 mk ($\beta_{zero} = 0.007$), and at mid-burnup the limit is 5 mk ($\beta_{mid} = 0.005$). The weights for the calculation of β_{mid} were each 0.5, corresponding to an approximately equal average cell neutron yield ($\nu\Sigma_f\phi$) from each of these isotopes at mid-burnup.

Any analysis of void reactivity feedback in the CANDU lattice cell will necessarily have the following two characteristics:

(1) high dependence on CANDU-specific literature, and

(2) high dependence on computer simulation.

The first point arises because the physics of coolant void reactivity is sensitive to lattice details such as fuel geometry and composition, lattice pitch, structural materials, coolant and moderator temperature, and burnup history. Although other non-CANDU studies of coolant void reactivity exist[22,23,24], they are of little relevance beyond the illustration of general concepts and methods. The second point arises because of the highly heterogeneous nature of the CANDU lattice cell and the extremely detailed spectral information that must be accurately modelled. With the advent of economical high-speed, high-memory computers it has become routine to analyze reactor lattices with a degree of spatial, spectral, and (if applicable) time subdivision that renders analytical and empirical modelling unnecessary (except where lattice analysis is integrated with larger space-time kinetics or burnup analysis[21,25]). This creates a reliance on numerical calculation which must be checked against experiment and more fundamental calculations, such as Monte Carlo (see next section). These two points, therefore, will also characterize the present dissertation.

1.9 Codes to be Used: WIMS-AECL and MCNP-4

The two-dimensional lattice cell and burnup code WIMS-AECL[26,27] will be used to provide the calculations used in this dissertation. WIMS-AECL uses the method of collision probabilities to solve the integral form of the steady-state Boltzmann neutron transport equation[28,29]. The collision probabilities, P_{ij}, represent the probability, in

cylindrical geometry, of a source neutron in region "i" having its first collision in region "j", and are based on the transport kernel in cylindrical geometry,

$$Ki_2(x) \equiv \int_0^{\pi/2} \cos\theta \, e^{\frac{-x}{\cos\theta}} \, d\theta \quad , \tag{1.15}$$

where the integration over θ represents a uniform source along the axial direction, and x is transport distance in mean free pathlengths. The more general functions $Ki_n(x)$ are known as n[th] order *Bickley functions*[28,30,31]. WIMS-AECL calculates group-wise, regional fluxes over a spatially clustered (PIJ option) or annular symmetry (PERSEUS option) lattice cell. Resonance region cross-sections are calculated on a case-dependent basis from tabulated resonance integrals, which are interpolated according to temperature and background, or potential, scattering cross-section. The library resonance integrals are applicable for homogenous mixtures of each isotope, and therefore an equivalence relation[2,28,32] is used to relate these values to heterogeneous geometries. For this purpose an *escape cross-section*, which is a function of the volume-to-surface ratio of an average fuel pin, is added to each nuclide's background scattering cross-section for interpolation in the tables. In addition to being calculated for an average pin geometry, the group resonance cross-sections are also calculated for an average pin composition and temperature. This model is acceptable for clusters of identical pins, but it will not provide proper resonance cross-sections if fuel composition or geometry varies within the fuel cluster.

Leakage is treated by an added absorption cross-section DB^2, where D is a Benoist diffusion coefficient (a simple transport calculation can also be chosen), and B^2 is a user-

supplied buckling value. WIMS-AECL can also calculate the buckling needed to create a critical lattice.

WIMS-AECL is based on a version of WIMS[33] supplied to AECL by the UKAEA in 1971, and since developed at AECL[34] for CANDU analysis. Two libraries can be used, a 69-group "Winfrith" library (24 thermal, 40 epithermal, 5 fast[1]) based on the library supplied by the UKAEA, and an 89-group "ENDF/B-V" library (24 thermal, 55 epithermal, 10 fast[2]) based on ENDF/B-V data[35,36]. The Winfrith library will be used here unless otherwise stated, due to the unavailability of the ENDF/B-V library to the author for most of the period of this project. In all cases the full library energy multigroup structure will be used.

WIMS-AECL is the main lattice code used by AECL-Research for CANDU analysis, and it has tested favourably against zero energy experiments and numerical benchmarks that include voided coolant conditions[37,38]. Nevertheless, it will be necessary to test the performance of WIMS-AECL under the non-standard geometries and compositions that will be examined in this dissertation. For such testing, the Monte Carlo code MCNP-4[39] will be utilized. MCNP-4 is a much more fundamental code than WIMS-AECL, relying on stochastic rather than deterministic methods, and employing a "quasi-continuous" point-wise cross-section library with as many as 22,500 points (for Au-197). The library is derived from ENDF/B-V and encompasses the energy range from 10^{-5} eV

---

[1] 0 eV ≤ thermal ≤ 0.625 eV ≤ epithermal ≤ 0.821 MeV ≤ fast ≤ 10 MeV.

[2] 0.2 meV ≤ thermal ≤ 0.625 eV ≤ epithermal ≤ 0.82085 MeV ≤ fast ≤ 10 MeV.

to 20 MeV. In many ways an MCNP-4 calculation can be considered a benchmark numerical calculation, within its own statistical calculation accuracy, the accuracy of its library evaluations, and of course the accuracy with which its user defines each problem.

In MCNP-4 a statistical picture of neutron distribution in three dimensions is assembled by sampling the transport probability,

$$p(x) = e^{-\Sigma_t x} \quad , \tag{1.16}$$

and the reaction probability (cross-sections) over a large enough number of "histories" to attain acceptable accuracy. In the case of a criticality calculation the code samples a source distribution which converges as enough histories are followed. A variety of different tallies can be compiled (fluence, current, reaction, energy deposition, etc.) and several estimates of criticality (k_{eff}) can be made, all accompanied by estimates of statistical accuracy.

The Monte Carlo method developed from early work by Fermi, von Neumann, and Ulam at the Los Alamos Laboratory during World War II. MCNP-4 is the descendent of this work, capable of tracking photons and electrons as well as neutrons. It is quickly becoming an worldwide industry standard for numerical benchmarking of deterministic analyses, although it is not routinely used as a routine analysis tool itself because of the time required for accurate calculations. Comparisons of MCNP-4 and WIMS-AECL for criticality and reactivity calculations have been made[40,41], raising some concerns that will be addressed when such comparisons are made in this dissertation.

It has only recently become practical to run a code like MCNP-4 on a personal

computer platform. Unless otherwise indicated, all calculations reported here with both MCNP-4 and WIMS-AECL were generated on an IBM-PC/486 computer.

1.10 Outline of Dissertation

The background information for this dissertation, along with a statement of intentions, has been presented in this chapter. This section will now summarize what is to follow in subsequent chapters, including indications of original contributions to the research in this field, where applicable.

Chapter 2 lays the groundwork for the present study, specifying important definitions, methodologies, and limitations. A critical review of methodologies for lattice cell parametric reactivity studies is presented. This includes a look at the varying interpretations of "void effect", and the sensitivity of the result when lattices with high supercriticality are examined. The latter situations include CANDU lattices at zero-burnup and CANDU lattices containing enriched or plutonium fuels. This review material, and the nomenclature suggested to clarify the interpretations, has not been presented before in the literature. This portion of Chapter 2 was presented as a separate paper[42] by the author to the 1994 Canadian Nuclear Society Simulation Symposium.

Also in this chapter are a comparison of the diffusion theory components of leakage between WIMS-AECL and MCNP-4 (presented as a separate paper[50] by the author to the 1994 American Nuclear Society Topical Meeting on Reactor Physics), and an investigation of the effect of accounting for changes in neutron lifetime in lattice cell

parametric studies. Similarly, the effect of accounting for heterogeneous void distributions is examined (presented as a separate paper[54] by the author to the 1992 American Nuclear Society Annual Conference). All of these investigations represent original contributions.

An important section in Chapter 2 formulates the methodology by which lattice cell results will be separated into factors affecting criticality. This separation is a formal process involving a Taylor expansion, with the result that the separated components sum exactly to the total effect. This treatment is not original in concept, but in practice it has not been used elsewhere since such internal consistency is only important when highly non-critical lattices are studied. The application here is therefore original, as is the code used to generate the components. This represents the main analysis tool used throughout the dissertation.

In Chapter 3 the spectral, geometric, and material causes behind the void effect in the current CANDU design are investigated. Most of this material has been reported in various forms before, but this chapter represents a comprehensive study which, in scope and detail of analysis, has not been published elsewhere. Certain figures, such as those showing the net change in both neutron spectrum and spatial distribution, are original presentations. The material in this chapter is necessary for an understanding of what is required to reduce the void effect. Most of this chapter comprises an invited paper[55] to be presented by the author to the 1995 American Nuclear Society Annual Conference.

Chapter 4 is a wide-ranging investigation of the many types of changes to the void

effect that can be effected by manipulating the material and geometric properties of the fuel. Also included, despite not being strictly within the goals of this dissertation, are the effects of making changes to the moderator and pressure tube materials. Many of these areas have been investigated or suggested in other reports, but this represents another comprehensive analysis and review that has not been seen elsewhere. This chapter provides the incentives for the modifications made in the next chapter, as well as providing the pointers indicating which category of modification is of more importance.

In Chapter 5 all remaining geometric constraints are removed and an optimum fuel shape is found in terms of void effect reduction. An annular shape located next to the pressure tube wall is the result, which is then evolved to become either a nested tubular or curved-plate fuel once thermalhydraulic considerations are taken into account. The final geometry is determined by numerical search based on thermalhydraulic criteria. Additional practicalities are addressed, including the issues of manufacturing and economics. Uranium enrichment and other fuel cycles are examined for both applicability and as measures to further reduce the void effect. The basic idea of confining CANDU fuel to an outer annular region is not new, but the present application in the form of tubular or curved-plate geometry for the purposes of void effect reduction in the CANDU lattice is original. The neutronic and thermalhydraulic justifications for the proposed designs, and the numerical algorithm performed to determine the final geometry, are also of original content.

Several modelling concerns with WIMS-AECL are also raised in Chapter 5, and a major issue concerns a deficiency in the calculation of resonance group cross-sections

for annular (tubular) fuel geometries. The *S/V Resonance Correction Model* is developed, based upon corrected modelling of the fuel surface-to-volume ratio (S/V). This correction circumvents the major cause of this deficiency, although remaining concerns about the resonance treatment are left uncorrected. This correction model for annular geometries in WIMS-AECL is an original contribution.

Finally, Chapter 6 is a summary of the work put forth in this dissertation. Conclusions and observations are stated, and suggestions for further analysis stemming from the work here are made.

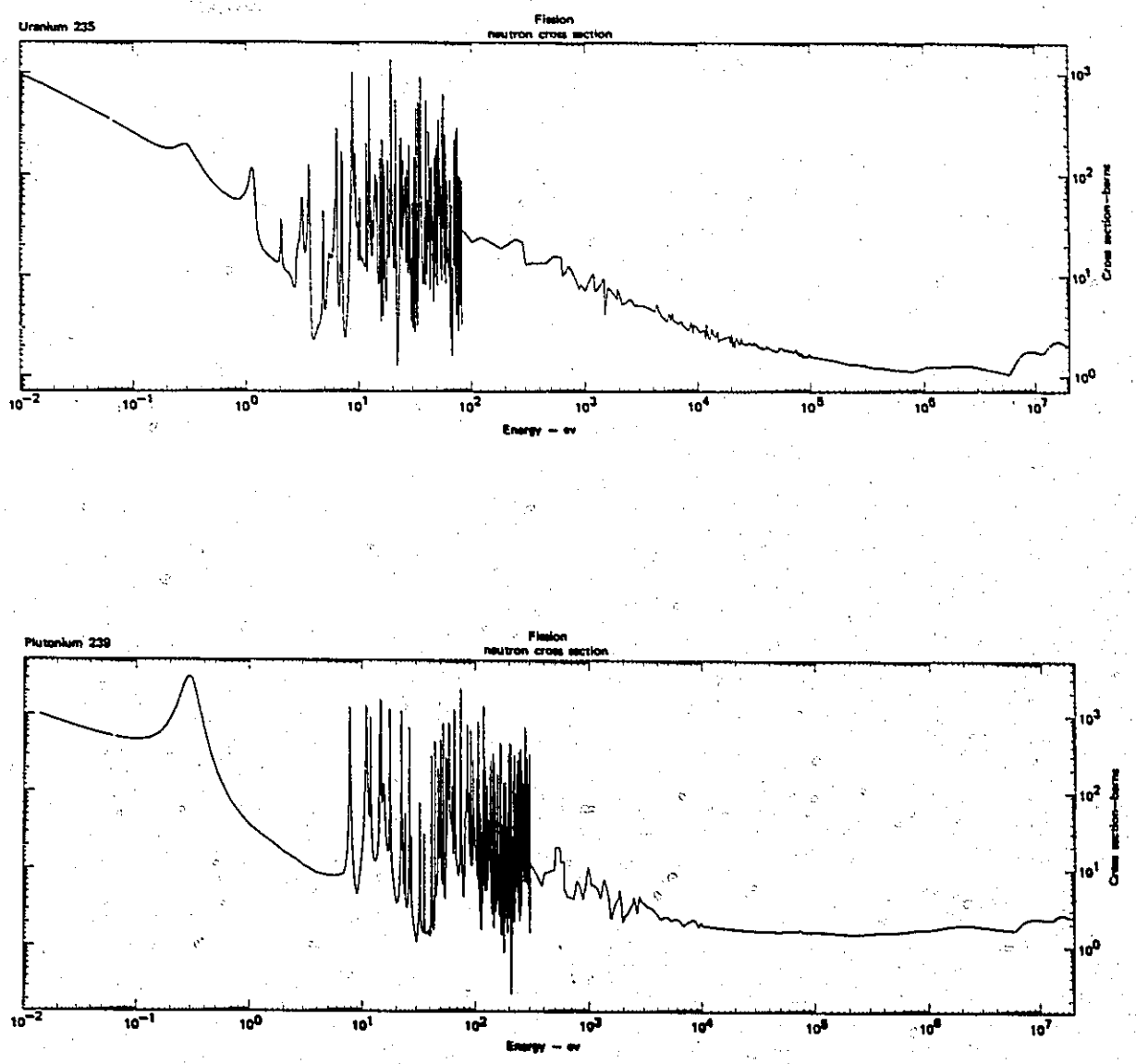

Figure 1.1 Fission Cross-Section (σ_f) vs. Energy for U-235 and Pu-239.

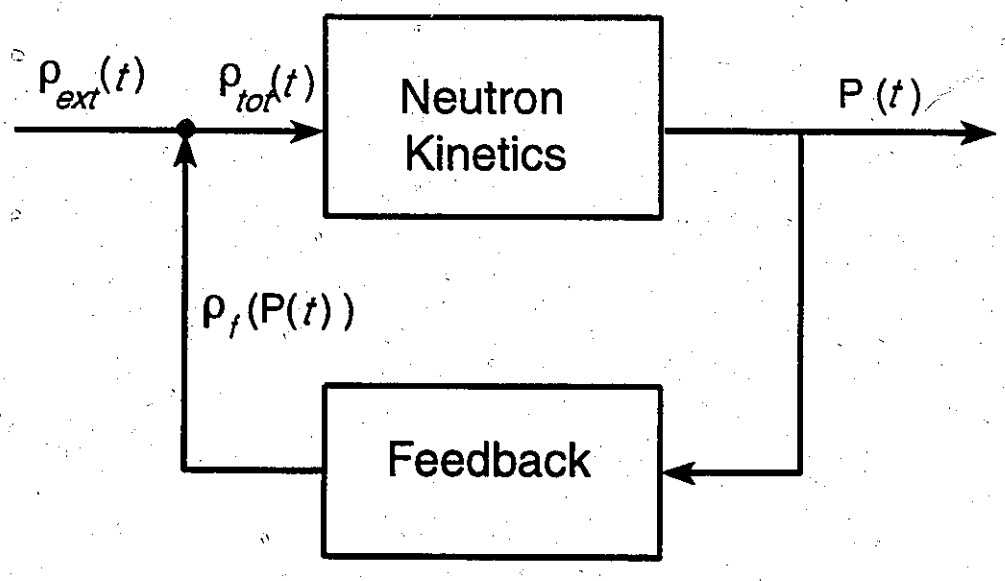

Figure 1.2 Model of Reactivity Feedback.

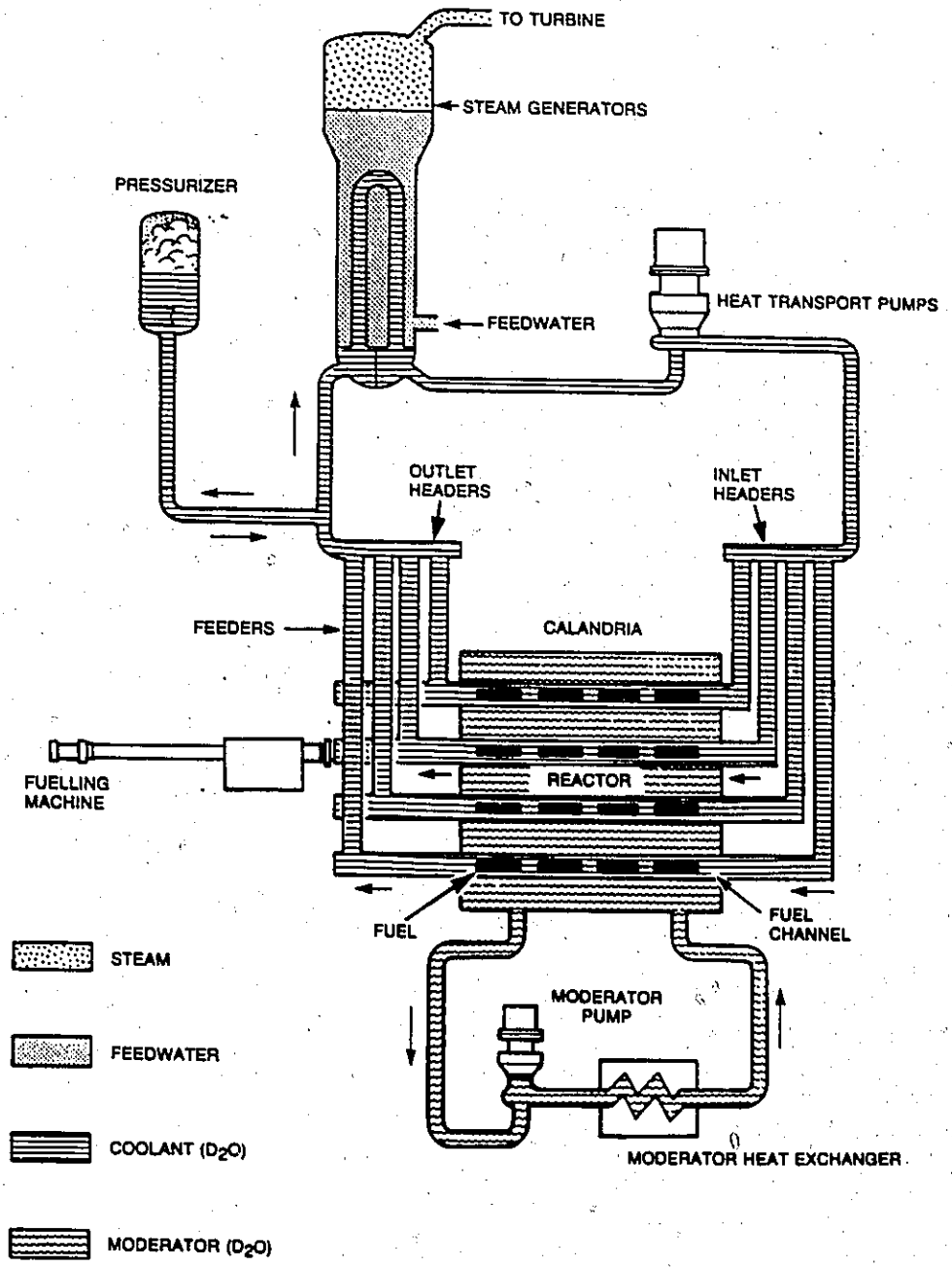

Figure 1.3 CANDU Steam Supply System.

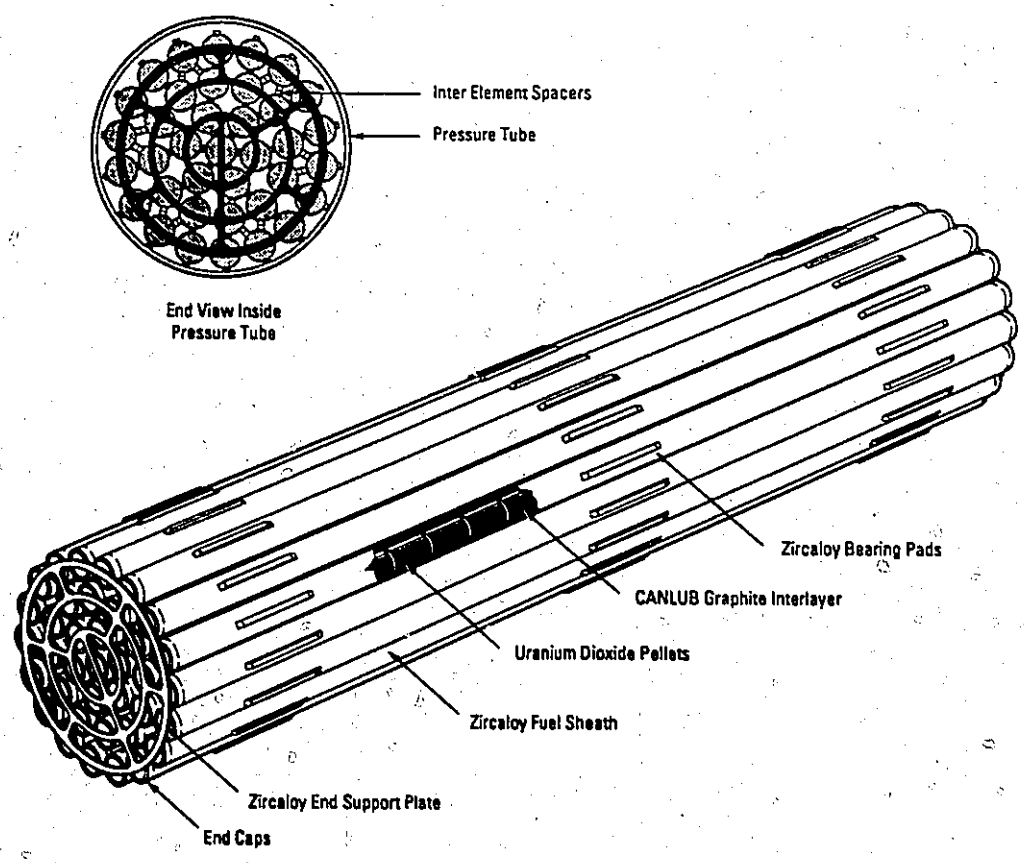

Figure 1.4 37-Element CANDU Fuel Bundle.

Chapter 2

Method of Calculating Void Effect

In this chapter the terms of reference for a study of void effect in CANDU are established, beginning with the definition of "void effect" itself. Several important issues regarding methods and assumptions are treated separately, leading in the end to a clear statement of position that will be adopted for the remainder of this work. It is intended that self-consistency will prevail, and although it is the intention of the author to remain consistent with the literature as much as possible, it will be necessary (where noted) to define certain non-standard concepts. This chapter will develop a methodology by which WIMS-AECL will be used the main analysis tool in this dissertation, and it will outline some of the limitations associated with such use.

Sections 2.1 and 2.2 have been combined in a separate paper by the author[42]. Also, material in Sections 2.2.4 and 2.4 is drawn from separate papers by the author, as indicated in those sections.

2.1 Definition of Void Effect

The coolant void coefficient is defined by Equation (1.14), where the state variable "x" in this case is coolant *void fraction*[43] or void-to-total volume ratio, α_C (to avoid

confusion however, the void coefficient in Equation (1.14) is usually denoted α_v). A rigorous calculation of this coefficient would take into account second-order effects associated with coolant voiding. These include lattice geometry changes due to reduced heat removal (for example, fuel swelling) and spatial void distributions that would depend on the degree of boiling and the fractional volume of coolant lost (for example, surface nucleate boiling versus channel stratification). One would also include the effects of global void distributions, given that the entire core may not be losing coolant simultaneously or at the same rate. At the same time consideration must be given to global flux redistributions initiated by these spatial effects. Such rigour would unnecessarily complicate and defocus the comparisons to be made here; therefore, for the present purposes, and in keeping with the intent of lattice cell coefficient calculations described in Section 1.6, it will be assumed that the total coolant inventory voids instantaneously. Furthermore, the response of the reactor's reactivity regulation system will not be accounted for, and neither will there be any accounting of concurrent reactivity effects during a LOCA (for example, fuel temperature coefficient or moderator density coefficient). Hence, the analysis reported in this dissertation will be of an isolated physical effect, but indicative of its contribution to core behaviour in a realistic upset scenario. This approach is consistent with that of industry[19,41,44].

The "isolated physical effect" just described is an integrated quantity that will be called the coolant *void effect*,

$$\rho_V \equiv \int_{\alpha_C=0}^{1} \frac{\partial \rho}{\partial \alpha_C} d\alpha_C \quad , \tag{2.1}$$

where α_C is the coolant volumetric void fraction, and the progression from $\alpha_C = 0$ to 1 is assumed to take place instantaneously. However, further qualification is needed before a complete definition can be adopted. The problem that arises in normal practice is that k_{eff}, as calculated by a lattice code before voiding, is almost never equal to unity, while the operational core which one wishes to model is always held by additional reactivity mechanisms at exactly $k_{eff} = 1.0$. The result of Equation (2.1), therefore, is usually expressed as a reactivity perturbation relative to the non-voided (or "cooled") case,

$$\Delta\rho_V \equiv \left(\frac{k_{eff}^V - 1}{k_{eff}^V}\right) - \left(\frac{k_{eff}^C - 1}{k_{eff}^C}\right) = \frac{\Delta k_{eff}}{k_{eff}^V k_{eff}^C} \quad , \tag{2.2}$$

where the superscripts V and C indicate "voided" and "cooled" cases, respectively (this notation will be used throughout this dissertation). Alternatively, it is equally valid to express reactivity changes in the lattice cell as a simple perturbation in k_{eff},

$$\Delta k_{eff,V} \equiv k_{eff}^V - k_{eff}^C \quad . \tag{2.3}$$

In this dissertation the *void reactivity effect*, $\Delta\rho_V$, will be defined by Equation (2.2), and the *void criticality effect*, Δk_{eff}, will be defined by Equation (2.3). Both terms will tacitly apply to coolant voiding only, and both will be measured in units of *mk* (although this is not rigorous). Both interpretations of void effect have been used in industry; however, the specific nomenclature applies only to this dissertation. It is proposed that this nomenclature be adopted by others, in the interest of clarity in reporting.

When k_{eff} is close to unity the two terms will be almost equal; when k_{eff} differs significantly from unity, the lack of normalization in Equation (2.3) will give a much

different numerical result from Equation (2.2), sometimes suggesting an opposite interpretation of the same physical effect. To illustrate, a result from a later chapter is introduced here, leaving the unnecessary details for later explanation. Figure 2.1 shows a plot of $\Delta\rho_V$ and Δk_{eff}, defined by Equations (2.2) and (2.3) respectively, as functions of fuel enrichment (natural to 2%wt.), illustrating an obvious discrepancy not only in magnitude of the "void effect", but, more importantly, also in direction of the trend. In both cases simple geometric bucklings ($B^2 = B_R^2 + B_Z^2 = 7.62\times10^{-5}\ \mathrm{cm}^{-2}$) typical of the CANDU core were used to generate k_{eff}.

The case comparing natural and 1.2% enriched fuel is presented in Table 2.1 for closer examination. Here the method of Equation (2.2) predicts a 4 mk decrease in the void reactivity effect if 1.2% enriched fuel were used instead of natural fuel, while the method of Equation (2.3) predicts a 1 mk *increase*. This relatively small difference of 5 mk between the two methods is not as important as the fact that one method leads to the conclusion of a benefit in moving to slightly enriched fuel in terms of void effect reduction, while the other suggests a detriment (for a zero-burnup core).

The question becomes: which definition is more meaningful? Equation (2.2) is certainly consistent with the neutron kinetics description in Equation 1.4, but "reactivity" by itself represents a perturbation to a critical system, making Equation (2.2) a perturbation to a perturbation. The first of these perturbations, as discussed, would really be zero in a critical core. On the other hand Equation (2.3), while deviating from the original definition of reactivity, still represents an intuitive expression of absolute change in neutron multiplication. In the context of lattice cell modelling (as opposed to system

modelling) one could reason that if the void reactivity effect (Equation (2.2)) were flawed, then a simple difference like the void criticality effect (Equation (2.3)) should still suffice to describe the proper trends. This question is further addressed in Section 2.2.2; however, as much as possible, both interpretations of "void effect" are used in this dissertation.

2.2 Concerns About Lattice Cell Modelling

There is a great advantage in using a lattice cell code like WIMS-AECL to estimate reactivity effects in a CANDU core. Geometry and material perturbations can be modelled with realistic detail, while the simplicity of a cell model still allows extensive parametric studies (including burnup) to be performed. Care must be taken, however, to recognize all the needs and shortcomings of this process when setting up cases and interpreting results.

2.2.1 Lattice Cell Approximation

Foremost of these concerns is the lattice cell approximation itself, which assumes a repetitive arrangement of identical cells out to infinity. Any cell perturbations are therefore global in nature. In Section 1.3 reactivity itself was described as a global parameter, but this is not the same thing: A lattice cell code cannot predict the "true" system reactivity of a localized perturbation.

This inherent feature means that results of simple WIMS-AECL calculations of

reactivity effects are valid only for homogeneously fuelled and homogeneously perturbed cores. CANDU cores past their commissioning stage are never homogeneously fuelled, typically containing fuel bundles at all stages of the fuel cycle[45], and therefore a WIMS-AECL calculation at mid-burnup comes close to modelling reality (even a CANDU core at start-up contains some depleted fresh fuel to aid in flux flattening[3]). Indeed, it has been reported[44] that the leakage spectrum at mid-burnup with geometric bucklings most closely models equilibrium conditions in a CANDU core. In CANDU simulations discharge fuel burnup can be estimated by integrating excess reactivity throughout the cycle until it equals zero[3], and using only WIMS-AECL this point can be approximated when the time-weighted average of k_{eff} equals about 1.02 (allowing approximately 20 mk for unmodelled control absorbers)[46]. This situation is illustrated in Figure 2.2. The point of mid-burnup then corresponds to a burnup fraction of 0.5, at which point a 100% coolant void condition can be modelled and a void effect calculation made. Void effect calculations can also be made at any other burnup fraction, although their usefulness will be in question.

A better approximation of the equilibrium CANDU core would not be at the point of mid-burnup, but the point of zero excess lattice reactivity. This is the point, also illustrated in Figure 2.2, where k_{eff} itself equals 1.02, once again allowing for control absorption. The difference between the points of mid-burnup and zero excess reactivity is shown in Figure 2.2 to be about 4% of burnup (about 300 MWd/Te), which is the situation for the reference 37-element case to be described in the next chapter. The difference in k_{eff} between these two points is about 4 mk, and the difference in the void

effect is negligible (< 0.1 mk). Since the much simpler estimation of mid-burnup lends itself readily to parametric calculations, this method is used in this dissertation. When a final design is arrived at, however, this approximation will once again have to be checked for validity (Section 5.5).

2.2.2 Void "Reactivity" Effect vs. Void "Criticality" Effect

The crux of the problem illustrated in Figure 2.1 is the significant amount of excess reactivity added to the CANDU lattice when enriched fuel is used. Under operating conditions this reactivity would be suppressed with adjustable or burnable absorbers, or with fuel shuffling. This situation could be approximated by adding enough buckling to the cell to produce a critical lattice (k_{eff} = 1.0), which will be referred to as using *critical bucklings*. Such an artificial state of criticality, however, should not be interpreted as an accurate model; spectrum effects corresponding to realistic reactivity suppression would not be included. It should be noted that a recent study[47] of temperature feedback in PWR lattices argues that the leakage spectrum under such artificial criticality is a reasonable approximation of the net leakage spectrum between adjacent core regions. On the assumption that k_{eff} = 1 on a regional basis within the core, this reference defines a more appropriate form of the right-hand side of Equation (2.2), with a single k_{eff} present in the denominator determined by averaging the unperturbed and perturbed k_{eff} values. Under the imposition of critical buckling, however, such an approach will not significantly alter the findings to be presented here.

Using the critical material bucklings supplied by the WIMS-AECL buckling search for the cases of natural and enriched fuel (B^2_{crit} = 2.85×10^{-4} cm^{-2} and 8.52×10^{-4} cm^{-2}, respectively), the summaries of results shown in Table 2.2 and Table 2.3 can be made for zero and mid-burnup cases, respectively. From Table 2.2 we see that the zero-burnup void effect drops by about 9 mk if 1.2% enriched fuel were used instead of natural fuel, according to the calculation using critical bucklings. This is in contrast to the 4 mk decrease calculated using geometric bucklings and Equation (2.2) and the 1 mk increase predicted using geometric bucklings and Equation (2.3). Thus, at the stage of zero-burnup when excess lattice reactivities are large, both the void reactivity effect and void criticality effect show sizeable discrepancies between the standard calculation and the artificially critical calculation. The void reactivity effect (Equation (2.2)), however, does demonstrate the same trend with both geometric and critical bucklings.

Looking only at the void reactivity effects in Table 2.2 (first row), an explanation is needed for the disparity between the 9 mk and 4 mk improvements in void effect, predicted using critical and geometric bucklings, respectively, when switching from natural to 1.2% enriched fuel. The answer lies in the relative importance of leakage vs. absorption to overall neutron loss in the cell. For the cases using geometric bucklings the proportion of leakage to overall cell loss is 3% for both natural and 1.2% enriched fuel (calculated from the WIMS-AECL output file information). When critical bucklings are used, however, this proportion increases from 9% for natural fuel to 22% for 1.2% enriched fuel, because of the larger bucklings necessary in the latter case in order to force criticality. Since both fast and epithermal leakage terms will increase upon voiding, this

greater leakage importance (by over a factor of two) with 1.2% enriched fuel and critical bucklings introduces a significant increase in neutron loss upon voiding, tending to counter the void effect contribution from a decrease in resonance absorption, while supplementing the contribution from an increase in fast absorption (these contributing effects will be explained in the following chapter). This is the major reason for the apparent difference in void effect improvement, by more than a factor of two, although it should be kept in mind that this is still just a numerical experiment at this point. It must also be pointed out that this criticality approximation relies heavily on the WIMS-AECL leakage calculation, which is suspect at this point[48].

Since excess lattice reactivity decreases with burnup, it is not surprising that the differences between the void reactivity and criticality effects are much smaller in Table 2.3 (≤ 1 mk). The two methods both predict about a 1 mk increase in mid-burnup void effect if 1.2% enriched fuel were used instead of natural fuel, and the calculations using critical bucklings give similar predictions. The void criticality effects with critical bucklings are about 1 mk less than with geometric bucklings, while the void reactivity effects are almost identical.

Therefore, based on this assessment the following summary can be made:

(1) Zero-burnup (startup) lattices present a special problem for reactivity effect prediction using a lattice code. Even though the assumption of a uniform material composition throughout the core is most realistic at this time, the high excess lattice reactivity — which is suppressed in an operating core — distorts the predictions made using conventional ideas of reactivity.

(2) The void reactivity effect ($\Delta\rho_V$), tends to produce results with geometric bucklings that are more consistent with the artificially critical situation shown here. There is no basis, however, for believing that the void reactivity effect will be preferred for every scenario.

(3) The analysis at mid-burnup shows little discrepancy between the void reactivity and criticality effects, and high consistency between geometric and critical buckling cases. This is simply due to excess lattice reactivity at this point being very close to zero. Since mid-burnup represents the best approximation that a lattice code like WIMS-AECL can make of an equilibrium CANDU core, it is therefore a good idea to always calculate the void effect at this point. The exception, of course, occurs when the void effect for a fresh core is sought.

2.2.3 Creating a "Critical" Zero-Burnup Lattice with Borated Moderator

The question that must be addressed is whether or not a lattice cell code like WIMS can be used estimate the void effect in a fresh CANDU core. The sensitivity of void effect to the choice of bucklings (geometric vs. critical) was demonstrated above, leading one to seek a realistic approximation of *system* criticality for our *component* (lattice cell) model. The inclusion in the model of a burnable poison such as boron, usually added to fresh CANDU core moderators, is examined here (the use[3] of slightly depleted fresh fuel (0.57%) in some centre-region bundles of a new CANDU core for the purposes of flux-flattening has been neglected). In this case, the same approach as with

critical bucklings is used: enough absorber is added to the moderator to create a critical lattice. The difference here is the spatial location of the extra absorption, which one expects would better approximate a realistic state of zero-burnup reactivity suppression.

With the same geometric buckling used previously ($B^2 = 7.62 \times 10^{-5}$ cm^{-2}), the concentration of soluble boron in the moderator required to create a critical lattice was found to be 0.001%wt (10 ppm) for the case of natural fuel, and 0.0042%wt (42 ppm) for the case of 1.2% enriched fuel. The void effects are about 21 mk for natural fuel and about 25 mk for 1.2% enriched fuel. These "borated moderator" void effects are compared in Table 2.4 with the void effects previously found using geometric and critical bucklings.

With boron added to the moderator at zero-burnup conditions, this model predicts a 5 mk penalty in void effect associated with the move from natural to 1.2% enriched fuel, in comparison with the 4 mk and 9 mk benefits predicted with the models using geometric and critical bucklings, respectively. Even more important is the large disagreement among the void effects predicted by the three models for each fuel type. The void effects when boron is included tend to be larger because the thermal flux decreases significantly in the moderator region of the lattice cell upon voiding (discussed in Chapter 3), adding positive reactivity because of the boron's presence in that region. In going from natural to 1.2% enriched fuel this effect is enhanced by the higher boron concentration (about fourfold higher) needed to bring about a critical lattice.

An important dependence on criticality modelling is thus demonstrated for the situation of a fresh CANDU core. Compared to the "reference" non-critical case of using

simple, geometric bucklings, the substitution of critical bucklings tends to reduce the void effect through enhanced leakage upon voiding in the epithermal and fast spectrum, while the addition of boron to the moderator tends to amplify the void effect through enhanced thermal utilization upon voiding.

2.2.4 Voided Lattice Leakage

The analysis here has employed identical buckling values for both the non-voided and voided lattices. With this assumption, the change in leakage upon voiding depends only on change in the WIMS-AECL diffusion coefficient and flux distribution, reflecting void-induced perturbations to material cross-sections and neutron energy spectrum, respectively. This assumption is conservative, since buckling will generally increase slightly with voiding due to increased leakage, reducing the void effect.

The issue that arises with the use of critical material bucklings and "critically" borated moderator, however, is the nature of any void-induced changes in the control of system criticality which these methods attempt to model. This would include automatic regulation such as the movement of control rods or adjustment of light-water zone control units; however, the definition of void effect in Section 2.1 clearly excludes such systemic factors, and therefore the analysis here is consistent with this definition. Furthermore, the results of single channel Monte-Carlo modelling[49] indicate little change in the axial component of buckling upon voiding.

It remains to question how well WIMS-AECL models leakage in a voided core

through a modified diffusion coefficient, especially in the axial direction where one would expect neutron streaming to increase significantly upon voiding. This is a question best answered through comparison with non-deterministic analysis, either by experiment or by Monte Carlo calculations. In Appendix A a paper[50] is included which compares WIMS-AECL and MCNP-4 in terms of the calculated relative perturbations in leakage and its diffusion theory components. The results show a minor overprediction in the size of the WIMS-AECL diffusion coefficient perturbations and a negative bias in the flux perturbations, with a resulting cancellation that leads to reasonable agreement in leakage perturbation. It should also be noted that the CANDU core is a low-leakage system in the first place; therefore, the relative discrepancies calculated in Appendix A will result in small absolute differences.

2.2.5 Consideration of Neutron Lifetime

When using lattice cell analysis alone to characterize reactivity perturbations the traditional parameter for the purposes of optimization and reporting of results is reactivity, ρ (or manifestations thereof, such as the two void effects defined here). This is despite the fact that Equations (1.4) and (1.7) for $N(t)$ and $C_i(t)$ really depend upon the ratios ρ/Λ and β/Λ, where β is the delayed neutron fraction and Λ is the mean prompt neutron generation time, defined by Equation (1.6). The validity of neglecting changes in mean generation time, Λ, upon voiding is examined here.

In Equation (2.4) we define[1,2] in multigroup diffusion form the prompt-neutron

lifetime, l, and effective multiplication, k_{eff}. Substituting these definitions into Equation (1.6) leads to Equation (2.5), the multigroup expression for mean generation time.

$$l \equiv \frac{\int dV \sum_{g=1}^{G} (1/\omega_g)\phi_g}{\int dV \sum_{g=1}^{G} (\Sigma_{a_g} + D_g B^2)\phi_g} \quad ; \quad k_{eff} \equiv \frac{\int dV \sum_{g=1}^{G} \nu_g \Sigma_{f_g} \phi_g}{\int dV \sum_{g=1}^{G} (\Sigma_{a_g} + D_g B^2)\phi_g} \tag{2.4}$$

$$\Lambda = \frac{\int dV \sum_{g=1}^{G} (1/\omega_g)\phi_g}{\int dV \sum_{g=1}^{G} \nu_g \Sigma_{f_g} \phi_g} \tag{2.5}$$

(Note of clarification: In the above equations, ω_g = *mean neutron velocity in group "g"*, and ν_g = *mean number of neutrons per fission for group "g"*.) The numerator in Equation (2.5) can be expected to decrease in value upon voiding due to *spectrum hardening* (ie., shift to higher energies), while the denominator can be expected to increase due to spectrum hardening (fast fission component) and loss of thermal upscattering (thermal fission component), although the latter component will also decrease due to loss of cell moderation; these concepts will be fully explained in Chapter 3. In general, one would therefore expect the neutron mean generation time, Λ, to decrease upon voiding, leading to a burnup-dependent increase in the kinetics parameters ρ/Λ and β/Λ beyond any behaviour predicted with the assumption of a constant Λ. The burnup dependence is caused by the effect of plutonium on thermal effective fission cross-section (also explained in Chapter 3). The question, then, is whether or not this extra effect is negligible.

With WIMS-AECL and a full 69-group library structure, Equation (2.5) can be approximated using cell-averaged fluxes and cross-sections, and taking the group neutron speed, ω_g, to be the flux-weighted average of group boundary speeds,

$$\omega_g \approx \langle \omega_g \rangle = \sqrt{\frac{2\langle E_g \rangle}{m_n}} \quad ; \quad \langle E_g \rangle \equiv \frac{E_g \phi_g + E_{g+1}\phi_{g+1}}{\phi_g + \phi_{g+1}} \quad , \tag{2.6}$$

where m_n is neutron rest mass. This was done for the "reference" case of a CANDU lattice voiding with geometric bucklings, at both zero-burnup and mid-burnup. It was found that the approximated values of Λ decreased by 5% for the zero-burnup case and 4% for the mid-burnup case.

With these changes in Λ taken into account the parameter ρ/Λ was found to increase by 30% upon voiding at zero-burnup and 77% at mid-burnup, compared with "constant-Λ" increases upon voiding of 23% and 69%, respectively. The parameter β/Λ was found to increase upon voiding by 6% and 4% at each zero-burnup and mid-burnup, respectively, compared with zero change if β and Λ are assumed to be constant with voiding. The delayed neutron fractions at zero and mid-burnup were approximated according to the method described in Section 1.8. These results are summarized in Table 2.5, along with the effect on the combined parameter $(\rho-\beta)/\Lambda$ which appears in Equation (1.4).

Thus, the effect of including changes in mean neutron generation time upon voiding in the reference CANDU lattice cell at mid-burnup is a greater increase in the kinetics parameter $(\rho-\beta)/\Lambda$ by about 10%, relative to the constant-Λ case. This effect

should be viewed within the context of the isolated voiding phenomenon which has been modelled here; concurrent physical effects such as thermal Doppler resonance broadening will also decrease the mean neutron generation time in, compounding the effect, while increasing cell absorption, countering the void effect. It is also important to note that full space-time kinetics analyses do make estimations of the changes in Λ. Within the context of the "void effect" defined here, however, it is sufficient to conclude that the effect on reactor kinetics at mid-burnup may be 10% higher than that implied by lattice cell calculations of void effect alone. At zero-burnup, with geometric bucklings and no boron, the difference in the effect on reactor kinetics is lower at 7%, but this is about 25% of the effect with Λ constant.

2.2.6 Uncertainty

In this dissertation the uncertainty associated with a WIMS-AECL coolant void calculation will not be quoted, and will be tacitly assumed to correspond to that obtained from AECL[21,40,51] (exceptions will occur when the fuel geometry is sufficiently altered from the standard design such that new analysis is needed). Since full verification of void reactivity feedback in an operating CANDU reactor is a practical impossibility, comparisons have been made by AECL between WIMS-AECL calculations and both zero-energy experimental reactors and Monte-Carlo calculations[40,51]. Experimental comparisons in a cold, clean test core suggest an upper limit of ±2 mk for uncertainty while Monte-Carlo comparisons suggest ±1 mk (also indicated by the results in Table A.2),

representing about 12% and 6% of the total effect, respectively, at this level of approximation. It is expected that error increases with burnup, perhaps by another 2 mk at mid-burnup. Added to this is the error associated with variability of input formulation for WIMS-AECL, which can affect reactivity calculations by about ±1 mk. A summary of current industry attempts to formulate a standard method of reporting void reactivity is given in Reference 21.

2.2.7 Summary

Lattice cell calculations of the coolant void effect have been shown in this section to be influenced significantly by large deviations from criticality. The nature of this influence is dependent upon the definition of void effect being used and the method used to model a critical system (for example, critical material bucklings or burnable moderator poison). Void effect calculations at mid-burnup, which come close to modelling an equilibrium CANDU core, benefit from lower excess reactivity which removes many of the inconsistencies, and the most consistent void effect predictions appear to be with the *void reactivity effect* ($\Delta\rho_V$) definition in Equation (2.2) at mid-burnup.

Modelling a CANDU core at zero-burnup presents a special problem for lattice cell codes because of the high excess reactivity of the fuel. If critical material bucklings, instead of geometric bucklings, are used to calculate system leakage, the predicted void effect is lower due to enhancement of the epithermal leakage contribution (normally negative) upon voiding. If the moderator is borated to achieve criticality, the predicted

void effect is higher due to enhancement of the thermal utilization contribution (normally positive) upon voiding. Both trends are more pronounced if higher enrichment fuel is used.

Neglecting changes in neutron lifetime can lead to an underestimation of the increase in point kinetics parameters upon voiding by about 10% at mid-burnup, estimated with a WIMS-AECL calculation of the reference CANDU lattice cell. If an increase in fuel temperature (not modelled here) accompanies the coolant channel voiding, then a further reduction in neutron lifetime would be additive with the void effect described here, which would be countered by the negative fuel temperature coefficient. Furthermore, advanced fuel designs could significantly alter the relative change in neutron lifetime upon voiding, and therefore studies like this dissertation seeking to optimize reactivity effects of any kind should not neglect, *a priori*, the other kinetics parameters.

Finally, the WIMS-AECL calculations for void reactivity effect and void criticality effect will have an assumed uncertainty of ±2 mk maximum in the remainder of this work.

2.3 Data Interpretation

This section deals with the interpretation of information given in the output file of a WIMS-AECL lattice cell calculation. In carrying out the analysis to be found in later chapters a sensitivity to subtle changes in output data interpretation was discovered. An examination of the problems of flux normalization is given here (a sensitivity to certain

input specifications was covered earlier in Section 2.2.2). Also included is a description of a FORTRAN code written by the author as an analysis tool for direct use with WIMS-AECL output data.

2.3.1 Flux Normalization

Lattice cell codes, by definition, cannot normalize flux profiles to global power levels, and so a local parameter is usually chosen. In the case of WIMS-AECL the user may decide between total absorption and total loss (absorption plus leakage), the former being the default. This has two implications of relevance to studies, such as this dissertation, which compare flux distributions between separate cases: (1) Only estimates of relative spectral shifts can be made, and never absolute magnitude shifts; and (2) All fluxes should be renormalized to an independent parameter, since perturbations in absorption (if normalized to absorption) will skew the ratios of WIMS-AECL flux distributions, $\bar{\phi}_{g,j}$, by a factor of

$$\frac{\sum_{g,j} \Sigma^2_{a_{g,j}} \bar{\phi}^2_{g,j}}{\sum_{g,j} \Sigma^1_{a_{g,j}} \bar{\phi}^1_{g,j}}, \tag{2.7}$$

where subscripts g and j indicate energy group and spatial division, respectively, and superscripts indicate case number. Normalizing to total flux, $\sum_{g,j} \bar{\phi}_{g,j}$, will lead to unbiased spectral comparisons, where the sum must be over *all* groups (even for the reporting of group-wise fluxes) in order to properly capture distribution shifts between

groups. An attempt was made to circumvent the restriction of the first point above by normalizing to total *cooled* (non-voided) flux and thereby including absolute changes, but this leads to the same skewing factor given in Equation (2.7), as Equation (2.8) illustrates:

$$\frac{\hat{\phi}^V}{\hat{\phi}^C} = \frac{\left(\frac{\bar{\phi}^V_{g,j}}{\sum_{g,j}\bar{\phi}^C_{g,j}}\right)}{\left(\frac{\bar{\phi}^C_{g,j}}{\sum_{g,j}\bar{\phi}^C_{g,j}}\right)} = \frac{\bar{\phi}^V_{g,j}}{\bar{\phi}^C_{g,j}} \times \frac{\sum_{g,j}\Sigma^C_{a_{g,j}}\bar{\phi}^C_{g,j}}{\sum_{g,j}\Sigma^V_{a_{g,j}}\bar{\phi}^V_{g,j}} \quad . \tag{2.8}$$

Accordingly, all fluxes (and corresponding reaction rates) will be normalized to unit total flux, with independent normalizations for the cooled and voided cases,

$$\hat{\phi}^C_{g,j} \equiv \frac{\bar{\phi}^C_{g,j}}{\sum_{g,j}\bar{\phi}^C_{g,j}} \quad ; \quad \hat{\phi}^V_{g,j} \equiv \frac{\bar{\phi}^V_{g,j}}{\sum_{g,j}\bar{\phi}^V_{g,j}} \quad . \tag{2.9}$$

2.3.2 Contribution of Reactivity Components

When discussing the neutron physics behind the coolant void effect it will prove useful, because of the vast spectral range of the neutron flux, to subdivide the effect into energy-dependent factors. A method which uses this same approach is the *six-factor formula*[2], expressed in Equation (2.10), a relatively simple approach that has been around since the early days of fission reactor analysis. Although modern lattice cell codes like WIMS-AECL permit much more precise calculations to be made, the analytical approach of the six-factor formula (with some modification) is still one of the most illuminating

ways of interpreting the results of reactivity calculations.

$$k_{eff} = \eta f p \epsilon P_{\mathrm{FNL}} P_{\mathrm{TNL}} \tag{2.10}$$

The formula expresses k_{eff} as a product of six factors: η (number of fission neutrons per fuel absorption), f (thermal utilization), p (resonance escape probability), ϵ (fast fission probability), P_{FNL} (fast non-leakage probability), and P_{TNL} (thermal non-leakage probability). From the point of view of this formula all neutrons are effectively thermal neutrons, with adjusting factors accounting for the probability of a source neutron (created with probability ηf from a thermal neutron) causing fast fissions (ϵ), avoiding resonance capture (p), and all the time remaining in the reactor core ($P_{\mathrm{FNL}}P_{\mathrm{TNL}}$). In this dissertation, the single resonance escape probability will be factored into more meaningful "few-group" escape probabilities, $p_{g'}$ (g' = 1, 2,..., G-1 ; G = thermal group) such that $p = p_1 p_2 \ldots p_{G-1}$, simply reflecting escape from loss in each group (see footnotes on page 19 for a description of the main few-group structure used here). Furthermore, the analysis will be simplified by treating leakage and (n,2n) reactions as positive and negative absorption terms (similar to the way it is treated in WIMS-AECL) and eliminating the total non-leakage probability, $P_{\mathrm{FNL}}P_{\mathrm{TNL}}$. This approach means that $p_{g'}$ does not equal the group g' absorption escape probability, although the approximation is close since leakage and (n,2n) reaction rates in the lattice cell are two orders of magnitude less than absorption rates. In this dissertation this modification of the six-factor formula will be referred to as the *criticality factor formula*, and its components the *criticality factors*, to make a distinction from the original notation.

In terms of WIMS-AECL few-group cell fluxes normalized to absorption,

$$\bar{\phi}_g \equiv \frac{\phi_g}{\sum_{g=1}^{G} \Sigma_{a_g} \phi_g} \quad ; \quad (g = 1, 2, \ldots, G) \quad , \tag{2.11}$$

the criticality factors η, f, $p_{g'}$, and ϵ can be approximated as follows:

$$\eta = \frac{\sum_{\text{fuel}} \nu_G \Sigma_{f_G} \bar{\phi}_G}{\sum_{\text{fuel}} \Sigma_{a_G} \bar{\phi}_G} \quad ; \quad (G = \text{thermal group}) \quad ; \tag{2.12}$$

$$f = \frac{\sum_{\text{fuel}} \Sigma_{a_G} \bar{\phi}_G}{\sum_{\text{cell}} \left(\Sigma_{a_G} + D_G B^2\right) \bar{\phi}_G} \quad ; \tag{2.13}$$

$$p_{g'} = 1 - \left[\frac{\left(\Sigma_{a_{g'}} + D_{g'} B^2\right) \bar{\phi}_{g'}}{\sum_{g''=g'}^{G} \left(\Sigma_{a_{g''}} + D_{g''} B^2\right) \bar{\phi}_{g''}} \right] \quad ; \quad (g' = 1, 2, \ldots, G-1) \quad . \tag{2.14}$$

$$\epsilon = \frac{\sum_{\text{fuel}} \left(\sum_{g=1}^{G} \nu_g \Sigma_{f_g} \bar{\phi}_g \right)}{\sum_{\text{fuel}} \nu_G \Sigma_{f_G} \bar{\phi}_G} \quad . \tag{2.15}$$

Although each of these calculations is straightforward it would be impractical to apply them manually in a parametric study. Appendix B lists the FORTRAN source code written by the author to process a WIMS-AECL output file using Equations (2.12) to (2.15) and then calculate void effect contributions (both types of "void effect"). The code runs checks on the WIMS-AECL output file to ensure that all data needed in Equations (2.12) to (2.15) is available, advising the user when something is missing. The number of few-group escape probabilities is set by the user's choice of few-group number in the WIMS-AECL input file, and is automatically accounted for by the code. The individual contributions to the void effect are approximated using multi-variable Taylor expansions[52] of Equations (2.2) and (2.3) truncated to second order,

$$\begin{aligned} \Delta\rho \approx (1-\rho) \Bigg[& \left(\frac{\Delta p}{p} + \frac{\Delta\epsilon}{\epsilon} + \frac{\Delta f}{f} + \frac{\Delta\eta}{\eta} \right) + \\ & \left(\frac{\Delta p \Delta\epsilon}{p\epsilon} + \frac{\Delta p \Delta f}{pf} + \frac{\Delta p \Delta\eta}{p\eta} + \frac{\Delta\epsilon \Delta f}{\epsilon f} + \frac{\Delta\epsilon \Delta\eta}{\epsilon\eta} + \frac{\Delta f \Delta\eta}{f\eta} \right) \Bigg] \quad , \end{aligned} \tag{2.16}$$

$$\begin{aligned} \Delta k_{eff} \approx & \; [\epsilon f \eta \, \Delta p + f \eta p \Delta\epsilon + \eta p \epsilon \, \Delta f + p \epsilon f \Delta\eta] + \\ & [\eta f \Delta p \Delta\epsilon + \eta \epsilon \, \Delta p \Delta f + \epsilon f \Delta p \Delta\eta + \\ & \eta p \Delta\epsilon \Delta f + f p \Delta\epsilon \Delta\eta + \epsilon p \Delta f \Delta\eta] \quad , \end{aligned} \tag{2.17}$$

where only one few-group escape probability, p, has been assumed here for simplicity. The second bracketed group of terms in each equation, containing the products of two "delta" terms, represents a second order adjustment that is divided up proportionally when determining individual factor contributions. As an example, the contribution of thermal utilization to the void reactivity effect would be calculated as

$$\delta f_{\Delta\rho_V} \approx (1-\rho)\left[\left(\frac{\Delta f}{f}\right) + \left(\frac{\frac{\Delta f}{f}}{\frac{\Delta p}{p} + \frac{\Delta\epsilon}{\epsilon} + \frac{\Delta f}{f} + \frac{\Delta\eta}{\eta}}\right)(2^{\text{nd}}\text{-order term})\right] , \qquad (2.18)$$

and the contribution to the void criticality effect as

$$\delta f_{\Delta k_{eff,V}} \approx \eta p \epsilon \Delta f + \left(\frac{\eta p \epsilon \Delta f}{\epsilon f \eta \Delta p + f \eta p \Delta\epsilon + \eta p \epsilon \Delta f + p \epsilon f \Delta\eta}\right)(2^{\text{nd}}\text{-order term}) \quad . \qquad (2.19)$$

The error in truncating the Taylor expansion after these terms is negligible (< 0.1 mk). If the truncation is made after the first term the error in some cases can be significant (~ 1 - 4 mk). Appendix B also includes a sample of this code's output, using a reference CANDU lattice cell output file from WIMS-AECL. A check of self-consitency is performed by summing the contributions and comparing against the effect calculated with Equations (2.2) and (2.3).

2.4 Heterogeneous Coolant Void Distributions

In keeping with the description of the simple void effect to be studied here (see Section 2.1), distributions of partial voiding will not be treated in subsequent analysis.

Partial voiding can be treated in a similar manner to the methods used here, after determining an effective coolant density based on void fraction. Before completely dismissing void distributions, however, one must first be satisfied that important reactivity feedback effects are not being overlooked. Highly distributed voids form as channel stratification[14] during LOCA scenarios, or as localized boiling phenomena during either routine operation or coolant pressure-drop scenarios. This section examines one phase of localized boiling, known as *film boiling*[53], using the results of a previous study[54] by the author, included in Appendix C.

Film boiling begins when heat is no longer transported efficiently from the fuel sheath by nucleate boiling. Bubbles coalesce and a period of *fuel sheath dry-out* begins, during which coolant no longer wets the surface. In a critical CANDU fuel lattice this condition is significant since it removes scattering material from a location (between fuel elements) of relatively high neutron importance. This boiling regime represents a radical departure from operating conditions and therefore the lattice is not expected to be critical at this time; however, it retains relevance to this discussion.

In the standard 37-element lattice cell the geometric maximum thickness of the dry-out film is about 0.9 mm (at this point the film from a neighbouring element would be met), representing a void fraction of about 43% if all elements had identical films. The main result of this situation, compared to the simple homogeneous treatment (effective coolant density), is given in Figure C.6 as a function of burnup. The homogeneous treatment underpredicts the void criticality effect at 43% void fraction by about 4% at zero-burnup and 11% at full-burnup (about 8% at mid-burnup), primarily

caused by a greater increase in fast flux in the heterogeneous case. Obviously the two predictions would converge as complete voiding is reached (see Figure C.3), and not follow the diverging trend suggested in Figure C.6. The effect is therefore minor in the reference lattice cell.

2.5 Summary of Method

The parameters optimized in this dissertation will be the void reactivity effect and the void criticality effect defined by Equations (2.2) and (2.3), respectively. In general these measurements are very close, but because of (a) the demonstrated possibility of significantly differing results, and (b) the use of both measurements by industry, as much as possible both interpretations of void effect will be reported here. The void effect corresponds to a response of lattice multiplication to total and instantaneous coolant voiding, without accounting for concurrent thermalhydraulic or material effects that might accompany loss of coolant.

It is recognized that a lattice cell code like WIMS-AECL will not, in general, model a critical lattice, and that methods to produce an artificially critical lattice can sometimes produce quite different results. This condition is considerably reduced in severity when mid-burnup fuel is modelled, which reasonably approximates equilibrium conditions within a CANDU core. The most accurate estimations of the void effect using WIMS-AECL are assumed to occur when critical bucklings are used for the leakage spectrum and mid-burnup fuel is modelled. For practical reasons, however, geometric

bucklings will be used in the calculation of k_{eff} and zero-burnup fuel will be modelled when many optimization runs are performed. The total error incurred by this method is considered minor and inconsequential as long as conditions are consistently applied to all cases. Important results will always include burnup effects.

Analysis of contributing physical factors to the void effect will use a method based on the six-factor formula which is encoded in a computer programme written for this dissertation. All spectral information will be normalized to unit neutron flux.

The method used here is understood to imperfectly represent the complete physical process of neutronic feedback to coolant voiding, although it will adequately indicate trends. Aside from the basic numerical error, assumed to be maximum ±2 mk, the neglect of changes in mean neutron lifetime, Λ, can effect an underestimation of the true change in kinetic parameters by up to 10%. If the model for fuel sheath dry-out is based on an interpolation of this method according to void fraction, results can be off by 8% (although the total effect is minor). The lattice cell code WIMS-AECL is therefore used purely as an "exploratory" (as opposed to design) tool in this dissertation, and this chapter has outlined its use as well as its limitations.

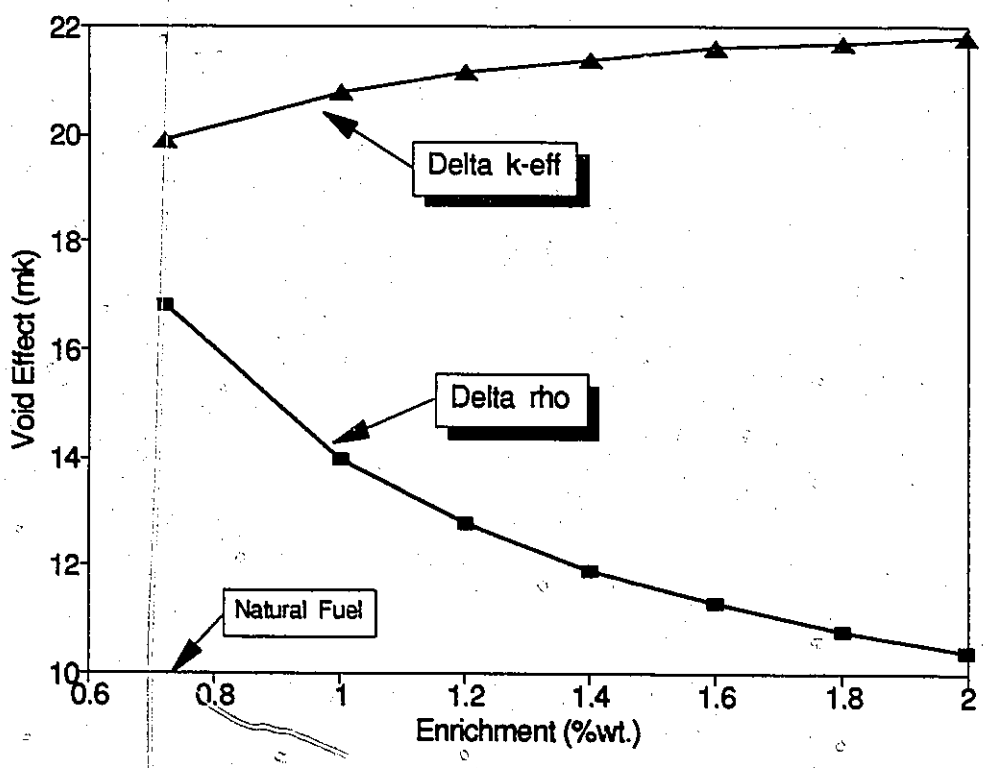

Figure 2.1 Zero-Burnup Void Effect vs. Enrichment: $\Delta\rho_V$ (Equation (2.2)) and $\Delta k_{eff,V}$ (Equation (2.3)).

Table 2.1 Zero-Burnup Void Effect for Natural and 1.2% Enriched 37-Element Fresh CANDU Fuel.

Method	Natural Fuel	1.2% Enriched
$\Delta\rho_V$ [Eqn. (2.2)]	17 mk	13 mk
$\Delta k_{eff,V}$ [Eqn. (2.3)]	20 mk	21 mk

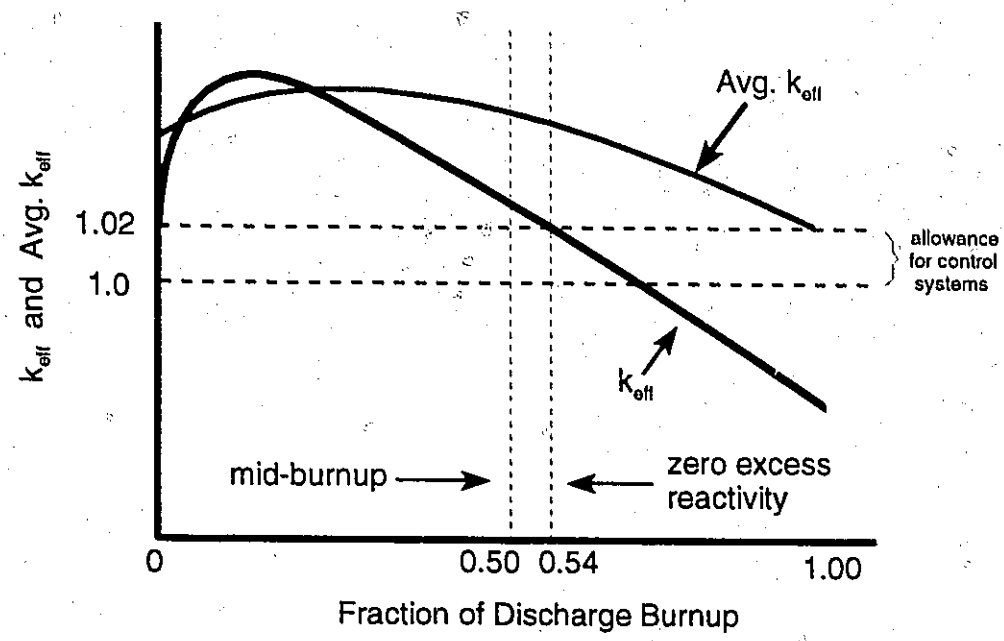

Figure 2.2 Method of Estimating Discharge Burnup: k_{eff} and Time-Averaged k_{eff} (Actually [Time-Averaged Yield] / [Time-Averaged Loss]) As a Function of Time (Illustration Only).

Table 2.2 Summary of Zero-Burnup Void Effects for Natural and 1.2% Enriched Fuel Lattice, With Geometric and Critical Bucklings.

Method For Calculating Void Effect	Natural Fuel		1.2% Enriched Fuel	
	With Geometric Bucklings	With Critical Bucklings	With Geometric Bucklings	With Critical Bucklings
$\Delta\rho_V$ [Eqn.(2.2)]	16.8 mk	15.7 mk	12.8 mk	6.8 mk
$\Delta k_{eff,V}$ [Eqn.(2.3)]	19.9 mk	15.9 mk	21.2 mk	6.8 mk

Table 2.3 Summary of Mid-Burnup Void Effects for Natural and 1.2% Enriched Fuel Lattice, With Geometric and Critical Bucklings.

Method For Calculating Void Effect	Natural Fuel (mid-burnup = 3800 MWd/Te)		1.2% Enriched Fuel (mid-burnup = 10300 MWd/Te)	
	With Geometric Bucklings	With Critical Bucklings	With Geometric Bucklings	With Critical Bucklings
$\Delta\rho_V$ [Eqn.(2.2)]	13.3 mk	12.9 mk	14.2 mk	13.8 mk
$\Delta k_{eff,V}$ [Eqn.(2.3)]	14.1 mk	13.0 mk	14.9 mk	14.0 mk

Table 2.4 Summary of Zero-Burnup Void Effects for Natural and 1.2% Enriched Fuel Lattice, Including the Case of Borated Moderator

Method For Calculating Void Effect	Natural Fuel			1.2% Enriched Fuel		
	With Geometric Bucklings	With Critical Bucklings	With Geometric Bucklings and Borated Moderator	With Geometric Bucklings	With Critical Bucklings	With Geometric Bucklings and Borated Moderator
$\Delta\rho_v$ [Eqn.(2.2)]	16.8 mk	15.7 mk	21.3 mk	12.8 mk	6.8 mk	25.1 mk
$\Delta k_{eff,v}$ [Eqn.(2.3)]	19.9 mk	15.9 mk	21.7 mk	21.2 mk	6.8 mk	25.8 mk

Table 2.5 Effect of Coolant Voiding on Point Kinetics Parameters, With and Without Accounting for Changes in Mean Generation Time, Λ.

		ρ/Λ	β/Λ	$(\rho-\beta)/\Lambda$
Zero-Burnup	Λ variable	+ 30%	+ 6%	+ 33%
	Λ constant	+ 23%	0%	+ 26%
Mid-Burnup	Λ variable	+ 77%	+ 4%	+ 99%
	Λ constant	+ 69%	0%	+ 90%

Chapter 3

Void Effect in Current CANDU Design

In this chapter the tools, methods, and assumptions outlined in previous chapters are utilized to describe the void effect in current CANDU design. This will provide a reference point for further analysis, while delineating the neutron transport physics that applies to voiding scenarios in any form of CANDU fuel. The description of the void effect is divided into three sections of increasing complexity: the purely spectrum-related effects are described first, followed by the spatial dependence, and finally by the material sensitivities. A growing synthesis links all three sections, which can therefore be taken as an increasingly detailed look at the same effect. The chapter begins with a brief introduction of the lattice cell of interest. Much of this chapter is also incorporated in a separate paper by the author[55].

3.1 37-Element CANDU Lattice Cell

The reference 37-element CANDU lattice cell for this dissertation is shown in Figure 3.1, and a listing of the WIMS-AECL input file used to model this cell for this dissertation is included in Appendix D. The natural UO_2 fuel meat in each element is 1.22 cm in diameter, surrounded by 0.47 mm thick zircaloy-4 cladding. Elements are

arranged into four "rings" of 1, 6, 12, and 18 elements starting from the lattice centre, with pitch circles located at radii of 0 cm, 1.49 cm, 2.88 cm, and 4.33 cm. For clarity, these rings will be referred to as Ring 1, Ring 2, Ring 3, and Ring 4 respectively. The fuel in all rings is at a nominal temperature of 882 °C. D_2O coolant at 290 °C surrounds the fuel elements to a pressure tube inner radius of 5.17 cm, giving a fuel-coolant-cladding volume ratio of 1 : 0.8 : 0.16.

The channel boundary is formed by a 0.45 cm thick zirconium-2.5%Nb pressure tube, surrounded by an insulating gap of thickness 0.83 cm and a zircaloy-4 calandria tube of thickness 0.15 cm. This channel arrangement is centred within a square lattice boundary of side 28.58 cm (not shown in Figure 3.1), and the volume between the calandria tube and this boundary is filled with D_2O moderator at 71 °C. The moderator comprises about 83% of the lattice cell volume, but contributes only 1% to total cell absorption.

3.2 Spectrum-Related Voiding Effects

In the CANDU lattice cell, the D_2O coolant accounts for only 0.03% of total cell absorption, implying that about 0.3 mk of the void effect arises from loss of absorption in the coolant. The remainder of the effect is tied to the coolant's role as a scattering medium within the lattice cell. The large cell pitch in CANDU, or (more precisely) the large moderator volume, creates two distinct neutron source regions: a fast source within the fuel pins and a well-thermalized source within the moderator. Criticality, and hence

reactivity, is affected by how well the fast neutrons from the fuel diffuse out to the moderator region, and by how well the thermal neutrons from the moderator diffuse inward to the fuel region — a situation illustrated in Figure 3.2. Voiding of the coolant affects both these processes significantly since the coolant is the main diffusion medium between the two regions. This section describes the physics of coolant voiding in terms of three spectral groups: fast, epithermal, and thermal (see footnote, page 19). All numerical results were calculated using the method described in Section 2.3.2, and are summarized in Table 3.1.

3.2.1 Fast Spectrum Effects

The loss of down-scattering of fission source neutrons by the coolant creates a hardened fast neutron spectrum in the fuel pins. This leads to increased parasitic absorption, mainly in U-238, contributing -3.4 mk to the void reactivity effect of an equilibrium lattice through the fast "loss" escape factor, p_F. At the same time the rate of fast fission in all fissile nuclides increases, contributing +5.4 mk to the void reactivity effect through the fast fission factor, ϵ. The net effect of the spectral shift in the fast range is therefore +2 mk in the equilibrium lattice, or about 16% of the total effect.

3.2.2 Epithermal Spectrum Effects

The largest contributor to the coolant void effect in the epithermal range is the change in the resonance escape probability of the lattice cell. A very common expression

of this escape probability is the exponential approximation[2], which assumes that all resonance absorption takes place in well-separated resonances,

$$p = \prod_i p_i \approx \exp\left[-\frac{N_A}{\xi\Sigma_S}\sum_i I_i\right] \quad , \tag{3.1}$$

where N_A is the concentration of absorbing nuclei, $\xi\Sigma_S$ is the *moderating power* of the cell, and I_i is the *effective resonance integral* of the cell for resonance region i,

$$I_i \equiv \int_{E_i} dE\, \sigma_\gamma^A(E)\, \phi(E) \quad , \tag{3.2}$$

which WIMS-AECL calculates for each case. Under operating conditions the coolant is a minor source of resonance flux in the fuel pins, most significantly from down-scattered source neutrons but also from high-energy epithermal neutrons re-entering the fuel channel before complete thermalization in the moderator. Upon voiding two competing forces affect the resonance integral: the reduction in epithermal flux reduces the effective resonance integral, increasing the reactivity, while the loss of extra scattering in the cell reduces the moderating power, decreasing the reactivity. Since the coolant is a minor contributor to the cell moderating power the first effect is predominant, leading to a net contribution to the void reactivity effect in an equilibrium lattice of +10.9 mk, or about 85% of the total effect. Clearly the increase in cell epithermal escape probability is the dominant phenomenon behind the coolant void effect in CANDU.

3.2.3 Thermal Spectrum Effects

As stated before, the moderator in the CANDU lattice cell can be thought of as a source of well-thermalized neutrons, created in a relatively large, high scattering, low absorbing, low temperature medium. The effect of the coolant, with its equally high scattering cross-section and 220 °C temperature difference compared to the moderator, is to rethermalize (ie., make "hotter") a portion of the incoming moderator flux and thus raise the effective neutron temperature of the lattice cell. Upon voiding of the coolant this up-scattering mechanism is removed and the thermal spectrum shifts to a lower temperature determined mainly by the moderator temperature. This shift is illustrated graphically in Figure 3.3 for the WIMS-AECL thermal group-wise spectrum in the coolant region around the central fuel pin, and in Figure 3.4 for the coolant region near the pressure tube boundary; both figures are calculated at mid-burnup.

The effect of this spectral shift towards cooler temperatures depends upon the cross-section behaviour of the fuel in this energy range. In uranium the $1/E^{1/2}$ dependence of its absorption/fission cross-section will cause an increase in both f ("thermal utilization", or fraction of thermal neutrons absorbed in the fuel) and η ("thermal yield efficiency", or thermal yield-to-absorption ratio of the fuel). This effect dominates any hardening of the thermal spectrum caused by loss of moderation in the coolant. In a zero-burnup lattice, for example, WIMS-AECL calculates a +1.8 mk void reactivity effect due to the increase in η upon voiding, and a +3.3 mk effect due to the increase in f, for a total thermal void reactivity effect of +5.1 mk. Another way to

examine this effect is to set the lattice coolant and moderator temperature equal to each other (at the temperature of the moderator), and in this case WIMS-AECL calculates a void reactivity effect that is 3.9 mk lower than the reference case. Since the thermal spectrum under operating conditions will be different from the reference case, this is not a rigorous test of the thermal spectrum "cooling" effect, but we can estimate the effect to be about 4 mk with an extra 1 mk coming from thermal spectrum hardening (η will decrease but f increases due to a U-235 thermal resonance).

In plutonium the effect differs because of an extremely large thermal Pu-239 and Pu-241 resonance at approximately 0.3 eV (see Figure 1.2). The "cooling" of the thermal spectrum upon voiding causes a drop in neutron yield and absorption in plutonium, with resulting reductions in η and f. In equilibrium CANDU fuel (estimated at mid-burnup), where the average cell concentration ratio of all plutonium isotopes to U-235 is about 0.5, the contribution to the void reactivity effect through thermal yield efficiency, η, is -2.1 mk, and through thermal utilization, f, is 2.0 mk. The latter contribution would be roughly five-fold larger without the negative effect of plutonium (this point will be made evident later in Section 3.4 where material-related effects are detailed). The total thermal void reactivity effect in mid-burnup CANDU fuel is therefore approximately zero. Whereas with zero-burnup fuel the "cooling" of the thermal spectrum increases the void reactivity effect, the opposite is true for equilibrium fuel. This can be further examined by setting the lattice coolant and moderator temperatures equal, and this time WIMS-AECL calculates a void reactivity effect that is 2.3 mk higher than the reference mid-burnup case. Again, this is not rigorous, but we can estimate the effect of thermal

spectrum "cooling" in equilibrium CANDU to be about −2 mk (compared with approximately +4 mk for zero-burnup fuel, as mentioned above).

3.2.4 Summary of Spectrum-Related Voiding Effects

Two dominant shifts in spectral distribution upon voiding have been described in this section: a "fast shift" consists of an increase in high-energy neutron flux (> 1 MeV) and a coupled decrease in upper-end epithermal neutron flux, both caused by a decrease in high-energy cell moderation; a "thermal shift" consists of a change to a lower effective thermal neutron temperature caused by loss of coolant upscattering, as well as a slight increase in low-end epithermal neutron flux caused by a decrease in low-energy cell moderation. Each shift can be associated with two loosely coupled "sources"; that is, the "fast shift" is associated with the fast neutron source in the fuel, and the "thermal shift" is associated with the thermal neutron source in the moderator. The complete picture of these spectral shifts, in terms of the WIMS-AECL group-wise spectrum, is illustrated in Figure 3.5 for a zero-burnup lattice, and in Figure 3.6 for a mid-burnup lattice, looking at the coolant region around the central fuel pin ("Ring 1") in both cases (the effect on the spectral distribution would be expected to be greatest in this region due to its distance from the moderator and, therefore, its sensitivity to coolant scattering). The main resonance region for the heavy nuclides (3 eV to 10 keV) is marked in both figures, along with the low-energy isolated resonances of the plutonium isotopes in Figure 3.6. The y-axes show absolute change in the normalized flux (normalized to unity).

These shifts in flux spectra upon voiding manifest themselves in reaction rate changes. The *criticality factor* spectral contributions to the void reactivity effect described in the previous subsections were calculated using the method described in Section 2.3.2. A summary of these results is given in Table 3.1 for both the void reactivity and the void criticality effect, and for both zero-burnup and mid-burnup lattices. The total void reactivity effect is 16.3 mk at zero-burnup and 13.0 mk at mid-burnup. As Table 3.1 illustrates, in a current CANDU lattice cell at mid-burnup the fast spectral effects (p_F and ϵ) almost cancel each other, as do the thermal effects (η and f), leaving the majority of the effect in the epithermal range (p_E). Since this range includes the nuclide resonances, this guarantees that the calculation of the void effect will be sensitive to the resonance treatment model used.

As described in Section 2.2.1, the detailed burnup history of CANDU fuel cannot be rigorously modelled using only a lattice cell code like WIMS-AECL, and satisfactory approximations can only be expected with a mid-burnup case (equilibrium core) or zero-burnup case (fresh, clean core). Nevertheless, criticality calculations as a function of burnup made with WIMS-AECL will correctly illustrate the trend, and a knowledge of the physics behind the spectral contributions in this section can provide an explanation for this trend. In Figure 3.7 both interpretations of void effect are plotted against burnup fraction, along with k_{eff} for the cooled case. Note that the rate of decrease with burnup is smaller for the void reactivity effect since it is normalized to decreasing criticality as burnup increases. The void reactivity effect also goes through a maximum shortly after zero-burnup which is not seen in the void criticality effect, corresponding to a local

minimum in k_{eff} caused by U-235 depletion before significant Pu-239 growth. Generally, however, burnup causes a decrease in void effect as U-235 depletes and plutonium and fission products "burn in", as will be described in detail in Section 3.4. All three of these burnup phenomena decrease the void effect by reducing or reversing the thermal spectrum effects described in Section 3.2.3; the fast spectrum effects are dominated by U-238 behaviour and are therefore highly unaffected by burnup. This fact is evident in the changes in criticality factor contributions summarized in Table 3.1.

3.3 Geometry-Related Voiding Effects

The same alteration in cell transport properties upon coolant voiding that leads to the spectral shifts just described also leads to a change in spatial flux distribution throughout the CANDU lattice cell. The drop in thermal absorption, decrease in thermal scattering, and increased streaming within the pressure tube, all caused by the loss of coolant scattering, creates a slight increase in thermal flux in the inner fuel regions (fuel rings 1 and 2) and a slight decrease in thermal flux in the outer fuel regions and moderator. One way to demonstrate any change in neutron transport properties is to compare the WIMS-AECL first-flight region-to-region collision probabilities (P_{ij}) before and after coolant voiding. Since the moderator is the effective bulk source of thermal neutrons in this case, it is illuminating to compare the thermal group P_{ij}'s from the moderator to each of the fuel rings. Table 3.2 makes this comparison by listing the ratios of P_{ij} (voided) to P_{ij} (cooled), where "i" is the moderator and "j" is each target fuel ring

in turn. As expected, the greatest relative effect occurs between the moderator and the central fuel pin, decreasing with radius (and therefore proximity to the moderator). Note that these results reflect a change in probabilities, not actual events. Note also that these results reflect only the change in streaming properties since the *first-flight* collision probabilities are being utilized; they are still indicative of the total thermal effect however.

The epithermal flux drops inside the pressure tube due to the loss of the coolant as a high-end epithermal source. In the moderator the epithermal flux increases due to the increase in the fast flux entering the moderator, and the corresponding increase in importance of the moderator as the sole thermalizing agent. The fast flux simply increases everywhere in the lattice cell due to spectral hardening.

The spatial shifts in each of these three main spectral groups are visualized in Figure 3.8, Figure 3.9, and Figure 3.10 for the thermal, epithermal, and fast groups, respectively. These plots are intended for trend illustration only since two limitations make them spatially inconsistent with a realistic CANDU lattice cell: (1) Flux is plotted as a function of WIMS-AECL regional mesh layout, which in general increases numerically with radius (separate coolant subregions were defined to facilitate this) although not perfectly because of the heterogeneous nature of the fuel pin cluster; (2) Average point-wise fluxes are given without accounting for differing mesh volumes. Both of these points affect the detailed structure of the plots but do not alter the general behaviour. To assist in the physical visualization of the spatial shifts, the mesh points corresponding to the four fuel rings and the moderator have been noted in each figure.

Furthermore, in order to illustrate absolute changes as well as distribution changes, all three plots are normalized to the total flux (also in accordance with the rule adopted in Section 2.3.1).

In Figure 3.8 a "stationary node" in the thermal spatial shift occurs around the location of the third fuel ring. Several spatial phenomena associated with thermal flux in a CANDU lattice cell are also evident: large thermal absorption in the fuel pins is reflected in the flux depressions at each fuel ring mesh point, and the dominating thermalization of the moderator is obvious (leading to the recognition of the moderator as the single thermal source in the cell, used in previous qualitative analysis). The overall relative change in the thermal proportion of total cell flux upon coolant voiding is −2.8 %, indicated in Figure 3.8, which can be attributed to the decrease in cell moderating power. In Figure 3.9 the epithermal flux distribution demonstrates a directional shift opposite to that of the thermal case, as the region within the pressure tube becomes a less important epithermal source and the moderator becomes more important upon coolant voiding. The "stationary node" in this case is in the pressure boundary region between coolant and moderator. The overall relative change in the epithermal proportion of total cell flux is +4.6 %. In Figure 3.10 the fast flux distribution is seen to increase at all mesh points, most significantly around the fuel as would be expected (note also the fast flux peaks at each fuel ring mesh point). The overall relative change in the fast proportion of total cell flux is +16.2 %.

Table 3.4 and Table 3.5 (for zero and mid-burnup, respectively) summarize the changes in flux at three sample locations in the lattice cell: the coolant region around the

centre fuel pin ("Ring 1"), the coolant region around the outer fuel pins ("Ring 4"), and in the bulk moderator. The proportion of flux within each group is given for the cooled and voided cases (normalized to 100% in each region), along with the difference between them. All of the trends illustrated qualitatively in Figure 3.8 to Figure 3.10 are reflected in these quantitative results (note the difference in normalization however: separate normalization is applied to each group), with Table 3.4 and Table 3.5 giving a better idea of the initial relative levels for group flux in each region.

The geometry-related effects of coolant voiding will create differential spectral void effects across the lattice cell. Table 3.6 and Table 3.7 subdivide the void effect spectral components of Section 3.2 into separate fuel ring contributions, for zero-burnup and mid-burnup lattices, respectively. Results are given in both absolute terms (simple difference in the component's value) and relative terms (percentage change in the component's value). In order to calculate the individual spatially-dependent contributions to be discussed here, and the material-dependent contributions discussed in the next section, the numerators in Equations (2.12) to (2.15) were subdivided into the portions contributed by each spatial (or material) category. These portions sum to the numerator given in the original equations.

Before discussing these results, a special note must be made concerning the perturbation to the fast fission factor, ϵ, in this section on spatial dependence and the next on material dependence. The fast fission factor was calculated in Equation (2.15) using the ratio of yield from all energy groups to the yield from the thermal group. Useful information will not be gained by simply partitioning the numerator Equation (2.15) into

its spatially dependent additive components, since the results will be skewed significantly by the large contributions of thermal fission. For example, it will suggest that U-235 contributes the most to fast fission simply because of its large contribution to thermal fission. Therefore, in the same spirit that the resonance escape parameter, p, was originally separated into multiple components in Equation (2.14) so that more relevant information would be conveyed, the fast fission factor has been separated into a thermal (ϵ_T) and non-thermal (ϵ_{NT}) component for the analysis in this section and the next,

$$\epsilon_T \equiv \frac{\sum_{\text{fuel}} \nu_G \Sigma_{f_G} \tilde{\phi}_G}{\sum_{\text{fuel}} \nu_G \Sigma_{f_G} \tilde{\phi}_G} \quad ; \quad \epsilon_{NT} \equiv \frac{\sum_{\text{fuel}} \left(\sum_{g=1}^{G-1} \nu_g \Sigma_{f_g} \tilde{\phi}_g \right)}{\sum_{\text{fuel}} \nu_G \Sigma_{f_G} \tilde{\phi}_G} \quad , \tag{3.3}$$

where G denotes the thermal group, and $\epsilon = \epsilon_T + \epsilon_{NT} = 1 + \epsilon_{NT}$. The perturbation in the "non-thermal" portion, ϵ_{NT}, will truly convey the spatial (or, in the next section, material) dependence of the fast-fission contribution to the void effect. Since the "thermal" portion, ϵ_T, is always equal to unity, its individual perturbation will always be zero. Only the relevant "non-thermal" parameter, ϵ_{NT}, appears in Table 3.6 and Table 3.7, and in the analysis appearing here and in the next section it will be referred to simply as the "fast fission factor". In the case of U-238 there is no difference between ϵ_{NT} and ϵ since it is not fissile in the thermal region.

In Table 3.6 and Table 3.7, the perturbations to both strictly thermal parameters, thermal yield efficiency (η) and thermal utilization (f), follow the same trend by fuel ring: the greatest relative increase is experienced in the inner fuel pin, decreasing with radial position and becoming negative in the outer fuel ring. This behaviour is not

unexpected after studying the thermal flux spatial shift in Figure 3.8. In the case of η the thermal yield of the inner fuel pins increases by a greater amount upon voiding than the total cell thermal fuel absorption, and the opposite is true in the outer fuel ring where the thermal flux decreases upon voiding. Similarly in case of f, the thermal fuel absorption of the inner fuel pins increases by a greater amount than the total cell absorption, with the opposite effect in the outer fuel pin. With both thermal components the positive effect of the inner pins dominates in a zero-burnup lattice (Table 3.6) and the total contribution is positive. In a mid-burnup lattice (Table 3.7) the negative influence on η of plutonium in the outer pins leads to an overall negative change in this component (Section 3.4 illustrates this influence in more detail).

The perturbations to the non-thermal parameters, fast (p_F) and epithermal (p_E) group escape probability and the fast fission factor (ϵ_{NT}), are all determined largely by U-238 behaviour and are thus virtually independent of burnup. The fast fission factor perturbation, as with the thermal parameters, increases by the greatest *relative* amount in the inner fuel ring. This occurs partly because of the increasing *absolute value* of ϵ_{NT} with radius, as fissile nuclei (U-238 in particular) become more abundant, and partly because of the slightly larger increase in fast flux in the centre fuel rings. For the same reasons the relative perturbations to p_F and p_E (a negative perturbation in the case of p_F) also slightly decrease with increasing radius. Note, however, that the perturbation to the epithermal group escape probability is significantly lower in the outer fuel ring, corresponding to the minor perturbation in epithermal flux in this region (see Figure 3.9, or Table 3.4 and Table 3.5).

As would be expected based on the trend of fuel volume with radius, for all spectral components the greatest *absolute* perturbations occur in the outer fuel rings.

3.3.1 Summary of Geometry-Related Voiding Effects

The loss of a scattering medium within the pressure tube leads to a redistribution of thermal and epithermal flux, and a general increase in fast flux, across the lattice cell. The increase in the relative importance of thermal absorption in the inner regions of the fuel cluster leads to positive local contributions to the void effect through the thermal spectrum parameters, while the depression of thermal flux in the outer region creates a negative local contribution. In a mid-burnup lattice this negative influence in the case of η is dominant, leading to a negative overall perturbation in this parameter.

The increase in fast absorption upon voiding creates an everywhere-negative contribution through the change in p_F, and an everywhere-positive contribution through the change in ϵ_{NT}, both decreasing with radius in terms of relative perturbations. The contribution through p_E is also everywhere-positive, although significantly smaller in the outer fuel ring.

3.4 Material-Related Voiding Effects

The void effect contributions of the principle fuel isotopes, U-235, U-238, and Pu-239, have been alluded to in the previous sections on spectrum and geometry-related effects; this section examines this material relationship in more detail. As a summary,

Figure 3.11 and Figure 3.12 plot the void criticality and void reactivity effects, respectively, as a function of burnup fraction, along with the contributions of the relevant fissile nuclides through their change in yield (Δ yield / total absorption). The point of mid-burnup is marked on both plots, and it is worth noting that the contributions from U-238 and Pu-239 at this point cancel each other, making the U-235 contribution approximately equal to the total effect. Once again, these two plots should be viewed as trend indicators only, except perhaps for the zero-burnup and mid-burnup cases.

Narrowing the focus to the void *reactivity* effect alone, Table 3.8 and Table 3.9 detail the spectral and geometric components of the contribution of each fissile material in a zero-burnup (Table 3.8) and mid-burnup (Table 3.9) lattice. The higher isotopes of plutonium have been excluded from these tables because of their negligible absolute contributions to all spectral perturbations. All other non-fissile materials in the lattice cell contribute only traces through p_F and p_E, and have been likewise excluded.

As with the spatial information given in Table 3.6 and Table 3.7, results are quoted in absolute and relative terms, and therefore Table 3.8 and Table 3.9 can be taken as a "material breakdown" of the previous spatial information. A comparison between the two sets of tables indicates the portion of each spatially-dependent absolute perturbation contributed by each nuclide. The analysis here is separated into a discussion of the "thermal" and "non-thermal" effects.

3.4.1 Thermal Range Material Effects

As Table 3.6 and Table 3.7 demonstrated, the general trend in the thermal range is for the greatest relative perturbation in criticality factors to occur near the centre of the fuel bundle, decreasing with radial position and becoming negative in the outer fuel region (Ring 4). In U-235 the negative shift of η and f in Ring 4 (caused by the negative shift in thermal flux here upon voiding) decreases with burnup due to depletion and competition for thermal absorption from burnup nuclides (fission products). The significant localized depletion in this area is illustrated in Table 3.10 comparing mid-burnup number densities by fuel ring, normalized to unity in the centre fuel pin in the case of U-235. Since the absolute perturbations to the U-235 thermal parameters in the inner fuel elements do not change as much with burnup as in the outer elements, the "outer ring effect" leads to an increase (about three-fold) in the thermal contribution of U-235 with burnup. This is evident when comparing the first two rows from the zero-burnup (Table 3.8) and mid-burnup (Table 3.9) results. In fact, during the initial fuel burnup this increasingly positive contribution dominates the effect of depletion, leading to a maximum in the U-235 curve in Figure 3.11 and Figure 3.12. Note that the void *reactivity* contribution of U-235 in Figure 3.12 is additionally inflated during early burnup by the rapid reduction in k_{eff}, which appears in the denominator of the void reactivity effect equation. The major isotope of uranium, U-238, does not contribute to the perturbation in η since it does not produce thermal fissions, and therefore η is therefore not associated with U-238 in the two tables. U-238 does contribute about 34% of the

thermal absorptions in a zero-burnup lattice and about 28% at mid-burnup. A significant portion of the increase in f upon voiding is therefore due to U-238, and this contribution increases with burnup for the same reason as for U-235.

By mid-burnup, Pu-239 supplies about half the lattice cell fission yield and has a significant influence on the void effect. The bottom row in Table 3.10 compares the ring-by-ring concentration of Pu-239 in equilibrium fuel, normalized in this case to unity in the outer ring. Observe that the radial distribution of Pu-239 is somewhat "flatter" than that of U-235 at mid-burnup, caused by the greater geometric self-shielding across the bundle in the case of U-235 compared with U-238 (which produces Pu-239). Nevertheless, the thermal void effect contribution of Pu-239 is still influenced by the radial dependence of thermal flux, as with U-235, and significant radial variation is again observed.

As outlined in Section 3.2.3 on "thermal spectral effects", plutonium has a negative influence on the void effect through the thermal parameters. This is caused by the shift of the equilibrium thermal spectrum to a cooler effective neutron temperature, away from plutonium's significant thermal resonances. It is important to note that the *isotopic* thermal yield/absorption ratio for Pu-239, for example, actually increases upon voiding, as shown in Table 3.11, which might lead to the conclusion of a *positive* influence on the void effect through the thermal parameters (as implied in Reference 19). This ratio, however, is not the same as plutonium's contribution to the thermal yield efficiency of the cell, η, and thus does not convey the same information. In this instance, although absorption in Pu-239 decreases upon voiding by a greater amount than yield,

leading to positive values in Table 3.11, *total* cell absorption slightly increases, leading to negative values in Table 3.9. For completeness, the isotopic yield/absorption ratio for U-235 is also given in Table 3.11, and in Table 3.12 for a zero-burnup lattice. The total perturbation, in both cases, is positive (like Pu-239) but very small.

In the inner fuel rings the significant rise in thermal flux (see Figure 3.8 or Table 3.4 and Table 3.5) counters the negative influence of Pu-239 just described, leading to slightly positive perturbations in η and f in Table 3.9; the opposite is true for the outer rings where the decrease in thermal flux adds constructively to the negative spectral effect in plutonium. The overall effect is a combined thermal contribution that is strongly negative, reducing the total cell f parameter by a factor of five (as pointed out previously in this chapter), and forcing the total cell η parameter significantly negative. The spatial "summary" of this information in Table 3.7 indicates that these two thermal effects effectively cancel each other.

3.4.2 Fast and Epithermal Range Material Effects

Not surprisingly, the perturbations to the non-thermal parameters (p_F, p_E, and ϵ_{NT}) are almost exclusively attributable to U-238, and therefore independent of burnup. As Table 3.8 and Table 3.9 indicated, these perturbations, expressed in relative terms, are greatest near the centre of the cell and decrease slightly towards the outer fuel ring (also evident in the geometry effects given in Table 3.6 and Table 3.7). Again the exception is p_E, which shows a much steeper reduction in its positive perturbation near the outer

fuel ring. In terms of absolute contributions, the most significant perturbation is to p_E for U-238, with about 80% of this occurring in the outer two fuel rings (see Table 3.8 and Table 3.9).

U-235 and Pu-239 make negligible contributions to the void effect through the non-thermal parameters, simply due to their low nuclide density. Note, however, that the relative perturbations to these parameters is comparable to U-238, with the notable exception that for both U-235 and Pu-239 the change in p_E is negative due to the dominance of their low-end epithermal absorption cross-sections. As indicated in Figure 3.5 or Figure 3.6, this is a region of increasing flux with voiding.

3.4.3 Summary of Material-Related Voiding Effects

The subdivided contributions listed in this section have been determined by apportioning the numerators in Equation (2.12) to Equation (2.15), with the modification expressed in Equation (3.3), by isotope. The denominators have been taken as cell quantities. This technique, while of limited value for determining the perturbation in each isotope's individual behaviour, is a valid way of separating the additive contribution of each isotope towards the void effect for the cell. This analysis is necessary for the optimization process in succeeding chapters.

The analysis in Table 3.8 and Table 3.9 shows that the major positive influences on the void effect are through ηf for U-235 and through p_E for U-238. With burnup and outer ring depletion the contribution of U-235 through η alone increases four-fold and

equals the U-238 contribution through p_E. At the same time the growth of plutonium in the fuel adds a strong negative contribution through ηf, thereby decreasing the overall void effect with increasing burnup. The data in the last column of Table 3.8 and Table 3.9 corresponds to that appearing in the last column of Table 3.6 and Table 3.7, respectively. The sum of all contributions for each component in Table 3.8 and Table 3.9 doesn't quite equal the corresponding value in the previous two tables, since minor contributions are made by other excluded materials in the cell.

As a summary of these material-related voiding effects, Table 3.13 and Table 3.14 (for zero and mid-burnup, respectively) compare the contribution to the void reactivity effect of each fissile nuclide through its perturbation to the overall cell yield. Results are listed by spectral group, and the totals for each nuclide reflect the graphical information previously given in Figure 3.11 at the zero and mid-burnup points. Since this way of looking at things ignores the contribution through changes in the relative importance of group absorption, only the fast group results are relevant for U-238, and thermal for U-235 and Pu-239. As with the information in the previous subsections, these results should only be viewed in the context of their definition; the neutron yield is highlighted in this case. Once again the negative influence of U-235 in the outer ring is evident, decreasing with depletion, as is the strongly negative contribution of Pu-239 in the outer ring and overall.

3.5 Summary of Chapter

The void effect in any configuration of CANDU lattice cell is the result of a competition between component effects with spectral, spatial, and isotopic dependence. In the positive direction the most overwhelming effects are the increase in the epithermal group escape probability in U-238, and the increase in thermal yield efficiency and utilization in U-235. In the negative direction the most important countering effect is the decrease in thermal yield efficiency and utilization in Pu-239, which builds as burnup progresses.

The figures in this chapter illustrating the spectral and spatial shifts caused by coolant voiding provide very clear evidence for the phenomena that lead to these isotopic effects. The loss of down-scattering in the coolant creates a hardened spectrum that leads to increased fast absorption and fission as well as decreased resonance absorption. In the thermal range this is countered by a loss of thermal up-scattering, reducing absorption and fission in Pu-239. At the same time a shift of the thermal and epithermal spatial flux distribution takes place, increasing the former and decreasing the latter in the inner fuel regions. The effects of increased thermal absorption and decreased epithermal absorption are therefore greatest, in relative terms, near the centre of the fuel cluster.

The information presented in this chapter will be used in the next chapters to attempt to design decreases in the void effect.

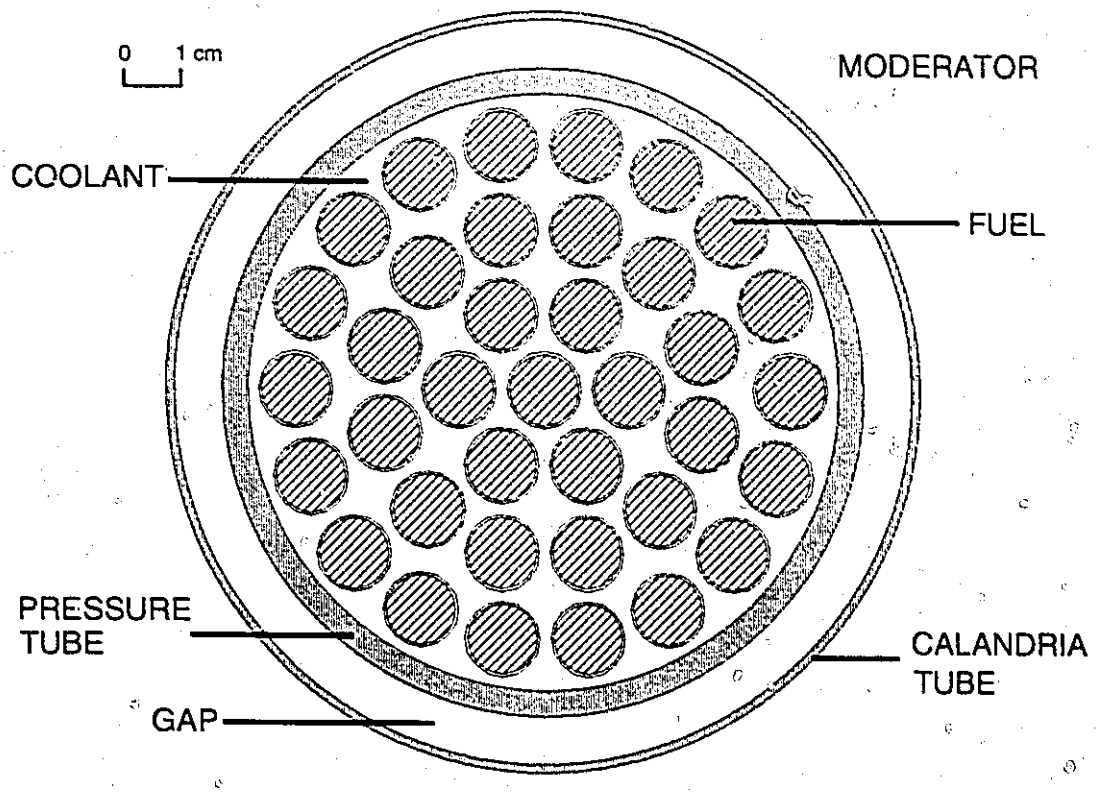

Figure 3.1 37-Element reference CANDU lattice cell.

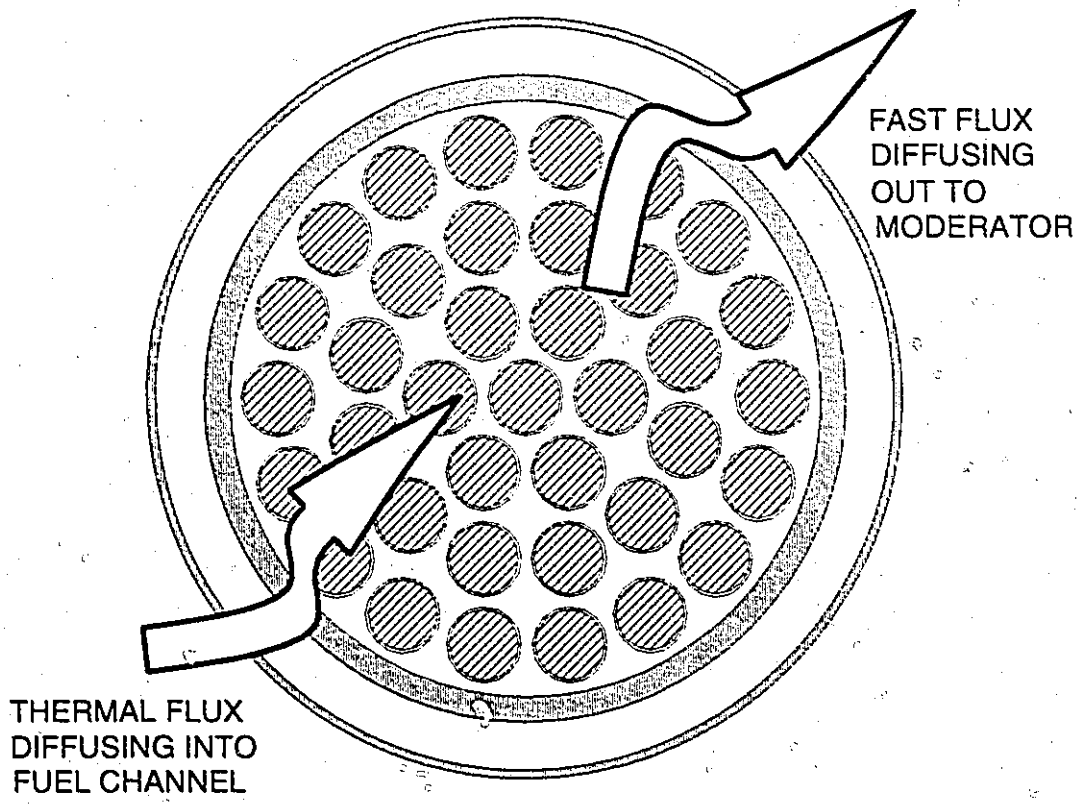

Figure 3.2 Simplified Concept of Separated Spectral Sources in CANDU Lattice Cell: Fast (and High-Energy Epithermal) Neutrons Born in the Fuel Channel and Diffusing out to the Moderator; Thermal (and Low-Energy Epithermal) Neutrons Born in the Moderator and Diffusing into the Fuel Channel.

Table 3.1 Summary of Total Void Effect and Criticality Factor Contributions in a Zero-Burnup and Mid-Burnup CANDU Lattice.

Criticality Factor	Void Criticality Effect		Void Reactivity Effect	
	Zero-Burnup (mk)	Mid-Burnup (mk)	Zero-Burnup (mk)	Mid-Burnup (mk)
η	2.2	−2.2	1.8	−2.1
f	3.9	2.1	3.3	2.0
p_F	−3.8	−3.5	−3.2	−3.4
p_E	11.7	11.5	9.9	10.9
ϵ	5.2	5.7	4.4	5.4
TOTAL EFFECT	19.3	13.6	16.3	13.0

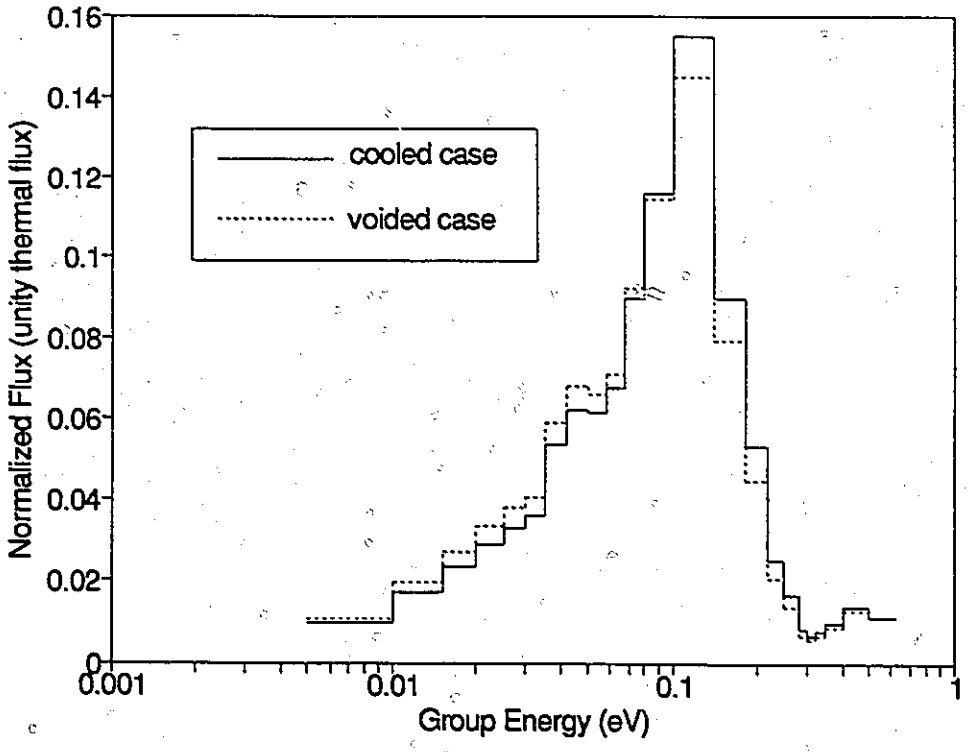

Figure 3.3 Effect of Coolant Voiding on Normalized Thermal Spectrum: Inner Coolant Region (Mid-Burnup Lattice).

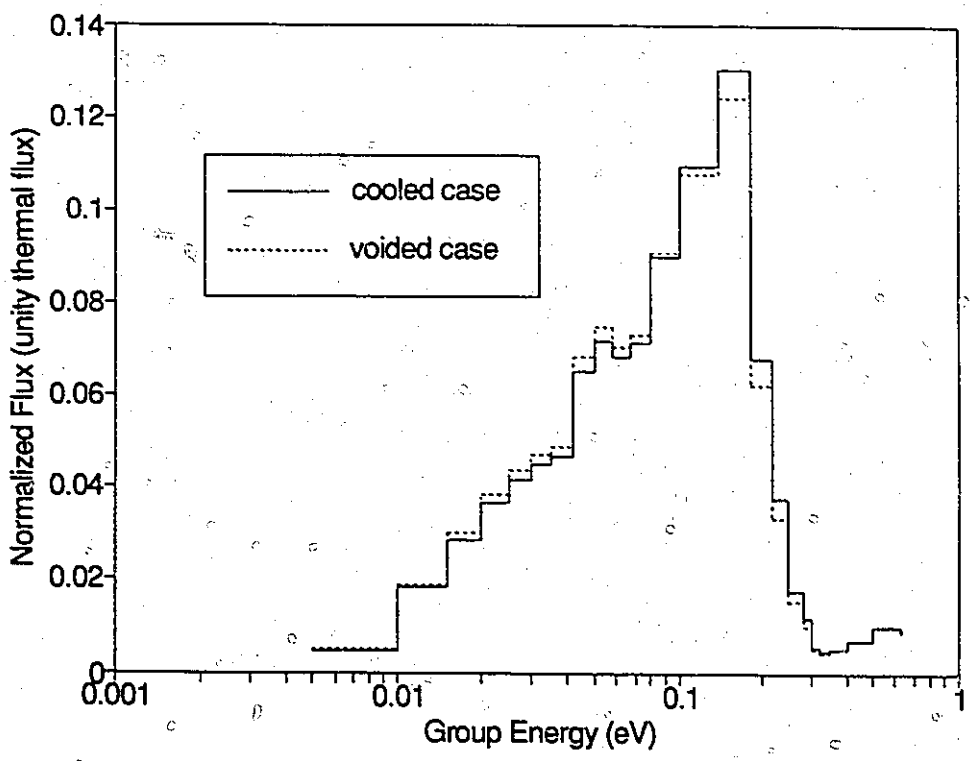

Figure 3.4 Effect of Coolant Voiding on Normalized Thermal Spectrum: Outer Coolant Region (Mid-Burnup Lattice).

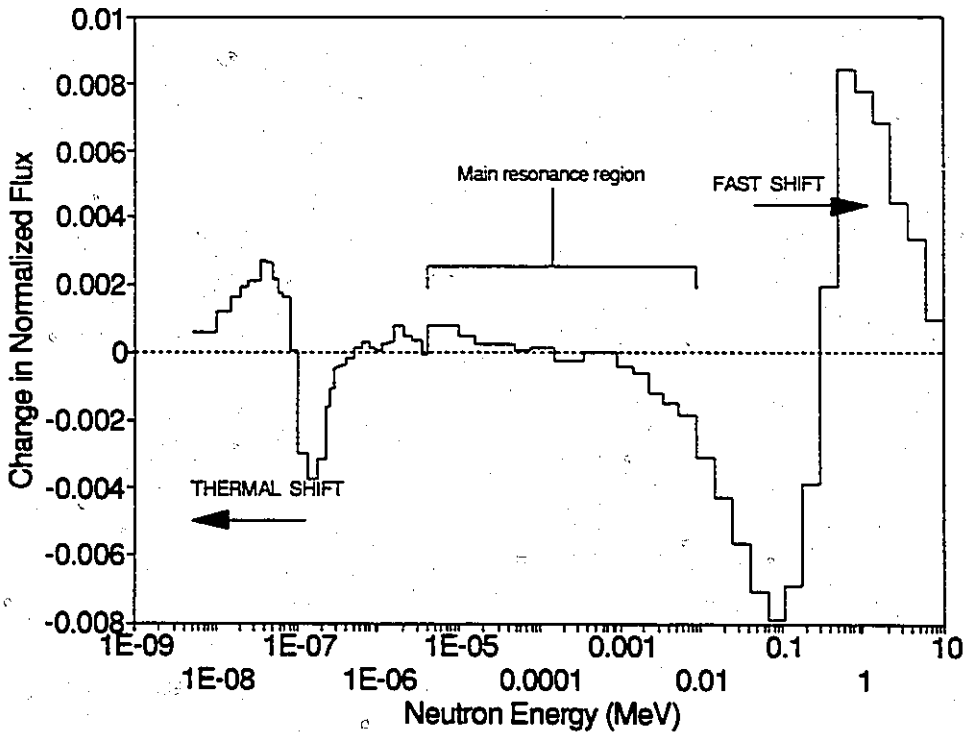

Figure 3.5 Change in Neutron Spectrum of Inner Coolant Region Upon Voiding: Zero-Burnup Lattice.

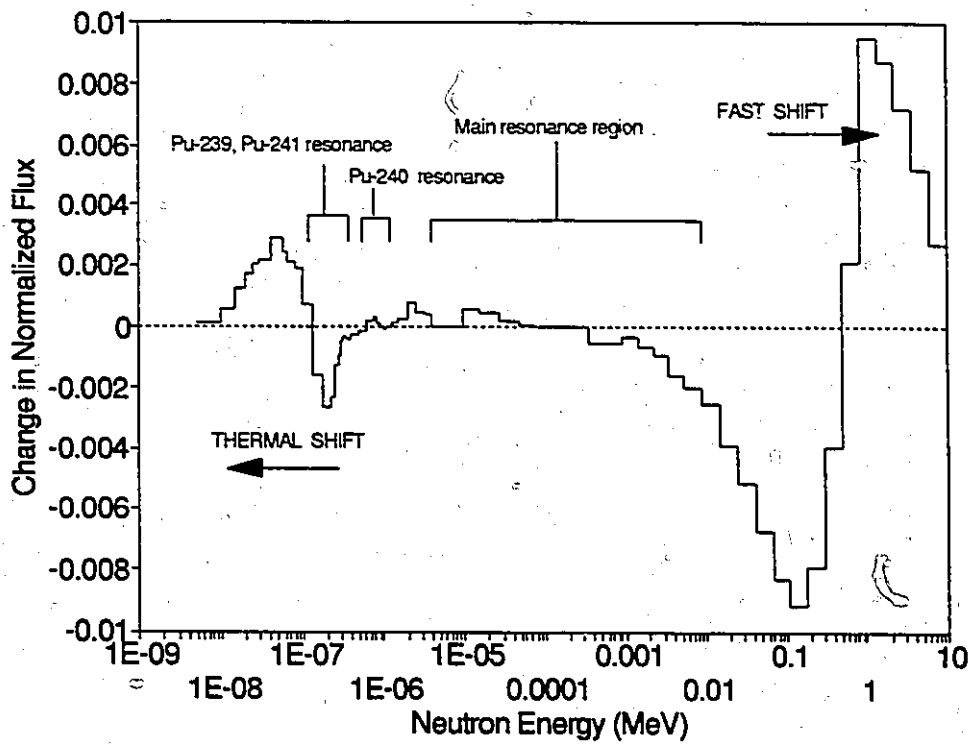

Figure 3.6 Change in Neutron Spectrum of Inner Coolant Region Upon Voiding: Mid-Burnup Lattice.

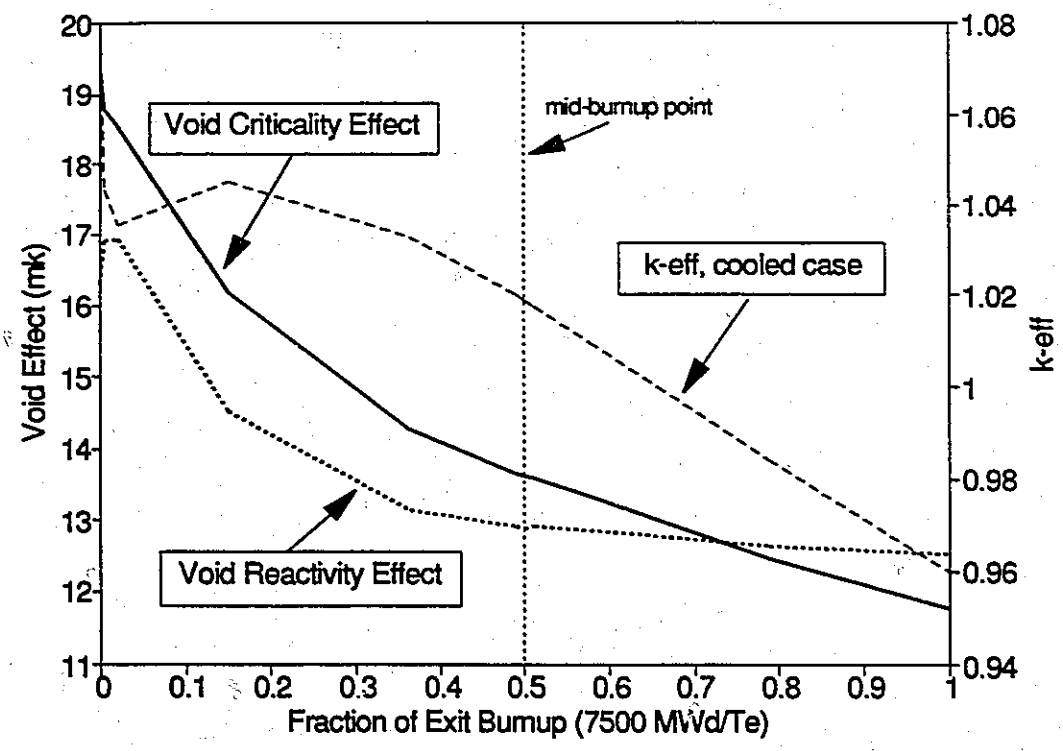

Figure 3.7 Void Reactivity Effect ($\Delta\rho_v$), Void Criticality Effect ($\Delta k_{eff,v}$), and k_{eff} (cooled case) vs. Burnup Fraction.

Table 3.2 Ratio of Average Thermal Group Moderator-to-Fuel Collision Probabilities: P_{ij} (voided) / P_{ij} (cooled).

Target Fuel Ring	Ring 1	Ring 2	Ring 3	Ring 4
Ratio	2.0	1.8	1.6	1.3

Table 3.3 Ratio of Average Fast Group Fuel-to-Moderator Collision Probabilities: P_{ij} (voided) / P_{ij} (cooled).

Source Fuel Ring	Ring 1	Ring 2	Ring 3	Ring 4
Ratio	1.3	1.3	1.2	1.2

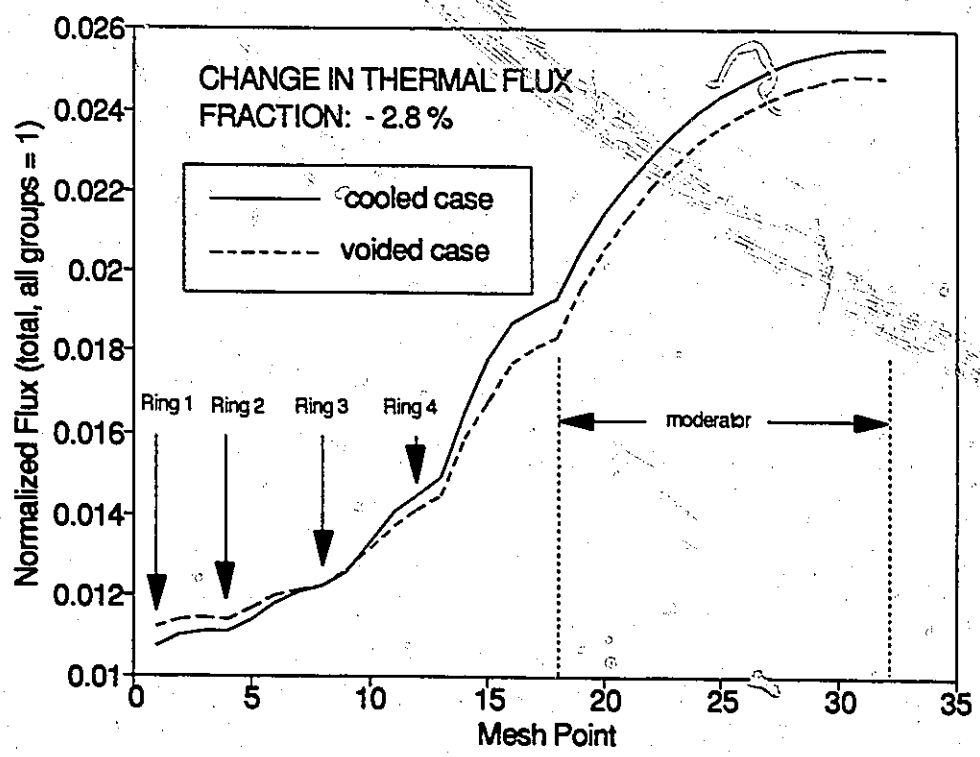

Figure 3.8 Normalized Spatial Distribution of Thermal Flux Across Mid-Burnup CANDU Lattice Cell for Cooled and Voided Cases.

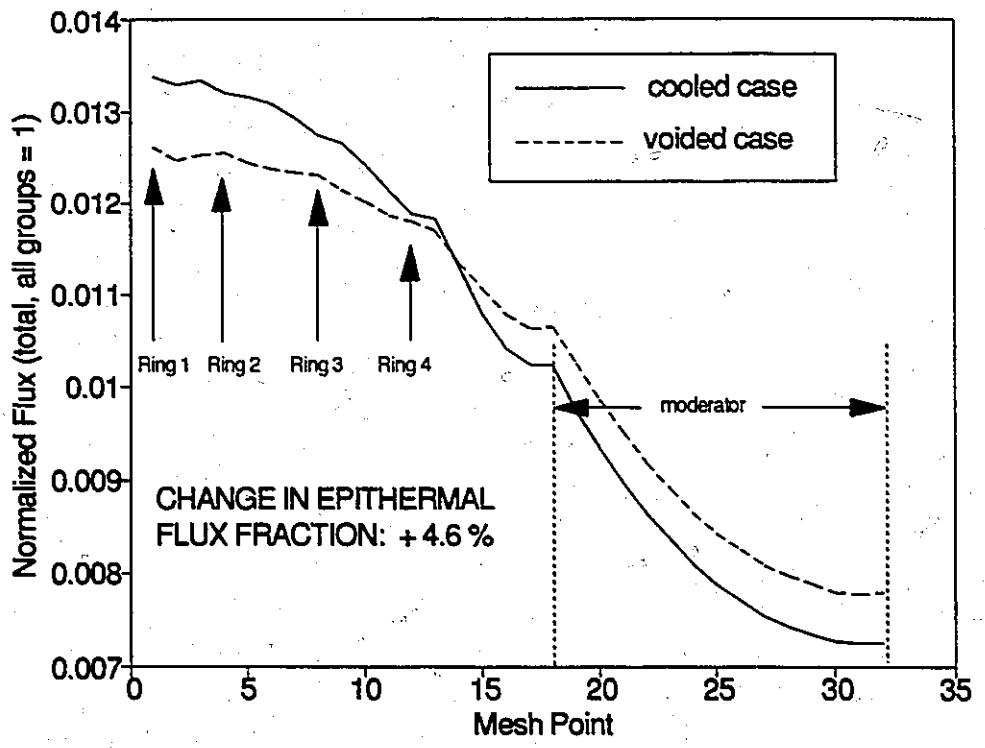

Figure 3.9 Normalized Spatial Distribution of Epithermal Flux Across Mid-Burnup CANDU Lattice Cell for Cooled and Voided Cases.

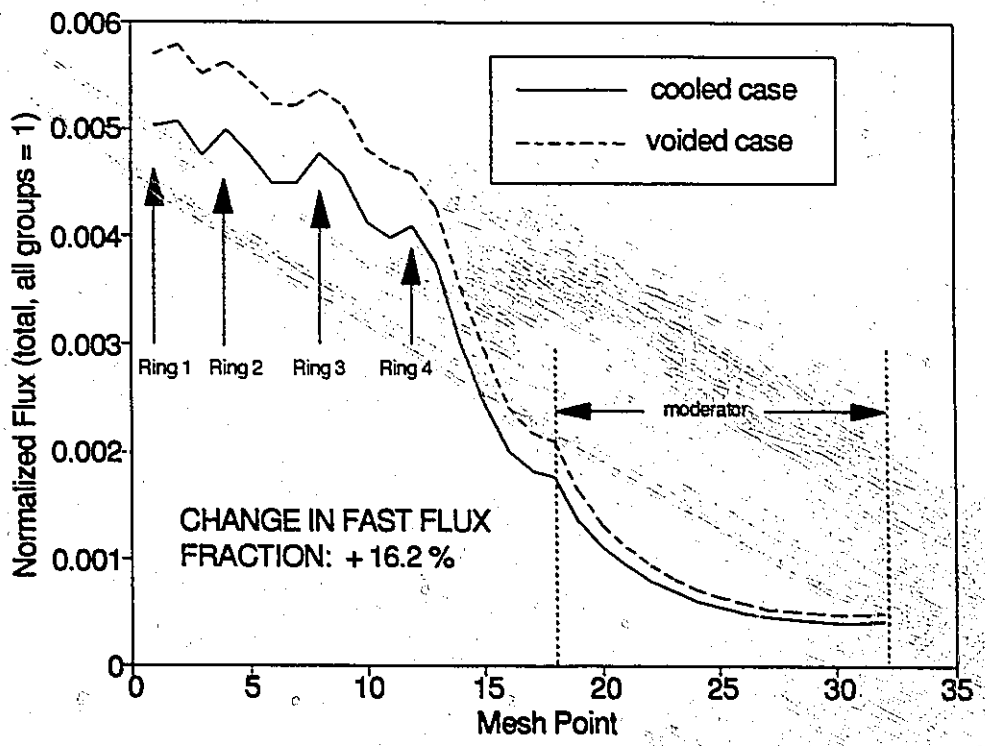

Figure 3.10 Normalized Spatial Distribution of Fast Flux Across Mid-Burnup CANDU Lattice Cell for Cooled and Voided Cases.

Table 3.4 Proportion of Total Flux by Location in Each Energy Group Before and After Voiding in a Zero-Burnup CANDU Lattice.

Lattice Cell Location	Energy Group	Proportion of Total Flux at Location		
		Cooled Case	Voided Case	Difference Upon Voiding
Coolant Near Ring 1	fast	16.1 %	18.4 %	+ 2.3 %
	epithermal	45.2 %	42.1 %	– 3.1 %
	thermal	38.7 %	39.5 %	+ 0.8 %
Coolant Near Ring 4	fast	9.6 %	11.3 %	+ 1.7 %
	epithermal	36.1 %	36.4 %	+ 0.3 %
	thermal	54.3 %	52.2 %	– 2.0 %
Moderator	fast	1.9 %	2.3 %	+ 0.3 %
	epithermal	24.0 %	25.6 %	+ 1.7 %
	thermal	74.1 %	72.1 %	– 2.0 %

Table 3.5 Proportion of Total Flux by Location in Each Energy Group Before and After Voiding in a Mid-Burnup CANDU Lattice.

Lattice Cell Location	Energy Group	Proportion of Total Flux at Location		
		Cooled Case	Voided Case	Difference Upon Voiding
Coolant Near Ring 1	fast	17.7 %	20.2 %	+ 2.5 %
	epithermal	49.3 %	45.5 %	– 3.8 %
	thermal	32.9 %	34.3 %	+ 1.4 %
Coolant Near Ring 4	fast	10.5 %	12.3 %	+ 1.8 %
	epithermal	39.3 %	39.4 %	+ 0.1 %
	thermal	50.1 %	48.3 %	– 1.8 %
Moderator	fast	2.1 %	2.5 %	+ 0.4 %
	epithermal	26.1 %	27.8 %	+ 1.7 %
	thermal	71.8 %	69.8 %	– 2.0 %

Table 3.6 Fuel Ring Contributions (Absolute and Relative) to Change in Criticality Factors Upon Voiding in a Zero-Burnup Lattice.

Criticality Factor	Change in Component Upon Voiding					
	type	Ring 1	Ring 2	Ring 3	Ring 4	TOTAL
η	abs. rel.	.0021 7.8 %	.0084 5.0 %	.0079 2.1 %	−.0158 −2.2 %	.0026 0.3 %
f	abs. res.	.0015 7.7 %	.0060 5.0 %	.0059 2.2 %	−.0101 −2.0 %	.0034 0.4 %
p_F	abs. rel.	−.0001 −11.5 %	−.0005 −11.4 %	−.0009 −10.6 %	−.0011 −9.8 %	−.0026 −10.4 %
p_E	abs. rel.	.0003 10.5 %	.0020 10.5 %	.0040 10.1 %	.0037 5.4 %	.0100 7.7 %
ϵ_{NT}	abs. rel.	.0002 7.1 %	.0010 6.9 %	.0018 6.1 %	.0021 5.3 %	.0050 5.9 %

Table 3.7 Fuel Ring Contributions (Absolute and Relative) to Change in Criticality Factors Upon Voiding in a Mid-Burnup Lattice.

Criticality Factor	Change in Component Upon Voiding					
	type	Ring 1	Ring 2	Ring 3	Ring 4	TOTAL
η	abs.	.0021	.0082	.0063	−.0196	−.0029
	rel.	7.7 %	4.7 %	1.6 %	−2.6 %	−0.3 %
f	abs.	.0016	.0064	.0059	−.0113	.0026
	rel.	8.3 %	5.4 %	2.2 %	−2.2 %	0.3 %
p_F	abs.	−.0001	−.0005	−.0009	−.0011	−.0026
	rel.	−11.6 %	−11.5 %	−10.7 %	−9.8 %	−10.5 %
p_E	abs.	.0003	.0021	.0041	.0038	.0103
	rel.	10.2 %	10.2 %	9.7 %	5.1 %	7.3 %
ϵ_{NT}	abs.	.0002	.0012	.0020	.0025	.0059
	rel.	7.9 %	7.7 %	7.0 %	6.2 %	6.8 %

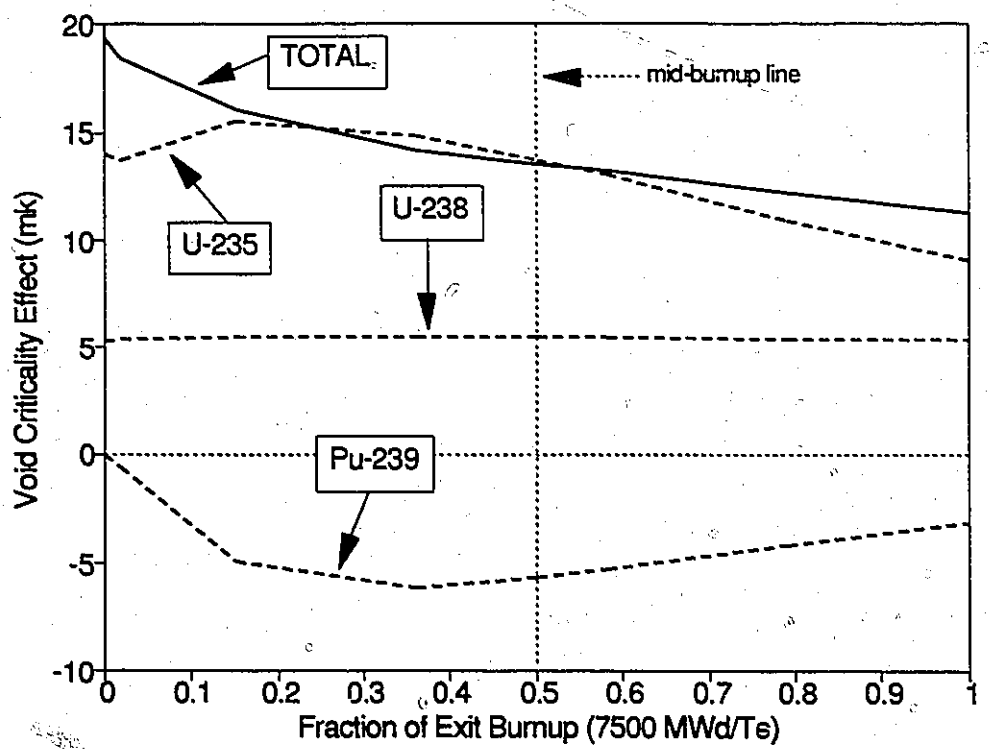

Figure 3.11 Contribution of Fissile Material to Void Criticality Effect Through Change in Neutron Yield vs. Burnup Fraction.

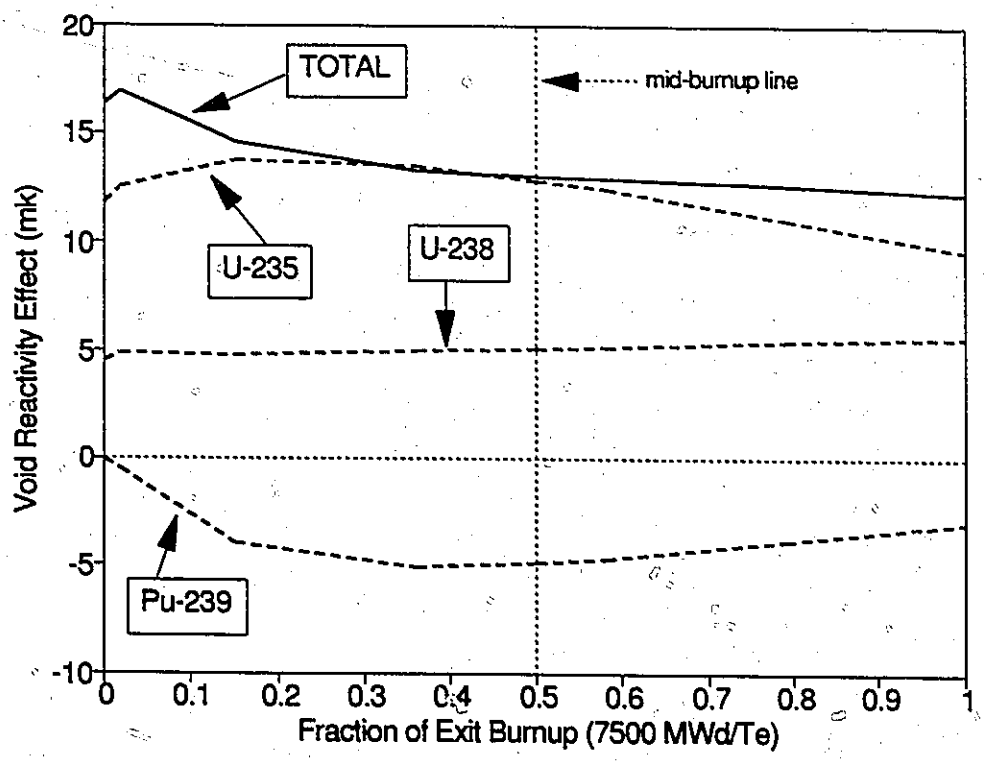

Figure 3.12 Contribution of Fissile Material to Void Reactivity Effect Through Change in Neutron Yield vs. Burnup Fraction.

Table 3.8 Material Contributions by Location (Absolute and Relative) to Change in Criticality Factors Upon Voiding in a Zero-Burnup Lattice.

Material	Criticality Factor	Change in Component Upon Voiding*					
		type	Ring 1	Ring 2	Ring 3	Ring 4	TOTAL
U-235	η	abs. rel.	.0021 7.8 %	.0084 5.0 %	.0079 2.1 %	−.0154 −2.2 %	.0030 0.3 %
	f	abs. rel.	.0009 8.0 %	.0039 5.2 %	.0040 2.3 %	−.0060 −1.9 %	.0028 0.5 %
	p_F	abs. rel.	.0000 −12.5 %	.0000 −12.5 %	.0000 −11.8 %	.0000 −11.1 %	−.0001 −11.6 %
	p_E	abs. rel.	.0000 −1.8 %	.0000 −1.5 %	−.0001 −1.4 %	−.0002 −2.0 %	−.0003 −1.7 %
	ϵ_{NT}	abs. rel.	.0000 0.8 %	.0000 0.5 %	.0000 0.4 %	.0001 0.8 %	.0002 0.6 %
U-238	f	abs. rel.	.0005 7.3 %	.0021 4.7 %	.0019 1.9 %	−.0040 −2.1 %	.0005 0.2 %
	p_F	abs. rel.	−.0001 −11.7 %	−.0005 −11.6 %	−.0009 −10.8 %	−.0011 −10.0 %	−.0025 −10.6 %
	p_E	abs. rel.	.0003 12.3 %	.0021 12.3 %	.0041 11.8 %	.0039 6.4 %	.0105 9.0 %
	ϵ_{NT}	abs. rel.	.0002 9.7 %	.0010 9.6 %	.0018 8.7 %	.0021 7.8 %	.0051 8.5 %

* Zero entry indicates negligible result.

Table 3.9 Material Contributions by Location (Abs. and Rel.) to Change in Criticality Factors Upon Voiding in a Mid-Burnup Lattice.

Material	Criticality Factor	Change in Component Upon Voiding*					
		type	Ring 1	Ring 2	Ring 3	Ring 4	TOTAL
U-235	η	abs.	.0016	.0070	.0080	–.0038	.0128
		rel.	11.0 %	7.6 %	3.9 %	–1.1 %	2.0 %
	f	abs.	.0007	.0029	.0034	–.0013	.0057
		rel.	11.1 %	7.7 %	4.1 %	–1.0 %	2.1 %
	p_F	abs.	.0000	.0000	.0000	.0000	.0000
		rel.	–12.5 %	–12.6 %	–11.8 %	–11.1 %	–11.7 %
	p_E	abs.	.0000	.0000	.0000	–.0001	–.0001
		rel.	–1.3 %	–0.9 %	–0.8 %	–1.8 %	–1.3 %
	ϵ_{NT}	abs.	.0000	.0000	.0000	.0001	.0001
		rel.	0.6 %	0.3 %	0.3 %	1.0 %	0.6 %
U-238	f	abs.	.0006	.0025	.0030	–.0019	.0042
		rel.	10.4 %	7.1 %	3.6 %	–1.2 %	1.5 %
	p_F	abs.	–.0001	–.0005	–.0009	–.0011	–.0025
		rel.	–11.8 %	–11.7 %	–10.9 %	–10.0 %	–10.7 %
	p_E	abs.	.0004	.0021	.0042	.0040	.0106
		rel.	12.7 %	12.6 %	12.1 %	6.6 %	9.3 %
	ϵ_{NT}	abs.	.0002	.0011	.0020	.0024	.0057
		rel.	10.3 %	10.2 %	9.3 %	8.4 %	9.1 %
Pu-239	η	abs.	.0005	.0011	–.0017	–.0151	–.0153
		rel.	3.7 %	1.4 %	–0.9 %	–3.9 %	–2.3 %
	f	abs.	.0002	.0002	–.0012	–.0071	–.0080
		rel.	2.8 %	0.6 %	–1.5 %	–4.2 %	–2.7 %
	p_F	abs.	.0000	.0000	.0000	.0000	.0000
		rel.	–12.5 %	–12.5 %	–11.7 %	–11.0 %	–11.5 %
	p_E	abs.	.0000	.0000	.0000	–.0001	–.0001
		rel.	–3.8 %	–3.3 %	–3.0 %	–2.6 %	–2.9 %
	ϵ_{NT}	abs.	.0000	.0000	.0001	.0001	.0002
		rel.	3.3 %	1.6 %	2.6 %	2.2 %	2.4 %

* Zero entry indicates negligible result.

Table 3.10 Relative Fuel Ring Nuclide Densities for U-235 and Pu-239 in a Mid-Burnup Lattice (Separate Normalization).

Nuclide	Ring 1	Ring 2	Ring 3	Ring 4
U-235	1	0.98	0.92	0.79
Pu-239	0.83	0.84	0.89	1

Table 3.11 Change in Thermal Yield/Absorption Ratio of U-235 and Pu-239, by Location, Upon Voiding in a Mid-Burnup Lattice.

Material	Ring 1	Ring 2	Ring 3	Ring 4	TOTAL
U-235	+0.3 %	+0.2 %	+0.2 %	+0.1 %	+0.2 %
Pu-239	+2.2 %	+1.9 %	+1.6 %	+1.0 %	+1.3 %

Table 3.12 Change in Thermal Yield/Absorption Ratio of U-235, by Location, Upon Voiding in a Zero-Burnup Lattice.

Material	Ring 1	Ring 2	Ring 3	Ring 4	TOTAL
U-235	+0.3 %	+0.3 %	+0.2 %	+0.1 %	+0.2 %

Table 3.13 Contribution (in mk) of Fissile Materials to Void Reactivity Effect Through Change in Neutron Yield in a Zero-Burnup Lattice.

Material	Energy Group	Contribution to $\Delta\rho_V$ through yield (mk)				
		Ring 1	Ring 2	Ring 3	Ring 4	TOTAL
U-235	fast	0.0	0.0	0.0	0.1	0.1
	epithermal	0.0	0.0	0.1	0.2	0.3
	thermal	1.5	6.8	7.7	−5.1	10.9
	TOTAL	1.5	6.8	7.8	−4.8	11.3
U-238	fast	0.2	1.0	1.7	2.1	5.0
	epithermal	0.0	0.0	0.0	0.0	0.0
	thermal	0.0	0.0	0.0	0.0	0.0
	TOTAL	0.2	1.0	1.7	2.1	5.0
				Total Effect:		16.3

Table 3.14 Contribution (in mk) of Fissile Materials to Void Reactivity Effect Through Change in Neutron Yield in a Mid-Burnup Lattice.

Material	Energy Group	Contribution to $\Delta\rho_V$ through yield (mk)				
		Ring 1	Ring 2	Ring 3	Ring 4	TOTAL
U-235	fast	0.0	0.0	0.0	0.0	0.0
	epithermal	0.0	0.0	0.0	0.1	0.1
	thermal	1.2	5.5	6.8	−0.3	13.2
	TOTAL	1.2	5.5	6.8	−0.2	13.3
U-238	fast	0.2	1.2	2.0	2.3	5.7
	epithermal	0.0	0.0	0.0	0.0	0.0
	thermal	0.0	0.0	0.0	0.0	0.0
	TOTAL	0.2	1.2	2.0	2.3	5.7
Pu-239	fast	0.0	0.0	0.0	0.0	0.0
	epithermal	0.0	0.0	0.1	0.1	0.2
	thermal	0.4	1.3	0.1	−8.0	−6.2
	TOTAL	0.4	1.3	0.2	−7.8	−6.0
				Total Effect:		13.0

Chapter 4

Reducing the Void Effect in the CANDU Lattice Cell

In this chapter several approaches to reducing the void effect in CANDU will be discussed, based on the constituent physical analysis of Chapter 3, continuing to utilize the methods of Chapter 2, and directed as much as possible toward the goals outlined in Chapter 1 (Section 1.8). There will be some exploration inconsistent with these goals, particularly in the area of modification to lattice components beyond the fuel channel, but such distractions will serve to deepen the knowledge of this phenomenon and add perspective. Other areas to be explored are changes in fuel material (including isotopic composition or enrichment) and changes in rod cluster geometry (size, position). Each of these modifications to the lattice cell will seek to reduce the void effect by either altering the spectrum shift observed in Section 3.2, or exploiting the spatial shift observed in Section 3.3, or exploiting the material dependence observed in Section 3.4, or a combination of these three approaches. The analysis explores several options and leads logically to the novel steps in CANDU fuel design taken in the following Chapter 5.

4.1 Effect of Moderator Changes

This section addresses the effect of making changes to the moderator volume,

composition, and temperature, although such modifications obviously imply system changes incompatible with the goals set forth in Section 1.8. The motivation for altering the moderator is primarily its dominance as a thermalizing agent in the lattice cell, supported not only by its relatively large volume but also by its cool temperature and low absorption cross-section. Since these characteristics all lead to good neutron economy, the aim here is to discover what amount of void effect reduction can be attained without unacceptable sacrifice.

4.1.1 Effect of Moderator Volume

The current lattice pitch in CANDU (about 28.6 cm) is determined largely by coolant piping and refuelling machine requirements, although as Figure 4.1 indicates this value is also close to the maximum of excess reactivity plotted as a function of moderator volume per unit length by changing the lattice pitch (all else equal). This result is also confirmed by buckling measurements for different geometries of 28-element fuel in the ZED-2 reactor[3]. As the moderator volume (or lattice pitch) is reduced the relative importance of the coolant as a thermalizing agent increases, which in turn reduces the void effect, as will be discussed shortly. Another way of stating this is that voiding makes the moderator more effective at creating thermal neutrons for return to the fuel, and reduction of the moderator volume makes this a smaller increase in effectiveness. This is shown in Figure 4.2, where the void criticality effect ($\Delta k_{eff,V}$) is calculated as a function of moderator volume/unit length (range: 119 to 2000 cm^2, corresponding to a

lattice pitch of 16 to 46 cm) in a zero-burnup lattice. Since the range of k_{eff} includes some quite unrealistic values for an operating core it makes more sense to look at the void criticality effect ($\Delta k_{eff,V}$) than the void reactivity effect ($\Delta\rho_V$) here. Similar analysis has been published elsewhere[44], although not with the inclusion of the criticality factor contributions as in Figure 4.2.

According to Figure 4.2, at a critical moderator volume/unit length of about 347 cm^2 (lattice pitch of about 22 cm) there is a "knee" in the curve of total void criticality, indicating the onset of coolant dominance as a cell thermalizing agent. At lattice pitches above this critical point, saturation occurs in almost all criticality factor contributions as the slowing-down process reaches equilibrium in the moderator. The exception is the contribution from thermal utilization (f) which increases slowly due to the drop in thermal flux upon voiding in the moderator, combined with the increasing size of the moderator. At lattices pitches below this critical point the perturbation to the epithermal escape factor (p_E) becomes negative and drops off rapidly while the perturbation to the fast fission factor (ϵ) rises rapidly, with the former (negative) effect dominating. At these low moderator volumes these two factors are affected the most because the coolant's large relative contribution to the cell slowing-down power leads to an increasingly important loss of moderation upon voiding (technically the system is *undermoderated*). At a moderator volume/unit length of about 180 cm^2, or a lattice pitch of about 18 cm, the void criticality effect goes to zero, but observe from Figure 4.1 that the system is subcritical ($k_{eff} < 1$) at this point. Reference 44 indicates that exit burnup goes to zero at a moderator volume of about 300 cm^2/unit length, or a lattice pitch of

about 21 cm, consistent with the onset of subcriticality in Figure 4.1.

The same beneficial effect of reducing lattice pitch can be achieved by maintaining the reference lattice pitch and inserting void regions into the moderator. In practice these might be low cross-section gas chambers placed between calandria tubes. In experiments[56] these situations have been modelled with air-filled aluminum cans surrounding the fuel channel. Figure 4.3 and Figure 4.4 display the WIMS-AECL calculations of k_{eff} (cooled case) and $\Delta k_{eff,V}$, respectively, for a reference lattice cell with moderator voids, modelled both as an decrease in average moderator density and as an added annular void region at the lattice cell outer boundary. Also shown in both figures are the results of reduced lattice pitch for comparison. In the region of interest ($k_{eff} > 1$) there is only a minor decrease in the void criticality effect, and little difference between the three different calculations. The changes in lattice pitch result in higher predictions of both k_{eff} and Δk_{eff} than the other two models, and the addition of a heterogeneous void region results in the lowest predictions of the three. The main contribution to the slightly lower void criticality effect in the "moderator density" and "moderator void" models is through the epithermal group escape probability, p_E. This suggests that backscattering of epithermal neutrons from the fuel in the annular moderator region immediately outside the calandria tube accounts for the small difference in results. In the "moderator density" and "moderator void" models this backscattering into the fuel region would be reduced, and a slightly lower epithermal flux in the fuel region would result.

4.1.2 Effect of Moderator Isotopic Composition

The effect of *downgrading* the moderator, or increasing the molecular fraction of H_2O, is shown in Figure 4.5. Both types of void effect increase initially and then pass through a maximum as the H_2O content increases. In the void reactivity effect curve ($\Delta\rho_V$) this maximum is both forward-shifted and amplified due to the rapidly decreasing value of k_{eff} with moderator denaturing (this is another illustration of the importance of definition indicated in Section 2.1). The presence of H_2O increases both the slowing-down power and the absorption cross-section of the moderator, both of which increase the void effect. The increase in slowing-down power achieves this by making the moderator more effective at thermalizing neutrons, thus amplifying the role of the coolant as a localized source of epithermal neutron flux. The increase in absorption cross-section does this because the thermal flux drops in the moderator upon voiding (see Figure 3.8), thus decreasing cell absorption. As the H_2O content increases to higher levels, however, the importance of the coolant as a cell thermalizing agent increases, leading to a decrease in the void effect.

The k_{eff} curve in Figure 4.5 indicates the high intolerance of the current CANDU configuration for moderator denaturing. Figure 4.6, on the other hand, shows the results of denaturing with sufficient fuel enrichment to maintain the reference criticality of $k_{eff} = 1.078$ at all times (note that this goal is unattainable after about 50% H_2O content). The curves of each type of void effect follow a similar trend as that of $\Delta k_{eff,V}$ in Figure 4.5, although the reduction in each effect occurs at much lower H_2O levels due to

the negative influence on the void effect of large fuel enrichments (see Section 4.2.1). The point of zero void effect is reached at an H_2O content of about 46%, requiring an enrichment of about 80 %wt for sufficient criticality. Clearly this is not an operating regime of practical interest.

4.1.3 Effect of Moderator Temperature

In Section 3.2.3 the effect of thermal upscattering by the hot coolant was described and estimated to add about 4 mk and –2 mk to the void reactivity effect in a zero-burnup and mid-burnup lattice, respectively. This was approximately the result found by setting the coolant temperature equal to that of the moderator (71 °C), a drop of 219 °C from the reference lattice cell case. One can also reduce coolant upscattering by raising the temperature of the moderator and thus obtaining a higher effective neutron temperature. This modification avoids the detriment to thermodynamic efficiency associated with a lower coolant operating temperature, but it is undesirable from a neutron economy point of view because of the thermal fission cross-section $1/E^{1/2}$ behaviour.

Figure 4.7 illustrates the minor effect of moderator temperature change (without changing density) on both types of void effect for a zero-burnup and mid-burnup lattice. The total decrease in these effects over a 50 °C range is each about 1.5 mk at zero-burnup and 0.5 mk at mid-burnup (discharge burnup is not altered significantly by this temperature range). Note that in this case the act of bringing the coolant and moderator temperatures closer together at mid-burnup creates a *decrease* in the void effect, which

is a different trend from the result in Section 3.2.3 referred to above. The difference here is that the moderator is made hotter instead of the coolant being made cooler. This creates a greater effective neutron temperature prior to coolant voiding and thus a greater fraction of thermal equilibrium flux with energies in the 0.3 eV plutonium resonance. The resulting greater negative influence on the void effect of this resonance (see description in Section 3.2.3) is reflected in the decreasing void effect curve with temperature. At the same time the decreasing degree of upscattering with increasing temperature will oppose this trend, leading to an extremely small slope in this curve.

Over this same 50 °C temperature range k_{eff} decreases by 3 mk in a zero-burnup lattice and increases by 4 mk in a mid-burnup lattice. The greater criticality in the mid-burnup case is also caused by the non-$1/E^{1/2}$ behaviour of plutonium's absorption cross-section in the upper end of the thermal range.

4.2 Effect of Fuel Material Changes

This section will deal with changes to the fuel material, including enrichment and the addition and substitution of material to the fuel meat, without altering the cluster geometry of the reference 37-element lattice cell. The main approach of AECL's Low Void Reactivity Fuel (LVRF) programme (see Section 1.7) is described here also.

4.2.1 Effect of Fuel Enrichment

Enriching the U-235 content in the fuel increases the thermal and epithermal

absorption cross-section of the lattice cell, as well as the fast fission cross-section. If the coolant were a significant absorber in the cell this increase in absorption cross-section would decrease the void effect, relative to the reference case, through a reduced thermal utilization factor (f) contribution. In a CANDU lattice, however, the relevant contributions to a change in void effect are made through the group escape factors (p_F and p_E) and the fast fission factor (ϵ).

This much is evident in Figure 4.8, which plots the void criticality effect, $\Delta k_{eff,V}$, along with its criticality factor formula contributions, against fuel enrichment up to 10 %wt in a zero-burnup lattice. The increasing importance of thermal fission with enrichment is indicated by the decreasing perturbation to ϵ, while the increasing importance of absorption in the epithermal and fast groups is indicated by the increasing perturbations to p_E and p_F in the positive and negative directions, respectively. At low enrichments (< 2 %wt) the void criticality effect increases primarily due to the change in p_E. Beyond this point the effect begins to decrease as p_F and ϵ start to have an effect, and at large values of enrichment (> 10 %wt) the void criticality effect is lower than the natural UO_2 (reference) case.

As with the moderator changes in Section 4.1 the values of the void criticality effect ($\Delta k_{eff,V}$) reveal a clearer picture of the phenomenon of enrichment than the void reactivity effect ($\Delta\rho_V$) due to the magnitude of k_{eff} for high enrichments. Since enrichment is of considerable practical interest, however, the results using the void reactivity effect have been included here also, in Figure 4.9. Observe that the void reactivity effect decreases rapidly, which is directly caused by k_{eff} increasing rapidly with enrichment (k_{eff}

increases from 1.078 to 1.715 over the enrichment range). The range from natural to 2%wt enrichment is expanded in Figure 4.10, a result which was quoted previously in Section 2.1 as an example of the sometimes large difference between $\Delta k_{eff,V}$ and $\Delta\rho_V$. In that section four different values of the difference in void effect at zero-burnup between natural and 1.2 %wt were found, depending upon definition and model: −4 mk for $\Delta\rho_V$, +1 mk for $\Delta k_{eff,V}$, −9 mk if artificial bucklings were employed to force criticality (and therefore $\Delta\rho_V \approx \Delta k_{eff,V}$), and +4 mk if moderator boration were used to force criticality. No clear conclusion was possible regarding which result is more realistic.

The effect of burnup with enrichment has been reported in Reference 44, which uses the $\Delta\rho_V$ definition of the void effect. Using this definition the two main competing contributions to the change in void effect with burnup are the reduction in k_{eff} (as U-235 depletes) and the negative influence on $\Delta\rho_V$ of plutonium as it burns in. Several scenarios are presented with different starting enrichments between natural and 1.3 %wt, with the "equilibrium" point (constant void effect vs. burnup) occurring at about 1.0 %wt.

4.2.2 Effect of Graphite in Fuel Pins

Since the majority of the void effect in CANDU can be traced to the coolant's role as a scattering agent in the lattice cell, one possible method of reducing the effect (without changing the geometry of the fuel cluster) is the addition of an extra, non-voidable scattering material to the fuel pins. This addition would reduce the coolant's role in creating the down-scattered epithermal flux and the upscattered thermal flux, and thus

reduce the spectral shift upon voiding illustrated in Figure 3.5 and Figure 3.6.

This section examines the effect of adding graphite to the fuel pins[57] in two geometries, depicted in Figure 4.11: (1) an outer graphite annulus surrounding a UO_2 core, and (2) an inner graphite core surrounded by a UO_2 annulus. No cladding is assumed to exist between the graphite and UO_2 layers in these cases, and the graphite is modelled at the average lattice cell fuel temperature (882 °C). For each geometry, two fuel enrichment scenarios are examined: (1) using natural UO_2 as in the reference lattice cell, and (2) employing "conservation of U-235 atoms" between the reference lattice cell (natural UO_2) and the modified geometry. Of the two proposed geometries, the first one would be expected to have the greater effect since the graphite is not shielded as much from the epithermal and fast neutron flux by the UO_2.

The effects on the void criticality effect ($\Delta k_{eff,V}$) and the void reactivity effect ($\Delta\rho_V$) in a zero-burnup lattice are reported in Table 4.1 and Table 4.2, each table representing one of the two proposed geometries. Within each table the results are shown for four different volume fractions of graphite within the fuel pin, including a zero volume fraction representing the reference lattice cell. The results for both geometries are very similar, indicating only a minor shielding effect (the "graphite annulus" cases do have a consistent but slight advantage over the "graphite core" cases).

Using natural uranium the maximum reductions in $\Delta k_{eff,V}$ and $\Delta\rho_V$ at the 67.7% graphite volume fraction are about 6 mk and 3 mk, respectively, although the lattice is subcritical at this point. With the U-235 content conserved the maximum reductions in $\Delta k_{eff,V}$ and $\Delta\rho_V$ are about 5 mk and 9 mk, respectively. This high $\Delta\rho_V$ result is due to the

large supercriticality of this lattice, and once again it makes more sense to consider only the $\Delta k_{eff,V}$ results in these cases. In terms of relative effects, the $\Delta k_{eff,V}$ results represent a reduction of 25% to 30% from the reference case, depending on the enrichment used. The reduction is attributable mainly to the epithermal group escape (p_E) and fast fission factor (ϵ) contributions, as would be expected (the spectral results are not included in Table 4.1 and Table 4.2).

4.2.3 Effect of Non-Fuel Substitution in Centre Pins

In Section 3.3 the significant role in the void effect played by the inner fuel rings was identified. Since this region is of lower importance where lattice criticality is concerned (see, for instance, the thermal flux distribution in Figure 3.8) the possibility arises of substituting non-fissile material in these centre fuel pins in an attempt to lower the void effect. In this section the cluster geometry of the reference lattice cell is maintained; in a later section (Section 4.4.2) this constraint will be removed.

Two material substitutions are examined: zirconium and graphite, both clad with zircaloy-4 as with regular fuel pins. Zirconium is chosen for its property of high neutron transparency, thus approximating the substitution of fuel with 'nothing', while graphite is used to substitute fuel with a significant scattering agent. Two geometric substitutions are also examined: replacing the centre seven fuel pins (the first two fuel rings), and replacing the centre nineteen fuel pins (the first three fuel rings). The effects of these two geometric substitutions on both types of void effect and their criticality factor formula

contributions are listed in Table 4.3 and Table 4.4, respectively, again using a zero-burnup lattice. The loss in k_{eff} for the cooled cases (not included in Table 4.3 and Table 4.4) is minor for the centre seven elements substitution: −12 mk with zirconium and −3 mk with graphite. For the centre nineteen elements substitution, however, the loss in k_{eff} is more severe: −66 mk with zirconium and −41 mk with graphite.

Using zirconium in the centre seven elements (Table 4.3), the total void criticality effect ($\Delta k_{eff,V}$) is reduced by about 4 mk and the void reactivity effect ($\Delta\rho_V$) by about 3 mk. With graphite these reductions are about 5 mk and 4 mk, respectively. Using zirconium in the centre nineteen elements (Table 4.4), $\Delta k_{eff,V}$ is reduced by about 9 mk and $\Delta\rho_V$ by about 7 mk, while the corresponding reductions with graphite are about 8 mk and about 6 mk, respectively. The close results from the two vastly different materials (the moderating power[2] of zirconium is about 200 times that of graphite) suggests that the prime role of these materials is the replacement of fissile material; graphite plays only a secondary role as a non-voiding scattering agent in the lattice cell, accounting for an extra 1 mk of reduction in the void effect.

Another effect to be considered is the increased absorption in the substitution material with voiding due to the increased thermal flux, which would also reduce the void effect. However, since the thermal absorption macroscopic cross-section of zirconium is an order of magnitude higher than that of graphite[2], and yet its substitution has a smaller influence on the void effect, this advantage is assumed to be minor. The low thermal flux at the cluster centre combined with the low thermal cross-section of both substitution

materials further supports this conclusion. A method that exploits a high thermal absorption cross-section in this region of the lattice cell is examined in the next section.

4.2.4 Effect of Adding High Absorption Material

In order to reduce the void effect by taking advantage of the slight increase in thermal flux upon voiding in the inner fuel rings (see Figure 3.8), a material with a very large cross-section is needed. This is the approach favoured by AECL's Low Void Reactivity Fuel (LVRF) Programme, described earlier in Section 1.7. Lattice studies[19] characterize one possible design that has a void reactivity effect ($\Delta\rho_v$) of −4.1 mk at zero-burnup and −1.9 mk at mid-burnup. This design employs 9.1 %wt natural dysprosium in the inner seven fuel pins of the 37-element lattice cell. In order to compensate for this extra absorption in the lattice cell, an average fuel bundle enrichment of 2.1 %wt is used, distributed non-uniformly throughout the bundle in order to reduce the element power peaking ratios. The range of ring enrichment is 1.10 %wt to 3.37 %wt, with the higher enrichments in the outer rings. Calculations have also shown[58] that this absorber content can be reduced if depleted uranium (0.25 %wt U-235) is used in the centre elements, in which case U-238 acts as a burnable absorber.

As mentioned in Section 1.7 this method runs counter to this dissertation's goal of reducing the void effect without significantly compromising CANDU's principle of neutron economy. The presence of relatively large amounts of neutron poison in the lattice cell is such a compromise, and therefore this approach is included here for

information purposes only. It is interesting to determine the void effect reduction achieved by using differential enrichment across the fuel bundle, but without the added burnable poison. Two such cases, each with 0.25 %wt depleted uranium in the inner seven elements but with different enrichments in the outer two fuel rings, for an average bundle enrichment of 0.72 %wt (natural uranium) and 1.51 %wt, are presented in Table 4.5. There is little or no improvement in the void effect, except for the $\Delta\rho_V$ results with the 1.51 %wt average bundle enrichment where the high criticality values again have an influence. It should be noted here that the resonance treatment in WIMS-AECL (see Section 1.9, and also References 28 and 32) does not differentiate between pins within a fuel cluster, and therefore radial variations in enrichment will not be taken into account in the evaluation of resonance cross-sections. This is not of prime concern here, however, since it is a thermal effect that is being sought.

Table 4.6 indicates the result if the third ring of twelve fuel pins also consists of 0.25 %wt depleted uranium, in addition to the inner seven pins. As before, the outer fuel ring is given the appropriate enrichment necessary to bring the average bundle enrichment again up to 0.72 %wt A reduction of about 6 mk in both types of void effect is found at zero-burnup, and a reduction of about 3 mk in both types is found at mid-burnup. The greater effect of the differential burnup in this case is caused by the greater volume of depleted uranium included in the third ring of 12 fuel pins. A followup calculation was performed for this case with "forced criticality" using critical bucklings, as described in Section 2.2.2, resulting in a predicted void effect (both types) of about 6 mk. This represents a 10 mk reduction from the reference lattice cell with critical bucklings (see,

for example, Table 2.2).

4.2.5 Effect of Using Pu-MOX Fuel

The analysis in Section 3.4.1 showed that the growth of plutonium with burnup has a negative influence on the void effect through the thermal parameters η and f. This suggests the strategy of mixing plutonium with the fuel at the outset and thus exploiting this advantage at lower values of fuel irradiation. Intended primarily to reduce uranium demand, plutonium mixed oxide (Pu-MOX) fuel cycles have been proposed for most thermal reactor types, including CANDU[11,59] and other heavy water pressure tube reactors[60,61]. In these fuel cycles, PuO_2 is mixed (in weight fractions of usually less than 1%) with either natural or depleted UO_2. From a reactor physics point of view such an addition would have the following significant differences compared to natural UO_2 fuel[2]: (1) The microscopic thermal fission cross-section, σ_f, of Pu-239 is about 1.3 times that of U-235; (2) The delayed neutron fraction, β, of Pu-239 is about 0.3 times that of U-235; and (3) The average neutron number per thermal fission, ν_T, of Pu-239 is about 1.2 times that of U-235.

In order to examine the effect of using Pu-MOX fuel the isotopic composition of the plutonium to be mixed was assumed to be the same as that of plutonium in the outer ring of fuel pins in a discharged reference fuel bundle, as estimated by a WIMS-AECL burnup calculation (discharge burnup = 7500 MWd/Te), thereby approximating the composition of plutonium recycled from CANDU spent fuel. The isotopic ratios used are:

$N_{Pu\text{-}239} : N_{Pu\text{-}240} : N_{Pu\text{-}241} : N_{Pu\text{-}242} = 1.0 : 0.44 : 0.09 : 0.03$.

Figure 4.12 is a plot of both types of void effect and k_{eff} as function of PuO_2 weight fraction up to 10 %wt, using only a zero-burnup lattice. The higher reactivity of PuO_2 is evident in the rapid increase in k_{eff} with its addition to the fuel mixture. As with previous modifications producing high k_{eff} values the void criticality effect, $\Delta k_{eff,V}$, is probably a better indicator of the realistic effect, while the void reactivity effect, $\Delta\rho_V$, is significantly reduced by its normalization. Within the usual mixture range of 0 - 1 %wt a reduction of 4 mk is achieved in $\Delta\rho_V$ relative to the reference case (0 %wt), after which $\Delta\rho_V$ continues to decrease slowly with increasing PuO_2 concentration. The behaviour of $\Delta k_{eff,V}$ within the 0 - 1 %wt range is quite different, displaying a minimum between 0.1 %wt and 0.2 %wt where $\Delta k_{eff,V}$ is reduced by about 1 mk, followed by a rapid increase that eventually peaks at about 3 %wt.

This interesting behaviour of $\Delta k_{eff,V}$ in the 0 - 1 %wt range is mainly due the trend in the contribution to $\Delta k_{eff,V}$ through η, which is shown along with the other criticality factor contributions in Figure 4.13. The reason for the minimum in the η contribution curve is mainly the different isotopic responses in plutonium. At low weight fractions the η contribution is reduced as expected by the addition of plutonium, coming mainly from the effect of the Pu-239 cross-section as described in Section 3.4.1. However, with greater concentrations the effect of Pu-241 becomes significant, while Pu-240 and Pu-242 both maintain insignificant η contributions due to their low thermal yield. The cross-sectional behaviour of Pu-241, although including a thermal resonance near 0.3 eV like

Pu-239, is such that its η contribution in the CANDU lattice is slightly positive. Since the negative η contribution of Pu-239 almost cancels the positive contribution of U-235, the total η contribution thus increases and eventually saturates at about the same level as in the reference lattice cell (0 %wt PuO_2).

The quantitative results at zero-burnup and mid-burnup for two arbitrary cases of initial PuO_2 concentration, 0.5 %wt and 1.0 %wt, are given in Table 4.7 along with those for the reference lattice cell (0 %wt) for comparison. Burnup is increased relative to the reference case by factors of 2.3 and 3.3, respectively, although there is no relative benefit to the void effect at mid-burnup. Table 4.7 also lists the average concentrations of Pu-239 in the mid-burnup fuel for each case, relative to both the reference case and the zero-burnup lattice of each case. Although the equilibrium Pu-239 concentrations of the Pu-MOX fuel are much higher than in the reference case, they are also less than what each Pu-MOX case started out with at zero-burnup.

In conclusion, a slight benefit in terms of the void criticality effect, Δk_{eff}, is achieved with low concentration MOX fuel (<1 %wt) using plutonium number densities estimated from spent CANDU fuel. This reduction is small in the current fuel design, but may become significant in a design with very low void effect. The increase in Δk_{eff} at concentrations greater that 1 %wt is caused by the positive contribution from the Pu-241 isotope. In Chapter 5 the ratio of the Pu-241 to Pu-239 concentrations in spent LWR fuel[92] is estimated to be about twice that of spent CANDU fuel (see Table 5.18), which would indicate that the influence of this positive contribution would be greater.

4.2.6 Effect of Using Th-MOX Fuel

Another potential CANDU fuel cycle takes advantage of the high η value of U-233, created by neutron capture in Th-232, to further extend fuel reserves. Several thorium fuel cycles have been studied[11,59,62,63] but the one to be examined here is a simple mixed oxide fuel (Th-MOX) consisting of natural UO_2 topped with a small amount of ThO_2. The incentive for looking at Th-MOX fuel in this dissertation is the smaller effective resonance integral of Th-232 compared with U-238; therefore, the void effect contribution through p_E would also be expected to be smaller in comparison[3].

Figure 4.14 is a plot of both types of void effect and k_{eff} as a function of ThO_2 weight fraction up to 6%wt. Beyond this point the lattice is subcritical and not of interest. The void criticality effect ($\Delta k_{eff,V}$) does decrease slightly with the addition of ThO_2, although the decreasing value of k_{eff} makes the void reactivity effect ($\Delta\rho_V$) increase substantially over this same range. Figure 4.15 illustrates the effect of adding enriched uranium fuel to the Th-MOX fuel in order to bring k_{eff} (and the corresponding burnup) up to acceptable levels. In this case the 1.0 %wt Th-MOX case was chosen, and the void effect is plotted as a function of U-235 enrichment up to 2.0 %wt. There is a negligible difference between this result and that for simple enrichment alone shown in Figure 4.10.

4.3 Effect of Zirconium Enrichment

In this section we consider the novel approach of enriching the zirconium used in the pressure and calandria tubes of the lattice cell. Following the discovery[64] of a

significantly lower thermal absorption cross-section for Zr-90 than previously reported, an interest developed in enriching this isotope in CANDU fuel channel materials[65]. In particular it is estimated[65] that using an isotopic mixture of 99%wt Zr-90 and 1%wt Zr-91 in these zirconium alloys (normal abundance is 51.5%wt Zr-90,11.2%wt Zr-91, 17.1%wt Zr-92, 17.4%wt Zr-94, 2.8%wt Zr-96) will reduce the effective absorption cross-section of the pressure tube by a factor of 3.04 and that of the calandria tube by a factor of 3.50.

A lower absorption in these materials will have two neutronic effects of relevance to this dissertation: (1) Criticality will be increased, which will further reduce $\Delta\rho_V$ relative to $\Delta k_{eff,V}$ through its normalization to criticality; and (2) Since the fuel channel materials are located in a region of decreasing thermal flux upon voiding (see Figure 3.8), the decrease in absorption in this region will be less important, and this will decrease the void effect.

The use of 99%wt enriched zirconium alloys can be approximated in WIMS-AECL by reducing the densities of the pressure tube and calandria tube materials by the factors given above. The results of such a calculation, given in Table 4.8, show a decrease of about 3 mk in the void effect and an increase in criticality of 35 mk. As expected, the main contribution to this decrease in void effect comes from the thermal utilization factor, *f*, since the lower absorption cross-section means a smaller change in the spatial distribution of thermal absorption upon voiding.

Thus, a small but significant decrease in the void effect can be achieved by utilizing enriched zirconium in lattice cell structural alloys. This strategy will be revisited

in Chapter 5, despite its breach of this dissertation's policy of modifying only the components within the CANDU pressure tube.

4.4 Effect of Fuel Cluster Geometry Changes

This section adds another degree of freedom by examining the effect of altering the geometry of the fuel cluster. Two broad categories are envisioned: (1) Changing geometric specifications while maintaining the "fuel pin cluster" concept, defined here as a fuel channel containing only cylindrical UO_2 pins encased in cladding and surrounded by coolant; and (2) Removing some pins and substituting spacer material for pins and coolant, which is a more radical move than the simple fuel meat substitution examined in Section 4.2.3. These two categories will be addressed in separate subsections, the latter subsection constituting a review of work already done in this area.

4.4.1 Effect of Changing Pin Diameter

The incentive for changing the fuel pin diameter stems from consideration of resonance absorption. If the volume of fuel is kept constant but the number of pins reduced, thus reducing the surface-to-volume ratio (S/V) of the fuel, the resonance integral of the lattice cell is reduced due to higher geometric self-shielding of the resonance energy flux[1,2]. Thus, one would expect the void effect to be reduced due to the lower importance of resonance absorption. A 19-element fuel cluster was examined (Figure 4.16), having a fuel volume identical to the reference 37-element lattice cell, but

an S/V ratio that is about 30% less. In Table 4.9 the results with this geometry are listed along with the results using the 37-element lattice cell as a reference. Also included are the results with a 19-element geometry and differential enrichment across the fuel cluster, using 0.25 %wt depleted fuel in the inner seven elements and 0.99 %wt enriched fuel in the outer twelve elements for an average bundle enrichment of 0.72 %wt.

Clearly, the 19-element case with natural uranium fuel effects a negligible (<1 mk) reduction in the void effect, although the largest partial contribution (−1.1 mk) does come from the epithermal escape factor (p_E) as predicted. A reduction in the S/V ratio by 30% therefore does not have a significant effect. With differential enrichment across the fuel cluster the reduction is slightly less than the reduction achieved with similar differential enrichment of a 37-element fuel cluster (see Table 4.6), partly because the volume fraction using depleted UO_2 was higher in the latter case.

Another case with graded pin diameters across the fuel cluster (Figure 4.17) was examined, also with both natural UO_2 and differential enrichment. The idea here is to reduce the S/V ratio as much as possible in the centre region where the relative increase in epithermal absorption is the largest upon voiding, while keeping the fuel volume again constant. The differential enrichment (0.25 %wt in the inner seven fuel pins, 1.4 %wt in the outer 22 fuel pins, average bundle enrichment 0.72 %wt) achieves the same goal as before of reducing thermally fissile material (U-235) from the centre region. The effect of the graded geometry is negligible, as shown in Table 4.10, and the effect using differential enrichment only slightly better than the 19-element case (Table 4.9) and 37-element case (Table 4.6), again due to a slightly higher volume fraction of fuel with

depleted UO_2. As in Section 4.2.4, it must be noted that the resonance cross-sections in WIMS-AECL do not account for variation in pin geometry or composition. In terms of differential enrichment this is not a significant issue since the effect sought is a thermal one, but the intended effect of the S/V reduction in the centre fuel elements will not be reflected in the resonance cross-sections. It is true that, with proper setup of the spatial mesh, the collision probabilities transport calculation will take the greater spatial self-shielding of these pins into account, but this is likely to be a second-order effect compared to the effect on the resonance group cross-sections.

This is an illustrative, rather than rigorous, examination of the effects of changing the cluster geometry with and without differential enrichment. However, it indicates that a much more radical approach is required if the void effect in the CANDU lattice is to be reduced to near zero or negative values, without compromising its neutron economy. Such a radical approach is the subject of the next chapter.

4.4.2 Effect of an Annular Fuel Cluster

Following similar reasoning to that summarized in Section 4.2.3 a new CANDU fuel bundle has been proposed[66,67] which takes the extra step of replacing the centre seven fuel pins and associate coolant with a permanent void region or a graphite spacer. The fuel cluster is thus restricted to an annular region consisting of the two outer fuel rings of the reference lattice cell, as shown in Figure 4.18. Whereas in Section 4.2.3 the simple substitution of graphite for fuel in the centre seven pins achieved a reduction in the void

reactivity effect ($\Delta\rho_V$) of 4 mk, or about 25% of the total effect, this annular cluster design achieves a reduction of about 40%. This result was originally calculated with an earlier version of WIMS-AECL, and similar calculations using both a permanent central void (air) and a central can of non-voidable D_2O were verified against experiment[67,68]. The 40% reduction in both types of void effect is also reproducible using the version of WIMS-AECL and reference lattice cell input file (slightly modified) of this dissertation.

Improvements to this design have been examined elsewhere[69] by making perturbations to other cell parameters such as zirconium enrichment, fuel enrichment, and pin size. Of these modifications the largest reduction in the void effect is achieved through fuel enrichment. Depending on the modifications, values of $\Delta\rho_V$ are reported between 4 and 6 mk for a zero-burnup lattice and between 0 and 5 mk at mid-burnup, achieved with U-235 enrichment of 1.2 %wt and higher. It should be noted that only values of $\Delta\rho_V$ and not $\Delta k_{eff,V}$ are reported, and therefore the concerns expressed here regarding lattice cell void effect representation with high k_{eff} values (see Section 2.1) must be kept in mind.

Since ample attention has been paid to this design elsewhere (see References 66 to 69), further treatment here is not necessary. The use of a central spacer and the resulting confinement of fuel to an annular region near the pressure tube will be revisited in the next chapter.

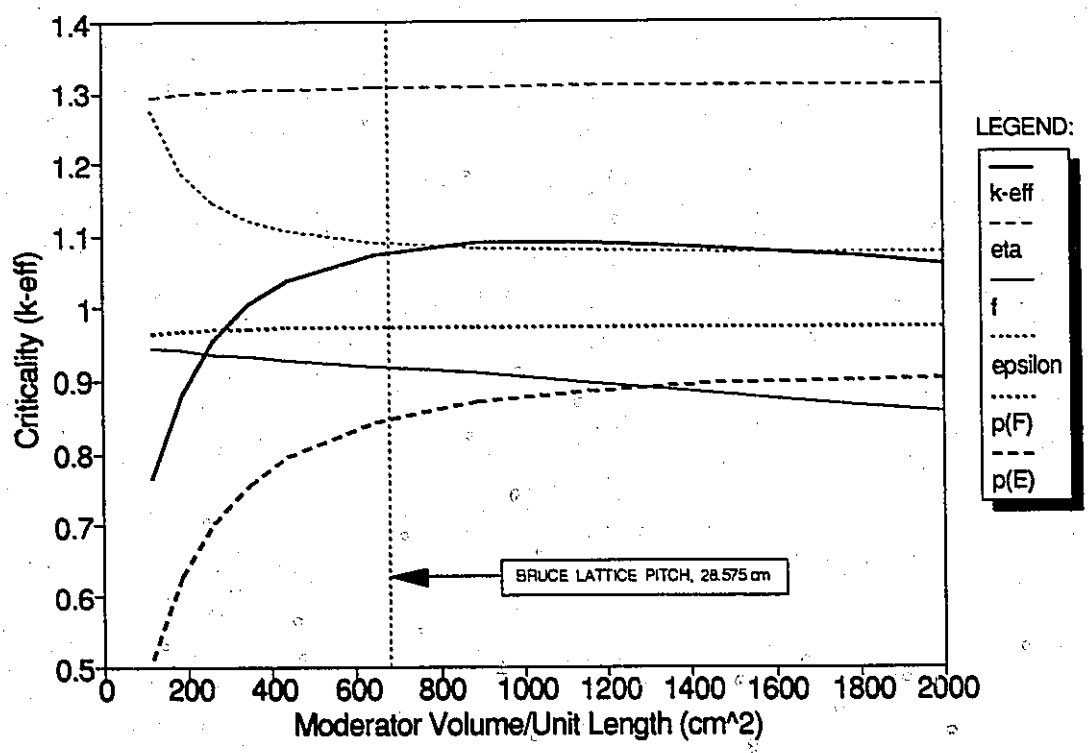

Figure 4.1 - k_{eff} (Cooled Case) and Criticality Factors as a Function of Moderator Volume, Modelled by Changing Lattice Pitch in a Zero-Burnup Lattice.

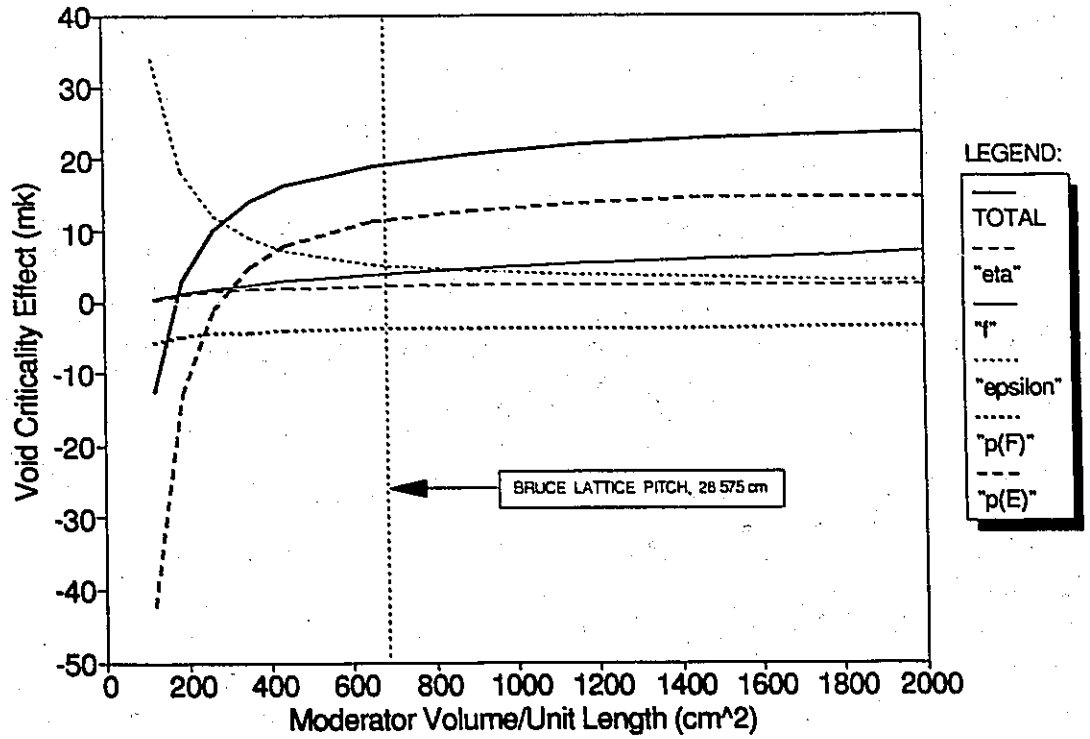

Figure 4.2 Void Criticality Effect ($\Delta k_{eff,V}$) and Criticality Factor Contributions as a Function of Moderator Volume, Modelled by Changing Lattice Pitch in a Zero-Burnup Lattice.

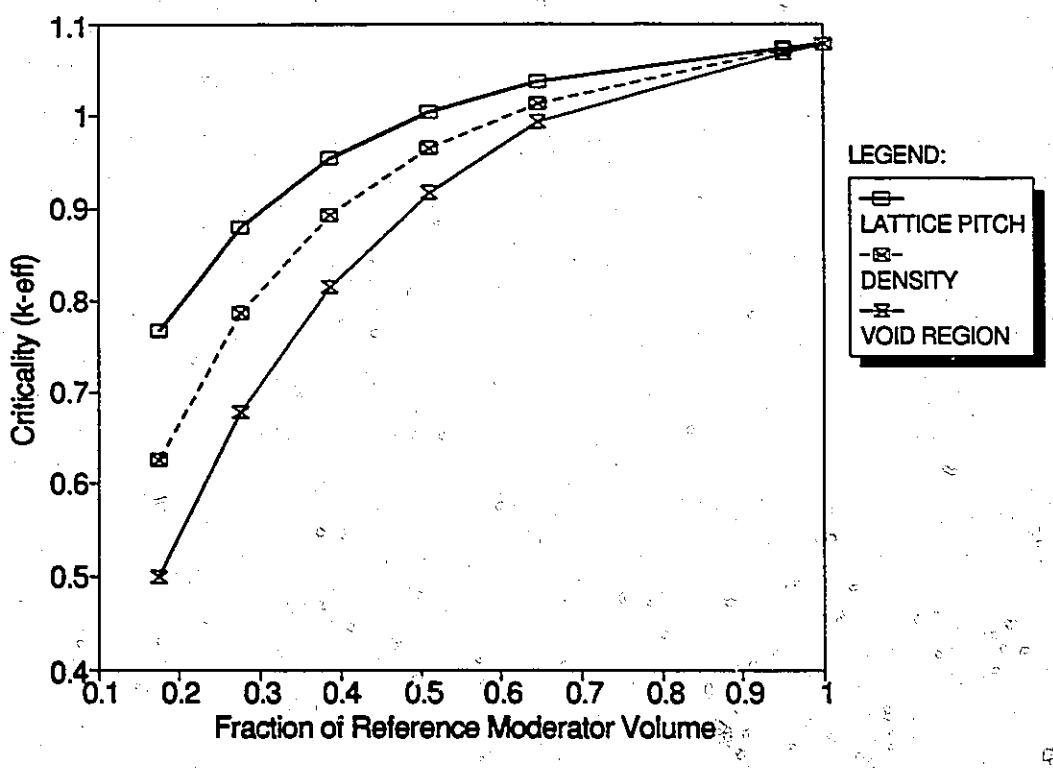

Figure 4.3 k_{eff} **vs. Moderator Volume Fraction (Zero-Burnup Lattice) as Modelled by Changing Lattice Pitch, Moderator Density, and Adding Moderator Void Regions.**

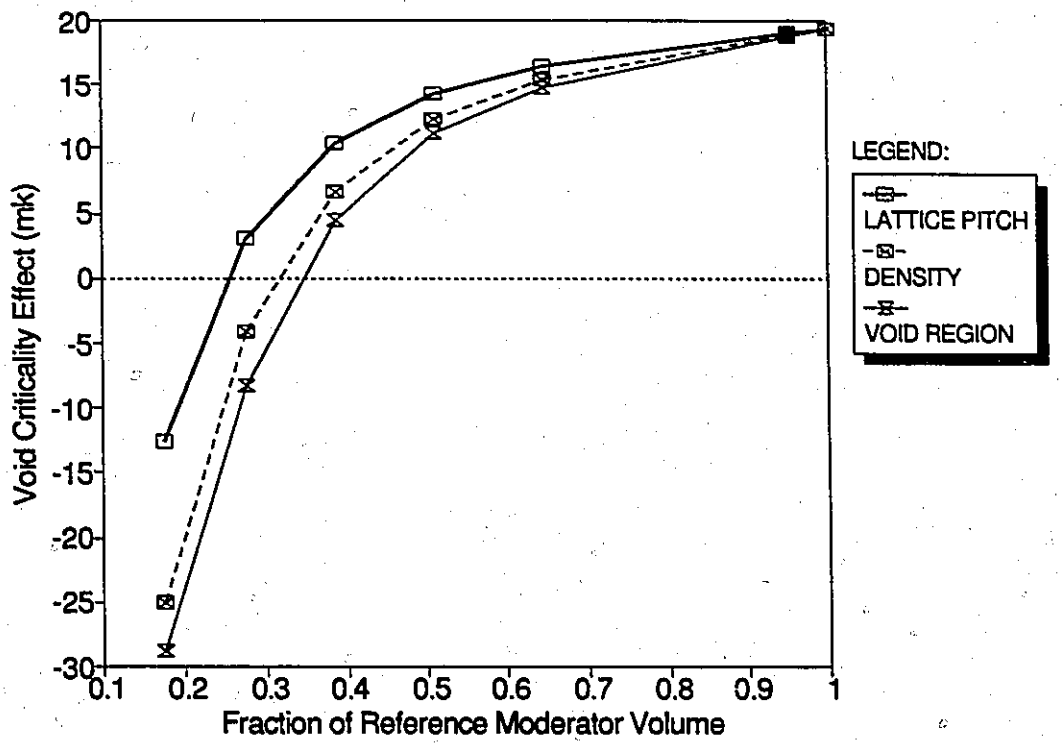

Figure 4.4 Void Criticality Effect ($\Delta k_{eff,V}$) vs. Moderator Volume Fraction (Zero-Burnup Lattice) as Modelled by Changing Lattice Pitch, Moderator Density, and Adding Moderator Void Regions.

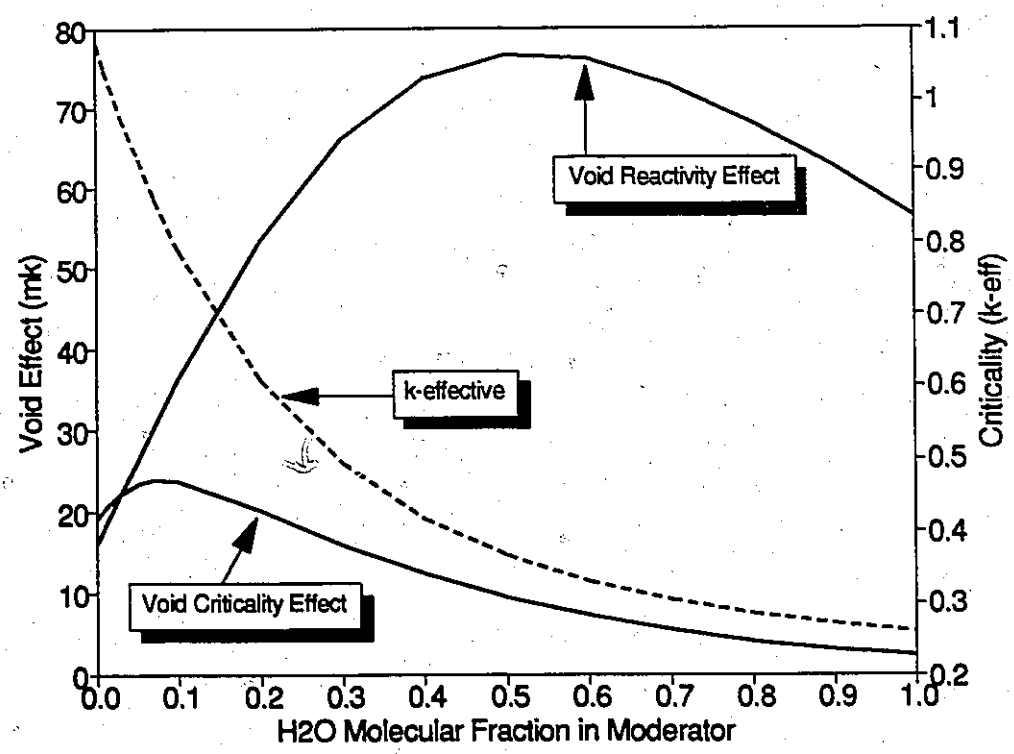

Figure 4.5 Void Criticality Effect ($\Delta k_{eff,V}$), Void Reactivity Effect ($\Delta\rho_V$), and k_{eff} vs. H_2O Fraction in Moderator (Zero-Burnup Lattice).

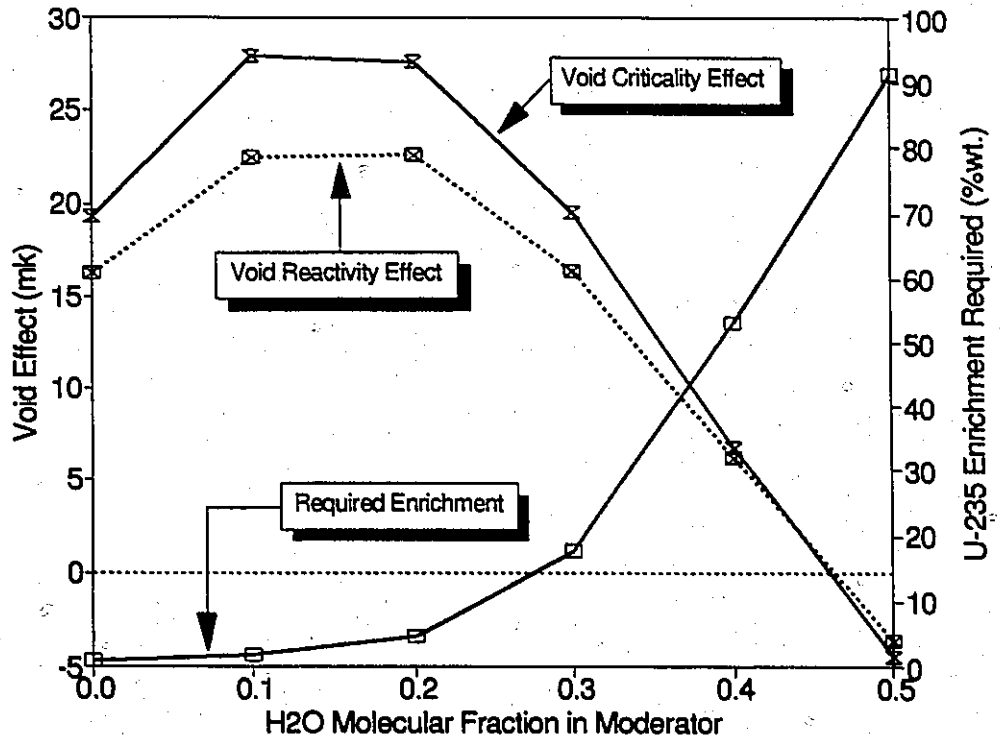

Figure 4.6 Effect of Moderator Denaturing on Void Effect with Sufficient Enrichment to Achieve Reference k_{eff} (1.078) in a Zero-Burnup Lattice.

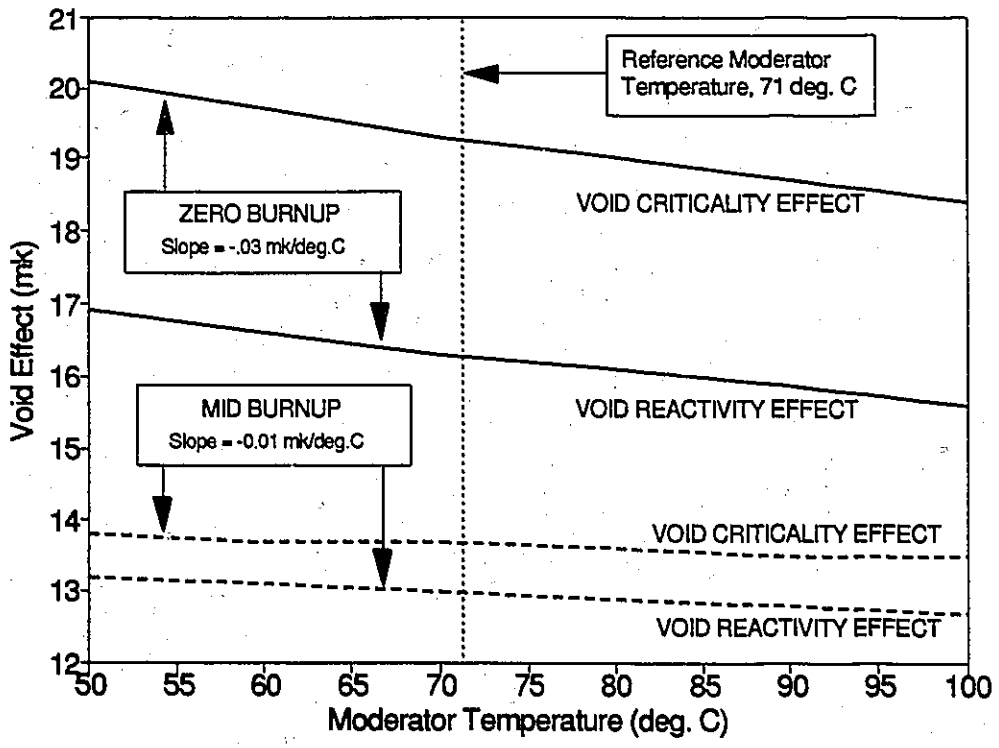

Figure 4.7 Void Criticality Effect ($\Delta k_{eff,v}$) and Void Reactivity Effect ($\Delta\rho_v$) vs. Moderator Temperature (°C) for a Zero-Burnup and Mid-Burnup Lattice.

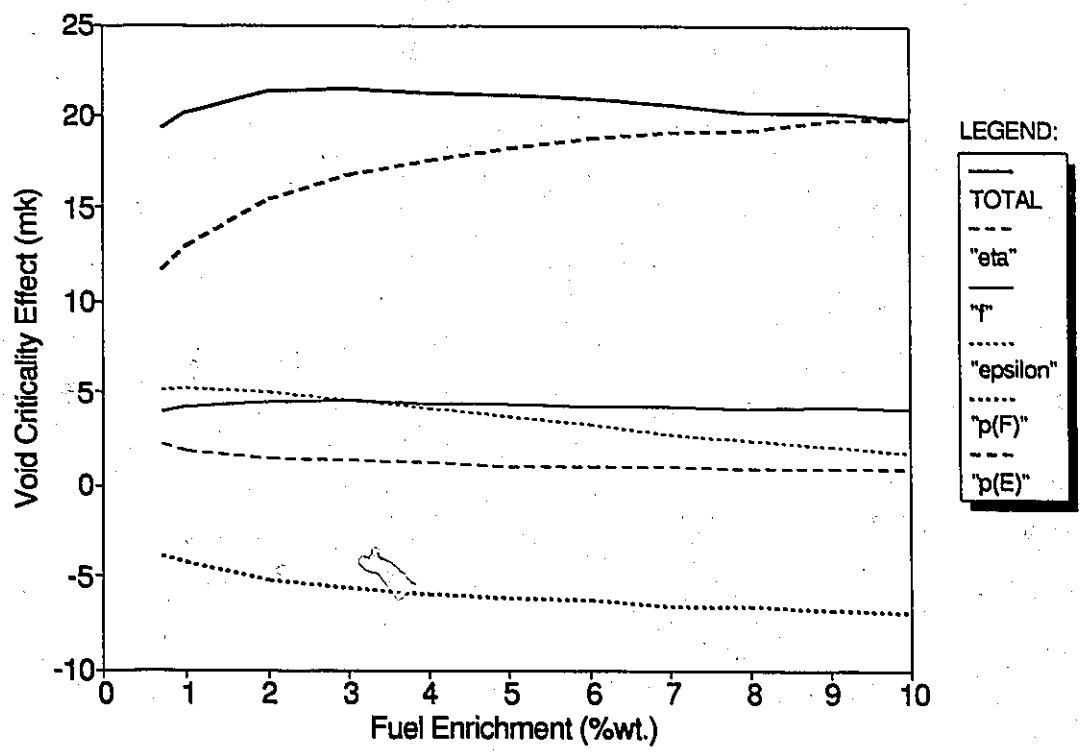

Figure 4.8 Void Criticality Effect ($\Delta k_{eff,v}$) and Criticality Factor Contributions vs. Fuel Enrichment in a Zero-Burnup Lattice: 0.72 %wt — 10 %wt.

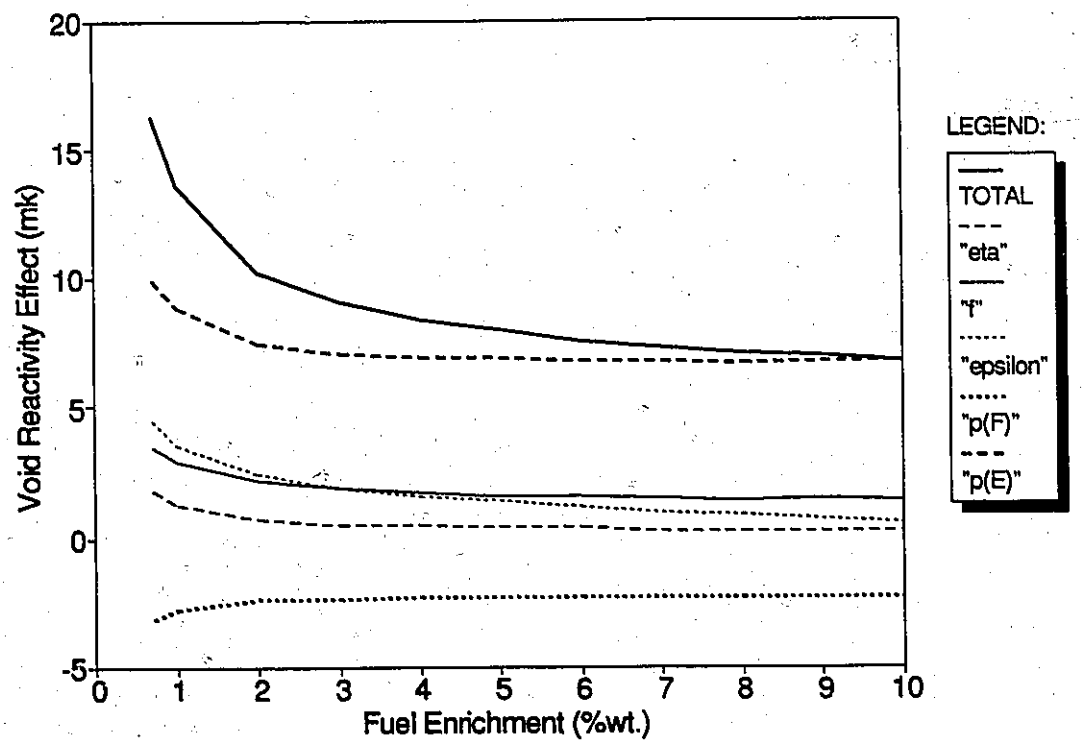

Figure 4.9 **Void Reactivity Effect ($\Delta\rho_v$) and Criticality Factor Contributions vs. Fuel Enrichment in a Zero-Burnup Lattice: 0.72 %wt — 10 %wt.**

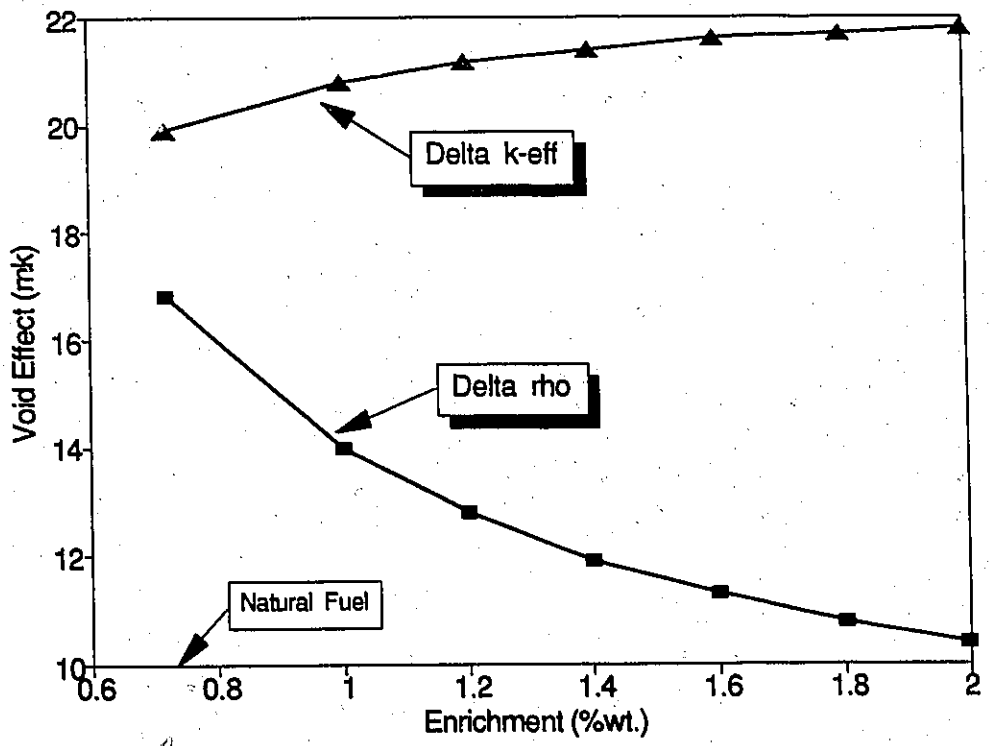

Figure 4.10: Void Reactivity Effect ($\Delta\rho_v$) and Void Criticality Effect ($\Delta k_{eff,v}$) vs. Fuel Enrichment in a Zero-Burnup Lattice: 0.72 %wt — 2 %wt.

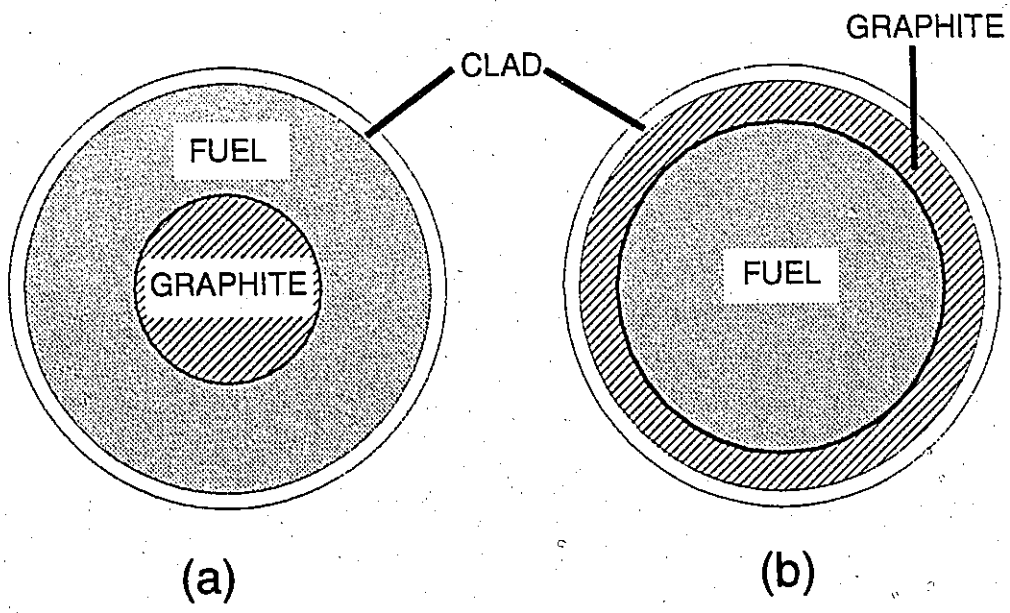

Figure 4.11 Geometry of Fuel Pins with Graphite Added: (a) Graphite Core, (b) Graphite Annulus. Outer Fuel Pin Diameter Same as in Reference Lattice Cell.

Table 4.1 Effect of Graphite Core Within Natural and Enriched Fuel Pins in a Zero-Burnup Lattice Cell. ("U-235 Content Conserved" Case Has Same U-235 Content as Reference Lattice Cell.)

Graphite's Volume Fraction of Fuel Pin	Graphite Core Diameter (cm)	Natural Uranium			U-235 Content Conserved			
		k_{eff} (cooled case)	$\Delta k_{eff,v}$ (mk)	$\Delta\rho_v$ (mk)	k_{eff} (cooled case)	%wt. U-235	$\Delta k_{eff,v}$ (mk)	$\Delta\rho_v$ (mk)
0.0%	0.0	1.078	19.3	16.3	n/a	n/a	n/a	n/a
10.8%	0.2	1.071	18.6	16.0	1.118	.81%	19.0	14.9
43.4%	0.4	1.040	16.4	15.0	1.271	1.27%	17.5	10.7
67.7%	0.5	0.979	13.6	14.0	1.429	2.23%	14.9	7.2

Table 4.2 Effect of Graphite Annulus Around Natural and Enriched Fuel Pins in a Zero-Burnup Lattice Cell. ("U-235 Content Conserved" Case Has Same U-235 Content as Reference Lattice Cell.)

Graphite's Volume Fraction of Fuel Pin	Graphite Annulus Thickness (cm)	Natural Uranium			U-235 Content Conserved			
		k_{eff} (cooled case)	$\Delta k_{eff,v}$ (mk)	$\Delta\rho_v$ (mk)	k_{eff} (cooled case)	%wt. U-235	$\Delta k_{eff,v}$ (mk)	$\Delta\rho_v$ (mk)
0.0%	0.0	1.078	19.3	16.3	n/a	n/a	n/a	n/a
10.8%	0.0337	1.071	18.4	15.8	1.118	0.81%	18.7	14.7
43.4%	0.1505	1.039	15.5	14.2	1.271	1.27%	16.8	10.3
67.7%	0.2623	0.977	13.1	13.5	1.425	2.23%	14.4	7.0

Table 4.3 Effect of Substituting Zirconium and Graphite for Fissile Material in Central Seven Elements (Zero-Burnup Lattice): Void Criticality Effect ($\Delta k_{eff,V}$), Void Reactivity Effect ($\Delta\rho_V$), and Criticality Factor Contributions.

Criticality Factor	Void Criticality Effect, $\Delta k_{eff,V}$			Void Reactivity Effect, $\Delta\rho_V$		
	Reference Cell (mk)	Subst. Zirconium (mk)	Subst. Graphite (mk)	Reference Cell (mk)	Subst. Zirconium (mk)	Subst. Graphite (mk)
η	2.2	2.3	2.3	1.8	2.0	1.9
f	3.9	3.2	3.6	3.3	2.8	3.1
p_F	–3.8	–3.2	–3.2	–3.2	–2.7	–2.7
p_E	11.7	8.9	7.4	9.9	7.7	6.3
ϵ	5.2	4.3	4.3	4.4	3.8	3.7
TOTAL EFFECT	19.3	15.6	14.4	16.3	13.5	12.3
k_{eff} (cooled case)	1.078	1.065	1.075	1.078	1.065	1.075

Table 4.4 Effect of Substituting Zirconium and Graphite for Fissile Material in Central Nineteen Elements (Zero-Burnup Lattice): Void Criticality Effect ($\Delta k_{eff,V}$), Void Reactivity Effect ($\Delta\rho_V$), and Criticality Factor Contributions.

Criticality Factor	Void Criticality Effect, $\Delta k_{eff,V}$			Void Reactivity Effect, $\Delta\rho_V$		
	Reference Cell (mk)	Subst. Zirconium (mk)	Subst. Graphite (mk)	Reference Cell (mk)	Subst. Zirconium (mk)	Subst. Graphite (mk)
η	2.2	2.7	2.5	1.8	2.6	2.3
f	3.9	2.2	3.3	3.3	2.1	3.0
p_F	−3.8	−2.1	−2.0	−3.2	−2.0	−1.9
p_E	11.7	4.5	5.2	9.9	4.4	4.7
ϵ	5.2	2.6	2.5	4.4	2.5	2.3
TOTAL EFFECT	19.3	9.9	11.3	16.3	9.5	10.4
k_{eff} (cooled case)	1.078	1.012	1.037	1.078	1.012	1.037

Table 4.5 Effect of Using Depleted Uranium (0.25 %wt) in Inner Seven Fuel Pins.

	Reference Lattice Cell		Average Bundle Enrichment: 0.72 %wt. (Enrichment of Outer Two Rings: 0.83 %wt.)		Average Bundle Enrichment: 1.51 %wt. (Enrichment of Outer Two Rings: 1.80 %wt.)	
	Zero-Burnup	Mid-Burnup (full burnup = 7500 MWd/Te)	Zero-Burnup	Mid-Burnup (full burnup = 8000 MWd/Te)	Zero-Burnup	Mid-Burnup (full burnup = 28000 MWd/Te)
k_{eff} (cooled case)	1.078	1.019	1.088	1.014	1.363	1.013
$\Delta k_{eff,V}$	19.3 mk	13.6 mk	16.7 mk	12.3 mk	18.4 mk	13.5 mk
$\Delta\rho_V$	16.3 mk	13.0 mk	13.9 mk	11.8 mk	9.7 mk	13.0 mk

Table 4.6 Effect of Using Depleted Uranium (0.25 %wt) in Inner 19 Fuel Pins.

	Reference Lattice Cell		Average Bundle Enrichment: 0.72 %wt. (Enrichment of Outer Two Rings: 1.22 %wt.)	
	Zero-Burnup	Mid-Burnup (full burnup = 7500 MWd/Te)	Zero-Burnup	Mid-Burnup (full burnup = 9000 MWd/Te)
k_{eff} (cooled case)	1.078	1.019	1.100	1.020
$\Delta k_{eff,V}$	19.3 mk	13.6 mk	12.7 mk	10.2 mk
$\Delta\rho_V$	16.3 mk	13.0 mk	10.4 mk	9.7 mk

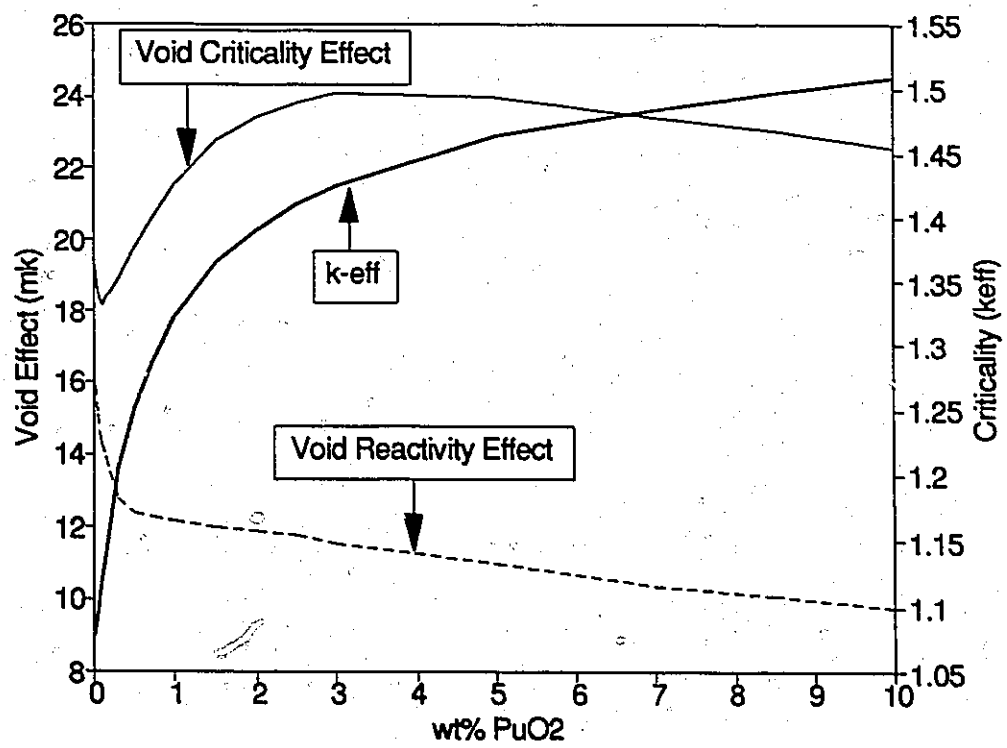

Figure 4.12 Effect of Using Pu-MOX Fuel as a Function of PuO_2 Weight Fraction (Zero-Burnup Lattice): Void Criticality Effect ($\Delta k_{eff,V}$), Void Reactivity Effect ($\Delta\rho_V$), and k_{eff}.

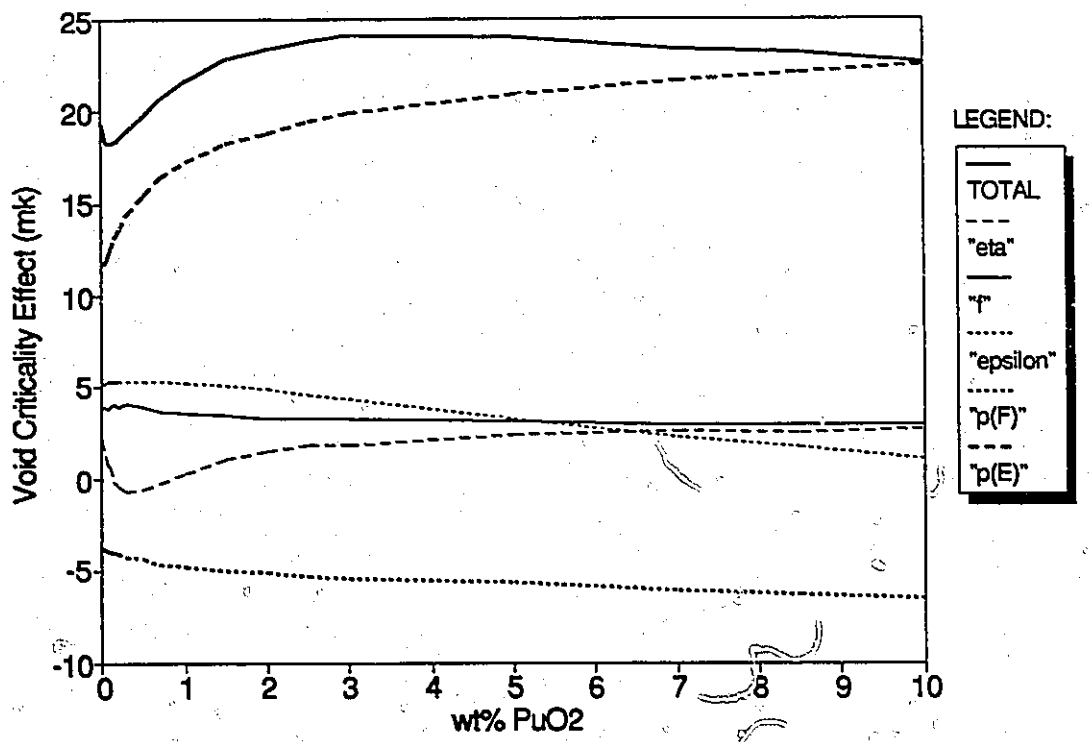

Figure 4.13 Void Criticality Effect ($\Delta k_{eff,V}$) and Criticality Factor Contributions for Pu-MOX Fuel as a Function of PuO_2 Weight Fraction (Zero-Burnup Lattice).

Table 4.7 Effect of Using 0.5 %wt and 1.0 %wt Pu-MOX Fuel: Zero-Burnup and Mid-Burnup.

PuO_2 Weight Fraction	Discharge Burnup (MWd/Te)	Void Criticality Effect, $\Delta k_{eff,V}$ (mk)		Void Reactivity Effect, $\Delta\rho_V$ (mk)		Average Pu-239 Nuclide Density at Mid-Burnup (Relative to 0 wt% Case)	Average Pu-239 Nuclide Density at Mid-Burnup (Relative to Own Zero Burnup Case)
		Zero-Burnup	Mid-Burnup	Zero-Burnup	Mid-burnup		
0 wt%	7500	19.3	13.6	16.3	13.0	1.0	n/a
0.5 wt%	17,400	19.5	13.9	12.4	13.6	1.6	0.9
1.0 wt%	24,800	21.6	14.9	12.2	14.5	1.9	0.6

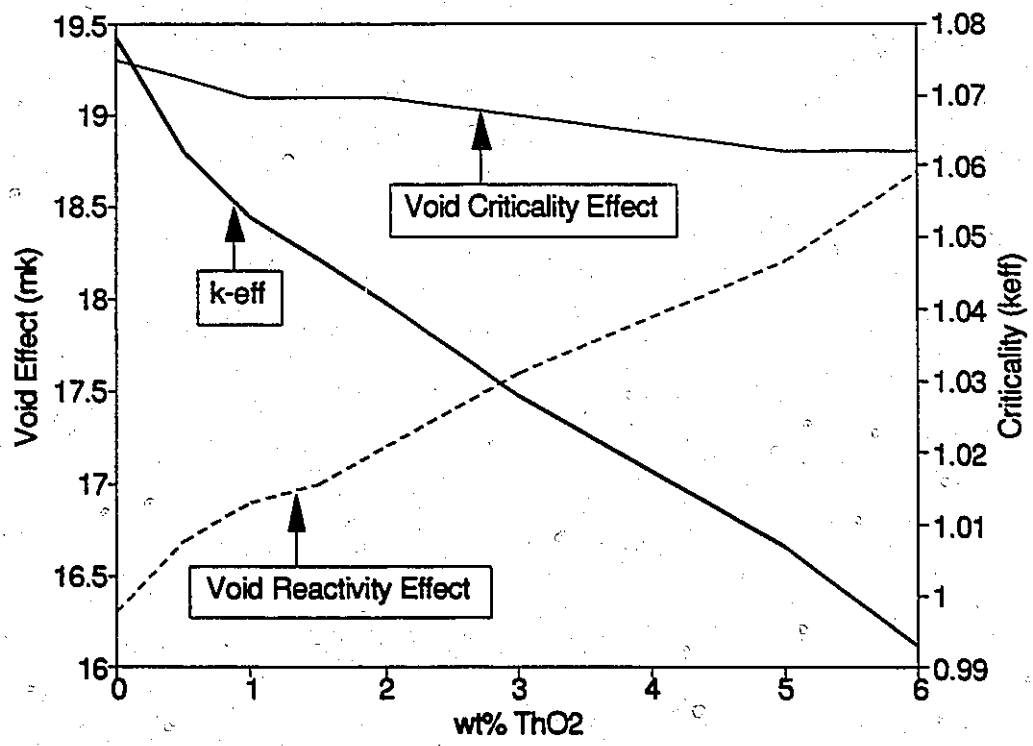

Figure 4.14 Effect of Using Th-MOX Fuel as a Function of ThO_2 Weight Fraction (Zero-Burnup Lattice): Void Criticality Effect ($\Delta k_{eff,V}$), Void Reactivity Effect ($\Delta\rho_V$), and k_{eff}.

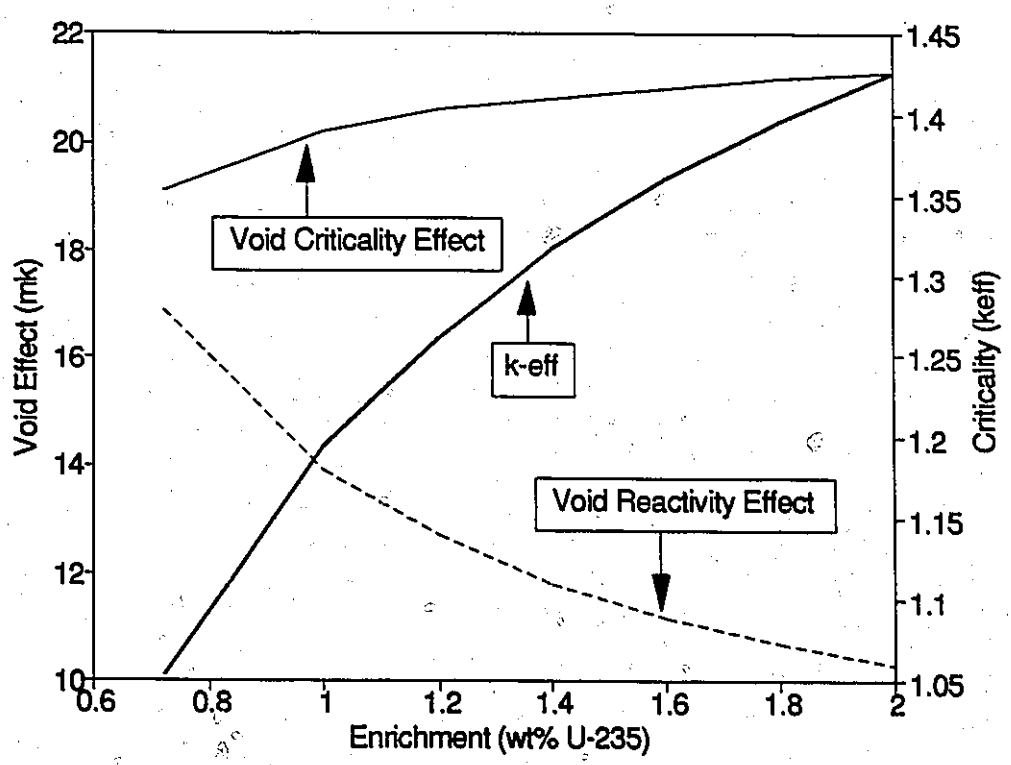

Figure 4.15 **Effect of U-235 Enrichment on 1.0%wt Th-MOX Fuel (Zero-Burnup): Void Criticality Effect ($\Delta k_{eff,v}$), Void Reactivity Effect ($\Delta\rho_v$), and k_{eff}**

Table 4.8 Effect of Utilizing 90 %wt Enriched Zirconium in Fuel Channel Alloys, Approximated by Density Adjustment (Zero-Burnup Lattice): Void Criticality Effect ($\Delta k_{eff,V}$), Void Reactivity Effect ($\Delta\rho_V$), and Criticality Factor Contributions.

Criticality Factor	Void Criticality Effect, $\Delta k_{eff,V}$		Void Reactivity Effect, $\Delta\rho_V$	
	Reference Cell (mk)	With Zr-90 Enrichment (mk)	Reference Cell (mk)	With Zr-90 Enrichment (mk)
η	2.2	2.3	1.8	1.8
f	3.9	2.0	3.3	1.6
p_F	−3.8	−3.7	−3.2	−2.9
p_E	11.7	11.0	9.9	8.8
ϵ	5.2	5.3	4.4	4.2
TOTAL EFFECT	19.3	16.9	16.3	13.4
k_{eff} (cooled case)	1.078	1.112	1.078	1.112

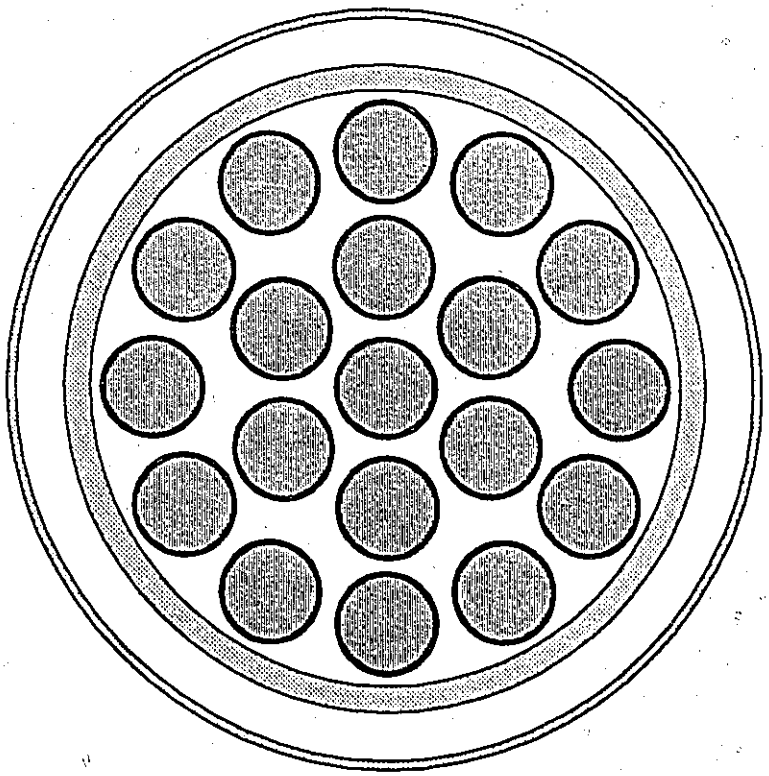

Figure 4.16 Geometry of 19-Element Fuel Bundle With Same Fuel Volume as Reference Case.

Table 4.9 Effect of Decreasing Surface-to-Volume Ratio of Fuel Pins: 19-Element Zero-Burnup Lattice Cell With Same Fuel Volume as Reference Case. "Differential Enrichment" Case Has Average Bundle Enrichment = 0.72%wt.

Criticality Factor	Void Criticality Effect, $\Delta k_{eff,V}$			Void Reactivity Effect, $\Delta\rho_V$		
	Reference Cell (mk)	Natural UO_2 (mk)	Differential Enrichment (mk)	Reference Cell (mk)	Natural UO_2 (mk)	Differential Enrichment (mk)
η	2.2	2.4	−2.3	1.8	2.0	−1.9
f	3.9	4.4	3.8	3.3	3.7	3.1
p_F	−3.8	−3.8	−3.7	−3.2	−3.2	−3.1
p_E	11.7	10.6	10.0	9.9	8.9	8.3
ϵ	5.2	5.2	5.7	4.4	4.4	4.6
TOTAL EFFECT	19.3	18.8	13.3	16.3	15.8	11.0
k_{eff} (cooled case)	1.078	1.082	1.096	1.078	1.082	1.096

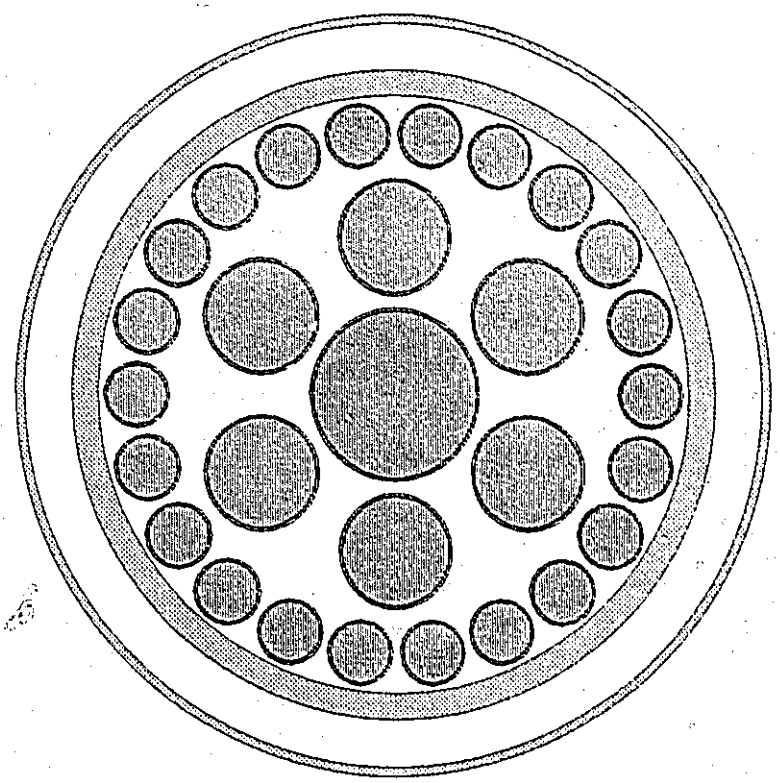

Figure 4.17 Geometry of 29-Element Graded Pin Cluster With Same Fuel Volume as Reference Case.

Table 4.10 Effect of Graded Pin Diameter: 29-Element Zero-Burnup Lattice Cell With Same Fuel Volume as Reference Case. "Differential Enrichment" Case Has Average Bundle Enrichment = 0.72%wt.

Criticality Factor	Void Criticality Effect, $\Delta k_{eff,V}$			Void Reactivity Effect, $\Delta\rho_V$		
	Reference Cell (mk)	Natural UO_2 (mk)	Differential Enrichment (mk)	Reference Cell (mk)	Natural UO_2 (mk)	Differential Enrichment (mk)
η	2.2	2.1	−6.6	1.8	1.8	−5.4
f	3.9	3.9	2.5	3.3	3.3	2.0
p_F	−3.8	−3.9	−4.0	−3.2	−3.3	−3.3
p_E	11.7	11.6	10.9	9.9	9.8	8.8
ϵ	5.2	5.5	6.6	4.4	4.7	5.4
TOTAL EFFECT	19.3	19.1	9.2	16.3	16.2	7.5
k_{eff} (cooled case)	1.078	1.079	1.107	1.078	1.079	1.107

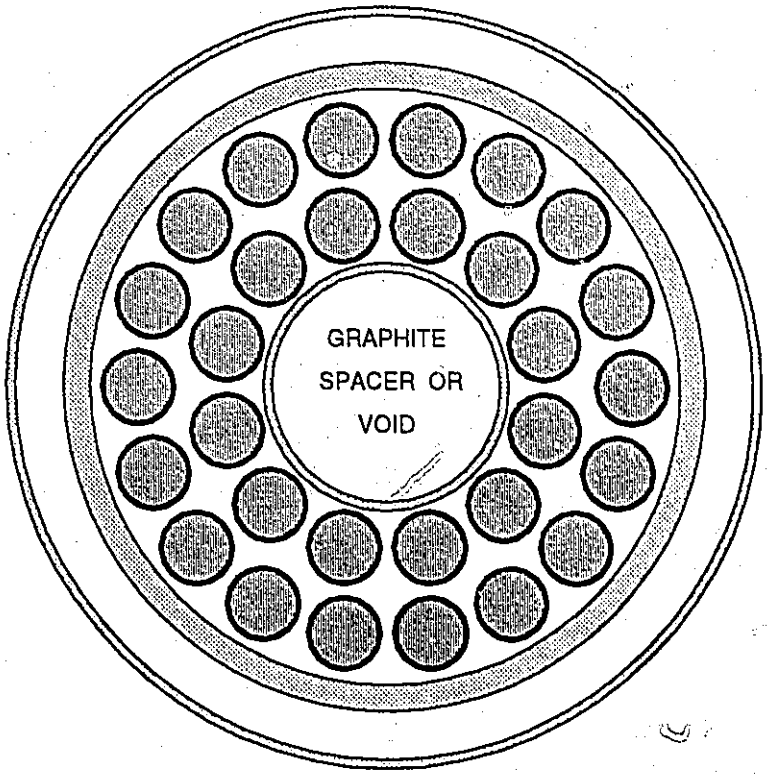

Figure 4.18 30-Element Annular Cluster Design From Reference 67.

Chapter 5

New Fuel Design

In this chapter a major radial relocation of the fuel within the pressure tube, requiring a departure from the "fuel pin cluster" concept, is examined as a strategy for low void effect CANDU fuel. An optimal design from a purely neutronics point of view is first developed, which is then modified to accommodate cooling and other engineering requirements. This modified result is then questioned further in areas of thermalhydraulic and material requirements, for which an extensive analysis transcends the current scope. The modelling methodology within WIMS-AECL is examined, primarily to test the ability of the code to handle such a highly modified geometry, and secondarily to test its sensitivity to input parameters. Several of the perturbations to fuel content that reduced the void effect in the previous chapter are also applied here with the hope of both further reducing the void effect and addressing some remaining practical concerns.

5.1 Optimum Geometry Based On Void Effect

This section will establish the optimum fuel geometry from a neutronics point of view, maintaining the fuel volume and fuel materials (ie., no substitutions, additions, or subtractions) as the reference fuel cell. The aim here is to develop a sense of direction

that will guide a practical analysis to be performed later.

5.1.1 Rationale for Optimum Geometry

If one were to abandon the pin cluster concept of CANDU fuel, what would be the optimum geometry in terms of the void effect? To answer this question, consider what has been found so far. In Section 3.2.2 the greatest contribution to the void effect was shown to come from the change in epithermal loss, accounting for 60% of the effect at zero-burnup and 85% at mid-burnup (see Table 3.1). In Section 4.4 an attempt was made to reduce this by reducing the surface-to-volume (S/V) ratio of the pin cluster fuel, which had a negligible effect. As a hypothetical scenario, consider a fuel arrangement with the lowest S/V ratio possible while maintaining the same fuel volume as in the reference lattice cell. Such an arrangement is illustrated in Figure 5.1(a), where all the fuel is located in a single lump at the centre of the fuel channel, surrounded by a coolant annulus. Cladding material has not been included in this case. The S/V ratio of the geometry in Figure 5.1(a) is reduced by about 84% from the reference cell case, and with the fuel volume so constrained, this geometry offers the least probability of an interaction between a resonance-energy neutron located in the coolant and a resonance absorber located in the fuel. This is reflected in the calculation of resonance integrals[2,32], and geometric reasoning provides an explanation: The moderator-coolant interface (ignoring the highly transparent pressure tube, calandria tube, and annular void regions) is about 40% greater than the fuel-coolant interface, and hence fast neutrons entering the annular

coolant region from the direction of the fuel are more likely to stream or be scattered into the moderator, compared to the case of a cluster of fuel pins.

In Section 3.3, however, the importance of proximity to the bulk moderator was introduced, and Figure 3.8 and Figure 3.9 clearly demonstrate the thermal and epithermal flux shifts that account for this. Accordingly, it was possible to obtain a significant reduction in the void effect by either removing fissile material altogether from the centre of the fuel channel in Section 4.2.3, or by reducing the amount of thermally fissile material (U-235) in the centre of the fuel channel in Section 4.2.4. It follows, therefore, that the thermal spectrum void effects should be reduced by locating the single lump of fuel in Figure 5.1(a) as close to the moderator as possible, which is the geometry shown in Figure 5.1(b). In doing so the lump becomes tubular in shape, as well as much smaller in width since volume is conserved. However, by thus creating a concave fuel boundary enclosing a coolant region, which is opposite to Figure 5.1(a), the probability of a source neutron downscattering into the resonance region and then encountering a resonance absorber nuclide will increase, and therefore so will the void effect. Also increasing the role played by resonance absorption in the void effect is the higher S/V ratio of the tubular fuel geometry of Figure 5.1(b), which is 39% of that of the reference cell case (compared to 16% for the geometry in Figure 5.1(a)). This positive influence on the void effect with fuel location will be countered somewhat by the proximity to the moderator, which allows source neutrons leaving the outer fuel surface to stream or diffuse directly into the moderator and become thermalized.

These hypotheses are tested by modelling the two geometries of Figure 5.1 in

WIMS-AECL (using the PERSEUS option[26,27] for annular cell geometry) and including several intermediate geometries as the central fuel lump in Figure 5.1(a) is "moved" outward to the location and shape of the tubular fuel lump in Figure 5.1(b). Annular symmetry and fuel volume is conserved at all test locations. The results of these calculations, without burnup, are examined in the remainder of this section. Later in Section 5.9.1, a significant deficiency in the resonance treatment for tubular geometries will be examined, and in light of this the effect of geometry on the epithermal parameters (p_E and Δp_E), as described in the following subsections, will probably be underestimated.

5.1.2 Void Effect of Optimum Geometry

The void criticality effect ($\Delta k_{eff,V}$) and its criticality factor contributions are plotted in Figure 5.2 as a function of radial fuel position. Here the x-axis represents the outside radius of the fuel lump, beginning at 3.70 cm, corresponding to the case where all fuel is located at the centre, and ending at 5.17 cm, the inner radius of the pressure tube (the inner radius of the fuel lump in the last case is 3.61 cm). Quantitative results for the two limiting cases depicted in Figure 5.1, as well as the reference lattice cell, are listed in Table 5.1 for both types of void effect.

Considering the void criticality effect ($\Delta k_{eff,V}$), a reduction of about 7 mk is achieved relative to the reference lattice cell when all fuel is lumped at the centre, and about 13 mk when all fuel is pushed against the pressure tube wall. In the intermediate geometries the void criticality effect peaks before dropping off (see Figure 5.2), caused

by the competing spectral mechanisms just described. With all fuel in the centre of the fuel channel, virtually all of the void effect is due to the combined thermal contribution, ηf, which is about 2.5 times the corresponding reference cell contribution. As the fuel location moves closer to the pressure tube the contributions from both η and f decrease, and at the outer limit where thermal flux drops upon voiding, the contribution from f becomes negative.

At all locations the void effect contribution through the epithermal escape probability, p_E, is much less than that for the reference cell (at most 1/3) due to the lower S/V ratio. With all fuel in the centre the p_E contribution is slightly negative; however, this is due to the increase in leakage upon voiding and not to an increase in resonance absorption. As the fuel location moves outward, the p_E contribution increases as the central coolant region, and thus the localized resonance flux, becomes larger. At positions near the pressure tube, proximity to the bulk moderator and the large size of the central coolant region, both affording greater thermalization, tend to counteract the effect of the localized resonance flux and the p_E contribution levels off. However, considering the problem to be discussed later in Section 5.9.1 regarding the inadequacy of the WIMS-AECL resonance treatment for annular geometry, the conclusions stated here for the behaviour of Δp_E are suspect. The trend in Δp_E is probably correct, but the relative value compared to the other void effect contributions is questionable.

In the fast spectrum both contributions behave as expected. The contribution of the fast fission factor, ϵ, increases along with the size of the central coolant region since this region was a source of downscattering out of the fast region. The same phenomenon

causes the decrease in the contribution of the fast escape factor, p_F, with increased size of the central coolant region.

5.1.3 Criticality of Optimum Geometry

Since the geometry being explored here represents a major departure from the conventional CANDU fuel configuration, it is appropriate to examine the effect on criticality of such a fundamental, albeit unrealistic, change. Figure 5.3 is a plot of k_{eff} for the cooled (non-voided) cases as a function of fuel position, along with the constituent criticality factors, and Figure 5.4 isolates k_{eff} for clarity. The quantitative results for the two limiting cases, as well as the reference case for comparison, are given in Table 5.2. The total gain in criticality, Δk_{eff}, between the reference cell and the cell with all fuel at the centre is +21 mk. As expected, a significant contribution to this increase is through the epithermal escape probability, p_E, because of the reduction in the S/V ratio. The decrease in thermalization around the fuel also leads to an increase in fast absorption and fission, indicated by a decrease in p_F and an increase in ϵ, respectively. The thermal parameters, η and f, are reduced by the presence of all the fuel within the region of lowest thermal flux across the cell.

As the fuel lump is "moved" to its annular limiting position where the thermal flux is the greatest within the pressure tube, these thermal parameters increase above their values in the reference case. In this sense the reference case can be thought of as producing a spatial average of the thermal parameters over the thermal flux distribution

within the pressure tube. With the growing S/V ratio the probability of escape from the fuel lump increases and therefore p_F becomes bigger and ϵ becomes smaller. The epithermal escape probability, p_E, also becomes smaller as the S/V ratio and the central coolant region increases, although in the outer limiting case it still remains larger than its value in the reference cell. Overall, k_{eff} increases by 8 mk between the two limiting geometries, for a total increase of 29 mk over the reference cell.

5.1.4 Uranium Isotopic Effects in Optimum Geometry

In a manner similar to that in Section 3.4 where material contributions to the void effect were examined, the contributions to the void criticality effect from the fissile nuclides as a function of radial fuel position are plotted in Figure 5.5. As would be expected based on Figure 5.2, the bulk of the effect is due to increased criticality of U-235 for the case with all fuel in the centre location, and of U-238 for the case with all fuel in the outer location. This suggests the beneficial use of differential enrichment within the fuel volume, a tactic that will be adopted later (Section 5.11).

5.2 Thermalhydraulic Considerations

Having established, in terms of void effect reduction, the conceptual desirability of relocating all fuel to the region near the pressure tube wall, it remains to develop a practical fuel design that exploits this strategy. Although an engineering design of any significant detail is beyond this dissertation's scope, several steps can be taken using basic

thermalhydraulic requirements. In fact, such an analysis must necessarily accompany the neutronic analysis if the goal, expressed in Section 1.8, of maintaining current CANDU system parameters, is to be achieved.

In this section approximate calculations will lead to modifications of the geometry in Figure 5.1(b) such that the following constraints can be addressed (detailed explanations follow later in this section):

1) maximum *fuel temperatures* must be acceptable;
2) total coolant *mass flow rate* must remain unchanged;
3) *pressure drop* across the channel should not exceed that of the current design;
4) a constant ratio of *mass flow rate to power deposition* must be maintained in all coolant subchannels (regions between fuel volumes); and
5) the *critical heat flux* (CHF) margin must be retained.

A casual appraisal of Figure 5.1(b) leads to the expectation that a significant amount of modification will be necessary before these constraints can be met, if at all. As geometry changes, so will the neutronics, and therefore characteristic parameters like criticality, burnup, and (of course) void effect will eventually be included again in the search. Where actual numbers are required in the following process (mean coolant temperature, nominal bundle power, etc.), operational values or reasonable approximations will be used. Many of the constraints are tested using a comprehensive FORTRAN code written by the author (see Section 5.2.7).

5.2.1 Maximum Fuel Temperature

A primary concern is that of adequate heat transfer within the fuel, and the need to keep maximum fuel temperatures below melting. For unirradiated UO_2 fuel the melting point is about 2800 °C, decreasing slightly with irradiation[2]. The temperature differences across the two limiting fuel geometries depicted in Figure 5.1 can be estimated by applying the equation of radial heat conduction[2],

$$\frac{1}{r}\frac{d}{dr}kr\frac{dT}{dr} = -q''' \quad , \tag{5.1}$$

for which Equations (5.2) through (5.5), to be presented shortly, are specific solutions. It is assumed that a constant thermal conductivity, k = 0.025 W/cm·°C, and a constant volumetric heat generation density, q''' = 300 W/cm^3, can be applied. The former is an average thermal conductivity[2] for UO_2 and the latter is estimated by dividing the nominal fuel bundle power[3] of CANDU-6 (640 kW) by the fuel volume per bundle (2124 cm^3).

The difference in temperature, ΔT, between the centreline and outer surface of the cylindrical fuel lump in Figure 5.1(a), given by[70],

$$\Delta T = \frac{q''' r^2}{4k} \quad , \tag{5.2}$$

is about 41,000 °C, where r is the cylinder radius. Similarly, ΔT across the ring of fuel in Figure 5.1(b), given by[70],

$$\Delta T = \frac{q'''}{4k}\left[2\, r_{out}^2 \ln\left(\frac{r_{out}}{r_{in}}\right) - \left(r_{out}^2 - r_{in}^2\right)\right] \quad , \tag{5.3}$$

is about 16,000 °C, where r_{in} and r_{out} are the inner and outer radii, respectively. In the latter case no heat transfer is assumed through the outer boundary of the fuel.

If the same ring of fuel in Figure 5.1(b) is assumed to be cooled on both boundaries to the same temperature (obviously unrealistic, given the existence of the pressure tube at the outer boundary), the maximum temperature rise can be calculated from[70]

$$\Delta T = T_{max} - T_{surface} = \frac{q''' r_{in}^2}{4k}(1 - \alpha + \alpha \ln \alpha) \quad , \tag{5.4}$$

where $\alpha = (r_{max}/r_{in})^2 = \left[(r_{out}/r_{in})^2 - 1\right]/(2 \ln r_{out}/r_{in})$,

$r_{max} = \sqrt{(r_{out}^2 - r_{in}^2)/(2 \ln r_{out}/r_{in})}$ = radius of maximum fuel temperature, and

T_{max}, $T_{surface}$ = maximum, surface fuel temperature .

The difference in temperature between the surface and r_{max} is now calculated to be 3639 °C, which is still unacceptable. At conventional power densities there is clearly a need to subdivide the tubular geometry of Figure 5.1(b) and further increase its S/V ratio in the interest of higher heat conduction to the coolant. It will be seen shortly that avoidance of the critical heat flux (CHF) will also require a maximizing of surface area, although not necessarily the S/V ratio.

Achieving this subdivision with as little compromise as possible to the "ideal" geometry (from a neutronics point of view) of Section 5.1 suggests the use of concentric, or "nested", tubular fuel. An arbitrary choice for such a geometry using two nested tubes is presented in Figure 5.6 as a basis for discussion. In keeping with the analysis strategy so far, the fuel volume is maintained equal to that of the reference lattice cell. The fuel

meat in each of the two tubes has an equal radial thickness of 0.89 cm, which is 0.33 cm less than the fuel pin diameter in the reference lattice cell. The spacing between the two tubes, also chosen arbitrarily, is 2.0 mm, as is the spacing between the outer ring and the inner wall of the pressure tube. Another modification introduced in this geometry is the addition of zircaloy-4 cladding around the fuel meat, identical in composition to that used in the reference lattice cell. The cladding is necessary for the containment of fission products and the prevention of contact between UO_2 and D_2O. In the reference lattice cell this material is of radial thickness 0.47 mm, while in the geometry of Figure 5.6 a radial thickness of 0.5 mm has been chosen. A determination of the actual thickness required would have to take into account the stresses experienced by cylindrical fuel cladding at the radii described in Figure 5.6. For the purposes of this dissertation the value chosen is sufficient, and minor perturbations to this value will not affect the neutronic analysis appreciably. Finally, omitted from Figure 5.6 are the zircaloy-4 spacers necessary for mechanical support between the concentric fuel tubes and between the outer ring and the pressure tube.

Equation (5.4), with the prior assumptions for k and q''', can be used to calculate the maximum temperature difference across each of the fuel tubes in Figure 5.6. The result is 1190 °C in both cases, due to the small difference in radius of each ring. To determine the suitability of this value of ΔT one must also calculate the temperature rise from the heated coolant, across the cladding, to the fuel surface. It is not necessary here to attempt to quantify the convective heat transfer coefficient between the outer clad surfaces and the coolant; it suffices to assume reasonably good heat transfer properties

and a resulting $\Delta T_{\text{clad}\rightarrow\text{coolant}}$ of approximately 20 °C[2].

For the temperature rise across the clad, integration of Equation (5.1), with $q'''=0$ inside the clad, results in

$$\Delta T_{\text{clad}} = \frac{q'''_{\text{fuel}}\left(r_{\text{out}}^2 - r_{\text{in}}^2\right)}{4\,k_{\text{clad}}} \ln\left(\frac{r_{\text{clad-out}}}{r_{\text{clad-in}}}\right) \quad , \tag{5.5}$$

where $r_{\text{clad-out}}$ and $r_{\text{clad-in}}$ are the cladding outer and inner radii, respectively, and r_{out} and r_{in} are the fuel outer and inner radii, respectively. For this integration it has been assumed that fission heat will be transferred in equal amounts through each surface of a fuel ring, as in a slab geometry. Also, the existence of a gap between the fuel and cladding has been ignored. With the prior assumption for q'''_{fuel} and k_{clad}=0.11 W/cm·°C (from Reference 2), the maximum value of ΔT_{clad} is calculated to be 16 °C.

If all other system thermalhydraulic parameters are assumed to be identical with the CANDU-6 design, then the maximum coolant temperature can be taken[3] to be 310 °C (assumed constant radially across the fuel channel), and the maximum fuel temperature can be roughly estimated at 310 °C + 20 °C + 16 °C + 1190 °C = 1536 °C. Even with an additional temperature rise of several hundred degrees across any inevitable fuel-clad gap (ignored here), it is clear that the maximum temperature difference will be well below the UO_2 melting point.

With this approximation, one can quickly assess the suitability of new fuel geometries from the standpoint of fuel temperature. The other practical concerns listed at the beginning of this section will be discussed presently, in the context of the multiple nested fuel annuli concept established here.

5.2.2 Effect of Subdivision on Void Effect

In moving from the idealized geometry of Figure 5.1(b) to the more practical (but still not finalized) geometry of Figure 5.6, the S/V ratio of the fuel is increased from 39% to 69% of that of the reference lattice cell. This increase, while necessary for adequate cooling, also increases the void effect. An increase in the contribution of the epithermal escape probability, p_E, would be directly caused by the increasing importance of this parameter. At the same time the necessary relocation of fuel closer to the centre of the fuel channel should produce a slight increase in the thermal parameters.

Table 5.3 compares both types of void effect and their criticality factor contributions, as calculated for the two geometries represented by Figure 5.1(b) and Figure 5.6. An increase of approximately 3 mk is experienced by both $\Delta k_{eff,V}$ and $\Delta\rho_V$, which are now calculated to be 9.2 mk and 7.6 mk, respectively, about 47% of the effect in the reference lattice cell. As expected, increases in the contributions from η, f, and p_E account for much of the increase. Additionally, the contribution of the fast fission factor, ϵ, is significantly reduced while the fast escape probability, p_F, is significantly increased (each by about 1 mk), both reflecting the decrease in the size of the central coolant region. Criticality is reduced by 11 mk in the more practical design compared with that of Figure 5.1(b), caused almost exclusively by a decrease in thermal utilization as fuel mass is shifted to a region of lower thermal flux.

5.2.3 Coolant Mass Flow Rate and Pressure Drop

Since the steady-state heat production rate in the core, $Q_{s\text{-}s}$, is assumed to be the same as in current CANDU designs, and since the increase in coolant enthalpy across the core, Δh_C, is also assumed to be identical, it follows from the heat balance relationship in Equation (5.6) that coolant mass flow rate, W_C, must also be maintained,

$$Q_{s\text{-}s} = W_C(\Delta h_C) \quad . \tag{5.6}$$

The coolant mass flow rate is given by

$$W_C = \rho_C A_C v_C \quad , \tag{5.7}$$

where ρ_C = coolant density, A_C = coolant cross-sectional flow area, and v_C = coolant linear velocity. It is further assumed that coolant pressure and temperature, and therefore density, are the same as in current designs. It is also the intent here to avoid altering the linear coolant velocity since this will affect heat transfer from the fuel, which is assumed to proceed under the same conditions as in current designs. It follows, therefore, that maintaining W_C implies that A_C must also be maintained. This last conclusion represents a direct constraint on lattice cell geometry.

At the same time, the pumping power of the cooling system, P_{pump}, is assumed to be the same as in current designs. The pressure drop across the system, Δp, is related to P_{pump} and the volumetric flow rate, $\dot{V}$, through[71]

$$P_{pump} = \Delta p \times \dot{V} = \Delta p \times \frac{W_C}{\rho_C} \quad , \tag{5.8}$$

from which it follows that Δp should be maintained as well. The pressure drop across the fuel channels, Δp_{FC}, provides a significant fraction of Δp, and represents the only portion assumed to be affected by changes in lattice cell geometry. Δp_{FC} can be further separated into the component contributed by the fuel geometry itself, Δp_F and by other restrictions in the fuel channel, Δp_{OTHER} (mainly the shield plug),

$$\Delta p_{FC} = \Delta p_F + \Delta p_{OTHER} \quad . \tag{5.9}$$

For a given set of fluid properties and assuming single-phase flow, the proportionality exists[72] for Δp_F,

$$\Delta p_F \propto \frac{W_C^{1.8}}{A_C^{1.8} D_F^{1.2}} \quad , \tag{5.10}$$

where $D_F \equiv 4A_C/S_F$, the *hydraulic diameter* of the flow region through the fuelled portion of the fuel channel, and S_F is the total wetted perimeter of this region. Note that, since W_C and A_C are assumed constant, Δp_F should vary as $S_F^{1.2}$.

Since it is recognized that an additional pressure drop can be supplied through the Δp_{OTHER} term in Equation (5.9), by, for example, modifying the shield plugs with added flow restricting orifices if necessary, the criterion of maintaining Δp_{FC} can be satisfied using

$$\frac{[\Delta p_F]_{\text{new design}}}{[\Delta p_F]_{\text{ref. cell}}} \approx \frac{\left[\dfrac{W_C^{1.8}}{A_C^{1.8} D_C^{1.2}}\right]_{\text{new design}}}{\left[\dfrac{W_C^{1.8}}{A_C^{1.8} D_C^{1.2}}\right]_{\text{ref. cell}}} \leq 1.0 \quad . \tag{5.11}$$

With both W_C and A_C assumed constant this ratio should be dependent upon the ratio of wetted surface areas: $([S_F]_{new\ design}/[S_F]_{ref.\ cell})^{1.2}$.

In summary, it has been determined here that:

1) the coolant cross-sectional flow area of any new design must equal that of the reference lattice cell; and

2) the pressure drop caused by the fuel must not exceed that of the reference lattice cell — a condition which can be approximated by the constraint Equation (5.11).

5.2.4 Central Coolant Spacer

The large coolant region in the centre of the fuel channel in Figure 5.6 presents a major problem for adequate cooling of the fuel. While the analysis of Section 5.2.1 assumed a constant coolant temperature radially across the fuel channel, this would not be the case since this central region will represent a much lower hydraulic resistance to the coolant flow than the subchannels around the tubular fuel. As such, this central region would experience a significantly higher flow rate than elsewhere in the fuel channel, to the detriment of the cooling ability of the other subchannels.

The solution to this problem is to insert a spacer of suitable radius in this central region, displacing coolant and forcing total flow into smaller subchannels around the fuel. From a neutronics standpoint the presence of this spacer will have several significant effects:

1) Cell absorption will change depending on the absorption cross-section of the

spacer material relative to the displaced D_2O. If cell absorption increases, cell criticality and burnup will decrease, and the redistribution of flux upon voiding will be affected.

2) Cell slowing-down power will change depending on the moderating power of the spacer material relative to the displaced D_2O. If slowing-down power decreases, the neutron spectrum will be "hardened" (shifted to higher energies) and criticality and burnup will depend on the degree of hardening. Hardening in the thermal range will tend to decrease criticality and burnup due to the reduction of thermal flux. Hardening in the epithermal range will cause a net decrease in resonance flux, shifted into the fast spectrum, and tend to increase criticality and burnup.

3) The smaller volume of coolant will reduce the total effect of coolant voiding on the rest of the cell. The amount of downscattering into the resonance region and rethermalization by the hot coolant under normal operating conditions will be reduced, and consequentially the values of $\Delta k_{eff,V}$ and $\Delta\rho_V$ should also become smaller.

The total effect on k_{eff} therefore depends on the cross-section of the spacer material relative to the coolant, while the total effect on $\Delta k_{eff,V}$ and $\Delta\rho_V$ is expected to be a decrease. In an attempt to explore the various neutronic effects, five different materials have been chosen for analysis:

1) *Graphite* (density[2] 1.6 g/cm^3) is a material commonly used in gas reactors, chosen here as a replacement moderator for the displaced D_2O, surrounded by 0.5 mm zircaloy cladding.

2) *Zircaloy-4* (density 6.4 g/cm^3) is the material of the fuel cladding and calandria tube, chosen as a material with negligible moderating power and low absorption cross-section.

3) *Quartz*, SiO_2 (density[73] 2.6 g/cm^3) is a common substance, chosen for its chemical inertness, natural abundance, and low absorption cross-section, surrounded by 0.5 mm zircaloy cladding..

4) *Non-voidable D_2O*, with the same properties as the coolant but designated as a separate material that does not void, surrounded by a nominal 0.5 mm zircaloy cladding. A separate analysis included a more practical zirconium-2.5%Nb tube with the same properties and thickness as the pressure tube (0.45 cm).

5) A *voided region*, approximated in WIMS-AECL as a low-density He gas, also enclosed in a zirconium-2.5%Nb tube of same thickness as pressure tube.

For the purposes of preliminary investigation, the above five materials, with two different container materials for the non-voidable D_2O were given radii ranging from zero to 2.59 cm and placed at the centre of the arbitrarily-chosen two-element geometry of Figure 5.6, leaving a 2 mm gap for coolant between the spacer and inner fuel element (similar to the other two coolant gaps). This limiting geometry is illustrated in Figure 5.7. There are, of course, practical problems associated with the placement of such materials in the fuel channel, especially with the creation of a separate D_2O region, but these matters are not of concern at this point.

Figure 5.8 is a plot of the void criticality effect ($\Delta k_{eff,v}$) as a function of spacer radius for each of these materials. Clearly the spectral changes induced in the lattice cell

by the spacers of different composition do not have a significant influence on the void effect, since the results are almost independent of composition. This demonstrates that the dominant factor is simply the decrease of the void effect by displacement of D_2O coolant. In all cases the void criticality effect is reduced by about half, to about 4.5 mk, at the maximum limit of spacer radius.

The criticality factor contributions using the graphite spacer are given as a function of spacer radius in Figure 5.9, with a listing of the quantitative results of the two limiting cases in Table 5.4. These results are also independent of composition and therefore only the graphite data is presented. Most of the individual contributions are reduced in magnitude as spacer volume in increased, as expected. The exception is the contribution of the thermal utilization factor, f, and fast escape factor, p_F, which increase slightly as the spacer volume increases. The main reason for this is the increase in leakage upon voiding, which gets significantly smaller as the voided coolant volume gets smaller. In this notation f is the ratio of thermal fuel absorption to total thermal neutron loss including leakage (see Equation (2.13)), and since the change in absorption upon voiding does not change appreciably with the size of the spacer, the f contribution increases slightly. Similarly, increased leakage of fast neutrons upon voiding becomes less important with increasing spacer radius, and the p_F contribution increases.

The insensitivity to spacer composition is not apparent in the calculations of absolute criticality. As Figure 5.10 illustrates, the trend of k_{eff} with spacer radius varies as the cross-sectional properties of each material. With an increasing volume of graphite in the fuel channel the localized source of resonance flux is reduced because of the lower

slowing down power of graphite. Criticality is therefore improved and graphite is the only one of the materials studied that has this beneficial effect. The non-voidable D_2O region with the thin cladding of course has a negligible effect on k_{eff}, depressing it slightly due to the extra small absorption in its cladding. This extra absorption becomes significant when the more realistic enclosure material is used (designated as "D2O*" in Figure 5.10). The voided region exhibits an interesting trend with spacer radius that goes through a minimum at approximately 2 cm. This is the result of two competing effects: the increasing volume of zirconium-2.5%Nb (same thickness as pressure tube at all spacer radii) adds significant absorption to the lattice cell, while the increasing voided volume puts upward pressure on k_{eff} through the same mechanisms as coolant voiding. For large void volumes, and consequently smaller and smaller incremental changes in zirconium-2.5%Nb volume, the latter effect begins to dominate. Finally, the zircaloy and SiO_2 spacers both decrease k_{eff} significantly through their added absorption, although only the zircaloy spacer is enough of an absorber to eventually force k_{eff} below that of the reference 37-element lattice cell.

The calculated void effects in a mid-burnup lattice are listed in Table 5.5. Once again an insensitivity to composition is displayed in the void effect, with $\Delta k_{eff,V}$ falling consistently within the small range of 2.2 to 2.6 mk. Discharge burnup is affected more noticeably, ranging from 6720 MWd/Te for the zircaloy-4 spacer case to 9190 MWd/Te for the graphite spacer case. Except for the zircaloy-4 case, all other values exceed the discharge burnup of the reference lattice cell, which was 7500 MWd/Te.

5.2.5 Balancing Coolant Mass Flow Rate and Power Deposition

At all locations in a reactor core the ratio of power deposition in the coolant, P_C, to coolant mass flow rate, W_C, must be constant for the system to be in equilibrium. This balanced condition must be maintained between coolant subchannels, as well as macroscopically between fuel channels. Assuring this balance between the fuel channels is trivial here once the assumption of identical system parameters to current designs is made; however, the situation between the coolant subchannels depends upon lattice cell geometry and presents another design constraint that will be addressed here.

Power deposition in the coolant subchannels can be approximated by assuming uniform heat production in the fuel and identical temperatures at each surface of a given tubular fuel element, as in Section 5.2.1. The formula used to calculate the radius of maximum fuel temperature, (r_{max} in Equation (5.4)), can then be used to determine the volumetric fraction of each element that will conduct heat through diffusion out to a given surface. If r_{in} and r_{out} represent the inner and outer radii, respectively, of a tubular fuel element, then the fraction of power deposited in the coolant through the outer radial surface is

$$\tilde{P}_{\text{C-OUT}} = \frac{1 + \dfrac{1-(r_{in}/r_{out})^2}{2\ln(r_{in}/r_{out})}}{1-(r_{in}/r_{out})^2} , \tag{5.12}$$

from which the fraction deposited in the coolant through the inner surface follows as

$$\tilde{P}_{\text{C-IN}} = 1 - \tilde{P}_{\text{C-OUT}} . \tag{5.13}$$

If it is further assumed that the fraction of total heat production produced by fuel element k is proportional to its fraction of total fuel volume,

$$\frac{P_k}{P_{\mathrm{TOT}}} \approx \frac{V_k}{V_{\mathrm{TOT}}} \quad , \tag{5.14}$$

then $\hat{P}_{jk}$, the fraction of total power deposited in coolant subchannel j by fuel element k can be estimated as

$$\hat{P}_{jk} = \frac{P_k}{P_{\mathrm{TOT}}} \tilde{P}_{\mathrm{C}\text{-}j} \approx \frac{V_k}{V_{\mathrm{TOT}}} \tilde{P}_{\mathrm{C}\text{-}j} \quad , \tag{5.15}$$

where j, in this case, is either "IN" or "OUT" according to the subchannel's position relative to fuel element k, as introduced in Equations (5.12) and (5.13). The actual fractional amount of power deposition in subchannel j is then found by summing the contributions from all fuel elements with a wetted surface bordering that subchannel,

$$\hat{P}_j = \sum_{k_{\mathrm{bordering}}} \hat{P}_{jk} \tag{5.16}$$

Equations (5.15) and (5.16) can then be used in a parametric search that does not have to calculate actual fission power distributions from the average fission reaction rate in each element k, $\Sigma_{fk}\phi_k$. The approximation is not a bad one since, as will be demonstrated later in the finalized geometries, the thermal flux does not vary widely with fuel element k. As an example, the two fuel elements in Figure 5.7 represent 42% and 58% of the total fuel volume, for the inner and outer elements respectively. A WIMS-AECL calculation of this lattice cell gives the distribution of fission power as 39% and 62%, respectively. The error is acceptable for a parametric search.

The fraction of total coolant mass flow rate drawn by each subchannel, $\hat{W}_j$, can also be calculated efficiently for a parametric search, using Equation (5.10) and the fact that Δp is constant in each subchannel (similar to electrical current division in a parallel resistor circuit),

$$\hat{W}_j = \frac{W_j}{W_{\mathrm{TOT}}} \approx \frac{A_j D_j^{2/3}}{\sum_n^J A_n D_n^{2/3}} \tag{5.17}$$

As an approximation, then, the provision that the ratio of flow rate to power deposition be constant is satisfied by ensuring simply that $\hat{P}_j = \hat{W}_j$, using Equations (5.16) and (5.17).

5.2.6 Critical Heat Flux (CHF)

Although steps can be taken to ensure that enough coolant passes down each subchannel to account for a prescribed steady-state power deposition, it remains to be seen whether the heat transfer across the fuel surface is adequate. Under normal operating conditions heat is transferred to the coolant either by *single phase convection* or by *nucleate boiling*[2,53,71], the latter being a preferred mode because of its high efficiency. However, if the heat flux through the fuel surface, q'', is high enough, then the nucleate boiling reaches a point where surface bubbles coalesce and an extremely inefficient heat transfer regime called *film boiling* is encountered. This is the situation examined for its neutronic implications in Section 2.4 and Appendix C.

This critical point is called the *departure from nucleate boiling* (DNB), and the heat flux corresponding to DNB is called the *critical heat flux* (CHF), which must be avoided in any practical fuel design. The value of CHF is a complicated function of fuel geometry and coolant conditions[2,53,71], and it will suffice in this dissertation to maintain surface heat fluxes and flow properties that are comparable with that estimated for the reference lattice cell.

The average heat flux of tubular fuel element k, q_k'', is estimated as

$$q_k'' = \frac{q_k''' V_k}{S_{k_w}} \propto \frac{A_k}{A_{\mathrm{TOT}} S_{k_w}} , \tag{5.18}$$

where q_k''' is the heat production density of the fuel element (assumed constant), S_{k_w} is the total *wetted* perimeter of the fuel element, and A_k and A_{TOT} are the element and total fuel cross-sectional areas, respectively. Here the assumption of Equation (5.14) has again been used to approximate the power distribution among the fuel elements.

Equation (5.18) can be used to compare values of q_k'' between prospective designs and the reference lattice cell. A suitable reference value of q_k''' is that of the outer ring of eighteen fuel pins in the reference cell, estimated using the distribution of fission power calculated by WIMS-AECL. The reference value of S_{k_w} is then the outer cladding circumference of a fuel pin multiplied by eighteen. The resulting reference value of q_k'' is the largest in the reference lattice cell, and will be assumed to represent an acceptable maximum value.

5.2.7 Numerical Search

In this section, the prescription for a practical design is described by a numerical parametric search. A summary of this search strategy follows, defined by the criteria of the previous sections:

For a given test geometry with coolant flow area, A_C, equal to that of the reference cell,

1) evaluate the temperature rise across the fuel using Equation (5.4), and determine the maximum fuel temperature,
2) evaluate the relative pressure drop (compared to the reference cell) using Equation (5.11),
3) evaluate the relative subchannel flows and power depositions using Equations (5.17) and (5.16), and
4) evaluate the relative heat fluxes for each fuel element using Equation (5.18).
5) If the test geometry meets the criteria tested in points 1 to 4, store it as a potential design and move to the next test geometry.

The starting point for this search is the generic geometry represented by Figure 5.7; that is, a central spacer of variable radius plus a number of nested tubular fuel elements of variable thickness and gap width between each element. The central spacer and all fuel elements are clad in 0.05 mm zircaloy-4 sheaths. Although up to this point in the analysis total fuel volume has been maintained equal to that of the reference lattice cell, it is recognized now that a successful geometry will require less fuel volume if the

criterion of equal A_C is to be satisfied. Thus, fuel volume, or more precisely, fuel cross-sectional area, A_F, is also a variable.

The source code for this search is listed in Appendix E. The search algorithm in this case assumed the use of two nested tubular elements; similar algorithms assuming the use of three and four elements were also used. The search algorithm boundaries and criteria are summarized in Table 5.6.

5.2.8 Summary of Thermalhydraulic Considerations

This section on thermalhydraulic considerations has taken the optimum geometry according to neutronic analysis at the end of Section 5.1, and developed a recipe for a more practical manifestation using a broad approximation. However, the numerical search based upon this recipe is sufficient to provide a new and realistic focus for the neutronic analysis. In general this tangential focus, while practically necessary, will be to the detriment of the search for a reduced void effect. This occurs because any practical configuration will require fuel subdivision and proximity to the centre of the fuel channel for thermalhydraulic reasons, and both are factors shown to increase the void effect in Chapter 4 and in Section 5.1 of this chapter. As pointed out in Section 5.2.4, however, one particular modification suggested in this section will decrease the void effect significantly: the central coolant spacer concept is as much a result of neutronic requirements as thermalhydraulic, although its practical merit seems more intuitive in the context of the latter. For this reason, the description of the need for a central spacer

progressed from thermalhydraulic constraints.

The results of the numerical search described in Section 5.2.7 will form the direction and content of the remainder of this chapter.

5.3 Fuel Throughput Considerations

Before conducting the numerical search described in Section 5.2.7, the effect on fuel throughput of discharge burnup and fuel volume must be discussed, since both these parameters will be allowed to vary. *Fuel throughput* is the refuelling rate of the core, which will be measured here by the number of fuel modules per unit energy extracted from the core (modules/MWd). A *fuel module* corresponds to a *fuel bundle* in ordinary CANDU terminology, although the term *bundle* has become inaccurate in this dissertation with the shift away from cluster geometries.

A high fuel throughput incurs an economic penalty due to the additional demand placed on the on-line refuelling machines, since a practical limitation occurs. Here, it is required that fuel throughput be at most comparable to that of current CANDU designs (a lower throughput would be an added benefit). Fuel throughput, F, is expressed as a function of burnup, B (MWd/Te), and initial fissile mass per module, M (Te/module), as

$$F \doteq \frac{1}{BM} \quad \text{[modules/MWd]} \quad . \tag{5.19}$$

Therefore, a decrease in either burnup or fissile mass per module will increase throughput, and this parameter must be checked after the results of the numerical search based on

thermalhydraulic parameters have been determined. Minimization of throughput will be sought through a combination of maximizing burnup and fissile mass.

An additional concern relates to the possibility of solutions with low values of M. If power output is to be maintained at current CANDU levels, lower values of M imply that either neutron macroscopic cross-section or flux must be increased. Increased flux is not desirable since the effects of component irradiation in the CANDU core have been well studied at current operating levels, and the goal of this project is to maintain system components from the pressure tube outward. Therefore, if solutions with less fissile mass occur, the neutron fission cross-section will have to be increased, either through enrichment, using fuels containing nuclides of higher fission cross-section, or increasing fuel density. These alternatives will be examined here.

5.4 Results of Numerical Search

As described in Section 5.2.7, three separate main categories were considered: two-element, three-element, and four-element nested tubular geometries. Within these categories the spacer radius, total fuel volume, distribution of fuel volume by element, element thickness, element position, and coolant gap were all varied.

5.4.1 Results for Two and Four-Element Geometry Search

When the criteria in Table 5.6, with the exception of the last item (maximum heat flux), are satisfied for the two-element category, the region of "success" illustrated in

Figure 5.11 emerges. The coordinates used for this plot are fuel cross-sectional area, A_F, and radius of the central coolant spacer, r_S, where r_S includes the spacer cladding. The requirement of a constant coolant flow area, A_C, equal to that of the reference lattice cell becomes the overriding influence affecting the shape of this region. A smaller fuel area requires a larger coolant spacer, and vice versa, resulting in a region with negative slope and a width determined by the size of acceptance margin for the A_C criterion (2%, as indicated in Table 5.6). The left and right cut-offs of this region are determined by the fuel temperature and minimum fuel thickness criteria, respectively. As the size of the central coolant spacer is reduced, more fuel area is required, corresponding to thicker fuel annuli with higher maximum temperatures. As the size of the spacer is increased the widths of the fuel annuli must be decreased until the lower limit is met. The bounds of the region in Figure 5.11 are

$$14.2 \text{ cm}^2 \leq A_F \leq 40.2 \text{ cm}^2 \qquad \text{and} \qquad 1.3 \text{ cm} \leq r_S \leq 3.1 \text{ cm}.$$

Within this region lie a range of fuel annuli widths and coolant subchannel widths which all satisfy the criteria of maximum fuel temperature and constant ratio of coolant mass flow rate to power deposition. The bounds of successful A_F values quoted above represent a range between 33% and 94% of the reference cell A_F.

Finally, all geometries within this region have much lower wetted surface areas, S_F, compared to the reference cell, leading to ratios of estimated channel pressure drop compared to the reference cell ranging from 0.6 to 0.8. As indicated in Section 5.2.3, this situation is not undesirable.

Unfortunately, lower surface areas also lead to higher surface heat fluxes. The

result of this immutable relationship is that none of the successful geometries within the region shown in Figure 5.11 has an average element heat flux less than 1.3 times the nominal heat flux described in Section 5.2.6. It will be shown in the next section that geometries with greater fuel volume are desirable, and for cases with greater volume in Figure 5.11 the heat flux ratios are about 1.6. For this reason the results for the two-element geometry are mentioned here but are considered unacceptable solutions and will not be considered further. The issue of high heat flux is addressed again in Sections 5.7.1 and 5.7.2 in terms of strategies for increasing CHF, but it is not clear if these measures are enough for the high fluxes encountered here.

Similarly, the category of four-element tubular geometry is removed from further consideration, but with different and perhaps more straightforward motivation. In this case the width of fuel elements is below the criterion of 0.3 cm, leading to impractical geometries.

5.4.2 Results for Three-Element Geometry Search

The question of optimum fuel subdivision therefore turns to the analysis of three-element nested tubular fuel. Figure 5.12 is an analogous plot to Figure 5.11, illustrating the region where the criteria are satisfied for the three-element geometry, in the coordinates of fuel cross-sectional area and coolant spacer radius. Once again the criteria of maximum heat flux is relaxed. Note in particular that the range of "success" is much smaller in both coordinates compared to Figure 5.11, a result of the third fuel element

being an extra constraining factor in the search process. In this case the bounds of the region in Figure 5.12 are

$$26.8\ \text{cm}^2 \le A_F \le 30.4\ \text{cm}^2 \qquad \text{and} \qquad 2.0\ \text{cm} \le r_S \le 2.3\ \text{cm}.$$

These bounds of A_F represent a range between 62% and 71% of the reference cell A_F. The pressure drop along the channel using these fuel geometries is estimated to fall between 90% and 102% of that of the reference cell. The larger surface areas that create these larger pressure drops, compared to the two-element case, also account for lower heat fluxes. The ratios of average heat fluxes for the cases in Figure 5.12 compared to the reference value have a range from 0.95 to 1.2.

A three-element nested tubular fuel geometry therefore exists which satisfies all of the criteria listed in Table 5.6. It remains to examine the neutronic aspects of these successful geometries in order to narrow the search further.

5.4.3 Burnup and Void Effect of Three-Element Geometries

The significant issues of fuel burnup and void effect for a three-element nested tubular design are now addressed. Predictions can be made through a qualitative neutronic assessment of the design; specifically, the effects of fuel mass and fuel location can be described.

In Section 5.4.2 the successful three-element geometries were described as having a fuel volume, and therefore mass, between 62% and 71% of that of the reference lattice cell. This lower fuel mass, located nearer to the moderator and therefore in a region of

higher thermal flux, will tend to decrease fuel burnup relative to the reference cell. The reason is related to the fact that power output, proportional to the total fission rate, is maintained the same as in the reference cell. In such a scenario the total fission product inventory, while identical to that of the reference cell, has a higher density in a region of higher thermal flux, resulting in greater parasitic absorption and shorter burnup. A second-order effect also occurs due to the higher flux needed to maintain the current power output. The relative importance of parasitic neutron absorption in Xe-135, for example, is increased, which leads to lower burnup.

In Section 5.2.2 it was discussed how subdivision of the fuel can increase the void effect through the necessary increase in the S/V ratio and the placement of fuel nearer to the centre of the fuel channel, both compared to the "ideal" geometry in Figure 5.1(b). Both these factors will also affect geometries resulting from the search, thereby tending to increase the void effect, with the added effect of the lower fuel mass, which will tend to decrease the void effect. One would expect an overall greater void effect compared to that found for the arbitrary design in Figure 5.7 (4.5 mk) since, as discussed, a significant increase in coolant volume is required for a practical two-element design.

It was found in Section 5.2.4 that the use of graphite as a central coolant spacer material provided the highest criticality, while the void effect was insensitive to material. For subsequent calculation purposes, therefore, graphite will be the material of choice. Calculations of fuel burnup and zero-burnup void criticality ($\Delta k_{eff,V}$) for the test geometries within the "success" region of Figure 5.12 are plotted in Figure 5.13 as a function of fuel cross-sectional area, A_F. This abscissa was chosen because burnup in particular

demonstrates a high degree of dependence on fuel mass, approximated by the least-squares curve fit shown in Figure 5.13. Void criticality demonstrates an increasing trend with fuel mass; however, other factors not included, such as spacing of fuel elements (and thus volume of coolant between fuel elements), size of central coolant spacer, and proximity to the pressure tube wall, are clearly also important. Even for a given fuel mass these variables result in a number of successful geometries. Note that the spread in void effect for a given fuel mass is still less than 1 mk however, and therefore minor. The inclusion of both burnup and void effect in one figure provides focus for the remaining choice of design.

In summary, discharge burnup increases, as expected, with fuel mass. However, the geometries with highest discharge burnup in Figure 5.13 still only attain 85% of the burnup of the reference cell (7500 MWd/Te), which was also an expected effect. Zero-burnup void criticality also generally increases with increasing discharge burnup, as a result of the increasing fissile mass in the lattice cell. If natural UO_2 is to be the fuel material, then a burnup penalty is expected, and this case is examined in Section 5.5. If enrichment is to be utilized then a different situation arises, and this case is described later.

5.5 Three-Element Natural UO_2 Design

Obviously many options remain; however, since the design of a low void-effect fuel lattice has been established in principle, it suffices at this point to concentrate on a

significant realization. Following the strategy of Section 5.3, a geometry which maximizes burnup and fissile mass will be chosen, which is a trivial process, since the results in Figure 5.13 indicate that such a geometry is uniquely determined. Since the range of void effects in Figure 5.13 is small, the parameter of significance in this maximization process becomes that of fuel element heat flux, the remaining parameter not included in the original search. Thus the case with maximum burnup and fissile mass which satisfies the heat flux criterion will be selected. This case is designated "3E-NU-GS" — a three-element, natural UO_2 case with a graphite coolant spacer. The geometry of 3E-NU-GS is shown to scale in Figure 5.14, and described fully in Table 5.7. Note the irregular coolant subchannel widths in Figure 5.14, resulting from the matching of coolant flow and power deposition during the search process. In particular, the two inter-element coolant subchannels receive the highest power deposition, being bounded on both sides by heat sources, and are therefore the largest. The WIMS-AECL input file for Case 3E-NU-GS is listed in Appendix F.

Table 5.8 lists the calculated values of k_{eff}, $\Delta k_{eff,V}$, and $\Delta\rho_V$ for the this case at zero and mid-burnup, including the values found if critical bucklings are used to force criticality as described in Section 2.2.2. Also given in Table 5.8 are the discharge burnup and the ratios of average element heat flux, pressure drop, and fuel throughput to that of the reference cell. The estimates of heat flux have been calculated using the actual fission power distribution calculated by WIMS-AECL, although the results do not vary significantly from that found using the search approximation based on cross-sectional area as described in Section 5.2.6. This result helps to justify that approximation. Additional

comparisons of heat flux were made with the mid-burnup and discharge burnup lattices, with identical results to those given in Table 5.8.

In summary, 3E-NU-GS represents a three-element, nested tubular natural UO_2 fuel design with a 13% penalty in burnup over the reference design, and 68% of the fuel mass. Its void effect (either definition) is about 45% of that of the reference case at zero-burnup, and about 21% at mid-burnup. With critical bucklings, these proportions are 17% and 13%, respectively. Criticality is slightly higher (< 10 mk) than for the reference case at zero-burnup, and about the same as for the reference case at mid-burnup. The higher fresh fuel criticality will enhance the refuelling ripple currently found in the CANDU core, and will require further study. Average element heat fluxes are estimated to be the same as the maximum element heat flux found in the reference design. Fuel throughput is about 70% higher than in the reference design (caused by the combination of discharge burnup and fissile mass both being lower).

The detailed results for 3E-NU-GS are next used to characterize the class of three-element tubular fuel designs in general. In Table 5.9 the criticality factors contributing to the void effect are presented, with and without the use of critical bucklings. Comparing these results to those for the reference lattice cell in Table 3.1, it is clear that the significant contribution to the reduced void effect comes from the epithermal escape probability, p_E, as expected. With critical bucklings the resulting enhanced neutron leakage has a strong negative influence on the perturbations to both p_E and p_F, which is the main reason for the much lower void effect, especially at zero-burnup. These results should be taken as indicators of the trend only, since quantitative results are subject to

the concerns about the WIMS-AECL resonance treatment expressed in Section 5.9.1.

The complete burnup history of k_{eff} (cooled case), $\Delta k_{eff,V}$, and $\Delta\rho_V$ is illustrated in Figure 5.15, subject to the validity concerns regarding burnup calculations expressed in Section 2.2.1. This can be compared to Figure 3.7 for the reference lattice cell. The profile and magnitude of k_{eff} is very similar to that of the reference case, and the profiles of $\Delta k_{eff,V}$ and $\Delta\rho_V$ are also similar but of lower magnitude. At this point the concern expressed in Section 2.2.1 about the validity of the mid-burnup approximation to equilibrium conditions should be reviewed since case 3E-NU-GS represents a final design much different from the reference case. In this case, the point of zero excess reactivity is greater than the point of mid-burnup by about 3% of burnup (100 MWd/Te), which is negligible and comparable to the difference found for the reference cell.

Finally, the thermal, epithermal, and fast flux distributions across the lattice cell are given in Figure 5.16, Figure 5.17, and Figure 5.18, respectively. These plots are normalized to the total neutron population of all groups, as in Figure 3.8, Figure 3.9, and Figure 3.10 for the reference lattice cell. Also as in the earlier reference cell figures, the abscissa is the WIMS-AECL calculation mesh and not the radial coordinate, so the given flux distributions are once again only representative of the actual spatial distribution. The important result to note here is that the perturbations to all three group distributions upon voiding are minor compared to the reference case. This is readily ascertained by noting the difference in y-axis scale between the reference case and the current one.

5.6 Three-Element Enriched UO_2 Design

At this point fuel enrichment is introduced in the geometry of Case 3E-NU-GS in order to solve the problem of high fuel throughput (see Section 5.3). As indicated in Table 5.8, fuel throughput is almost twice that of the reference case, due to the lower volume of fissile material in the lattice cell coupled with the lower burnup. The goal now is to reduce the fuel throughput to the level of the reference case, or lower, without increasing the void effect.

The method used here will lower the fuel throughput by increasing burnup, through the use of fuel enrichment. It was also indicated in Section 5.3 that enrichment can be used to increase the power output of a fuel module without increasing the thermal flux in the module. Hence, the goal becomes two-fold: using enrichment, compensate for the effect of lower fuel volume on (1) fuel throughput, and (2) average module thermal flux. (Cost-effectiveness must be considered as well, balancing the cost of enrichment against the cost of high fuel throughput, but this is outside the scope of this dissertation.)

The effect of enrichment on the zero-burnup void effect of the 3E-NU-GS geometry is illustrated in Figure 5.19 and Figure 5.20 for $\Delta k_{eff,V}$ and $\Delta\rho_V$, respectively, for the range of 0.2 %wt to 2.0 %wt. Also included are the criticality factor contributions to $\Delta k_{eff,V}$ and $\Delta\rho_V$. In comparing these results with those for the reference cell in Figure 4.8 and Figure 4.9, which were plotted over a larger range, it is apparent that the maximum in $\Delta k_{eff,V}$ occurs at a much lower U-235 abundance. The location of this peak

depends on the relative importance of the p_E contribution: increasing enrichment increases the importance of epithermal absorption in both the reference cell and the 3E-NU-GS geometry (see Section 4.2.1), but the overall importance of p_E in the 3E-NU-GS geometry is significantly less. There is, therefore, a net benefit in terms of both $\Delta k_{eff,V}$ and $\Delta\rho_V$ with the use of enrichment, although the benefit is small regardless of which definition of void effect is used (compared to natural fuel, 0.72%wt). Void effect will therefore not play a part in the determination of optimum enrichment.

Using Equation (5.19) the necessary discharge burnup for the geometry of Case 3E-NU-GS which would achieve a fuel throughput equal to that of the reference case is calculated to be 11 GWd/Te. This represents a 70% increase in burnup relative to the current value for Case 3E-NU-GS, and a 50% increase over the reference cell. Figure 5.21 is a plot of discharge burnup as a function of fuel enrichment for both the 3E-NU-GS and reference cell geometry, indicating that a burnup of 11 GWd/Te corresponds to an initial enrichment of 0.87 %wt in the 3E-NU-GS geometry. The WIMS-AECL data is fit to a straight line for both geometries, and although a slight curvature of the data is suggested, these linear approximations are satisfactory for the purposes here. As indicated in Figure 5.21, the gain in discharge burnup as a function of enrichment is greater in the reference cell.

The second goal above is concerned with maintaining the same fission energy in the fuel without increasing flux levels. A first-order approximation for the degree of enrichment required to meet this goal above would maintain the same amount of U-235 in the fuel as in the reference case. This works out to an initial enrichment of 1.1 %wt,

indicated in Figure 5.21 with its corresponding discharge burnup (17 GWd/Te). Since this burnup is greater than the value, determined above, which satisfies the fuel throughput criterion (11 GWd/Te), this case will be isolated as another final design, with an enrichment level of 1.1 %wt. Such an enrichment level is also attractive because, unlike the value of 0.87 %wt required for throughput equivalence, the increase in U-235 content may be large enough to justify the capital expense accompanying any move to enriched fuel production from a natural fuel cycle.

The designation for this case is "3E-EU-GS" — three-element nested tubular fuel, enriched uranium, graphite spacer, with the same geometry as Case 3E-NU-GS. The calculated results for this design are given in Table 5.10 along with those for the reference cell. Discharge burnup increases by 227% relative to that of the reference cell, and by 262% over that of Case 3E-NU-GS (see Table 5.8).

The void effect with geometric bucklings is only slightly affected by the move to 1.1 %wt enriched fuel. However, a striking reduction in the zero-burnup void effect occurs when critical bucklings are employed, echoing a similar finding for 37-element fuel discussed in Section 2.2.2. In both situations a significant increase in the importance of cell leakage accounts for a large negative influence on criticality upon voiding. This phenomenon is represented by a much larger contribution through the p_F and p_E factors. These criticality factor contributions are summarized in Table 5.11 for Case 3E-EU-GS, and can be compared with the contributions for the natural UO_2 case in Table 5.9. Again, the resonance modelling problem to be described in Section 5.9.1 must be kept in mind when interpreting these results.

The estimates of heat flux and pressure drop are the same for Case 3E-EU-GS as for Case 3E-NU-GS, since only geometry affects these approximations. Estimated fuel throughput is now only 70% of that of the reference cell, however, since the burnup is larger than that required to equalize this parameter.

5.7 Remaining Thermalhydraulic Concerns

The issue of whether sufficient cooling can be provided for the three-element fuel geometry is not yet closed, since a number of important concerns remain to be addressed. As stated earlier, the scope of this dissertation does not include detailed analysis in this area, but several significant points will be mentioned and suggestions made.

5.7.1 Avoidance of CHF: Subchannel Mixing

The avoidance of CHF (see Section 5.2.6) at fuel element surfaces was a goal of the geometry search, using the comparison of average element heat flux to maximum heat flux in the reference cell as a criterion. Although this criterion is satisfied with the 3E-NU-GS geometry, it is possible that this test is not strict enough and therefore further measures to avoid CHF should be examined. The importance of this is clear when one notes that CHF is a function of fuel geometry and coolant conditions, neither of which can be equated here with the 37-element cluster case.

One primary difference between the reference geometry and the 3E-NU-GS geometry is the isolation of coolant subchannels. In current CANDU fuel design the

many interconnected subchannels create turbulence and flow mixing, tending to raise CHF by preventing high steam quality regions from collecting anywhere[74]. In the 3E-NU-GS geometry shown in Figure 5.14 such mixing is absent and low CHF regions might occur at the top of each subchannel.

One way around this potential problem (other than reorienting CANDU cores vertically, an impractical option) is to allow mixing between the coolant subchannels. A modification[74] to the three-element geometry which accomplishes this is illustrated in Figure 5.22. Note that this figure is only a conceptual depiction, since the slots are drawn with arbitrary width and location, and their shape would be more rounded to remove points of high stress. It is conceivable that the design would also require special modifications to the fuelling machine, ensuring approximate orientation in the fuel channel as pictured in the figure, in order to prevent low CHF values at the top of each tubular fuel element.

The subdivision of the three-element geometry into physically separate quadrants (or, in general, sectors) changes the search problem slightly, but it is not expected that any of the neutronic results would be significantly different. The complexity of this geometry precludes precise modelling with a code like WIMS-AECL, however. With the removal of separate flow channels the pressure drop across the fuel channel is predicted to decrease, but this does not take into account the turbulence set up by the new geometry, which would increase the pressure drop.

5.7.2 Avoidance of CHF: Flow Turbulence

There is an additional need to create more turbulence within each subchannel, since the flow conditions around the reference cell fuel surfaces are quite turbulent. This is a desired condition since it increases CHF and thus maximum channel power in the CANDU core[75], and much research has been conducted into inducing further turbulence for this purpose[74,76].

One envisions, therefore, similar modifications to the subchannels of the three-element nested tubular geometry. Besides the necessary spacers (see Section 5.7.3) between fuel elements, which will add turbulence, extra fins can be added to impart a swirling motion to the flow. Also, the endplates that hold the three fuel elements and central spacer in place can also be appropriately designed to provide additional turbulence. All of these modifications will increase the pressure drop across the fuel channel, which was one of the reasons for allowing this parameter to be less than that of the reference fuel geometry. The bare 3E-NU-GS geometry in particular was estimated to have about 10% less pressure drop than the reference geometry.

5.7.3 Avoidance of Subchannel Blockage

An additional concern is that of subchannel blockage in an accident scenario involving fuel element swelling. Swelling can be caused by thermal expansion of the fuel meat during a high temperature transient, or ingress of the high pressure coolant into the fuel elements through cladding breaches. Such swelling scenarios are not a subject of

analysis in this dissertation, but once again a cursory assessment can be made. In particular, the identical curvature of all the tubular fuel elements suggests that element expansion will occur in the same radial direction, which is the motivation behind the curvature of plate fuel in MTR test reactors[77], for example. Should the tubular elements make contact, however, the subchannels in the 3E-NU-GS geometry of Figure 5.14 will become blocked and lead to flow stagnation, and therefore this situation must be prevented.

In the reference 37-element geometry flow can never be stagnated in this manner because the interconnection of subchannels will always provide a free path if one subchannel becomes blocked[74]. The subchannels interconnections suggested in Section 5.7.1 will perform this role also, although the optimum placement of these interconnections would not necessarily be as shown in the conceptual illustration of Figure 5.22. In addition to these interconnections, spacers can be added between the elements in a configuration that minimizes element expansion. Such an arrangement of spacers is suggested in Figure 5.23, which also includes the subchannel interconnections of Figure 5.22. The number and size of these spacers, both chosen arbitrarily in Figure 5.23, would effect a corresponding reduction in coolant flow area that would require a further geometry modification to return this parameter to its nominal value. On the other hand, the presence of spacers would help in both heat transfer to the coolant and coolant mixing through additional induced turbulence.

5.8 Materials Concerns

This section addresses briefly the concerns that arise with the nested tubular geometry from a fuel materials point of view. Two areas of concern are singled out: manufacturing of the fuel elements, and choosing a suitable material for the central coolant spacer.

5.8.1 Manufacturing of Tubular Fuel Elements

In the geometry of Case 3E-NU-GS the fuel consists of three different-radii thin-walled tubes of UO_2 fuel of approximate thickness 0.4 cm. In the modified geometry of Figure 5.22 the fuel is best described as curved plate fuel in a concentric arrangement. In either case the manufacture of such fuel elements in mass production is predicted to be much more expensive than current CANDU fuel manufacturing, although no technical impediment is anticipated[72,78]. A further design requirement that must be met[74] is the flexibility needed to pass unimpeded through a slumped pressure tube; this concern will not be addressed here.

On a prototype basis the tubular elements could be made by filling each tube with UO_2 under vibration until a suitably high packing density is obtained, but this is not a suitable process for mass production[72]. Also of concern is the thinness of the tube walls, which would make manufacture of separate zircaloy tubes difficult. It has been suggested[78] that coextrusion of the fuel meat and cladding might be a way around this potential problem.

The concepts of concentric tubular fuel and highly curved plate fuel are not new to reactor engineering. Production reactors at Hanford and Savannah River have used this geometry[79,80], with target regions formed in the centre of the nested tubes. The proposed New Production Reactor — Heavy Water Reactor (NPR-HWR)[81] of the US DOE continues the use of nested tubular geometry, with targets in the centre and around the perimeter of the fuel. The High-Flux Isotope Reactor (HFIR)[82] and the proposed Advanced Neutron Source (ANS)[83] at Oak Ridge National Laboratory both utilize high-curvature plate fuel, while SPR III-M[84], the new fast burst research reactor at Sandia National Laboratories, uses rings of uranium alloy. An example of particular interest is the Plutonium Recycle Test Reactor (PRTR)[79,85] at Hanford which used nested tubular UO_2 fuel under similar coolant temperature, pressure, and velocity conditions as those found in the CANDU system. For that project, much work was performed in the area of manufacturing ceramic UO_2 fuel elements in a variety of shapes[85].

It is concluded, therefore, that the manufacture of either the nested tubular UO_2 fuel designs or the curved UO_2 plate designs described in this dissertation, and the use of these fuel designs in the CANDU core, are technically achievable goals. The cost of such mass manufacturing is likely to be high, but not prohibitive, in comparison with current CANDU fuel manufacturing.

5.8.2 Central Coolant Spacer Material

In terms of lattice criticality, the cursory analysis of Section 5.2.4 isolated graphite

as the material of choice for the central coolant spacer. It is possible, however, that problems of irradiation behaviour or chemical compatibility may preclude the use of graphite in the CANDU lattice, and this section therefore briefly examines these potential problems and the use of alternate materials.

The potential problems of irradiation behaviour include irradiation-induced growth, heating and energy storage (or self-heating). Growth can be ruled out as a problem because studies show that graphite actually shrinks by a small percentage with high irradiation at high temperatures[86], such as that found in the CANDU core. Likewise, heating caused by neutron absorption is not a problem either, due to the high thermal conductivity of graphite (about 1 W/cm·°K), its high melting point (> 3000 °C), and the contact of coolant with the spacer surface. Finally, the problem of energy storage, or self-heating, due to neutron bombardment is reduced by the self-annealing[86] that takes place at the operating temperatures of the CANDU coolant, about 300 °C.

The question of chemical compatibility is related to accident analysis, since under normal operation the coolant spacer is isolated from other lattice materials by its own cladding. The two most important reactions that can take place in an accident scenario are the carbon-hydrogen reaction, producing mostly methane gas, and carbon oxidation. Oxidation is a minor concern since core flooding is a reliable safety measure, but it is something to consider in analyses of emergency coolant failure. Methane production increases with pressure and temperature, and would be expected to proceed extremely slowly[86]. However, the carbon-hydrogen reaction rate is known to increase with irradiation, and the degree to which it is increased is larger at both higher pressures and

lower temperatures[86]. Once again, this would be an area requiring analysis in accident scenarios.

In Section 5.2.4 several alternate materials, representative of different categories of neutronic and chemical compatibility in the lattice, were examined. For the sake of completeness, the more practical of these materials, zircaloy and SiO_2, are examined now as candidate materials for the coolant spacer in the 3E-NU-GS and 3E-EU-GS designs. In addition, a new candidate material, silicon carbide (SiC, density[73] 3.2 g/cm^3), is included with the hopes that it combines the favourable neutronic characteristics of carbon with the chemical compatibility of materials like SiO_2. SiC is chemically inert in a water environment and melts at 2700 °C.

Table 5.12 lists the results for zero-burnup $\Delta k_{eff,V}$ and discharge burnup for each of these materials, plus the graphite case for comparison. As in the scoping results of Figure 5.9 and Figure 5.10, there is little dependence of the void effect upon spacer material, but a significant dependence of criticality, and hence burnup. This latter variation with spacer material is less pronounced when 1.1 %wt enriched fuel is used, and all of the materials tested have enriched fuel burnups exceeding the estimated required value of 11 GWd/Te in Section 5.6. If required, the enrichment levels could also be adjusted slightly to compensate for low criticality.

The enriched UO_2 cases, 3E-EU-ZS, 3E-EU-QS, and 3E-EU-SS, are therefore all potential designs alongside the graphite spacer case, 3E-EU-GS.

5.9 Modelling Concerns

The methodology of the lattice cell calculations used in all of the analysis here requires verification in several areas. In Chapter 2 this methodology was found to be sufficient for pursuing the goals of this dissertation, but the significant deviation from cluster geometry found in this chapter demands a second look at this question. In this section the validity of the WIMS-AECL resonance treatment with nested tubular geometries is questioned, and WIMS-AECL results are compared with results from a Monte Carlo code. The habit of ignoring neutron lifetime in lattice call parametric studies is again addressed, the effect of arbitrary changes in input specification is examined, and calculations are checked against those using the 89-group ENDF/B-V library.

5.9.1 Resonance Treatment in WIMS-AECL

Of utmost concern is the model used in the creation of resonance group cross-sections in WIMS-AECL, and how it applies to annular geometries such as those examined in this chapter. As described in Section 1.9, resonance integrals are interpolated from tabulations in the nuclear data library, using fuel temperature and background scattering cross-section as interpolation parameters[28,32]. This library data is based upon homogeneous nuclide mixtures, and an equivalence relationship is invoked to calculate heterogeneous integrals. This relationship involves adding to the background scattering cross-section a quantity known as the *fuel escape cross-section*,

$$\Sigma_e \equiv \frac{S_f}{4\,V_f} \quad , \tag{5.20}$$

which accounts for neutron leakage through the fuel surface. As the S/V ratio increases, so does the probability of a resonance energy neutron from the coolant or moderator penetrating the fuel mass and encountering U-238. The ratio is therefore directly related to the level of resonance flux within the fuel, and consequently the resonance integral. This calculation of resonance group cross-sections is based upon a simplified pin cell geometry, in which the S/V (surface-to-volume) ratio is the *only* link by which the heterogeneity of the original cell enters the calculation.

The problem that arises, when solving for annular geometries under the "PERSEUS" option of WIMS-AECL, concerns the calculation of the fuel escape cross-section. An investigation of the output of the resonance cross-section module ("CHAIN 3") reveals that it lumps all tubular fuel into a single rod of equivalent volume, with the implication that the S/V ratio, and thus the resonance group cross-sections, are calculated too low. Geometry effects are still accounted for in the main transport calculation, but the results will be affected by the error in the resonance cross-sections. This error will next be estimated, and then a model will be introduced which corrects for much of the deficiency.

A first-order estimate of the importance of the S/V ratio in the case of natural UO_2 is made by starting with the reference 37-element lattice cell and reducing the number of fuel pins while conserving fuel, clad, and coolant volume. Ideally, all aspects would be conserved except for the S/V ratio, but in this exercise a secondary geometry effect is included due to the arbitrary placement of these pins. All attempts are made to keep the amount of coolant surrounding each pin constant, in order to minimize the secondary

effects. The S/V ratio will vary from a minimum of 1.21 (five pins) to a maximum of 3.29 (37 pins), or in relative terms normalized to the five-pin case: 1 to 2.72. In Figure 5.24 the relative contribution to $\Delta k_{eff,V}$ (normalized to the five-pin case) of the epithermal escape parameter, Δp_E, is plotted as a function of "relative S/V" — S/V normalized to the five-pin case. This result suggests almost a 1:1 correspondence between the two plotted parameters, although the geometry effect must also be taken into consideration before applying the result to general geometries. The straight line in Figure 5.24 is a least-squares fit, and serves as an illustration of the trend only. In absolute terms, the value of Δp_E in this comparison varies from 5 mk to 12 mk as a function of "relative S/V".

A method is now developed by which the resonance cross-section module in WIMS-AECL can be "tricked" into using a value of S/V close to that of the tubular fuel geometry being modelled. By running the code in "PIJ", or pin cluster, mode, one can specify a number of false "fuel pins" located within one of the tubular fuel elements, as shown in Figure 5.25. The size and exact location of these "fuel pins" does not matter, as long as they are within a fuel annulus. The "trick" relies on the fact that WIMS-AECL calculates the resonance cross-sections using an average fuel pin of volume V/N, where V is the total volume of all fuel material in the cell (including, in this case, material in the false "fuel pins" and the fuel annuli combined), and N is the number of fuel pins ("NRODS" in the WIMS-AECL input file). Knowing the value of V, the required value of N is obtained by equating the S/V ratio of the N "fuel pins" to that of the original nested tubular geometry,

$$N = \frac{S^2}{V 4\pi} \quad . \tag{5.21}$$

It is easily shown that only a discrete set of S/V ratios can be represented this way, determined by the value of V, which is fixed for a particular case. For the 3E-NU-GS geometry, the closest value of S/V that can be represented is 4.79, which is 1.5% greater than the actual value of 4.71. This corresponds to N=53 false "fuel pins", the case shown in Figure 5.25.

Assuming that the S/V ratio represented is close to the actual value, as it is in this case, this method should account for much of the effect of heterogeneity in the resonance cross-section calculations. It will be insufficient in the following areas:

1) It will not properly reflect certain transport probabilities, such as the probability of a neutron leaving the fuel and entering the moderator. In the actual geometry the fuel volume is concentrated near the moderator, while the resonance cluster treatment assumes a evenly distributed arrangement.

2) It will homogenize the central coolant spacer material with the coolant material.

The second point is likely not significant in the generation of cross-sections, but the first deficiency may overestimate the actual resonance group cross-sections. In this dissertation the representation described here, and illustrated in Figure 5.25, will be called the *S/V Resonance Correction Model* for tubular fuel geometry.

Applying the S/V Resonance Correction Model to Case 3E-NU-GS at zero-burnup, it is found that the Δp_E contribution to void criticality ($\Delta k_{eff,V}$) increases from 1.4 mk (the value in Table 5.9) to 7.7 mk, a factor of 5.5. In comparison, the first-order estimation

of the effect on Δp_E shown in Figure 5.24 suggests a factor of about 3, using the relative S/V ratio modelled for Case 3E-NU-GS (4.79). The overall value of $\Delta k_{eff,V}$ increases from 8.6 mk to 14.8 mk, a factor 1.7. Using the estimated factor of 3 for the change in Δp_E, the new $\Delta k_{eff,V}$ would be 11.4 mk, or a factor of 1.3 greater than the original.

These results are summarized in Table 5.13, along with those for Case 3E-EU-GS, at zero and mid-burnup for each case. For the mid-burnup results, the nuclide densities used were those belonging to the previous calculation that didn't account for the S/V ratio. It was found that the error incurred with this approximation is minor, and the effect on the void effect unchanged. Such an approximation will make it easier to similarly check the cases that follow in this dissertation. Note that the estimation using the results in Figure 5.24 cannot be taken as being very meaningful since the estimation in Figure 5.24 was with natural UO_2 fuel.

In terms of $\Delta\rho_V$, the S/V Resonance Correction Model applied to Case 3E-NU-GS increases the zero-burnup effect to 12.8 mk (from 7.2 mk), and the mid-burnup effect to 8.6 mk (from 2.9 mk). Applied to Case 3E-EU-GS, the zero-burnup effect increases to 9.7 mk (from 5.2) and the mid-burnup effect to 8.6 mk (from 3.1 mk).

These approximations suggest a significant increase in the void effect over that predicted using WIMS-AECL without accounting for the S/V ratio. It is prudent at this point, therefore, to compare the calculations of WIMS-AECL against a more reliable calculation, and for this purpose the Monte Carlo code MCNP-4 is used (see Section 1.9).

To expedite the MCNP-4 calculation, a simplified infinite lattice cell, shown in Figure 5.26, was created with tubular geometry. This cell contains a central graphite

spacer, one fuel region, and two coolant regions. Identical cases corresponding to this geometry were modelled using both WIMS-AECL and MCNP-4, with all nuclide temperatures and abundance ratios consistent between the two codes. All temperatures correspond to nominal MCNP-4 library values, including fuel at 300 °K, in order to avoid concerns[40] about temperature modelling in MCNP-4. The input files for both the MCNP-4 and WIMS-AECL cases are listed in Appendix G. A total of 12 million MCNP-4 neutron histories were calculated for each of the cooled and voided cases.

Table 5.14 summarizes the results of these calculations. The infinite lattice criticality calculated by WIMS-AECL is greater than that of MCNP-4 by 13 mk (or 1.3% error), but the void effects are in agreement. Disagreements between these two codes in terms of criticality is not a new phenomenon[41,50], and it is not clear how much of this error is contributed by each code under normal circumstances. In this case, however, an additional difference would be caused by the lack of proper representation of the S/V ratio in WIMS-AECL. It would be expected that the resonance integral in WIMS-AECL would be calculated too low, and hence criticality would be calculated too high, as is the case here in comparison with MCNP-4.

From the results in Table 5.14 it appears that a cancellation of errors leads to reasonable agreement in perturbation calculations like the void effect. The statistical error quoted for the MCNP-4 results corresponds to one standard deviation, and the resulting relative error of about 0.08 is considered to be acceptable[39]. This agreement in the void effect contradicts the result found with the S/V Resonance Correction Model, and thereby raises questions about the usefulness of that result. It is possible that the deficiencies in

geometry representation mentioned earlier account for the discrepancy, but it is unknown to what extent this is true. The S/V Resonance Correction Model is not a complete adjustment for the inadequacies of WIMS-AECL in calculating resonance cross-sections for tubular fuel geometries, and it is plausible that other factors not described here are involved. A more detailed study, including a variety of MCNP-4 geometries, would be necessary to determine this.

In conclusion, it cannot be concluded that the void effect calculations for the modified geometries in this dissertation are reliable results. Comparison with a Monte Carlo calculation lends support to the results here, but the analysis of the WIMS-AECL resonance treatment for these geometries, and the S/V Resonance Correction Model that resulted from this analysis, suggest otherwise. With this warning in mind, WIMS-AECL results without the S/V correction will continue to be reported in the analyses to follow, while results using the S/V correction will be mentioned in significant cases for comparative purposes. All of the results given in tables like Table 5.9 will not include the S/V correction.

Results for criticality should not be accepted as reliable within about 20 mk, and for this reason emphasis on these results have not been emphasized in this chapter. It should be noted, however, that a lower initial criticality would reduce the enhancement of the power ripple mentioned in Section 5.5, and also reduce discharge burnup.

5.9.2 Revisiting Neutron Lifetime

In Section 2.2.7 it was concluded that the effect of perturbations to neutron lifetime should be estimated before drawing conclusions about kinetic behaviour in radically changed fuel geometries, based solely on lattice cell calculations. The method of approximation used in Section 2.2.5 is applied again here to Case 3E-NU-GS.

In Section 2.2.5 the main parameter appearing in the point kinetics equations, $(\rho-\beta)/\Lambda$, was estimated to increase upon voiding by an amount 7% greater if the variation in mean generation time, Λ, was taken into account at zero-burnup, and 9% at mid-burnup. Performing the calculation on the WIMS-AECL results for Case 3E-NU-GS, these discrepancies are 5% at zero-burnup and 4% at mid-burnup. The reduction is mainly due to the lower value of ρ to begin with.

This approximation therefore indicates that the level of concern about unmodelled perturbations to neutron lifetime does not increase with the nested tubular geometries.

5.9.3 Effect of Changing WIMS-AECL Input Parameters

There is much flexibility in the specification of input for WIMS-AECL cases, and it was mentioned in Section 2.2.6 that such variation can affect void effect calculations by about ±1 mk. To explore the dependence on input formulation of Case 3E-NU-GS at zero-burnup, several input specifications were changed or removed, as described in this section and summarized in Table 5.15. The choice of specifications used in this dissertation was made to achieve the most accurate result from the WIMS-AECL

calculation, and therefore the effects of changing these specifications do not necessarily indicate a range of valid responses. The intent here is simply to demonstrate a range of possible responses. In the following, the anachronistic term "card" refers to separate input command lines.

ANNULUS card: Input geometries for "PIJ" calculations require subdivision into concentric annuli using the ANNULUS card. For "PERSEUS" calculations a separate mesh is set up either manually or by the code. The "PERSEUS" calculations used for all the purely tubular geometries in this dissertation include ANNULUS cards mainly as delimiters of physically different materials, and a check was made to ensure the ineffectiveness of these cards by adding many more and recalculating. The result, using an extra annulus within the spacer material and fifteen more in the moderator (for an average annuli thickness in both cases of about 0.5 cm as recommended[27]), is exactly the same as the original result.

BENOIST card: The Benoist method[87,88] of multiregion, directional diffusion coefficient calculation is considered to be more accurate than the other methods of simple diffusion coefficient calculation available in WIMS-AECL. The BENOIST card, which selects this method, was removed to test the affect of using the default calculation based upon the transport cross-section, $D = (3\Sigma_u)^{-1}$. The result was an increase of 1 mk, or about 12%, in the void effect and no increase in criticality. The extra 1 mk was contributed through the perturbation in thermal utilization, *f*, indicating that the Benoist method predicts a higher increase in thermal leakage upon voiding. This discrepancy may become significant

NEWRES card: Two optional resonance treatments are available in WIMS-AECL, and the newer one was selected in this dissertation by including the card NEWRES in the input files. Removing this card selects the default calculation, which is the "old" method when using the Winfrith data library (the "new" calculation is the default with the ENDF/B library). The effect of thus changing resonance treatments, using all defaults for factors related to the "old" treatment, was found to be an increase of about 3 mk in void effect and no increase in criticality. The void effect increase is contributed mainly through the perturbation in the epithermal group escape factor, p_E, as expected. The S/V Resonance Correction Model was not invoked in this comparison.

5.9.4 Effect of Changing WIMS-AECL Libraries

Near the end of this project an IBM-PC version of the ENDF/B-V cross-section library[36] for WIMS-AECL became available. For the purpose of proper comparison, all results in this dissertation are generated using the Winfrith library, but it would be informative to recalculate a couple of significant cases using the ENDF/B-V library since it is a newer database. The ENDF/B-V library for WIMS-AECL[27] has 89 energy groups, which is 20 more than the Winfrith library. The extra groups include 5 more in the fast range and 15 in the epithermal range.

The results of recalculating the 37-element reference cell and Case 3E-NU-GS using the ENDF/B-V library are given in Table 5.16, looking at both zero and mid-burnup, and using both geometric and critical bucklings. With the reference cell the

largest difference is a 3 mk disagreement using critical bucklings at zero-burnup, and this the only disagreement in Table 5.16 of any significance. The results for Case 3E-NU-GS are almost unaffected by the choice of cross-section library.

5.10 Alternate Fuel Cycles

In Section 4.2.5 some success was found in reducing the void effect by exploiting the beneficial effect of plutonium in MOX fuel. In this section this same strategy is used with the nested tubular geometry in an effort to find a design with even lower void effect. In the same vein as MOX fuel cycles is the DUPIC fuel cycle, which is also examined here. Both cycles solve the problem of adequate fuel throughput without requiring enrichment, although the problem of high flux levels remains and is not addressed in this section. Another tack taken here to avoid uranium enrichment is to find suitable fuel material with high enough uranium density.

All of the designs discussed here are variations of Case 3E-NU-GS, using the same geometry and altering the fuel constituents.

5.10.1 MOX Fuel Cycle

The results of using MOX fuel in the reference 37-element lattice cell are given in Figure 4.12, indicating a minimum in $\Delta k_{eff,V}$ within the PuO_2 abundance region of 0 - 1 %wt. The same plot is shown in Figure 5.27 using the nested tubular geometry of Case 3E-NU-GS, and in this case both $\Delta k_{eff,V}$ and $\Delta\rho_V$ display minima around the point

of 0.3 %wt PuO_2. A detailed calculation was performed for this particular case, designated "3E-MOX-GS" — three-element, MOX fuel, graphite spacer, and the results are listed in the first column of Table 5.17.

The zero-burnup value of $\Delta k_{eff,V}$ for Case 3E-MOX-GS is reduced by 2 mk compared with both the natural and enriched UO_2 cases (3E-NU-GS and 3E-EU-GS, respectively), and the results at mid-burnup are similar to both these earlier cases. Discharge burnup is estimated at 12.5 GWd/Te, which is more than the 11 GWd/Te needed for the fuel throughput criterion, resulting in an estimated throughput rate that is about 90% of the reference case.

With the S/V Resonance Correction Model applied, as described in Section 5.9.1, the values of $\Delta k_{eff,V}$ at zero and mid-burnup are 13.4 mk and 8.5 mk, respectively. The values of $\Delta\rho_V$ at zero and mid-burnup are 9.1 mk and 8.5 mk, respectively.

5.10.2 DUPIC Fuel Cycle

A fuel cycle of current interest to CANDU owners is DUPIC[89,90], or "Direct Use of Spent PWR Fuel in CANDU". This cycle utilizes PWR spent fuel in a CANDU lattice after removing most of the volatile and semi-volatile fission products (Xe, Cs, Ru, Kr, I, etc.), and is therefore one potential solution to the problem of nuclear waste disposal.

For economic reasons[91] this fuel cycle could be a suitable match for the nested tubular designs discussed here: the reprocessing and refabrication components of the DUPIC fuel cycle are an added expense compared to conventional fuel cycles, and against

such costs, the economics of fabricating nested tubular fuel (see Section 5.8.1) would be a smaller increment. Furthermore, the DUPIC fuel cycle presumably benefits from high neutron economy since the spent PWR fuel still contains many parasitic fission products. For this reason, a major reduction in neutron economy such as that of the LVRF programme of AECL (see Section 1.7) would not be preferable.

To approximate the effect of using DUPIC fuel in the 3E-NU-GS geometry, the fissile content of spent PWR fuel[92] was assumed, ignoring all fission products. This is essentially mixed-oxide fuel with a different isotopic mixture of both uranium and plutonium from that discussed in Section 5.10.1. This isotopic mixture is given in Table 5.18, and corresponds to a U-235 enrichment of 0.87 %wt, and a PuO_2 fraction of 0.7 %wt. Since this PuO_2 weight fraction differs from that which produces a void effect minimum in Figure 5.27, one would expect a higher void effect for this case. Also, the concentration ratio of Pu-241 to Pu-239 from Table 5.18 is about twice that estimated in Section 4.2.5 for the maximum in CANDU spent fuel. That section indicated that the positive thermal contribution to the void effect from Pu-241 countered the negative effects of Pu-239, and thus one would expect a higher void effect for this reason also. The designation for this case is "3D-DUP-GS" — three-element, DUPIC fuel, graphite spacer, and the results of the WIMS-AECL calculation are listed next to the 0.3 %wt PuO_2 results in Table 5.17.

The zero-burnup value of $\Delta k_{eff,V}$ does turn out to be 3 mk higher than that found for the MOX case, while $\Delta\rho_V$ is unchanged. This value of $\Delta k_{eff,V}$ is also slightly higher (<1 mk) than that found for the natural and enriched UO_2 cases. At mid-burnup both

$\Delta k_{eff,V}$ and $\Delta\rho_V$ are almost 2 mk higher than the MOX case and UO_2 cases. Discharge burnup is twice the value for the MOX case, leading to a ratio of fuel throughput compared to the reference cell of 50%. In terms of the criteria of this dissertation, therefore, DUPIC fuel is estimated to be compatible.

With the S/V Resonance Correction Model applied, the values of $\Delta k_{eff,V}$ at zero and mid-burnup are 16.7 mk and 8.7 mk, respectively. The values of $\Delta\rho_V$ at zero and mid-burnup are 10.3 mk and 9.7 mk, respectively.

5.10.3 High Natural Uranium Density Fuels

In Section 5.3 it was suggested that increasing fuel density was another solution to the problem of high fuel throughput and thermal flux levels. This strategy will be explored here, focusing on two candidate fuels: UN and U_3Si_2. The properties of these two fuel materials are listed in Table 5.19 along with the calculational results found by substituting them for UO_2 in the 3E-NU-GS geometry.

Uranium nitride (UN) is especially attractive for its high melting point and for having one of the higher uranium densities[70], and is currently being investigated[93] at AECL-Research for its compatibility in CANDU fuel. Of concern is its chemical reactivity in water. Another concern is the relatively high microscopic absorption cross-section[2] of nitrogen, almost four orders of magnitude greater than that of oxygen. As shown in Table 5.19, with natural uranium this leads to a subcritical lattice, despite the high density, and UN is therefore ruled out as an alternative to enrichment.

Uranium silicides (U_3Si_2, U_3Si) are another class of material that has been of interest to AECL-Research[94,95]. U_3Si_2 is chosen here for its higher melting point (1660 °C compared to 960 °C), although it is not as chemically compatible[70] with hydrogen and water as U_3Si. Silicon has a microscopic absorption cross-section almost three orders of magnitude greater than oxygen[2], but as Table 5.19 indicates, the higher uranium density is enough to allow a critical lattice. Unfortunately, the discharge burnup is only 7 GWd/Te, which falls far short of the 11 GWd/Te estimated to be required in this chapter. U_3Si_2 is therefore also ruled out as an alternative to enrichment, although it would require less enrichment if the two strategies were combined.

Uranium carbide (UC) is another material with high density (13.63 g/cm^3), but its rapid dissolution in hot water removes it from consideration in the CANDU core, although it is a candidate fuel for gas-cooled reactors[70].

It is concluded, therefore, that U-235 enrichment is the best strategy for decreasing the fuel throughput and thermal flux requirements of the nested tubular fuel geometry developed in this chapter.

5.11 Differential Enrichment

In Chapter 4 a significant reduction in the void effect was achieved through a radial distribution of U-235 enrichment, placing more U-235 near the pressure tube wall and less near the centre of the fuel channel. This strategy is now applied to Case 3E-EU-GS, which used 1.1 %wt enriched fuel to achieve suitable fuel throughput and thermal

flux conditions.

The case studied here is designated "3E-DE-GS" — three-element, differential enrichment, graphite spacer. It also has an average fuel enrichment of 1.1 %wt, but achieved with the following distribution: 0.20 %wt in the inner fuel element, 0.72 % (natural UO_2) in the middle fuel element, and 1.91 %wt in the outer fuel element. As a consequence of this strategy the distribution of power production across the fuel has been altered significantly, and the 3E-NU-GS geometry is no longer the optimum one. However, as a preliminary analysis this mismatch can be ignored and the neutronic affect of using differential enrichment can be observed.

The results of Case 3E-DE-GS are compared with Case 3E-EU-GS in Table 5.20, and it is clear that this strategy, as with the reference geometry, is successful. While criticality and burnup are not affected, both $\Delta k_{eff,V}$ and $\Delta\rho_V$ are reduced by about half at zero-burnup, and by about 80% (to almost zero) at mid-burnup. The void effect using critical bucklings is negative at both burnup values.

With the S/V Resonance Correction Model applied, the values of $\Delta k_{eff,V}$ at zero and mid-burnup are 10.0 mk and 6.8 mk, respectively. The values of $\Delta\rho_V$ at zero and mid-burnup are 6.1 mk and 6.0 mk, respectively.

Table 5.20 indicates a significant radial variation in the estimated heat flux ratios compared with the reference cell, caused by the distributed enrichment. The high heat flux ratio of the outer element is unacceptable and the entire geometry search process must be recalculated using the adjusted power distribution of this enrichment strategy. The degree of success of such a strategy, however, is indicated by a comparison with

identical geometries as in Table 5.20.

The geometry search was recalculated using the approximation in Equation (5.22) for element power fraction, in place of Equation (5.14),

$$\frac{P_k}{P_{\mathrm{TOT}}} \approx \frac{V_k E_k}{V_{\mathrm{TOT}} E_{\mathrm{AVG}}} \quad , \tag{5.22}$$

where E_k is the enrichment of element k, and E_{AVG} is the average module enrichment. The average enrichment chosen was 0.72 %wt, or natural abundance, and a MOX case (0.3 %wt PuO_2) was calculated based on the successful geometry with largest fuel volume. This case, with slightly higher fuel volume than the 3E-NU-GS geometry, is designated "3E-MOX-DE-GS" — three-element, MOX fuel, differentially enriched UO_2, graphite coolant spacer. The fuel is a mixture of 0.3 %wt PuO_2 and depleted or enriched UO_2 with the following distribution, from the inside out: Element 1, 0.40 %wt U-235; Element 2, 0.65 %wt U-235; Element 3, 1.00 %wt U-235. Case 3E-MOX-DE-GS is illustrated to scale in Figure 5.28 and described fully in Table 5.21.

Table 5.22 compares the calculated results of this case with the MOX case using natural UO_2, 3E-MOX-GS. Although fuel volume does not vary much between the two cases, the geometries are quite different (compare Figure 5.14 and Figure 5.28) and hence the results in Table 5.22 are not the pure result of differential enrichment. However, it can be assumed that the geometry effect is minor. Compared to 3E-MOX-GS, the void effect using differential enrichment is reduced by 35% at zero-burnup and 50% at mid-burnup. With critical bucklings the void effect is highly negative at zero-burnup and effectively zero at mid-burnup. Estimated fuel throughput is 90% of the reference cell

for both cases.

With the S/V Resonance Correction Model applied, the values of $\Delta k_{eff,V}$ at zero and mid-burnup are 11.2 mk and 7.6 mk, respectively. The values of $\Delta\rho_V$ at zero and mid-burnup are both 7.6 mk.

5.12 Zirconium Enrichment

The use of zirconium alloys highly enriched in Zr-90 was estimated in Section 4.3 to reduce the void effect in the reference lattice cell by 3 mk. This strategy can be expected to have the same general effect on the cases discussed in this chapter, and a survey of such results is given in Table 5.23.

Several observations can be made from these results. Generally, void effects for all cases are reduced by a constant value of about 3 mk. Discharge burnup is increased for Case 3E-NU-GS to 9.7 GWd/Te, but this is still lower than the 11 GWd/Te estimated to be needed for adequate fuel throughput. The same is true for the case using U_3Si_2 fuel. The case using UN fuel has increased criticality, but is still subcritical.

Three cases of interest are singled out for further analysis, including a look at mid-burnup results. These are Case 3E-EU-GS (1.1 %wt UO_2 fuel), Case 3E-MOX-GS (0.3 %wt PuO_2 mixture with natural UO_2), and Case 3E-MOX-DE-GS (same as the previous case, but with differential enrichment). The results for the first two are listed in Table 5.24, where the designation "EZ", for "enriched zirconium", has been added to their case names. The void effects using geometric bucklings for each of these two cases

is about zero at mid-burnup, and slightly negative using critical bucklings.

The third case of interest, designated "3E-MOX-DE-EZ-GS", is considered separately in Table 5.25 since it actually represents a "cumulative case" accounting for all the successful strategies discussed thus far: three-element nested tubular geometry, 0.3 %wt MOX with differentially enriched UO_2, 99 %wt Zr-90 enriched zirconium alloys, and a graphite coolant spacer. Within the approximations used to simulate these strategies, and within the approximations of the lattice cell method in general, this case represents the "best" result of this project.

The void effect of Case 3E-MOX-DE-EZ-GS ranges from slightly positive to slightly negative at mid-burnup (with the exception of the highly negative value using critical bucklings at zero-burnup, a result of the high excess supercriticality at this point). Discharge burnup is about 14 GWd/Te and estimated fuel throughput is 80% of the reference case.

With the S/V Resonance Correction Model applied, the values of $\Delta k_{eff,V}$ at zero and mid-burnup for Case 3E-MOX-DE-EZ-GS are 8.6 mk and 5.6 mk, respectively. The values of $\Delta\rho_V$ at zero and mid-burnup are both 4.0 mk.

5.13 Summary of Chapter

The development of the nested tubular concepts described in this chapter began with an optimum geometry search based solely on void effect. With fuel volume as the only constraint, this exercise determined that locating all fuel in an annular region next

to the pressure tube wall produced the lowest void effect. The two major factors leading to this geometry were: (1) locating the fuel in the region of smallest thermal flux change upon voiding; and (2) reducing the S/V ratio of the fuel to reduce the importance of resonance absorption. A reduction of 13 mk in the void effect, or about 33% of the reference cell value, was achieved with this strategy.

Several steps were then taken to develop a more practical design, beginning with subdivision of this relocated fuel to permit adequate cooling. At the same time a central coolant spacer was added to increase flow around the fuel, with the added neutronic benefit of reducing the void effect to about 25% of the reference cell value. The subdivision created a nested tubular geometry, and the number, size, and spacing of these nested elements were determined by a numerical search. The parameters used in this search were: maximum fuel temperature, total coolant flow rate and pressure drop, the ratio of subchannel flow rate to power deposition, and surface heat flux. Fuel volume was left as a variable.

The result was a three-element nested tubular design (Case 3E-NU-GS) with a zero-burnup void effect at 45% of the reference case, and 20% at mid-burnup. This design is characterized, like all subsequent designs in this chapter, by a significantly lower fuel volume compared to the reference cell, and also by lower burnup. The combination makes Case 3E-NU-GS unacceptable for reasons of fuel throughput and necessary thermal flux levels, and these problems were solved by enriching the UO_2 fuel (Case 3E-EU-GS). This case had little change in the void effect, but almost a three-fold increase in discharge burnup. It is worth noting that the move to a nested tubular geometry

removed the gains made in reducing the S/V ratio by relocating the fuel near the pressure tube wall.

With the neutronic aspects addressed, several practical concerns remained. The nested tubular design, as shown in Figure 5.14, presents problems of adequate coolant mixing and turbulence, as well as the possibility of subchannel blockage due to fuel swelling. Modifications were suggested, including subchannel interconnections, turbulence-inducing attachments, and strategically located element spacers, which deal with these concerns without significant detriment to the neutronic goals. Other practical concerns addressed were the manufacturing of the tubular fuel elements and the material used in the central coolant spacer. It was concluded that neither aspect presented an insurmountable technical obstacle to the design.

Several questions about the modelling process with WIMS-AECL were raised, beginning with the calculation of resonance cross-sections. A correction was applied to the WIMS-AECL model which would make it account properly for the surface-to-volume ratio of the fuel, and this modification caused a significant increase in the void effect. The results of this correction are questionable, however, since a comparison between the uncorrected result and that of a Monte Carlo code was favourable in terms of the void effect (although criticality showed a significant discrepancy). An estimation of the effect on neutron lifetime, and thus the characteristic kinetics parameter $(\rho-\beta)/\Lambda$, did not indicate a major deviation from the reference case results. Finally, several WIMS-AECL input parameters, including the cross-section library, were changed without raising any doubts about the methodology used in the design approximations.

Attention then turned to alternate fuel cycles, with the goal of either reducing the void effect further or eliminating the need for fuel enrichment. A 0.3 %wt PuO_2 MOX fuel case (3E-MOX-GS) decreased the zero-burnup void effect another 2 mk, at the same time extending burnup sufficiently to meet the fuel throughput criterion. With critical bucklings the void effect was highly negative at zero-burnup, while at mid-burnup all measures of void effect are the same as with natural UO_2 fuel. The question of the necessary magnitude of thermal flux levels remains with this case, however, since although reactivity is higher than the natural UO_2 case, the fissile mass in the lattice cell is still lower than in the reference cell. A related fuel cycle, DUPIC, was tested for compatibility with the goals of this design, and was successful despite a slightly higher void effect. Two higher uranium density fuels, UN and U_3Si_2, were determined to be unsatisfactory for reasons of low criticality and high fuel throughput, respectively, although the void effect was estimated to be higher in each case also.

Differential enrichment, using depleted uranium in the inner element, natural uranium in the middle element, and enriched uranium in the outer element, decreased the mid-burnup void effect by 80% compared to the uniformly enriched (1.1 %wt) case, although geometry was not altered and the case was thus not compatible with the criterion for acceptable heat fluxes. A differentially enriched MOX case meeting this criterion (3E-MOX-DE-GS), having an average module enrichment 0.72 %wt, showed a 33% reduction in the zero-burnup void effect compared to the uniformly enriched MOX case. Its mid-burnup void effect was near zero.

Finally, the novel strategy of Zr-90 enrichment in the fuel channel materials (a

modification outside the goal of this thesis) was estimated to reduce the void effect, regardless of the design variant, by another 2 to 3 mk. Three cases were singled out for a closer examination, including a "cumulative case", 3E-MOX-DE-EZ-GS, utilizing MOX fuel, differential uranium enrichment, and enriched zirconium. This optimum scenario was calculated with geometric bucklings to have effectively no void effect at zero-burnup and a slightly negative void effect at mid-burnup. With critical bucklings the void effect is highly negative at zero-burnup and slightly negative at mid-burnup.

It is therefore concluded that the nested tubular geometry presented here is a feasible strategy for reducing the coolant void effect in the CANDU reactor. It is amenable to a variety of fuel cycle modifications that bring its neutronic and thermalhydraulic behaviour within acceptable limits, as well as extending some parameters beyond the nominal values of the current design. A plethora of practical concerns demand an extensive research and development programme, which will likely combine with a higher manufacturing cost to raise questions of economic viability. Such viability will be determined by accounting for both the benefits to be gained by this concept and the offsetting cost of new fuel cycles such as DUPIC. One of the goals of this dissertation, which was the defining of a low (or zero, or negative) void effect CANDU fuel option that preserves as much as possible the philosophy of neutron economy, appears to be achieved by the nested tubular design variants presented in this chapter. While it did become necessary to reduce neutron economy, evident in the slightly lower burnup values using natural UO_2 fuel, the compromise was kept to a minimum. The dominating requirement for fuel enrichment in these designs is the need to restore the

energy output of the fuel to nominal levels, due to the reduction in fissile mass. The reduction in neutron economy is a secondary factor here.

Final conclusions about the neutronic suitability of this new design concept requires analysis with a lattice code better suited to nested tubular geometries, particularly in the area of the resonance group cross-section treatment. In addition, full-core spatial analysis is needed to determine how well these cell calculations extrapolate to realistic conditions.

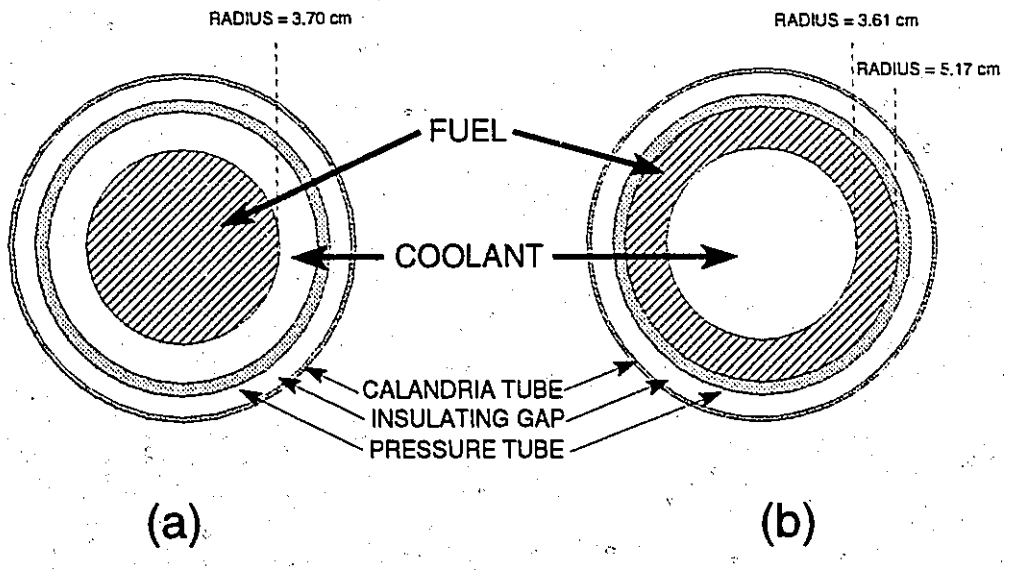

Figure 5.1 **Two Single Lump Fuel Geometries With Same Fuel Volume as in Reference Cell: (a) All Fuel at Centre; (b) All Fuel Near Pressure Tube.**

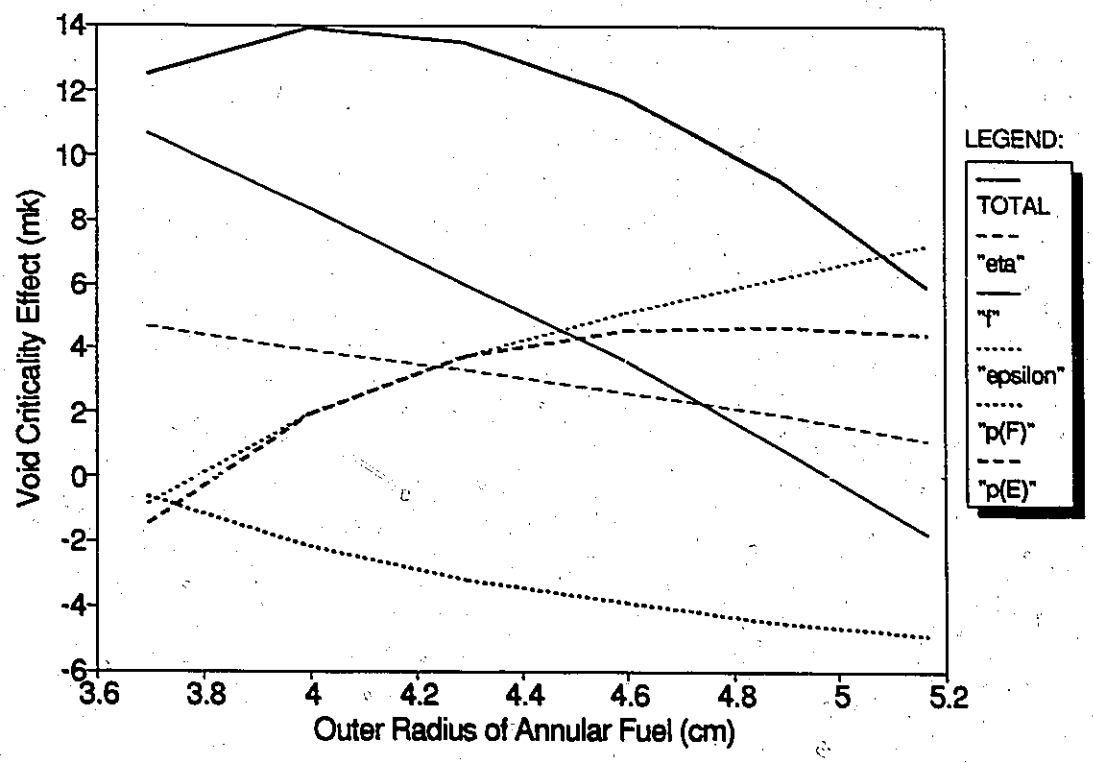

Figure 5.2 **Zero-Burnup Void Criticality Effect ($\Delta k_{eff,v}$) and Criticality Factor Contributions For a Single Lump of UO_2 Fuel With Same Volume as Reference Cell vs. Radial Position.**

Table 5.1 Zero-Burnup Void Effect and Criticality Factor Contributions for Single Lump Fuel Geometries at Centre and Outer Region of Fuel Channel, As Shown In Figure 5.1.

Criticality Factor	Reference 37-Element Cell		Single Lump at Centre (fuel vol. same as ref. cell)		Single Lump Near Pressure Tube (fuel vol. same as ref. cell)	
	$\Delta k_{eff,V}$ (mk)	$\Delta\rho_V$ (mk)	$\Delta k_{eff,V}$ (mk)	$\Delta\rho_V$ (mk)	$\Delta k_{eff,V}$ (mk)	$\Delta\rho_V$ (mk)
η	2.2	1.8	4.7	3.9	1.1	0.9
f	3.9	3.3	10.7	8.8	−1.8	−1.5
p_F	−3.8	−3.2	−0.6	−0.5	−4.9	−4.0
p_E	11.7	9.9	−1.5	−1.2	4.4	3.6
ϵ	5.2	4.4	−0.9	−0.7	7.2	5.8
TOTAL EFFECT	19.3	16.3	12.5	10.2	5.9	4.8
Size of S/V ratio compared to reference cell	100%		16%		39%	

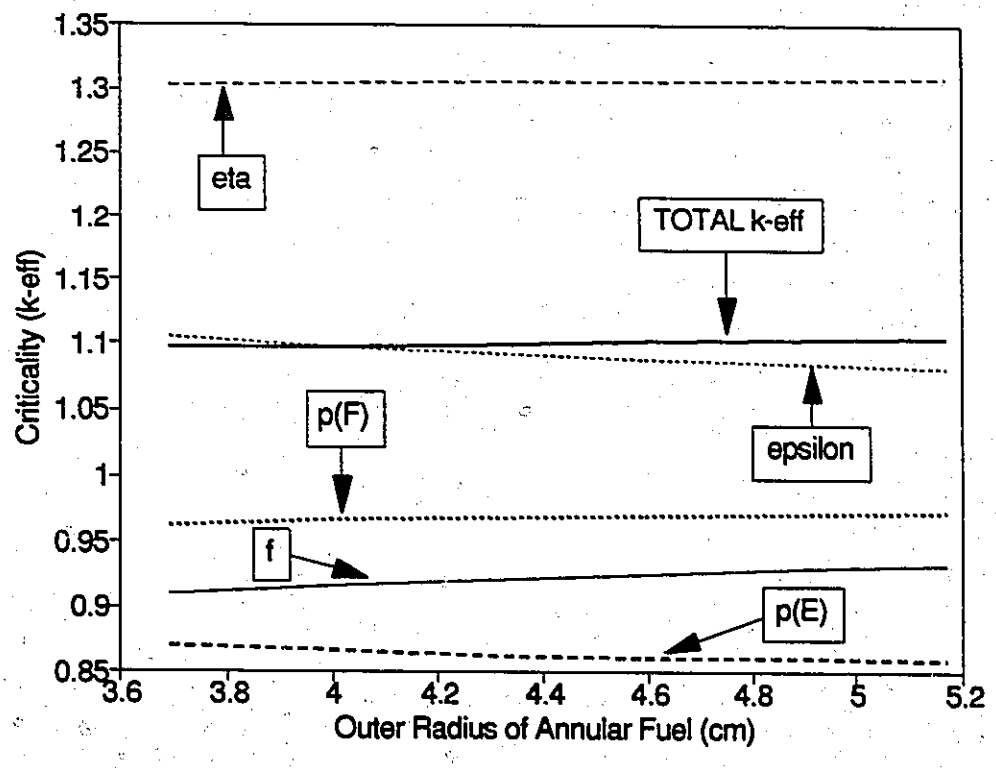

Figure 5.3 Zero-Burnup Criticality (k_{eff}) and Criticality Factors for a Single Annular Lump of UO_2 Fuel (Non-Voided Case) With Same Volume as Reference Cell vs. Radial Position.

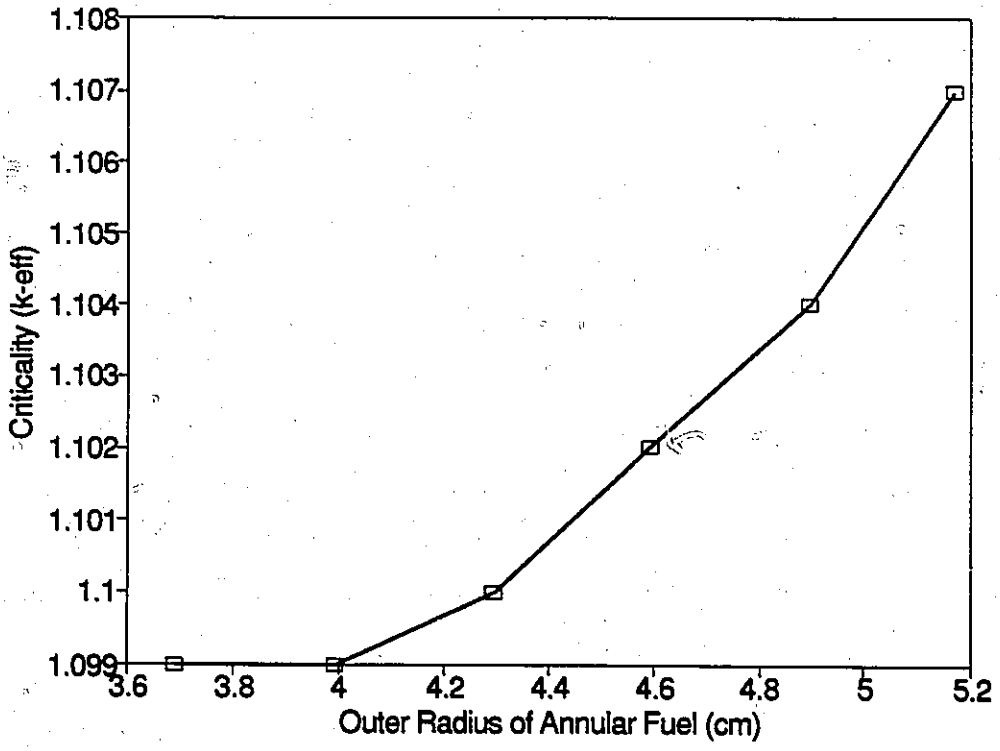

Figure 5.4 Zero-Burnup Criticality (k_{eff}) for Single Annular Lump vs. Position.

Table 5.2 Zero-Burnup Criticality (k_{eff}) and Criticality Factors for Single Lump Fuel Geometries at Centre and Outer Region of Fuel Channel, As Shown In Figure 5.1.

Criticality Factor	Reference 37-Element Cell	Single Lump at Centre (fuel vol. same as ref. cell)	Single Lump Near Pressure Tube (fuel vol. same as ref. cell)
η	1.307	1.303	1.309
f	0.918	0.910	0.934
p_F	0.972	0.964	0.973
p_E	0.849	0.870	0.859
ϵ	1.088	1.106	1.083
TOTAL k_{eff}	1.078	1.099	1.107
Reduction in S/V compared to reference cell	0%	84%	61%

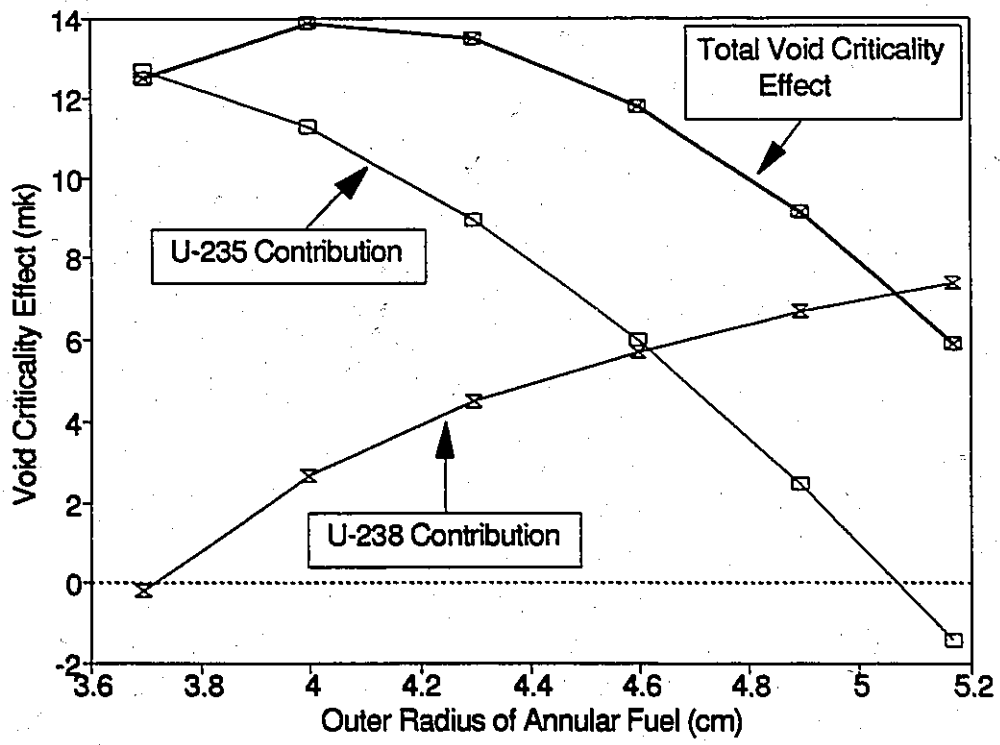

Figure 5.5 **Void Criticality Effect ($\Delta k_{eff,v}$) For a Single Lump of UO_2 Fuel With Same Volume as Reference Cell vs. Radial Position: Contributions From Fissile Fuel Isotopes (Zero-Burnup).**

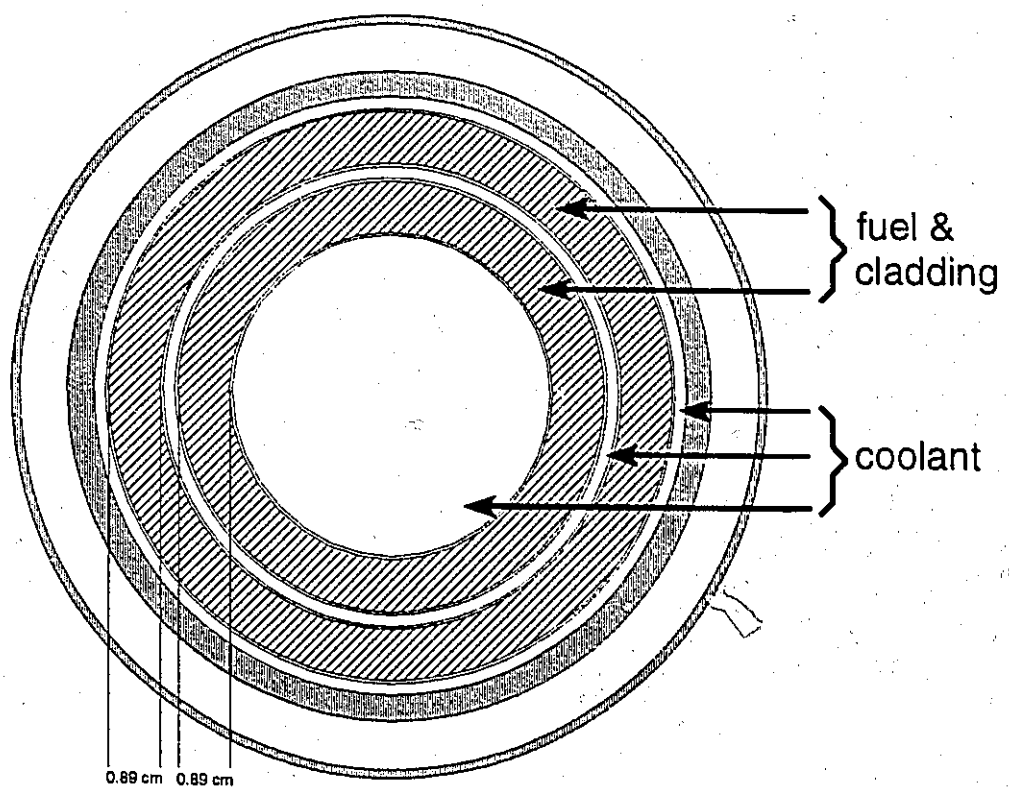

Figure 5.6 Nested Tubular Fuel Geometry With Two Concentric Tubes of Equal Radial Thickness, and Total Fuel Volume Same as Reference Lattice Cell.

Table 5.3 Zero-Burnup Void Effect, Criticality Factor Contributions, and k_{eff} for Two-Element Nested Tubular Design of Figure 5.6, Compared With Single Lump Annular Geometry at Outer Region of Fuel Channel.

Criticality Factor	Single Lump Near Pressure Tube, No Cladding (fuel vol. same as ref. cell)		Two-Ring Nested Annular Design, With Cladding (fuel vol. same as ref. cell)	
	$\Delta k_{eff,V}$ (mk)	$\Delta\rho_V$ (mk)	$\Delta k_{eff,V}$ (mk)	$\Delta\rho_V$ (mk)
η	1.1	0.9	1.5	1.3
f	−1.8	−1.5	0.7	0.6
p_F	−4.9	−4.0	−4.3	−3.5
p_E	4.4	−3.6	5.1	4.2
ϵ	7.2	5.8	6.1	5.0
TOTAL EFFECT	5.9	4.8	9.2	7.6
k_{eff}	1.107		1.096	
Size of S/V ratio compared to reference cell	39%		69%	

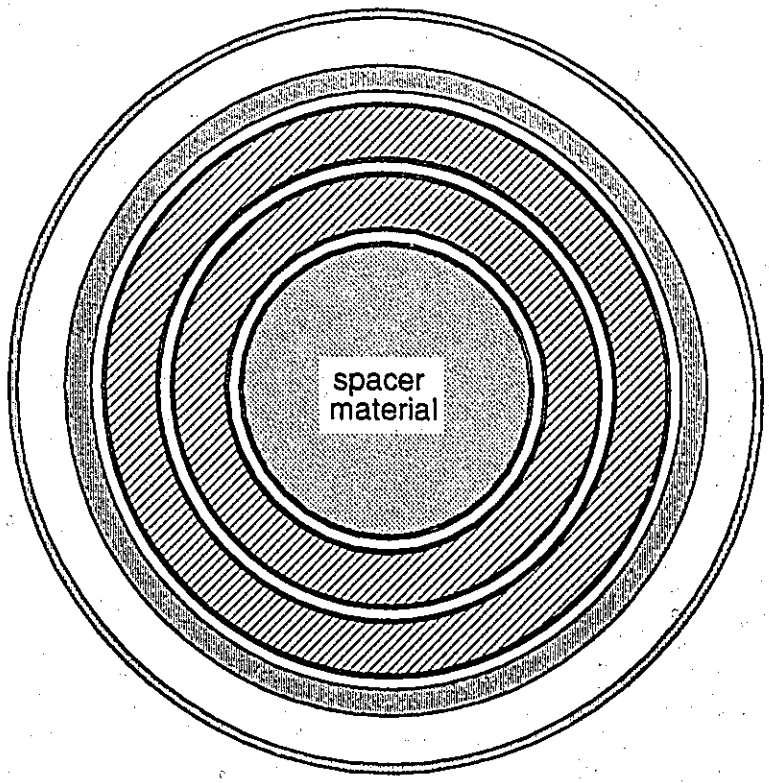

Figure 5.7 Two-Element Nested Tubular Geometry With Central Spacer of Radius 2.59 cm, Including 0.5 mm Zircaloy Cladding. All Coolant Subchannels Are of Thickness 2.0 mm.

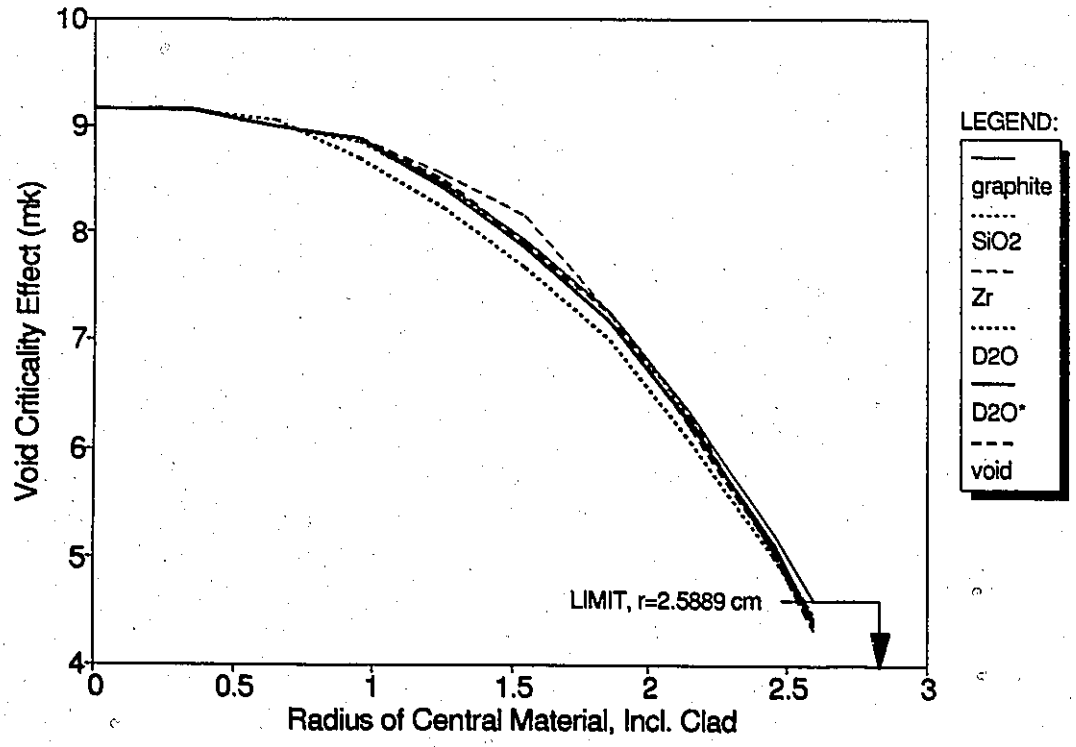

Figure 5.8 **Zero-Burnup Void Criticality Effect ($\Delta k_{eff,V}$) vs. Radius of Central Spacer Material: Five Different Materials ("D_2O*" and "void" Are Within Zirconium-2.5% Nb Tube, Same Thickness as Pressure Tube; All Others Are Within 0.5 mm Zircaloy Cladding).**

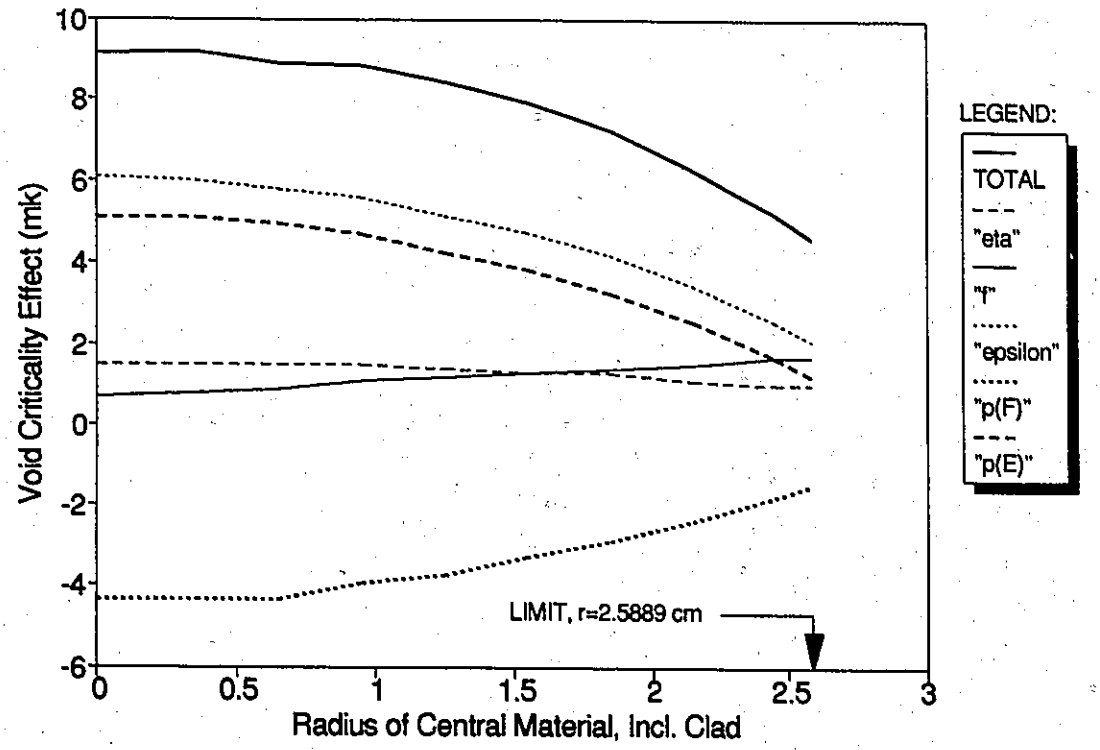

Figure 5.9 **Zero-Burnup Void Criticality Effect ($\Delta k_{eff,V}$) and Criticality Factor Contributions vs. Radius of Central Graphite Spacer With 0.5 mm Zircaloy Cladding.**

Table 5.4 Zero-Burnup Void Effect, Criticality Factor Contributions, and k_{eff} for Two-Element Nested Tubular Fuel With and Without Graphite Spacer (With 0.5 mm Cladding) at Largest Diameter, 2.59 cm.

Criticality Factor	No Graphite Spacer (fuel vol. same as ref. cell)		Graphite Spacer with Cladding, Total Diameter 2.59 cm (fuel vol. same as ref. cell)	
	$\Delta k_{eff,V}$ (mk)	$\Delta\rho_V$ (mk)	$\Delta k_{eff,V}$ (mk)	$\Delta\rho_V$ (mk)
η	1.5	1.3	1.0	0.8
f	0.7	0.6	1.7	1.4
p_F	−4.3	−3.5	−1.5	−1.2
p_E	5.1	4.2	1.2	1.0
ϵ	6.1	5.0	2.1	1.7
TOTAL EFFECT	9.2	7.6	4.6	3.8
k_{eff}	1.096		1.098	
Coolant flow area compared to reference cell	100%		43%	

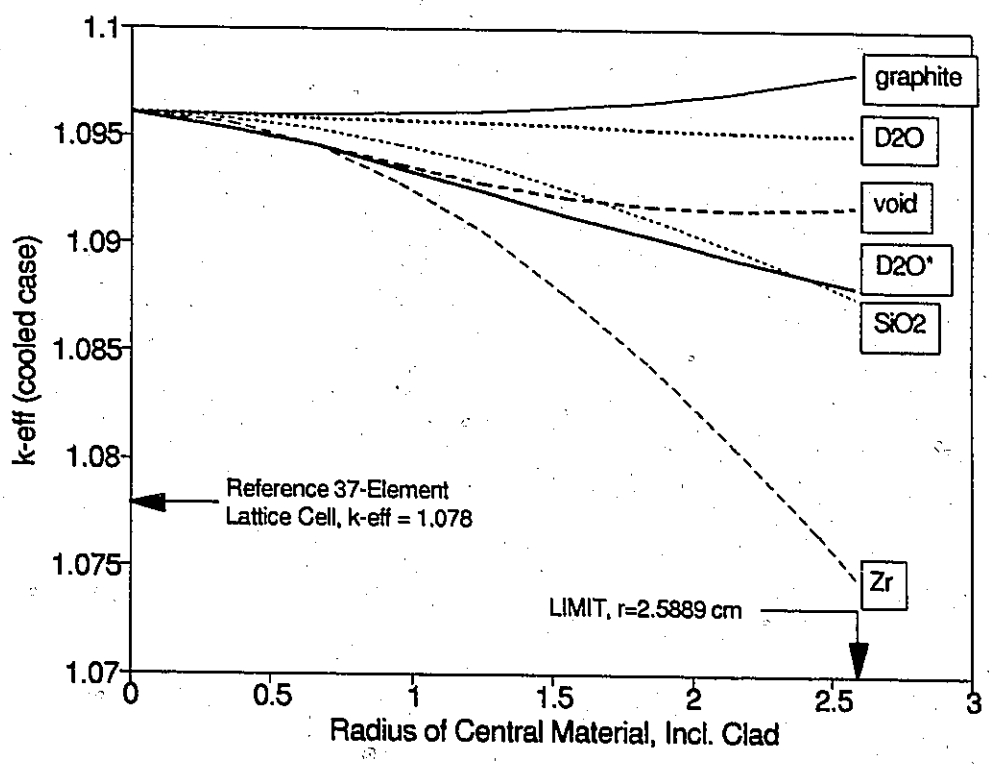

Figure 5.10 **Zero-Burnup Criticality (Cooled Case) vs. Radius of Central Spacer Material: Five Different Materials ("D_2O*" and "void" Are Within Zirconium-2.5% Nb Tube, Same Thickness as Pressure Tube; All Others Are Within 0.5 mm Zircaloy Cladding).**

Table 5.5 Void Effect at Mid-Burnup for Six Different Materials ("D_2O*" and "void" Are Within Zirconium-2.5% Nb Tube, Same Thickness as Pressure Tube; All Others Are Within 0.5 mm Zircaloy Cladding)

Spacer Material	Predicted Discharge Burnup (MWd/Te) (REFERENCE CELL: 7500 MWd/Te)	Void Effect	
		$\Delta k_{eff,V}$ (mk)	$\Delta\rho_V$ (mk)
graphite	9190	2.3	2.2
SiO_2	8160	2.3	2.2
Zircaloy-4	6720	2.2	2.1
D2O	8160	2.5	2.4
D2O*	8000	2.6	2.5
void	8320	2.3	2.2

Table 5.6 Search Boundaries and Criteria.

Test Parameter		Criterion
Description	Formula	
Max. fuel temperature, minus clad-coolant ΔT	$T_{max} = T_{cool} + \Delta T_{clad} + \Delta T_{fuel}$	≤ 2000 °C
Min. subchannel width	$(\Delta r_S)_{min}$	0.1 cm
Max. relative deviation between relative flow rate and relative power deposition in each subchannel	$\frac{\lvert \hat{P}_j - \hat{W}_j \rvert}{\hat{W}_j}$	0.02
Min. fuel element thickness	$(\Delta r_F)_{min}$	0.3 cm
Max. relative deviation between flow area of test and reference geometry	$\frac{\lvert A_C^{test} - A_C^{ref} \rvert}{A_C^{ref}}$	0.02
Max. ratio of pressure drops for test and reference cell	$\frac{\Delta p_{test}}{\Delta p_{ref}}$	≤ 1.1
Max. ratio of fuel element heat fluxes for test and reference cell	$\frac{q''_{k_{test}}}{q''_{RING\,4}}$	≤ 1.0

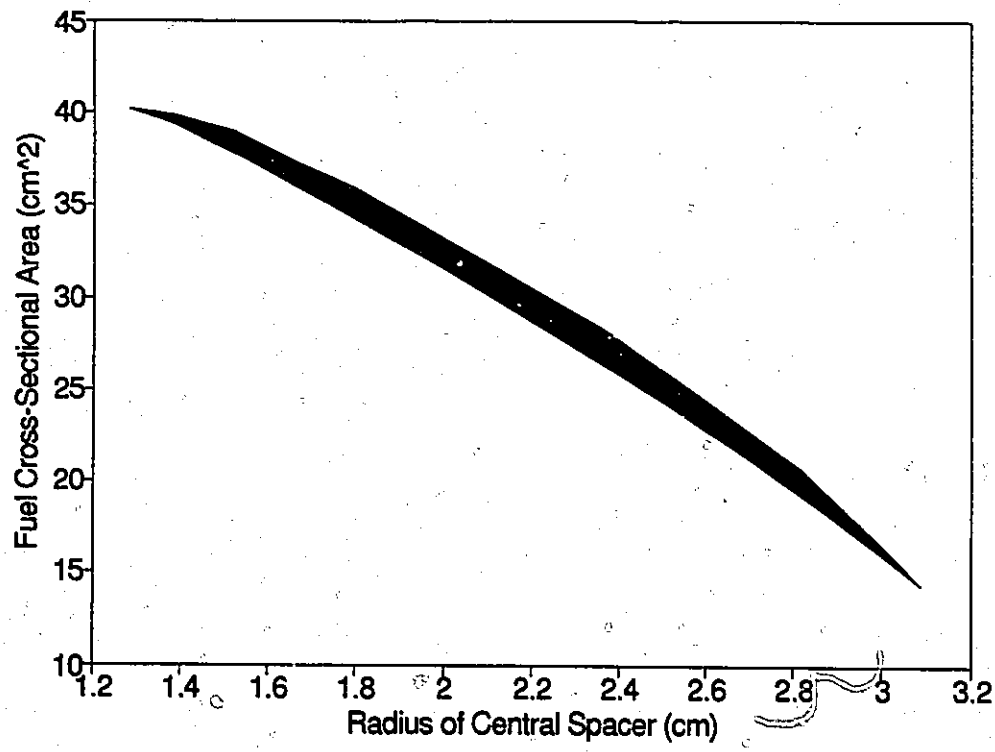

Figure 5.11 **Region of Criteria Satisfaction (except Maximum Heat Flux) for Two-Element Nested Tubular Fuel, Using Coordinates of Fuel Cross-Sectional Area and Central Spacer Radius.**

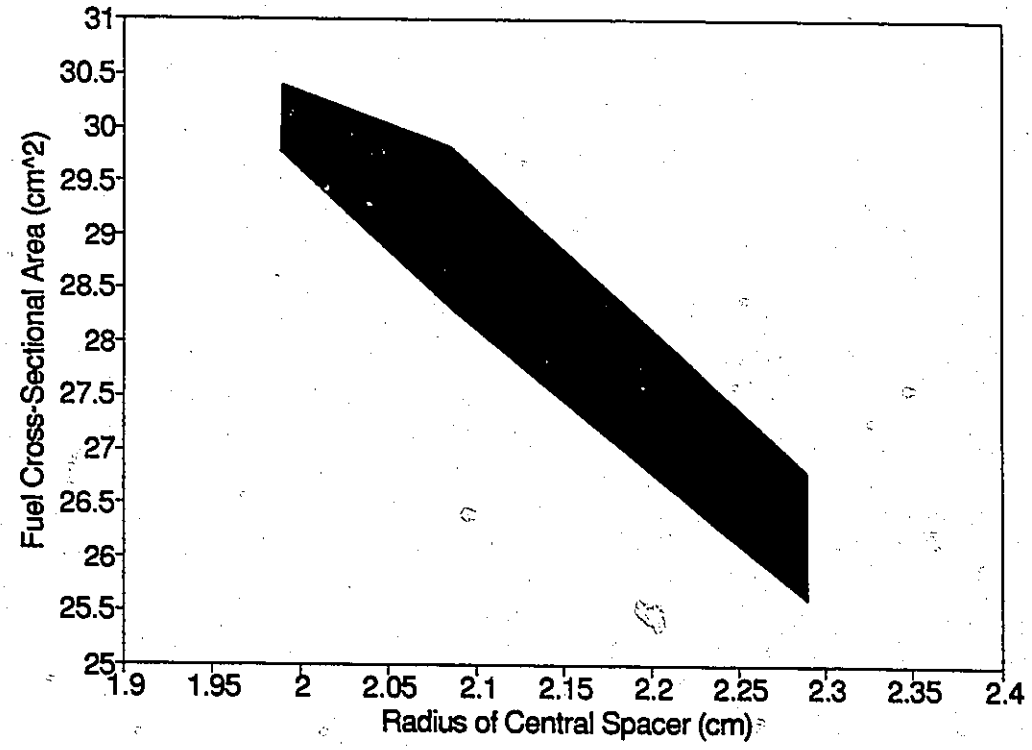

Figure 5.12 **Region of Criteria Satisfaction (Except Maximum Heat Flux) for Three-Element Nested Tubular Fuel, Using Coordinates of Fuel Cross-Sectional Area and Central Spacer Radius.**

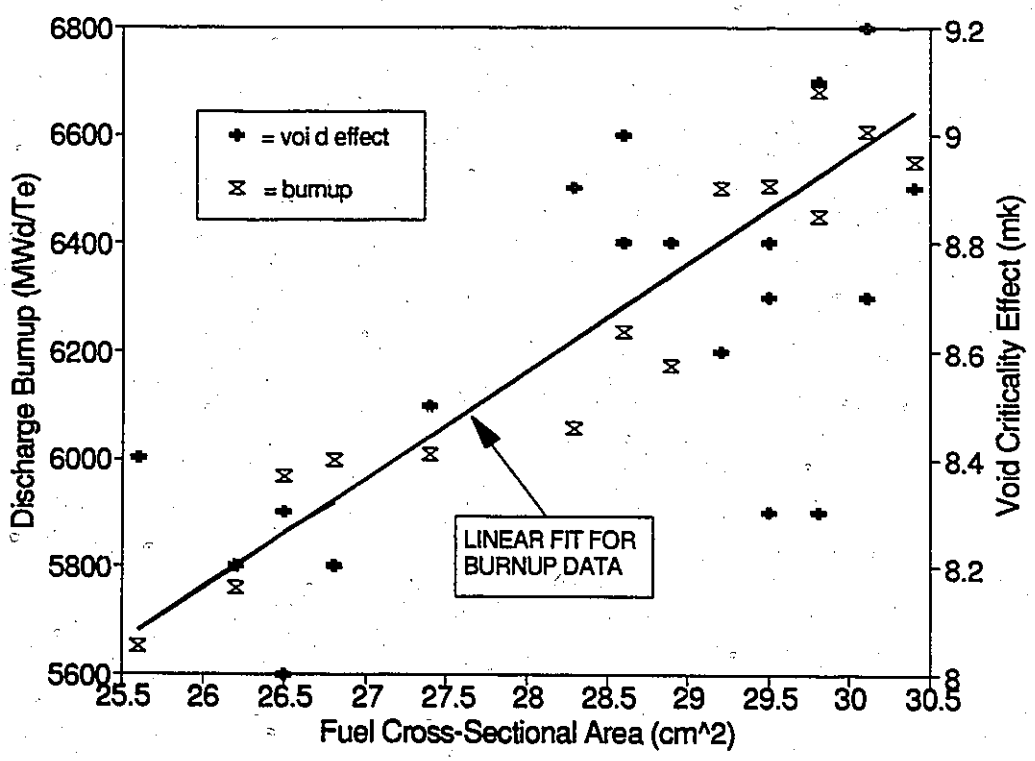

Figure 5.13 Discharge Burnup and Zero-Burnup Void Criticality ($\Delta k_{eff,v}$) as a Function of Fuel Cross-Sectional Area for a Three-Element Nested Tubular Design with Graphite Coolant Spacer.

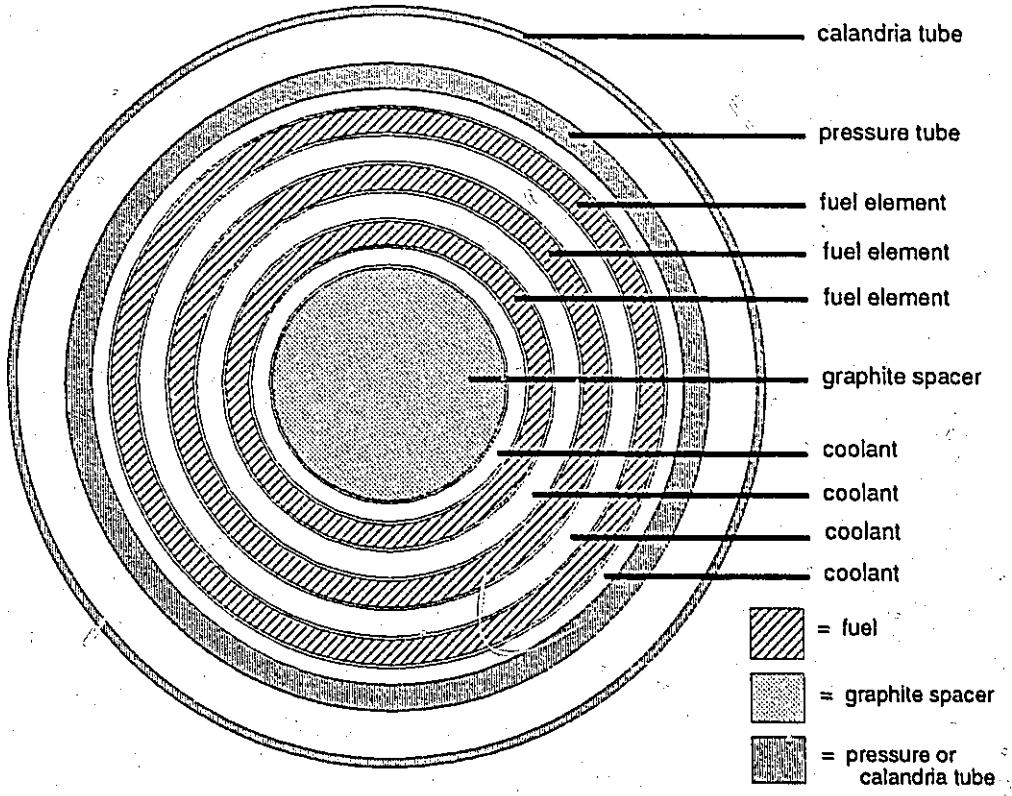

Figure 5.14 Geometry for Case 3E-NU-GS: Three-Element, Natural UO_2, Nested Tubular Fuel With Graphite Coolant Spacer.

Table 5.7 Specifications for Case 3E-NU-GS.

Specification	Value	Specification	Value
radius of graphite spacer	2.04 cm	inner radius of Element 3 cladding	4.36 cm
outside radius of spacer clad	2.09 cm	inner radius of Element 3 fuel meat	4.41 cm
inner radius of Element 1 cladding	2.40 cm	outer radius of Element 3 fuel meat	4.83 cm
inner radius of Element 1 fuel meat	2.45 cm	outer radius of Element 3 cladding	4.88 cm
outer radius of Element 1 fuel meat	2.86 cm	inner radius of pressure tube	5.17 cm
outer radius of Element 1 cladding	2.91 cm	total fuel cross-sectional area	29.2 cm^2
inner radius of Element 2 cladding	3.36 cm	width of Element 1 fuel meat	0.41 cm
inner radius of Element 2 fuel meat	3.41 cm	width of Element 2 fuel meat	0.44 cm
outer radius of Element 2 fuel meat	3.85 cm	width of Element 3 fuel meat	0.42 cm
outer radius of Element 2 cladding	3.90 cm	ratio of total fuel volume to ref. cell	68%

Table 5.8 Case 3E-NU-GS: Calculated Results Compared with Reference Lattice Cell.

Calculation	Reference Cell	3E-NU-GS
zero-burnup k_{eff} (cooled case)	1.078	1.086
zero-burnup $\Delta k_{eff,V}$	19.3 mk	8.6 mk
zero-burnup $\Delta \rho_V$	16.3 mk	7.2 mk
zero-burnup $\Delta k_{eff,V}$ with critical bucklings	15.9 mk	2.8 mk
mid-burnup k_{eff} (cooled case)	1.019	1.017
mid-burnup $\Delta k_{eff,V}$	14.1 mk	3.0 mk
mid-burnup $\Delta \rho_V$	13.3 mk	2.9 mk
mid-burnup $\Delta k_{eff,V}$ with critical bucklings	13.0 mk	1.7 mk
discharge burnup	7500 MWd/Te	6500 MWd/Te
estimated ratio of avg. heat flux for Element 1, to max. reference cell value	1.0	0.9
estimated ratio of avg. heat flux for Element 2, to max. reference cell value	1.0	1.0
estimated ratio of avg. heat flux for Element 3, to max. reference cell value	1.0	1.0
estimated ratio of pressure drop across fuel to that of reference cell	1.0	0.9
estimated ratio of fuel throughput to that of reference cell	1.0	1.7

Table 5.9 Case 3E-NU-GS: Summary of Total Void Effect and Criticality Factor Contributions for Zero-Burnup and Mid-Burnup Lattice.

Criticality Factor	Void Criticality Effect		Void Reactivity Effect		Void Effect, Critical Bucklings	
	Zero-Burnup (mk)	Mid-Burnup (mk)	Zero-Burnup (mk)	Mid-Burnup (mk)	Zero-Burnup (mk)	Mid-Burnup (mk)
η	2.4	−1.9	2.0	−1.8	2.2	−1.8
f	3.5	1.4	2.9	1.4	2.0	1.0
p_F	−3.1	−2.9	−2.6	−2.8	−4.4	−3.2
p_E	1.4	1.6	1.1	1.6	−1.5	1.0
ϵ	4.4	4.7	3.7	4.5	4.5	4.7
TOTAL EFFECT	8.6	3.0	7.2	2.9	2.8	1.7
k_{eff} (cooled case)	1.086	1.017	1.086	1.017	1.000	1.000

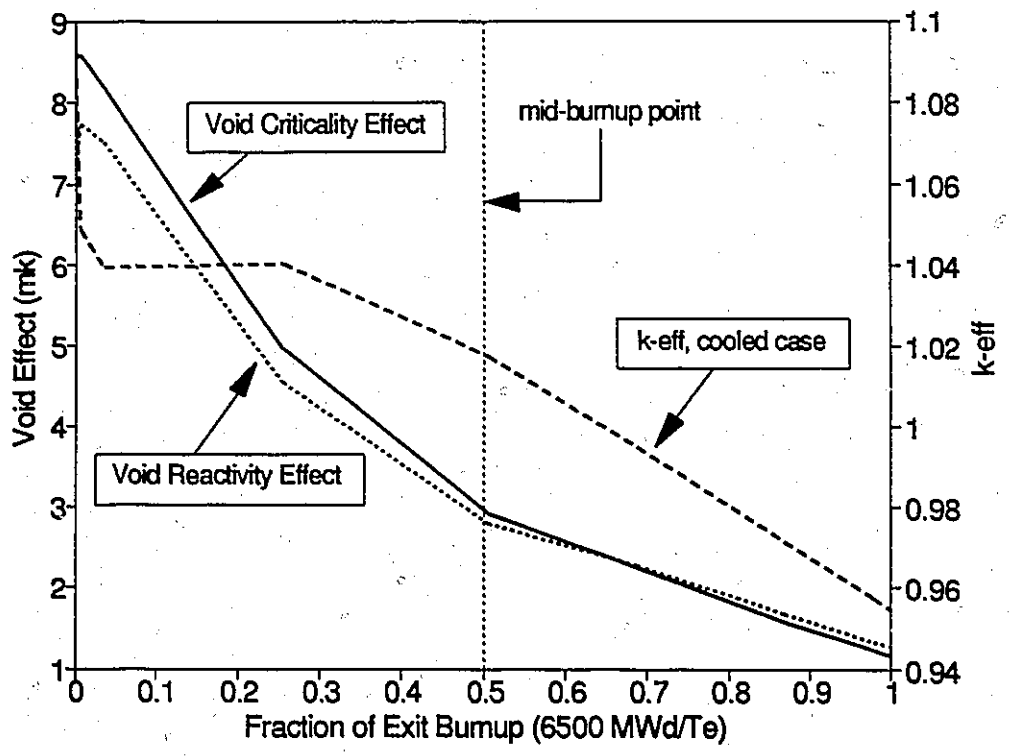

Figure 5.15 Case 3E-NU-GS: Void Reactivity Effect ($\Delta\rho_v$), Void Criticality Effect ($\Delta k_{eff,v}$), and k_{eff} (cooled case) vs. Burnup Fraction.

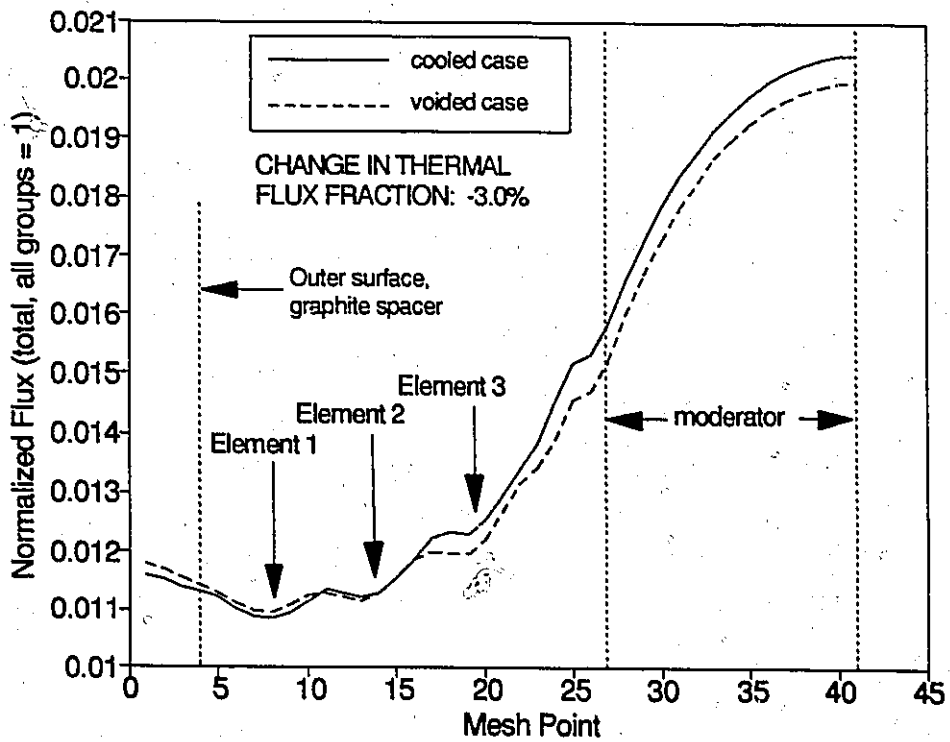

Figure 5.16 Case 3E-NU-GS: Normalized Spatial Distribution of Thermal Flux Across Mid-Burnup Lattice Cell for Cooled and Voided Cases.

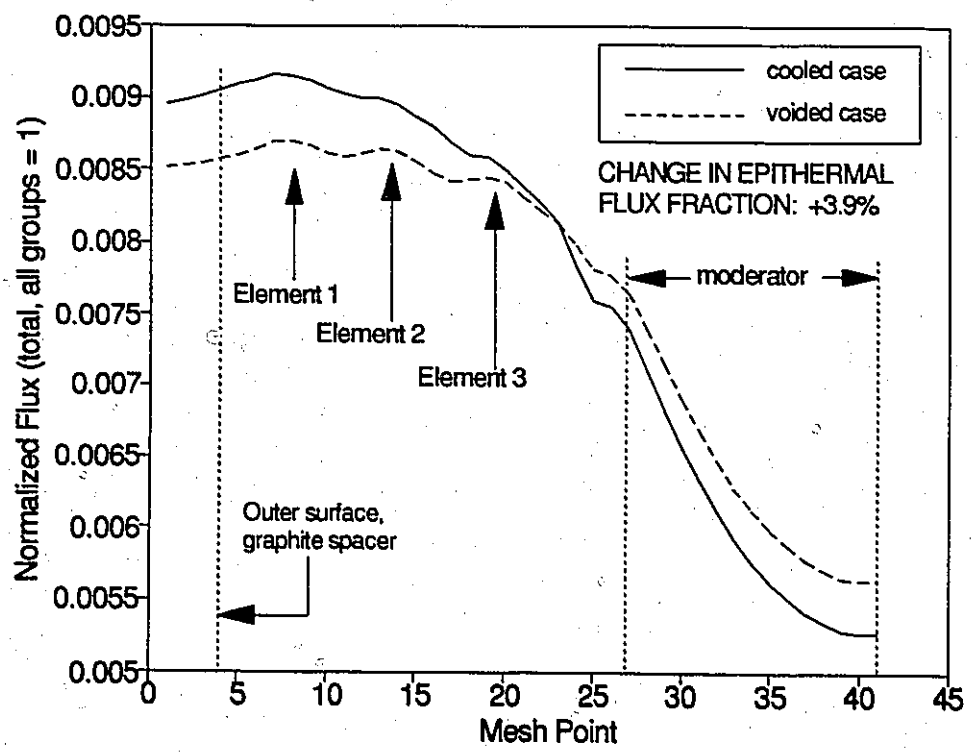

Figure 5.17 Case 3E-NU-GS: Normalized Spatial Distribution of Epithermal Flux Across Mid-Burnup Lattice Cell for Cooled and Voided Cases.

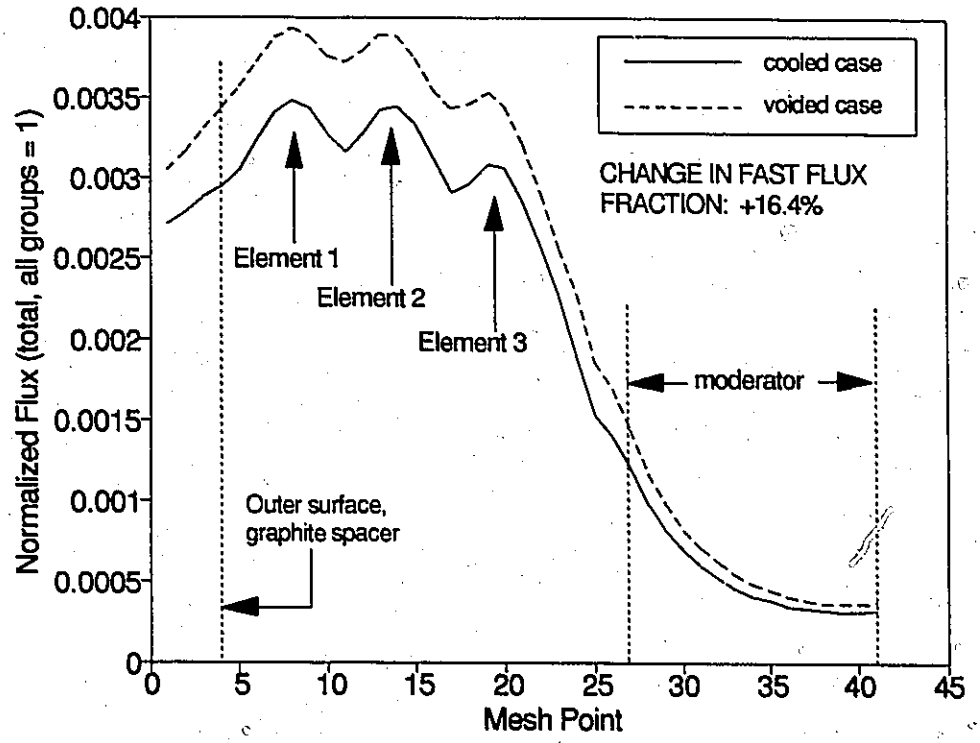

Figure 5.18 Case 3E-NU-GS: Normalized Spatial Distribution of Fast Flux Across Mid-Burnup Lattice Cell for Cooled and Voided Cases.

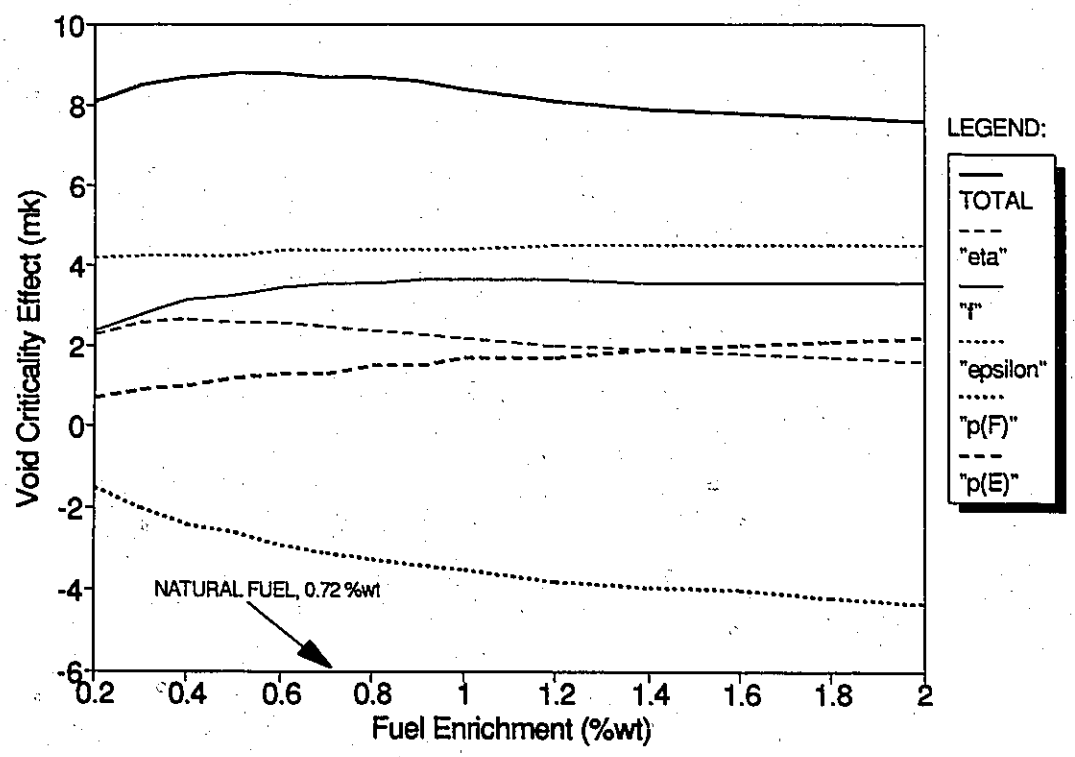

Figure 5.19 Effect of Enrichment on Case 3E-NU-GS: Zero-Burnup Void Criticality Effect and Criticality Factor Contributions.

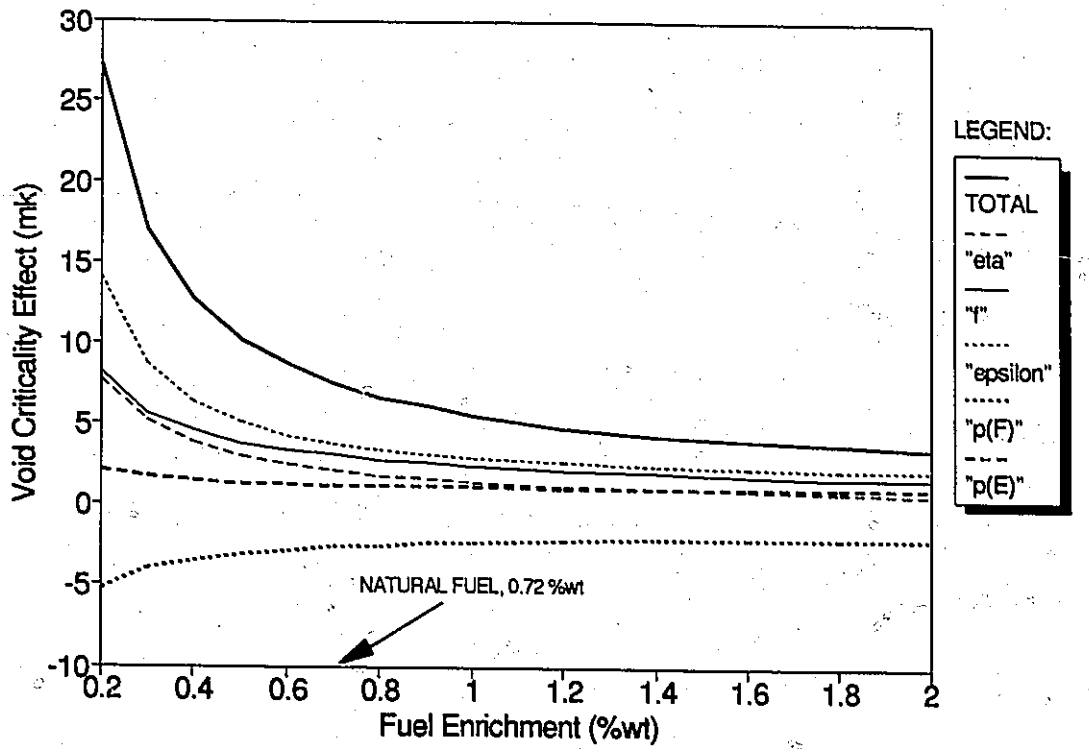

Figure 5.20 Effect of Enrichment on Case 3E-NU-GS: Zero-Burnup Void Reactivity Effect and Criticality Factor Contributions.

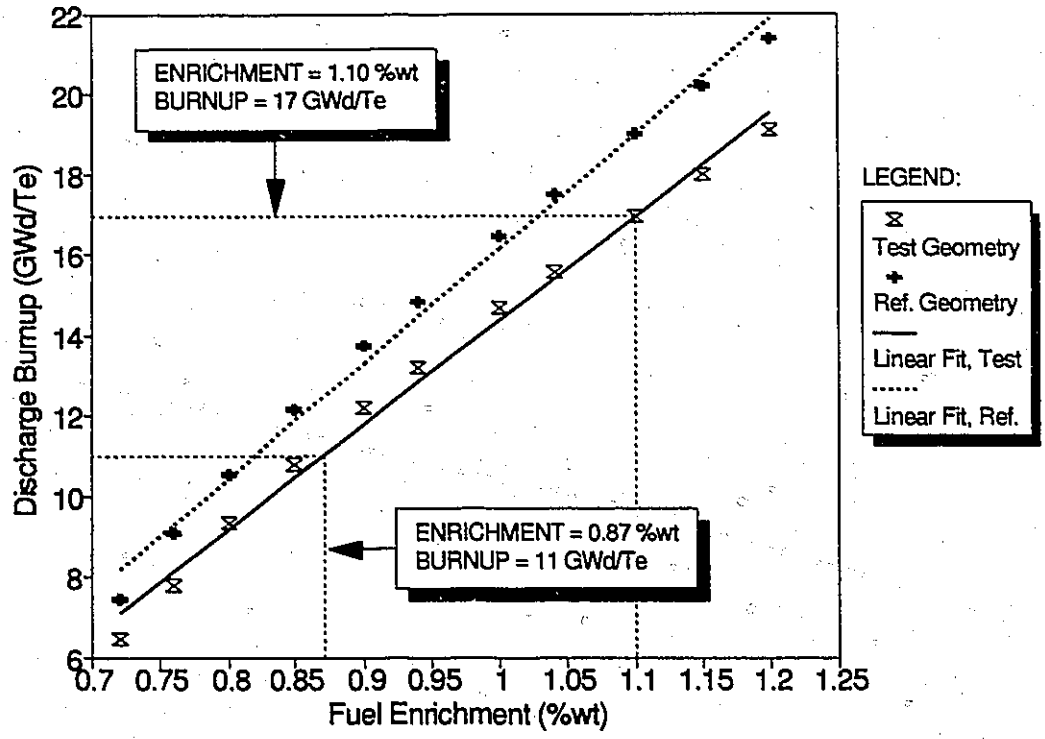

Figure 5.21 Discharge Burnup vs. Fuel Enrichment for 3E-NU-GS Geometry and Reference Cell Geometry, With Least-Squares Linear Fit.

Table 5.10 Case 3E-EU-GS: Calculated Results Compared with Reference Lattice Cell.

Calculation	Reference Cell	3E-EU-GS (1.1 %wt UO_2)
zero-burnup k_{eff} (cooled case)	1.078	1.263
zero-burnup $\Delta k_{eff,V}$	19.3 mk	8.4 mk
zero-burnup $\Delta \rho_V$	16.3 mk	5.2 mk
zero-burnup $\Delta k_{eff,V}$ with critical bucklings	15.9 mk	-8.0 mk
mid-burnup k_{eff} (cooled case)	1.019	1.022
mid-burnup $\Delta k_{eff,V}$	14.1 mk	3.2 mk
mid-burnup $\Delta \rho_V$	13.3 mk	3.1 mk
mid-burnup $\Delta k_{eff,V}$ with critical bucklings	13.0 mk	1.6 mk
discharge burnup	7500 MWd/Te	17000 MWd/Te
estimated ratio of avg. heat flux for Element 1, to max. reference cell value	1.0	0.9
estimated ratio of avg. heat flux for Element 2, to max. reference cell value	1.0	1.0
estimated ratio of avg. heat flux for Element 3, to max. reference cell value	1.0	1.0
estimated ratio of pressure drop across fuel to that of reference cell	1.0	0.9
estimated ratio of fuel throughput to that of reference cell	1.0	0.7

Table 5.11 Case 3E-EU-GS: Summary of Total Void Effect and Criticality Factor Contributions for Zero-Burnup and Mid-Burnup Lattice.

Criticality Factor	Void Criticality Effect		Void Reactivity Effect		Void Effect, Critical Buckings	
	Zero-Burnup (mk)	Mid-Burnup (mk)	Zero-Burnup (mk)	Mid-Burnup (mk)	Zero-Burnup (mk)	Mid-Burnup (mk)
η	2.2	−2.2	1.4	−2.1	1.7	−2.2
f	3.7	1.0	2.3	1.0	0.4	0.7
p_F	−3.7	−2.9	−2.3	−2.8	−8.1	−3.3
p_E	1.8	2.7	1.1	2.5	−7.0	1.8
ϵ	4.4	4.7	2.8	4.4	4.8	4.7
TOTAL EFFECT	8.4	3.2	5.2	3.1	−8.0	1.6
k_{eff} (cooled case)	1.263	1.022	1.263	1.022	1.000	1.000

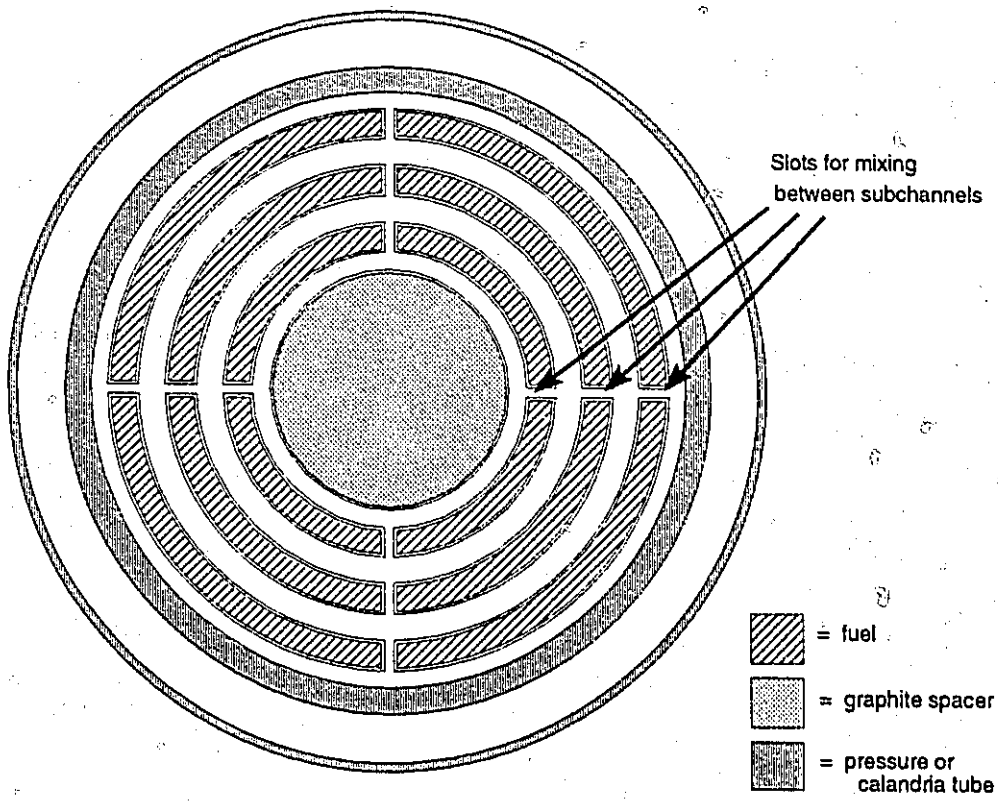

Figure 5.22 Conceptual Illustration of Three-Element Nested Geometry Modified to Allow Coolant Mixing Between Annular Subchannels. Actual Slots Would Require Rounded Edges.

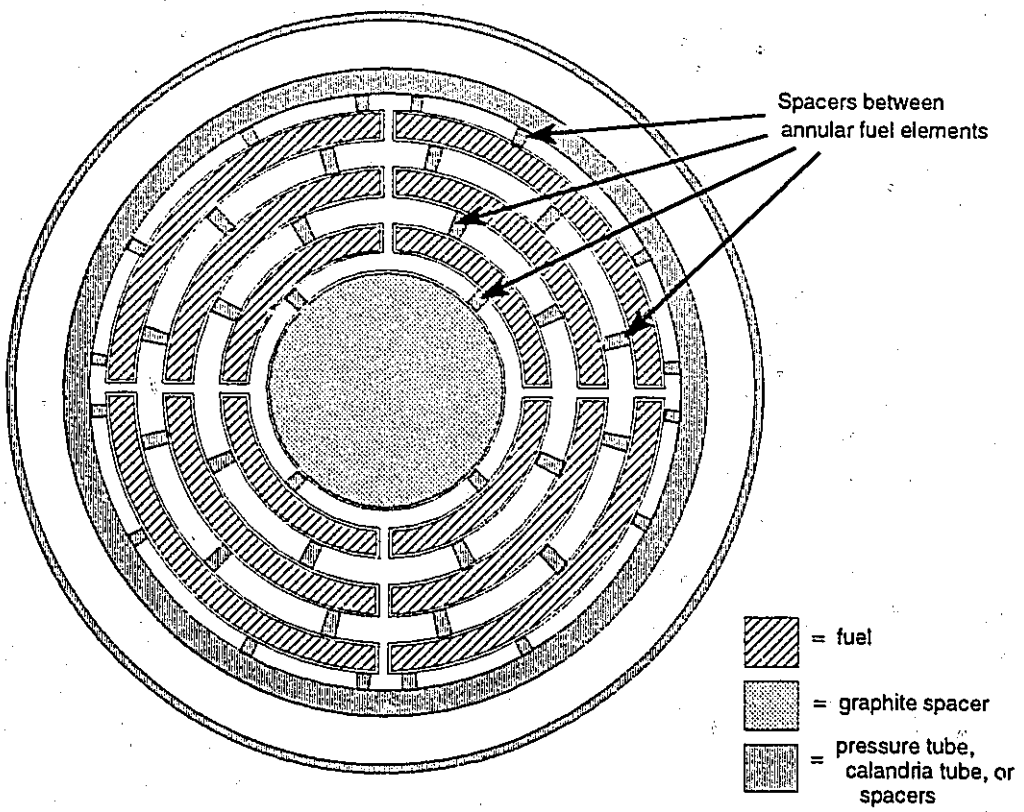

Figure 5.23 Conceptual Illustration of Three-Element Nested Geometry With Inter-Element Spacers to Prevent Subchannel Blockage.

Table 5.12 Zero-Burnup Void Criticality Effect ($\Delta k_{eff,v}$) and Discharge Burnup of Three-Element Nested Tubular Lattice Cell With Different Coolant Spacer Materials.

Spacer Material	Natural UO_2			1.1 %wt Enriched UO_2		
	Case	$\Delta k_{eff,v}$ (mk)	Discharge Burnup (MWd/Te)	Case	$\Delta k_{eff,v}$	Discharge Burnup (MWd/Te)
Graphite	3E-NU-GS	8.6	6500	3E-EU-GS	8.4	17000
Zircaloy 4	3E-NU-ZS	8.0	4000	3E-EU-ZS	7.7	15500
SiO_2	3E-NU-QS	8.1	5600	3E-EU-QS	8.0	16400
SiC	3E-NU-SS	8.3	4600	3E-EU-SS	7.5	15900

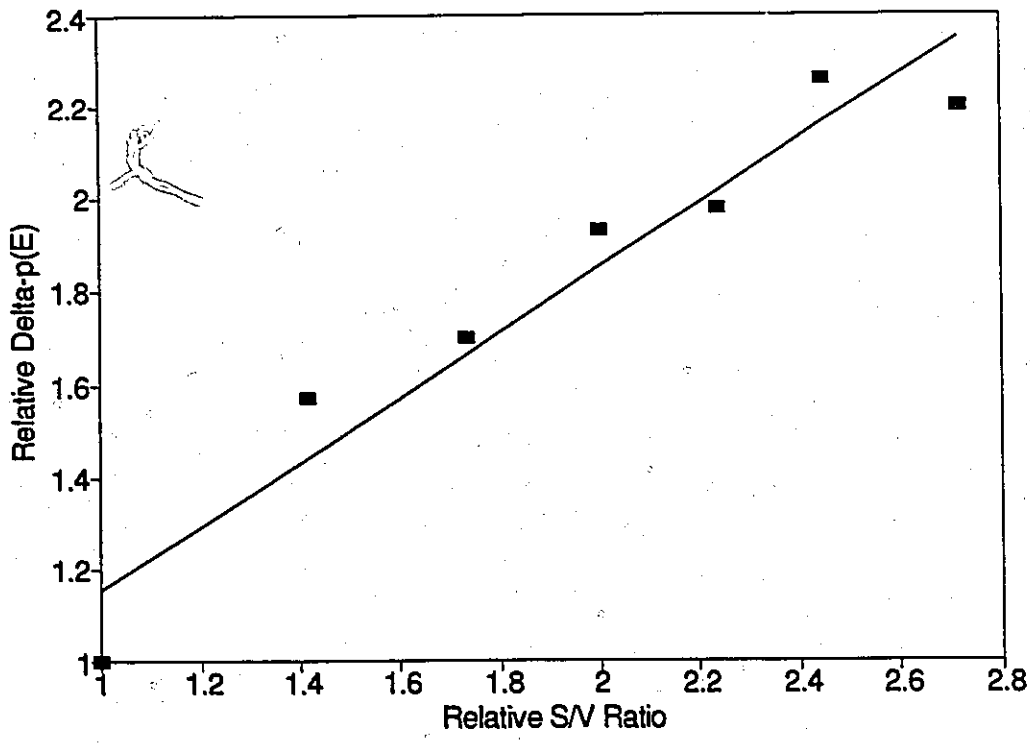

Figure 5.24 **Estimate of Effect of Fuel Surface-to-Volume Ratio (S/V) on Epithermal Group Escape Contribution to Void Criticality Effect (Δp_E).**

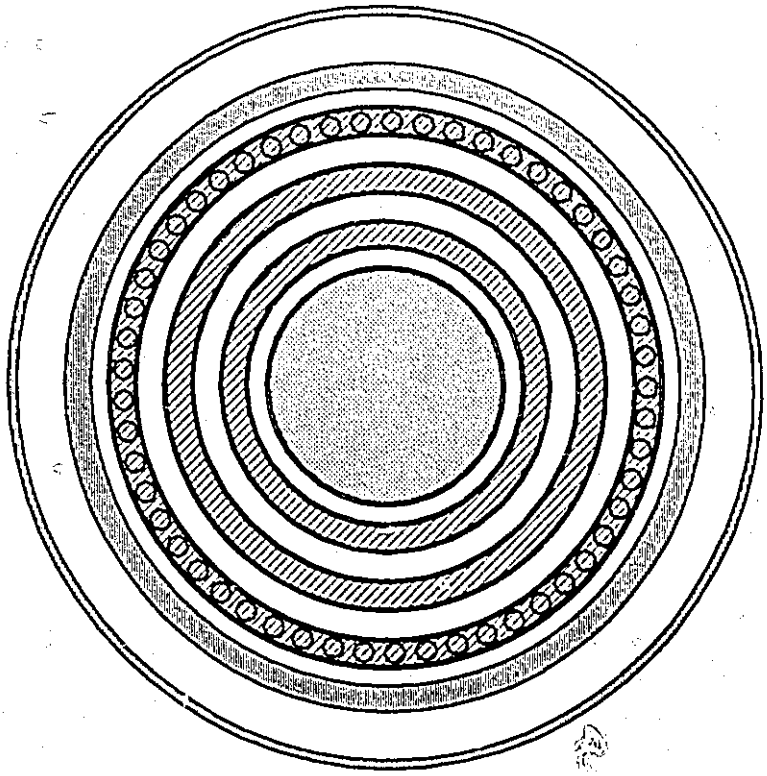

Figure 5.25 3E-NU-GS Geometry With 53 False "Fuel Pins" Embedded Within Outer Element.

Table 5.13 Estimated Effect on $\Delta k_{eff,V}$ of Accounting for Proper S/V Ratio in Case 3E-NU-GS and Case 3E-EU-GS.

Case	Burnup	$\Delta k_{eff,V}$ From Previous Calculation (From Table 5.9 and Table 5.11) (mk)	Estimated From Figure 5.24		S/V Resonance Correction Model	
			Relative Increase in $\Delta\rho_E$	$\Delta k_{eff,V}$ (mk)	Relative Increase in $\Delta\rho_E$	$\Delta k_{eff,V}$ (mk)
3E-NU-GS	zero-burnup	8.6	3.0	11.4	5.5	14.8
	mid-burnup	3.0	3.0	6.2	4.6	8.7
3E-EU-GS	zero-burnup	8.4	3.0	12.0	4.7	15.1
	mid-burnup	3.2	3.0	8.6	3.0	8.8

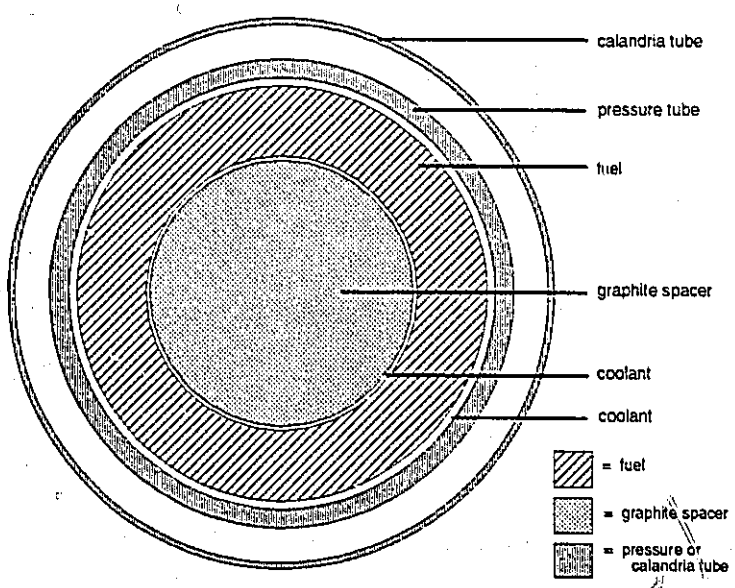

Figure 5.26 Simplified Geometry Used to Benchmark WIMS-AECL Using MCNP-4.

Table 5.14 Comparison of Criticality and Void Effect Between WIMS-AECL and MCNP-4, Using Geometry of Figure 5.26.

Parameter	WIMS-AECL	MCNP-4 (12×10^6 histories)
k_∞ (cooled case)	1.1618	1.1496 ± 0.0001
k_∞ (voided case)	1.1648	1.1522 ± 0.0001
$\Delta k_{\infty,V}$	2.9 mk	2.6 ± 0.2 mk
$\Delta\rho_V$	2.2 mk	2.0 ± 0.2 mk

Table 5.15 Effect of Changing Various WIMS-AECL Input Parameters (Using Case 3E-NU-GS).

Change to Input File	Net Effect on $\Delta k_{eff,V}$ (NOMINAL VALUE: 8.6 mk)	Net Effect on $\Delta\rho_V$ (NOMINAL VALUE: 7.2 mk)	Net Effect on k_{eff} (cooled case)	Criticality Factor Contribution Affected
more annuli added	none	none	none	none
simple D coefficient calculation	+1.1 mk	+0.9 mk	none	f
old resonance treatment	+2.8 mk	+2.2 mk	+1 mk	p_E

Table 5.16 Comparison Between Winfrith and ENDF/B-V Libraries Using Reference and 3E-NU-GS Lattice Cells.

				Winfrith Library (mk)	ENDF/B-V Library (mk)
reference 37-element lattice cell	zero-burnup	geometric bucklings	$\Delta k_{eff,V}$	19.3	18.8
			$\Delta\rho_V$	16.3	15.8
		critical bucklings	$\Delta k_{eff,V}$	15.9	12.7
	mid-burnup	geometric bucklings	$\Delta k_{eff,V}$	14.1	13.7
			$\Delta\rho_V$	13.3	12.9
		critical bucklings	$\Delta k_{eff,V}$	13.0	11.9
3E-NU-GS Lattice cell	zero-burnup	geometric bucklings	$\Delta k_{eff,V}$	8.6	8.6
			$\Delta\rho_V$	7.2	7.2
		critical bucklings	$\Delta k_{eff,V}$	2.8	2.6
	mid-burnup	geometric bucklings	$\Delta k_{eff,V}$	3.0	3.5
			$\Delta\rho_V$	2.9	3.3
		critical bucklings	$\Delta k_{eff,V}$	1.7	2.0

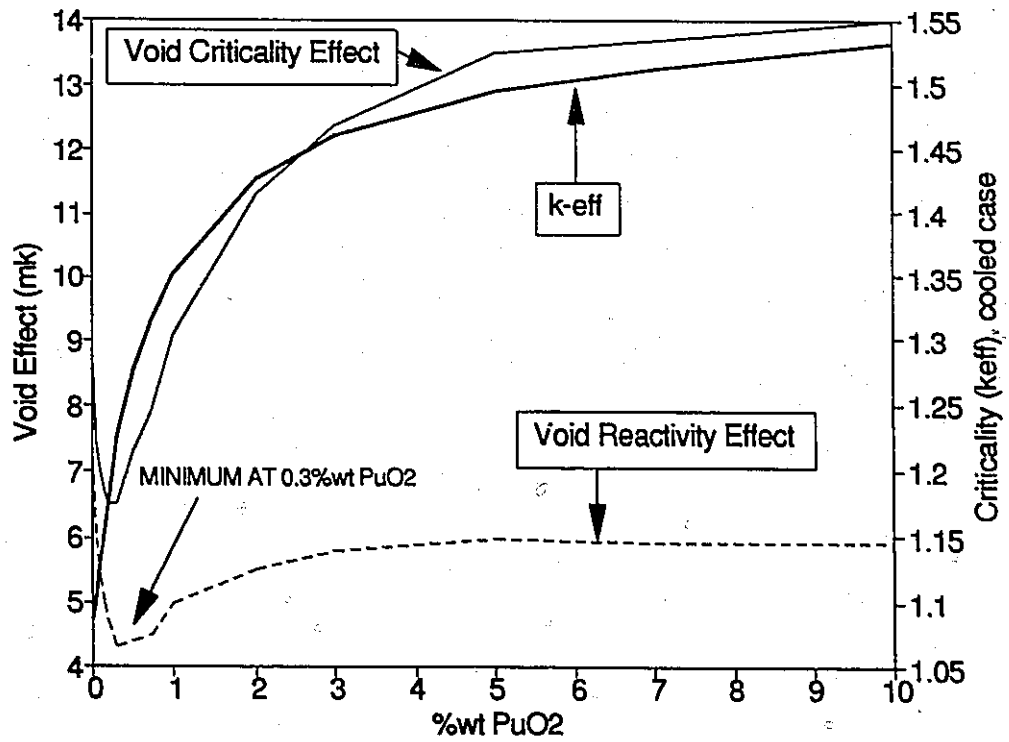

Figure 5.27 **Effect of Using Pu-MOX Fuel in 3E-NU-GS Geometry, as a Function of PuO_2 Weight Fraction (Zero-Burnup Lattice): Void Criticality Effect ($\Delta k_{eff,V}$), Void Reactivity Effect ($\Delta\rho_V$), and k_{eff}**

Table 5.17 Calculated Results for 3E-NU-GS Geometry with Alternate Fuel Cycles: 0.3 %wt PuO_2 MOX (Case 3E-MOX-GS) and DUPIC (Case 3E-DUP-GS).

Calculation	3E-MOX-GS	3E-DUP-GS
zero-burnup k_{eff} (cooled case)	1.225	1.398
zero-burnup $\Delta k_{eff,V}$	6.5 mk	9.3 mk
zero-burnup $\Delta \rho_V$	4.3 mk	4.7 mk
zero-burnup $\Delta k_{eff,V}$ with critical bucklings	-8.5 mk	-16.4 mk
mid-burnup k_{eff} (cooled case)	1.014	1.041
mid-burnup $\Delta k_{eff,V}$	3.0 mk	4.8 mk
mid-burnup $\Delta \rho_V$	2.9 mk	4.4 mk
mid-burnup $\Delta k_{eff,V}$ with critical bucklings	2.0 mk	1.9 mk
discharge burnup	12500 MWd/Te	24000 MWd/Te
estimated ratio of avg. heat flux for Element 1, to max. reference cell value	0.8	0.8
estimated ratio of avg. heat flux for Element 2, to max. reference cell value	1.0	0.9
estimated ratio of avg. heat flux for Element 3, to max. reference cell value	1.0	1.0
estimated ratio of pressure drop across fuel to that of reference cell	0.9	0.9
estimated ratio of fuel throughput to that of reference cell	0.9	0.5

Table 5.18 Composition of Approximated DUPIC Fuel.

Isotope	Abundance (%wt)
U-234	0.014
U-235	0.762
U-236	0.373
U-238	86.165
Pu-239	0.484
Pu-240	0.194
Pu-241	0.115
Pu-242	0.045
O-16	11.847

Table 5.19 Properties[70] and Calculational Results for High Density Fuels.

Material	Melting Pt. (°C)	Density (g/cm³)	U Density Relative to Ref. Cell	$\Delta k_{eff,V}$ (mk)	$\Delta\rho_V$ (mk)	k_{eff} (cooled case)	Discharge Burnup (MWd/Te)
UN	2630	14.32	1.40	9.7	12.2	0.888	n/a
U_3Si_2	1660	12.20	1.17	9.4	7.8	1.093	7000

Table 5.20 Calculated Results for 3E-NU-GS Geometry Using Differential Enrichment: Case 3E-DE-GS (Element Enrichments From Inside Out: 0.20 %wt, 0.72 %wt, 1.91 %wt) Compared With Case 3E-EU-GS. Average Enrichment In Both Cases = 1.1 %wt. Note that Geometry of Case 3E-DE-GS Is Not Optimized for Heat Flux.

Calculation	3E-EU-GS (from Table 5.10)	3E-DE-GS
zero-burnup k_{eff} (cooled case)	1.263	1.275
zero-burnup $\Delta k_{eff,V}$	8.4 mk	3.6 mk
zero-burnup $\Delta\rho_V$	5.2 mk	2.2 mk
zero-burnup $\Delta k_{eff,V}$ with critical bucklings	-8.0 mk	-13.2 mk
mid-burnup k_{eff} (cooled case)	1.022	1.026
mid-burnup $\Delta k_{eff,V}$	3.2 mk	0.6 mk
mid-burnup $\Delta\rho_V$	3.1 mk	0.5 mk
mid-burnup $\Delta k_{eff,V}$ with critical bucklings	1.6 mk	-1.3 mk
discharge burnup	17000 MWd/Te	17000 MWd/Te
estimated ratio of avg. heat flux for Element 1, to max. reference cell value	0.9	0.2
estimated ratio of avg. heat flux for Element 2, to max. reference cell value	1.0	0.6
estimated ratio of avg. heat flux for Element 3, to max. reference cell value	1.0	1.7
estimated ratio of pressure drop across fuel to that of reference cell	0.9	0.9
estimated ratio of fuel throughput to that of reference cell	0.7	0.6

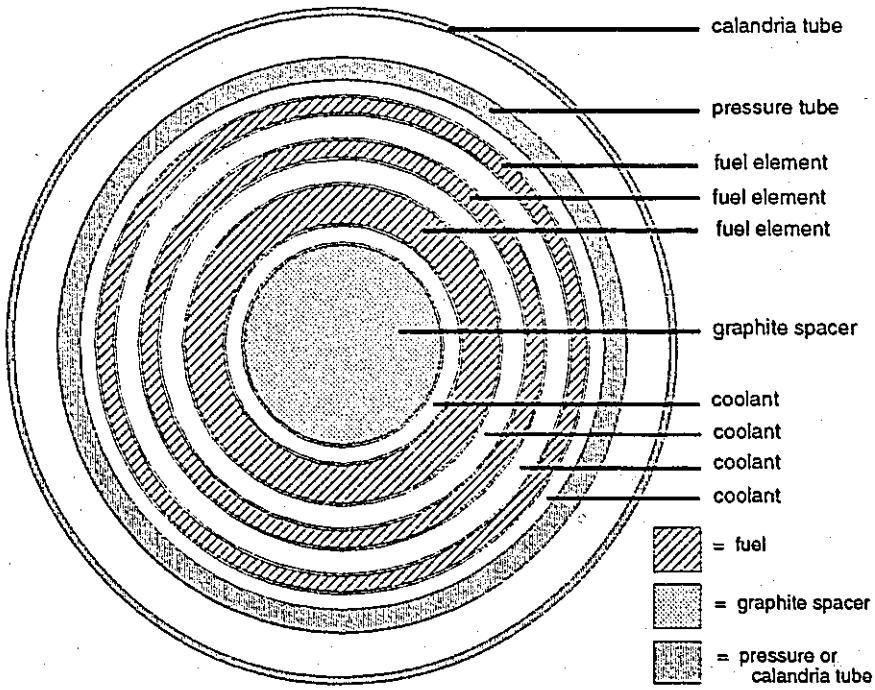

Figure 5.28 Geometry for Case 3E-MOX-DE-GS: Three-Element, Differentially U-235 Enriched, 0.3%wt MOX, Nested Tubular Fuel With Graphite Coolant Spacer. Element Enrichments, From Inside Out: 0.4%wt, 0.65%wt, 1.0%wt. Average U-235 Enrichment = 0.72%wt.

Table 5.21 Specifications for Case 3E-MOX-DE-GS.

Specification	Value	Specification	Value
radius of graphite spacer	1.94 cm	inner radius of Element 3 cladding	4.47 cm
outside radius of spacer clad	1.99 cm	inner radius of Element 3 fuel meat	4.52 cm
inner radius of Element 1 cladding	2.31 cm	outer radius of Element 3 fuel meat	4.83 cm
inner radius of Element 1 fuel meat	2.36 cm	outer radius of Element 3 cladding	4.88 cm
outer radius of Element 1 fuel meat	3.10 cm	inner radius of pressure tube	5.17 cm
outer radius of Element 1 cladding	3.15 cm	total fuel cross-sectional area	29.6 cm^2
inner radius of Element 2 cladding	3.59 cm	width of Element 1 fuel meat	0.74 cm
inner radius of Element 2 fuel meat	3.64 cm	width of Element 2 fuel meat	0.33 cm
outer radius of Element 2 fuel meat	3.97 cm	width of Element 3 fuel meat	0.31 cm
outer radius of Element 2 cladding	4.02 cm	ratio of total fuel volume to ref. cell	69%

Table 5.22 Calculated Results for Case 3E-MOX-DE-GS Compared with Case 3E-MOX-GS: Effect of Differential Enrichment.

Calculation	3E-MOX-GS (from Table 5.17)	3E-MOX-DE-GS
zero-burnup k_{eff} (cooled case)	1.225	1.236
zero-burnup $\Delta k_{eff,V}$	6.5 mk	4.3 mk
zero-burnup $\Delta \rho_V$	4.3 mk	2.8 mk
zero-burnup $\Delta k_{eff,V}$ with critical bucklings	-8.5 mk	-10.2 mk
mid-burnup k_{eff} (cooled case)	1.014	1.015
mid-burnup $\Delta k_{eff,V}$	3.0 mk	1.3 mk
mid-burnup $\Delta \rho_V$	2.9 mk	1.2 mk
mid-burnup $\Delta k_{eff,V}$ with critical bucklings	2.0 mk	0.3 mk
discharge burnup	12500 MWd/Te	12500 MWd/Te
estimated ratio of avg. heat flux for Element 1, to max. reference cell value	0.8	1.0
estimated ratio of avg. heat flux for Element 2, to max. reference cell value	1.0	0.7
estimated ratio of avg. heat flux for Element 3, to max. reference cell value	1.0	1.0
estimated ratio of pressure drop across fuel to that of reference cell	0.9	0.9
estimated ratio of fuel throughput to that of reference cell	0.9	0.9

Table 5.23 Estimated Effect of 99 %wt Zr-90 Enrichment in Fuel Channel Alloys at Zero-Burnup.

Case	Natural Zirconium				90 %wt Zr-90 Enriched Zirconium			
	$\Delta k_{eff,V}$ (mk)	Δp_V (mk)	k_{eff} (cooled case)	Burnup (GWd/Te)	$\Delta k_{eff,V}$ (mk)	Δp_V (mk)	k_{eff} (cooled case)	Burnup (GWd/Te)
3E-NU-GS	8.6	7.2	1.086	6.5	5.8	4.6	1.129	9.7
3E-EU-GS (1.1 %wt UO_2)	8.4	5.2	1.263	17.0	5.3	3.1	1.306	19.7
UN fuel in 3E-NU-GS geometry	9.7	12.2	0.888	n/a	7.6	9.0	0.912	n/a
U_3Si_2 fuel in 3E-NU-GS geometry	9.4	7.8	1.093	7.0	6.6	5.1	1.130	9.9
3E-DUP-GS (DUPIC fuel)	9.3	4.7	1.398	24.0	6.6	3.2	1.398	27.0
3E-MOX-GS (MOX fuel)	6.5	4.3	1.225	12.5	3.9	2.4	1.263	15.0
3E-MOX-DE-GS (MOX fuel, differential enrichment)	4.3	2.8	1.236	12.5	1.3	0.8	1.254	13.8

Table 5.24 Calculated Results for Cases 3E-MOX-EZ-GS and 3E-EU-EZ-GS: Two Previous Cases (3E-MOX-GS and 3E-EU-GS) With Enriched Zirconium Substituted.

Calculation	3E-MOX-EZ-GS	3E-EU-EZ-GS
zero-burnup k_{eff} (cooled case)	1.263	1.306
zero-burnup $\Delta k_{eff,V}$	3.9 mk	5.3 mk
zero-burnup $\Delta \rho_V$	2.4 mk	3.1 mk
zero-burnup $\Delta k_{eff,V}$ with critical bucklings	-14.3 mk	-14.8 mk
mid-burnup k_{eff} (cooled case)	1.015	1.017
mid-burnup $\Delta k_{eff,V}$	0.3 mk	0.4 mk
mid-burnup $\Delta \rho_V$	0.3 mk	0.3 mk
mid-burnup $\Delta k_{eff,V}$ with critical bucklings	-0.7 mk	-0.9 mk
discharge burnup	15000 MWd/Te	19700 MWd/Te
estimated ratio of avg. heat flux for Element 1, to max. reference cell value	0.8	0.8
estimated ratio of avg. heat flux for Element 2, to max. reference cell value	1.0	1.0
estimated ratio of avg. heat flux for Element 3, to max. reference cell value	1.0	1.0
estimated ratio of pressure drop across fuel to that of reference cell	0.9	0.9
estimated ratio of fuel throughput to that of reference cell	0.7	0.6

Table 5.25 Calculated Results for the "Cumulative Case" 3E-MOX-DE-EZ-GS Compared with Reference Cell: Three-Element Nested Tubular Fuel, 0.3 %wt PuO_2 MOX with Differentially Enriched Uranium, and 99 %wt Zr-90 Enriched Alloys.

Calculation	Reference Cell	3E-MOX-DE-EZ-GS
zero-burnup k_{eff} (cooled case)	1.078	1.254
zero-burnup $\Delta k_{eff,V}$	19.3 mk	1.3 mk
zero-burnup $\Delta \rho_V$	16.3 mk	0.8 mk
zero-burnup $\Delta k_{eff,V}$ with critical bucklings	15.9 mk	-15.2 mk
mid-burnup k_{eff} (cooled case)	1.019	1.010
mid-burnup $\Delta k_{eff,V}$	14.1 mk	-1.2 mk
mid-burnup $\Delta \rho_V$	13.3 mk	-1.1 mk
mid-burnup $\Delta k_{eff,V}$ with critical bucklings	13.0 mk	-1.9 mk
discharge burnup	7500 MWd/Te	13800 MWd/Te
estimated ratio of avg. heat flux for Element 1, to max. reference cell value	1.0	1.0
estimated ratio of avg. heat flux for Element 2, to max. reference cell value	1.0	0.7
estimated ratio of avg. heat flux for Element 3, to max. reference cell value	1.0	1.0
estimated ratio of pressure drop across fuel to that of reference cell	1.0	0.9
estimated ratio of fuel throughput to that of reference cell	1.0	0.8

Chapter 6

Summary and Conclusions

This dissertation has proceeded from a statement of goals in Chapter 1, through a description of methodology in Chapter 2, an analysis of component effects in Chapter 3 and amelioration strategies in Chapter 4, to a comprehensive look at a new design concept in Chapter 5. The content of these chapters and the major findings therein are summarized here, along with concluding remarks and suggestions for further work.

6.1 Incentive and Goals

One of the main determinants of the safety shutdown capability of CANDU is the reactivity insertion on loss of coolant. The positive reactivity coefficient of coolant voiding in CANDU is not a barrier to safe operation, and in fact provides a fast trip signal via neutronic rather than thermalhydraulic processes. Regardless of system safety however, the simple existence of a positive void coefficient may become an obstacle in potential markets with established non-CANDU power reactor programmes. An incentive therefore exists for the development of a low void reactivity CANDU fuel bundle that does not compromise the established system design already familiar in these markets.

The approach taken by AECL involves the strategic placement of neutron poison

material within the contemporary bundle geometry, compensated by the use of slightly enriched uranium elsewhere in the bundle. In calling for the addition of neutron poison to the lattice cell, this tactic represents a significant departure from the guiding principle of maximum neutron economy in CANDU design. This dissertation therefore set out to explore an alternate strategy which preserves this principle, as a research goal in its own right and as supplementary research to the AECL programme.

The primary goal of this project was a preliminary design, based on lattice cell calculations using WIMS-AECL, of a low void effect CANDU fuel bundle that does not rely on added neutron poisons in the lattice. This new fuel design would be capable of use within a conventional CANDU core, implying that the design should not require a modification to (1) system thermalhydraulic parameters, and (2) system components beyond the boundary of the pressure tube. The target void effect is anything less than that inducing prompt criticality, for while negative reactivity satisfies the requirement of some customers, a low positive reactivity (sub-prompt critical) retains the neutronic trip characteristic described above.

A secondary goal of this dissertation was a critique of methodology for analyzing the CANDU void effect using lattice cell codes, and the establishment of a consistent approach to such analysis. This approach could then be applied to both the contemporary CANDU lattice cell and a collection of perturbations that capitalize on one or several component neutronic effects.

As such, this dissertation would then form a definitive statement of background, methodology, causal analysis, perturbation analysis, and new design.

6.2 Description of Methodology

A generalized, consistent approach is necessary in the analysis of CANDU void reactivity. The concept of "void reactivity" itself is expressed in several slightly different manners throughout the literature, resulting in significantly different numerical results when k_{eff} is far from unity. In this dissertation the *void criticality effect* is defined as Δk_{eff} upon 100% instantaneous voiding, and the *void reactivity effect* is defined as $\Delta\rho$ under the same conditions.

Several aspects of lattice cell modelling bear scrutiny. The assumption of an infinite lattice means that non-uniform core fuelling cannot be accurately modelled, although mid-burnup results are a good approximation of equilibrium conditions. Imposing critical conditions upon the lattice will avoid the problems of normalization, but the void effect is sensitive to the method of forcing criticality (added absorption or added leakage). In view of this sensitivity, and the time required to model criticality in each case of a parametric study, the supercritical lattice is used in this dissertation. The critical lattice with added leakage is reported in significant cases for completeness.

Several other aspects of lattice cell modelling are briefly visited in this dissertation, but not explicitly accounted for in the parametric analysis. Core leakage is a minor phenomenon in the CANDU core, and the contribution of changes in leakage to the void effect is correspondingly minor. WIMS-AECL has been shown to reasonably reflect these changes through its diffusion coefficient, and any such effects are treated as added absorption in the analysis. Another neglected parameter in the analysis is the

change in neutron lifetime, which is estimated to increase the actual void effect, in terms of point kinetics parameters, by up to 10% when compared with the lattice cell results at mid-burnup. Finally, the uncertainty associated with the WIMS-AECL calculations is not quoted here, but is estimated to be about 2 mk at zero-burnup and increasing slightly with burnup. The error associated with heterogeneous void distributions (partial voiding) is judged to be insignificant.

Small vagaries in data manipulation can sometimes skew one's interpretation of results. Absolute group flux, for instance, is a meaningless quantity in terms of lattice cell calculations, but relative group flux can also become meaningless when the normalization is not performed with care. The best approach is to normalize to total flux summed over all energy groups, with separate normalizations for the cooled and voided cases. A valuable technique for interpreting data is to separate all effects into their traditional "six-factor formula" components. A consistent method, with slight deviations from the exact "six-factor" formulation, is found in the *criticality factor* approach defined and used extensively in this dissertation. This approach accounts for partial contributions through a second-order Taylor series expansion, which is a detail not found in the literature.

The examination of methodology found here serves as a comment on the techniques in general, as well as a necessary preparation for the analysis to follow.

6.3 Analysis of Component Effects

An attempt to manipulate the void effect in CANDU begins with a detailed look at the component phenomena that create the effect. These phenomena have spatial, spectral, and isotopic dependence, and consist of many opposing constituent forces producing a net overall effect. The essential condition at the root of all else is the heterogeneous distribution of spectral sources within the lattice: high energy neutrons originating in the fuel region and low energy neutrons originating in the moderator region. The chief neutronic role of the coolant is to create an epithermal flux from these two sources, through down or up-scattering, and consequently the largest contributor to the void effect is a decrease in epithermal absorption. Smaller contributions come from the increase in fast fission and, in low-burnup cases, thermal utilization. In equilibrium or high burnup cases the presence of plutonium causes a net decrease with voiding of thermal utilization and fission neutrons per fuel absorption, leading to a lower void effect.

The voiding of coolant also effects a spatial redistribution of thermal flux, increasing in the centre region of the fuel bundle and decreasing in the outer region and moderator. In high burnup cases the decrease in the outer fuel region is a dominating negative influence on the void effect, acting mainly through the strong decrease in η for Pu-239. Countering this localized effect, the negative influence of U-235 in the outer fuel region decreases with burnup due to both depletion and absorption competition from fission products. At all burnup steps, however, the combined "outer ring" contribution of U-235 and Pu-239 to the void effect is significantly negative.

6.4 Amelioration Strategies

Strategies for reducing, or reversing, the void effect in CANDU exploit the spectral, spatial, or material dependence of the phenomenon. Although changes to the moderator are incompatible with the goals of this dissertation, reduction in moderator volume is a clear example of the spectral approach. The void effect in this case is reduced by decreasing lattice moderation, and therefore increasing the moderating importance of the coolant. The spectral approach can also be taken by increasing the moderator temperature. The void effect is decreased, albeit only slightly, by thus reducing the significance of rethermalization in the coolant. Increasing the moderator D_2O purity, and thereby reducing absorption in a region of thermal flux depression upon voiding, is an example of a spatial approach. The benefit achieved in this manner is negligible however.

Several strategies involve modifying the content of the fuel pins, while maintaining the conventional 37-element fuel bundle geometry. Enriching the U-235 abundance in the fuel increases absorption throughout the spectrum and actually increases Δk_{eff} at low enrichment levels, while decreasing $\Delta\rho$ due to the increase in criticality to which it is normalized. A clear benefit, regardless of definition, is gained by deploying different isotopic abundances of U-235 across the bundle, from depleted UO_2 in the centre to slightly enriched in the outer ring. This strategy works by placing most of the thermally fissile material in the outer ring where thermal flux changes the least upon voiding.

The next logical step is to remove fuel from the centre pins of the fuel bundle

altogether, and examples using zirconium and graphite as substitution materials demonstrate a small benefit of this approach. A more promising approach replaces the central seven pins with a spacer material, leaving only two outer rings of fuel. The use of a central spacer is crucial to the new fuel design presented in this dissertation. Another idea in this vein is to leave the central fuel pins, but with high absorption material added to them, using natural or depleted fuel in this region and enriched fuel in the outer region. This strategy is not in keeping with the goal of neutron economy established for this dissertation, although it does have the advantage of simplicity in fuel redevelopment and represents the approach of AECL.

Incorporating plutonium into the fuel cycle at the outset, known as a Pu-MOX (Plutonium-Mixed Oxide) cycle, has the advantage of reaping the beneficial spectral effects of plutonium throughout the burnup cycle. When an initial isotopic mixture of plutonium corresponding to that of spent CANDU fuel is added as an oxide to UO_2, this benefit is realized only at very low PuO_2/UO_2 ratios in the case of Δk_{eff}. As with the case of U-235 enrichment, the increased criticality makes $\Delta\rho$ lower than conventional fuel at any oxide ratio.

Shifting the concept of enrichment to the material of the fuel channel tubes, although another area beyond the intent of this dissertation, achieves another small but significant decrease in the void effect. In this case the Zr-90 isotope, with much lower cross-section than Zr-91, is enriched to 99%, and the reduction in void effect results because of the lower absorption in the outer region of the lattice cell.

Finally, the reduction in resonance absorption upon voiding can be lessened by

increasing the surface-to-volume ratio of the fuel and thus decreasing the importance of resonance absorption. Within the limitations of a cluster geometry, this means increasing the diameter of the fuel pins slightly, but the effect turns out to be negligible. The concept can be better realized if the pin cluster geometry concept is abandoned, and this, along with several other of the void effect amelioration strategies mentioned here, forms the basis of this dissertation's discussion of a new design.

6.5 New Design Concept

A significant reduction in the void effect is achieved by lumping the fuel volume into one mass and locating this mass in an annular shape next to the pressure tube. In this manner the effect of both resonance absorption and thermal flux redistribution is minimized. A practical manifestation of this approach has this annular fuel lump subdivided into separate rings with coolant passages between each. A coolant spacer is located in the centre of the pressure tube, significantly reducing the void effect further through coolant displacement. This latter effect is fairly insensitive to spacer material, although a scattering agent such as carbon will produce the best results in terms of cell criticality.

An example of this concept, significantly modified to meet thermalhydraulic and structural constraints, consists of three nested tubular fuel elements of irregular width and spacing, a central carbon coolant spacer, and natural UO_2 as fuel. The void effect of this fuel at mid-burnup is about 3 mk, which is less than prompt critical and therefore meets

the criteria in terms of void effect reduction. The fuel volume is much less than in contemporary CANDU fuel, however, and therefore fuel throughput, total energy output, and — to a lesser degree — burnup, all suffer. With uranium enrichment all of these drawbacks are removed, and with differential use of enrichment across the fuel module the void effect is removed altogether at mid-burnup.

Several variations on this theme are worth considering. The most successful uses a 0.3 %wt mixture of PuO_2 and UO_2 (Pu-MOX fuel) in conjunction with differential uranium enrichment. The intent here is to avoid net uranium enrichment by having an average module enrichment equal to natural uranium. Another practicality is fuel development cost, and for this reason the concepts presented here are perhaps best suited to CANDU fuel cycles under consideration, such as DUPIC, which incur high fuel development costs in themselves. One variation that violates the goal of maintaining all non-fuel components, but which provides further reductions in the void effect (becoming negative), is enrichment of zirconium in the pressure tubes.

Several other practical concerns must be addressed, although a detailed treatment is beyond the scope of this dissertation. For reasons of necessary coolant mixing between subchannels each ring of fuel must be further subdivided into sectors. For reasons of structural integrity and the prevention of flow blockage, each of these sectors must then be held in position with spacers. The result is a nested arrangement of "curved plate" fuel, and a preliminary analysis indicates the manufacturing of such fuel for CANDU to be feasible.

Other concerns involve the ability of WIMS-AECL to model the nonstandard fuel

geometries of this dissertation. The most important issue concerns the calculation of resonance group cross-sections preceding the transport calculation, and a geometric model developed to help the code approximate the correct heterogeneous parameters causes a significant increase in the void effect. However, comparison with a Monte Carlo calculation tends to support the void effect calculation, albeit with a significant discrepancy in the absolute criticality (k_{eff}) calculation. Furthermore, reasonable variations in the WIMS-AECL input file, including the cross-section library, do not alter the result significantly, and concerns about the exclusion of neutron lifetime in lattice cell void effect calculations are not made more acute with the nonstandard designs.

6.6 Conclusions and Observations

In summary, the following conclusions and observations can be drawn from this dissertation:

1) A need exists for a CANDU fuel design with low, zero, or negative coolant void reactivity, and a design which preserves the original CANDU philosophy of neutron economy is desirable.

2) The definition of "void effect" is not standard, and lattice cell calculations are sensitive to this definition. Calculations at mid-burnup avoid much of this problem. Distinctive nomenclature is recommended as a measure against confusion.

3) Calculations with high excess reactivity, such as at zero-burnup, can be made

artificially critical, but the method of achieving this must be chosen carefully since it affects the value of the void criticality effect.

4) Neglecting neutron lifetime in lattice cell calculations can lead to non-conservative estimates of void reactivity, if based solely upon lattice cell results. Lattice cell parametric studies involving significant departures from conventional cell properties should take this into account.

5) Heterogenous void distributions do not have an associated void effect that is significantly different from that found by a homogeneous approximation. However, the level of significance of this difference may change if low void effects are considered.

6) The void effect in CANDU is caused primarily by the existence of two highly separated sources of fast and thermal neutrons, and the considerable influence that the coolant has on cell resonance escape probability as a result. Second in importance is the coolant's influence on both the thermal spectrum and thermal spatial distribution.

7) Within the two combined goals of (a) maintaining non-fuel CANDU components as in contemporary designs, and (b) maximizing neutron economy, the most successful approach to reducing the void effect involves the substitution of low-absorption material for fuel or coolant, or a combination of both. A similar effect that doesn't compromise fissile content can be achieved with the use of differential enrichment across the fuel.

8) A model for improving the resonance treatment in WIMS-AECL when working

with tubular fuel geometries, called here the S/V Resonance Correction Model, permits inclusion of the most important parameter in the calculation of resonance group cross-sections. This parameter is the surface-to-volume ratio (S/V). In light of a preliminary comparison with a Monte Carlo result, it is not clear whether or not the combined effect of less important parameters tends to counter the effect of using this model. This may be an artifact of the particular geometries used in this dissertation.

9) A nested tubular or curved-plate fuel design with a central coolant spacer appears to meet the goals set for this dissertation, although a definitive statement cannot be made in lieu of more accurate modelling of these geometries. The use of differentially enriched fuel, or Pu-MOX fuel, or a combination of both, further lowers the void effect and achieves compatible heat fluxes, pressure drops, and fuel throughput.

10) The fuel development and manufacturing costs of the fuel design variants suggested here are likely to be high, but no fatal technical impediment can be foreseen. Projected costs should be weighed against the advantages of a more flexible and marketable product. To a certain degree, costs may be absorbed if development is incorporated within an existing programme, such as DUPIC, for which new fuel design is required anyway.

6.7 Extensions to Present Work

Further research and analysis is required in the following areas:

1) More understanding is required of the effect of supercritical infinite lattices on calculation of void effect, with a view to developing a consistent strategy for forcing a critical lattice in these situations. This problem is diminished at mid-burnup (or equilibrium) lattice calculations, but not removed completely since the nuclide densities at these burnups will be sensitive to the spectrum assumed at low-burnup.

2) A consistent approach to accounting for neutron lifetime in lattice cell calculations should be established, in order that a more accurate kinetics representation may be included in conclusions based upon parametric lattice cell studies.

3) Consideration of heterogeneous partial void distributions should be given in studies of low void effect fuel, since it is plausible that partial voiding may become significant when the total void effect is low.

4) A more accurate lattice cell calculation of tubular geometry fuel is required, including a capability to model enriched UO_2, MOX fuel, and other variants on contemporary fuel materials. This effort should include a proper accounting of resonance effects in WIMS-AECL, perhaps by including the S/V Resonance Correction Model directly in the code, along with modifications to account for other effects of the geometries described here. These other effects must be sought and fully understood. The designs presented in this dissertation should be fully

analyzed using a Monte Carlo code like MCNP-4, which is recognized to be a time-consuming process, but absolutely essential.

5) Assuming that more accurate lattice cell calculations confirm the positive results found in this scoping study, a more detailed design analysis is then required to determine the feasibility of the enriched fuel, plutonium fuels, DUPIC fuels, and other variants explored here. A complete thermalhydraulic analysis of the nested tubular fuel geometry is required, in order to properly address the many concerns raised here, and others that may develop.

6) The question of manufacturing the nested tubular fuel modules requires extensive study, including a determination of the fuel densities that can be expected, and an analysis of the development and manufacturing costs involved.

References

1. Henry, A.F., *Nuclear-Reactor Analysis*, MIT Press, Cambridge, Massachusetts, 1975.

2. Duderstadt, J.J. and L.J. Hamilton, *Nuclear Reactor Analysis*, John Wiley and Sons, Inc., New York, 1976.

3. Griffiths, J., "Reactor Physics and Economic Aspects of the CANDU Reactor System," AECL Technical Report, *AECL-7615*, 1983.

4. Lewis, W.B., "An Atomic Power Proposal," AECL Technical Report, *AECL-186*, 1951.

5. "CANDU Nuclear Power System", AECL Technical Report, *TDSI-105*, 1982.

6. Lewis, W.B., "Low Cost Fuelling Without Recycling," AECL Technical Report, *AECL-382*, 1956.

7. Lewis, W.B., "Designing Heavy Water Reactors for Neutron Economy and Thermal Efficiency," AECL Technical Report, *AECL-1163*, 1961.

8. Foster, J.S., "Neutron Economy in the Canadian Nuclear Power Program," AECL Technical Report, *AECL-1947*, 1964.

9. Lewis, W.B., "Neutron Economy," AECL Technical Report, *AECL-975*, 1960.

10. Lewis, W.B., "Cost Comparison for Enriched Versus Natural Uranium Fuel and for Zirconium Versus Stainless Steel Fuel Sheathing in Bidirectional Slug Fuelled Reactors," AECL Technical Report, *AECL-651*, 1958.

11. Green, R.E., Boczar, P.G., Hastings, I.J., "Advanced Fuel Cycles for CANDU Reactors," AECL Technical Report, *AECL-9755*, 1988.

12. Hare, M.G., "Neutron Economy and Canada's Long-Term Approach to Nuclear Power," *Eng. J.*, p.91, Fall, 1974.

13. Slater, J.B., "Future Prospects for CANDU Advanced Fuel Cycles," *Proc. 10th Ann. Conf. Can. Nucl. Soc.*, Vol.2, p.1-1, 1989.

14. Meneley, D.A., and Hancox, W.T., "LOCA Consequence Predictions in a CANDU-PHWR," AECL Technical Report, *AECL-7767*, 1982.

15. Azeez, S., Bonechi, M., and Rib. L., "CANDU and US NRC Requirements," *CNS Bulletin*, **14**, 2, p.3, 1993.

16. Driedger, A.A., et al., *Report of the AECL Research and Development Advisory Panel for 1992*, AECL Report, 1992.

17. Howieson, J.Q., and Snell, V.G., "Chernobyl — A Canadian Perspective," AECL Technical Document, *AECL-9334*, 1987.

18. Chan, P.S.W., AECL CANDU, private communication, 1995.

19. Dastur, A.R., and Buss, D.B., "The Influence of Lattice Structure and Composition on the Coolant Void Reactivity in CANDU," *Proc. 11th Ann. Conf. Can. Nucl. Soc.*, p.3-15, 1990.

20. Boczar, P.G., "First LVRF Bundles Fabricated at CRL," *Inter-Comm*, AECL Research Internal Newsletter, **8**, 14, p.1, 1993.

21. Diamond, D.J., "Positive Void Reactivity: An Assessment of its Treatment in Safety Analysis," AECB Research Report, *INFO-0423*, 1992.

22. Aihara, N., et al., "Axial Dependence of Partial Void Reactivity in a Light Water-Cooled, Heavy Water-Moderated, Pressure-Tube Reactor," *Nucl. Sci. Eng.*, **109**, p.158, 1991.

23. Chan, P.S., and Dastur, A.R., "The Physical Basis for the Void Reactivity Effect and Its Dependence on Absorber Rod Configuration in the RBMK-1000," *Nucl. Sci. Eng.*, **103**, p.283, 1989.

24. Weissglas, P., "Theoretical Calculation of the Effect on Lattice Parameters of Emptying the Coolant Channels in a D_2O-Moderated and Cooled Natural Uranium Reactor," *Nukleonik*, **3**, No.2, 5, 1961.

25. Mao, A.O., Rouben, B., and Jenkins, D.A., "A Review of the History-Based Local Parameter Methodology for Simulating CANDU Reactor Cores," *Proc. INC '93 — Intl. Nucl. Conf.*, Toronto, 1993.

26. Donnelly, J.V., "WIMS-CRNL — A User's Manual for the Chalk River Version of WIMS," AECL Technical Report, *AECL-8955*, 1986.

27. Griffiths, J., *WIMS-AECL Users Manual*, AECL Research unpublished report, 1994.

28. Stamm'ler, R.J.J., and Abbate, M., *Methods of Steady-State Reactor Physics in Nuclear Design*, Academic Press, London, 1983.

29. Anderson, D.W., "The WIMS 'E' Module W-PIJ: A Two-Dimensional Collision Probability Code With General Boundary Conditions," UKAEA Technical Report, *AEEW-R862*, 1973.

30. Danielsen, T.M., Havie, T., and Stamm'ler, R.J.J., "On the Numerical Calculation of Bickley Functions," Kjeller Technical Report, *KR-55*, 1963.

31. Carlvik, I., "Collision Probabilities for Finite Cylinders and Cuboids," *Nucl. Sci. Eng.*, **30**, p. 150, 1967.

32. Donnelly, J.V., "Description of the Resonance Treatment in WIMS-AECL," AECL Technical Report, *AECL-10550*, 1993.

33. Askew, J.R., Fayers, F.J., and Kemshell, P.B., "A General Description of the Lattice Code WIMS," *J. Brit. Nucl. Eng. Soc.*, **5**, p.564, 1966.

34. Donnelly, J.V., "Progress in the Development of WIMS at Chalk River," AECL Technical Report, *AECL-8807*, 1985.

35. Heming, P.B., "Development of ENDF/B System," *Proc. 3rd Conf. Neutron Cross-Sections and Technology*, USAEC CONF-71031, p.348, 1971.

36. Festarini, G.I., "The ENDF/B-V WIMS Library," AECL Technical Report, *CRNL-2784*, 1985.

37. Kay, R.E., "Lattice Measurements with 37-Element Bruce Reactor Fuel in Heavy Water Moderator: Detailed Lattice Cell Parameters," AECL Technical Report, *AECL-5307*, 1976.

38. Donnelly, J.V., "Validation of WIMS with ENDF/B-V Data for Pin-Cell Lattices," AECL Technical Report, *AECL-9564*, 1988.

39. "MCNP-4 — Monte Carlo Neutron and Photon Transport Code System", RSIC Computer Code Collection, *CCC-200A/B*, Oak Ridge National Laboratory, 1991.

40. Milgram, M.S., "Void Reactivity Predictions for an Infinite Lattice of 37-Element CANDU Fuel," *Proc. 4th Intl. Conf. Simul. Meth. Nucl. Eng.*, Montreal, 1993.

41. Milgram, M.S., "Estimates of Axial Leakage and Void Reactivity in a CANDU Reactor," *Trans. Am. Nucl. Soc.*, **69**, p.471, 1993.

42. Whitlock, J.J., "On the Calculation of Void Effect in CANDU Using a Lattice Cell Code," *Proc. 1994 Sim. Symp. Can. Nucl. Soc.*, 1994.

43. Van Wylen, G.J., and Sonntag, R.E., *Fundamentals of Classical Thermodynamics*, 3rd Ed., John Wiley & Sons, Inc., 1985.

44. Griffiths, J., "Lattice Characteristics that Influence the Change in Reactivity with Coolant Voiding in CANDU Lattices," *Proc. 13th Ann. CNS Simulation Symposium*, 1987.

45. Bonalumi, R.A., "In-Core Fuel Management in CANDU-PHW Reactors," in Ronen, Y., Ed., *CRC Handbook of Nuclear Reactors Calculations*, CRC Press, Boca Raton, Florida, 1986.

46. Milgram, M.S., AECL-Research, private communication, 1990.

47. De Kruijf, W.J.M., and Janssen, A.J., "On the Definition of the Fuel Temperature Coefficient of Reactivity for Pin-Cell Calculations of an Infinite Lattice", *Ann. Nucl. Energy*, **20**, 9, pp. 639-648, 1993.

48. Milgram, M.S., AECL Research, private communication, 1994.

49. Milgram, M.S., "Determination of Axial Diffusion Coefficients by the Monte-Carlo Method", presented at *INS/ENS International Conference on Reactor Physics and Reactor Computations*, Tel Aviv, 1994.

50. Whitlock, J.J., Milgram, M.S., and Garland, Wm.J., "Estimates of Relative Change in Axial Leakage Due to Voiding in a CANDU Reactor," presented at the *ANS Reactor Physics Division Topical Meeting*, Knoxville, TN, 1994.

51. Griffiths, J., "An Assessment of the WIMS-AECL Error in Predicting the Coolant Void Reactivity in Cold-Clean Zero-Energy Experiments," AECL-Research Technical Report, *RC-611*, 1991.

52. Arfken, G., *Mathematical Methods for Physicists*, 3rd Ed., Academic Press, Inc., Orlando, Florida, 1985.

53. Collier, J.G., *Convective Boiling and Condensation*, 2nd Ed., McGraw-Hill, Inc., 1981.

54. Whitlock, J.J. and Garland, Wm.J., "Dependence of Calculated Void Reactivity on Film Boiling Representation," *Trans. Am. Nucl. Soc.*, **66**, p.525, 1992.

55. Whitlock, J.J., Milgram, M.S., and Garland, Wm.J., "Component Effects Contributing to the Positive Void Coefficient in CANDU," to be presented to the 1995 American Nuclear Society Annual Conference, June 1995.

56. Green, R.E., "Reactivity Effect of Moderator Voids in a CANDU Lattice," AECL Technical Report, *AECL-3002*, 1968.

57. Veeder, J., AECL-Research, private communication, 1994.

58. Dastur, A.R., Chan, P.S.W., and Bowslaugh, D., "The Use of Depleted Uranium for the Reduction of Void Reactivity in CANDU Reactors," *Proc. 13th Ann. Conf. Can. Nucl. Soc.*, 1992

59. Slater, J.B., "Potential of Advanced Fuel Cycles in CANDU Reactors," *Nucl. Energy*, **20**, p.421, 1981.

60. Kato, H., Haga, T., Ohtemi, S., "Core-Management of the FUGEN Heavy-Water-Moderated Plutonium-Uranium Mixed Oxide Reactor," *Nucl. Sci. Eng.*, **87**, p.361, 1984.

61. Kowata, Y., and Fukumura, N., "Influence of Burnable Gadolinia Poison on Coolant Void Reactivity in a Pressure-Tube-Type Heavy Water Reactor," *Nucl. Sci. Eng.*, **115**, p.205, 1993.

62. Milgram, M.S., "Once-Through Thorium Cycles in CANDU Reactors," AECL Technical Report, *AECL-7516*, 1982.

63. Milgram, M.S., "Thorium Fuel Cycles in CANDU Reactors: A Review," AECL Technical Report, *AECL-8326*, 1984.

64. Lone, M.A., and Bartholomew, G.A., "Zr-90 Studies with Thermal Neutrons," *Proc. 3rd Intl. Symp. on Neutron Capture Gamma-Ray Spectroscopy and Related Topics*, Brookhaven National Laboratory, 1978.

65. Townes, B.M., AECL-Research unpublished report, 1982.

66. Roshd, M.H.M., "Nuclear Fuel Bundle Design With Reduced Void Effect," Canadian Patent Application, S.N.247, 483, filed on March 9, 1976.

67. Roshd, M.H.M., French, P.M., Jones, R.T., "Nuclear Fuel Bundle Design with Reduced Void Effect," *Trans. Am. Nucl. Soc.*, **26**, p. 603, 1977.

68. French, P.M., and Jones, R.T., private communication, AECL unpublished report, 1976.

69. Marczak, J.V., *Low Enriched Uranium Fuel Cycle in Heavy Water Reactors*, Ph.D. Dissertation, McMaster University, 1990.

70. Etherington, H., Ed., *Nuclear Engineering Handbook*, 1st ed., McGraw-Hill Book Company, Inc., New York, 1958.

71. Glasstone, S. and Sesonske, A., *Nuclear Reactor Engineering*, D. Van Nostrand Company, Inc. Princeton, New Jersey, 1963.

72. Veeder, J., AECL-Research, private communication, 1994.

73. *Handbook of Chemistry and Physics*, 63rd ed., CRC Press, Boca Raton, Fla., 1984.

74. Zariffeh, E.K., AECL-Research, private communication, 1994.

75. Marinelli, V., "Critical Heat Flux: A Review of Recent Publications," *Nuclear Technology*, **34**, p.135, 1977.

76. Groeneveld, D., AECL-Research, private communication, 1994.

77. Butler, M., McMaster Nuclear Reactor, private communication, 1994.

78. Carter, T., AECL-Research, private communication, 1994.

79. McLain, S., and Martens, J.H., eds., *Reactor Handbook*, 2nd Ed., Vol. 4, John Wiley and Sons, Inc., New York, 1964.

80. Hennelly, E.J., "Savannah River Reactor Sets New Records," *Nuclear News*, p.19, June 1965.

81. Bergeron, K.D., Slezak, S.E., and Leach, C.E., "Proposed Deterministic Severe Accident Criteria for the Heavy Water Reactor - New Production Reactor Containment," *Nuclear Safety*, **34**, 1, p.20, 1993.

82. Cheverton, R.D., and Sims, T.M., "HFIR Core Nuclear Design," ORNL Technical Report, *ORNL-4621*, 1992.

83. West, C.D., "The Advanced Neutron Source: A New Reactor-Based Facility for Neutron Research," *Trans. Am. Nucl. Soc.*, **61**, p.375, 1990.

84. Miller, J.D., "Design Optimization Analysis of the New SPR III-M Reactor," *Proc. ANS Topl. Mtg. Adv. React. Phys.*, Vol. 1, p.251, Knoxville, 1994.

85. Dietrich, J.R., and Zinn, W.H., *Solid Fuel Reactors*, Addison-Wesley Publishing Company, Inc., Reading, Mass., 1958.

86. McIntosh, A.B., and Heal, T.J., *Materials for Nuclear Engineers*, Interscience Publishers, Inc., 1960.

87. P. Benoist, *Nucl. Sci. Eng.*, **77**, 1, 1981.

88. Y. Ronen, *Handbook of Nuclear Reactor Calculations*, Vol. II, CRC Press Inc., Boca Raton, Florida, 1986.

89. Lee, S. et al., "A Study on the Direct Use of Spent PWR Fuel in CANDU (DUPIC)," KAERI Technical Report, *KAERI/RR-1238/92*, 1992.

90. Choi, H., Rhee, B., and Park, H., "Parametric Analysis of the DUPIC Cycle," *Proc. 1994 CNS Simulation Symposium*, p.71, 1994.

91. Boczar, P., AECL-Research, private communication, 1994.

92. AECL Research unpublished report, 1984.

93. Verrall, R., AECL-Research, private communication, 1994.

94. Sears, D., AECL-Research, private communication, 1994.

95. Chalder, G.H., et al., "U_3Si As a Nuclear Fuel", AECL Technical Report, *AECL-2874*, 1967.

Appendix A

The following is adapted from a paper presented at the 1994 ANS Reactor Physics Topical Meeting, April 11-15, Knoxville, TN.

ESTIMATES OF RELATIVE CHANGE IN AXIAL LEAKAGE DUE TO VOIDING IN A CANDU REACTOR

by

Jeremy J. Whitlock [a], Michael S. Milgram [b, a], William J. Garland [a]

[a] McMaster University, Department of Engineering Physics
[b] AECL Research, Reactor Physics Branch

The Monte-Carlo method and a deterministic method are used to estimate the relative perturbation in axial leakage from a lattice cell upon complete and instantaneous coolant voiding. With a Monte-Carlo code the ratio of net current tallies at the axial boundary of the fuel channel is calculated and compared with estimates from a two-dimensional deterministic lattice code, using estimated axial bucklings and two different methods for calculating the diffusion coefficient. Results are grouped into four energy bins.

A.1 INTRODUCTION

It is important to be able to accurately model each of the component mechanisms that contribute to positive reactivity feedback induced by coolant voiding in an operating CANDU reactor. These mechanisms comprise a complicated mixture of spectral and spatial effects[1,2], thought to include a change in neutron leakage from the core. Leakage is expected to increase upon voiding since spectrum hardening and increased streaming both lead to larger cell diffusion coefficients. Generally, infinite-lattice cell codes (like WIMS-AECL[3]), which provide these coefficients, are not designed to implicitly account for core boundary effects and require an explicit adjustment in the form of user-supplied buckling values. In this paper we investigate the accuracy of this methodology by comparing estimates of relative change in axial leakage upon 100% instantaneous coolant voiding in CANDU, using WIMS-AECL and the Monte-Carlo code MCNP-4[4]. Since MCNP-4 is a much more fundamental code this can be considered a benchmark study of WIMS-AECL, within the statistical accuracy of our MCNP-4 results. The routine application of Monte-Carlo codes to extended criticality problems such as that described here, made possible by advances in computer hardware, is a powerful addition to the suite of analysis tools available to the reactor physicist. Previous studies of CANDU void reactivity in both infinite and finite geometries using MCNP-4 have been reported elsewhere[5,6].

A.2 DESCRIPTION OF WIMS-AECL AND MCNP-4

WIMS-AECL uses collision-probabilities to solve the multi-group neutron transport equation in a two-dimensional infinite lattice (the PIJ transport option was used here). It has been developed by AECL from a version of WIMS provided by the UKAEA in 1971. Diffusion coefficients can be calculated using either the Benoist method[7,8] or a simple transport calculation[9], and both methods have been used in this paper. The ENDF/B-V WIMS cross-section library was used in its full 89-group format. MCNP-4 is a stochastic (Monte-Carlo) three-dimensional particle tracking code, used in analog neutron transport mode with a continuous-energy cross-section library also derived from ENDF/B-V. Both codes were run on a workstation.

A.3 DESCRIPTION OF MODEL

The lattice cell for WIMS-AECL and MCNP-4 was a cylindrical 37-element CANDU fuel bundle

surrounded by fuel channel material and moderator with a square reflective boundary of side 28.55 cm (see also References 5 and 6), shown in Figure A.1(a). D_2O coolant and moderator temperature (600 K and 300 K, respectively) corresponded to MCNP-4 library values. Fuel temperature (300 K) also corresponded to the nominal MCNP-4 library value, to avoid concerns[5] about temperature modelling.

Axial CANDU geometry was modelled in MCNP-4 by six adjacent 50.0 cm fuel bundles in a 300.0 cm half-channel, terminated by a 25.0 cm iron slab at one end and a reflection symmetry plane at the other, as shown in Figure A.1(b). A void region of zero importance terminated this geometry axially. Partial currents were tallied at the plane interface between the fuelled and termination regions. Additional calculations used unrealistic half-channel lengths of 125.0 cm and 60.0 cm in order to improve tally statistics at this interface[10]. In WIMS-AECL these varying channel lengths were reflected in energy-independent axial bucklings derived from MCNP-4 using the method of Reference 10. These bucklings are listed in Table A.1, along with diffusion theory bare-core values[9] for comparison. Since the estimation of collision probabilities in any 2-D lattice code such as WIMS-AECL includes an axial integration to infinity, the adequacy of such a code's radial flux calculation should decrease with shorter fuel channels. For example, the cell diffusion length in CANDU is on the order of 20 cm and therefore one would suspect the accuracy of a flux solution for the 60 cm half-channel case; however, the relative perturbation in axial leakage upon voiding should be unaffected.

A.4 DESCRIPTION OF METHOD

The subject of interest in this study is the accuracy of the relative change in axial leakage upon 100% instantaneous voiding,

$$R \equiv \frac{\left(L_z^{voided\,100\%} - L_Z^{cooled}\right)}{L_z^{cooled}} \quad . \tag{A.1}$$

where L_Z is net surface-integrated leakage, defined by Equation (A.2):

$$L_Z \equiv \int_S \left(J_Z^+ - J_Z^-\right) \cdot ds = L_Z^+ - L_Z^- \quad . \tag{A.2}$$

Here s denotes the axial surface area. The surface-integrated partial currents, L^+_Z and L^-_Z, can be calculated directly using the direction cosine current tally option in MCNP-4, which normalizes the tallies to one starting neutron. The statistical uncertainty in L_Z is reduced by $2cov(L^+_Z, L^-_Z)$, the error correlation term associated with the partial currents, which can be extracted from MCNP-4 indirectly[7]. The statistical errors in the tallies for the two cases (cooled and voided) are assumed to be uncorrelated.

In WIMS-AECL leakage is treated by a user-supplied geometric buckling. Two-dimensional collision probabilities integrated to infinity in the axial direction account for an average over the third dimension, so that axial leakage can be estimated using classical diffusion theory (assuming D_Z is independent of z),

$$L_Z \approx -\int_V D_Z \nabla^2 \phi \, dV = V D_Z B_Z^2 \overline{\phi} \quad . \tag{A.3}$$

The cell-averaged neutron flux, $\overline{\phi}$, was normalized to a unit source in accordance with the normalization in MCNP-4. The axial diffusion coefficient, D_Z, was calculated with and without the Benoist method selected (the code default is a simple transport calculation). Note that the bucklings listed in Table A.1 are

virtually independent of voiding, and therefore the ratio in Equation (A.1) is affected mainly by the change in cell diffusion coefficient and flux.

A.5 RESULTS AND DISCUSSION

After 24 million neutron histories (24 Mh) the MCNP-4 values of k_{eff} and k_∞ (using the correlated value from three different estimates[4]) converged to the values in Table A.2, compared there with the corresponding WIMS-AECL results. Despite an overall discrepancy of 5 mk (0.5%) in criticality between the two codes (thought to be related to differences in temperature treatment), there is excellent agreement in the predictions of void reactivity (Δk_{eff} or Δk_∞), including the WIMS-AECL case without the Benoist option. The presence of a constant 5 mk discrepancy between the two codes in both the k_{eff} and k_∞ calculations demonstrates that the overestimation by the lattice code is not due to the finite axial geometry.

The relative changes in axial leakage upon voiding, calculated with MCNP-4 (24 Mh) and WIMS-AECL using Equations (A.2) and (A.3), respectively, are given in Table A.3 for four energy bins. Although similar energy bins were used for both codes, the respective cross-section libraries do have different low-energy and high-energy cut-off points: 2×10^{-3} eV to 10 MeV for WIMS-AECL, and 10^{-5} eV to 20 MeV for MCNP-4. This is not significant since about 0.1% of the net current has energy below the WIMS-AECL low-energy cut-off point (estimated from an auxiliary MCNP-4 run) and about 0.1% of the fission spectrum[9] is above the WIMS-AECL high-energy cut-off point.

Both codes calculate a slight decrease in thermal group axial leakage upon voiding, along with increases of approximately 10% and 30% in the resonance and fast groups, respectively. With Benoist diffusion coefficients the increase in total axial leakage (bottom row) calculated by WIMS-AECL is twice the amount calculated by MCNP-4. The results for the subdivided energy groups suggest that a modelling problem occurs in the resonance range, while the results for the thermal and fast groups are satisfactory. When the simple transport calculation for the diffusion coefficient is used the results are almost a complement of those using the Benoist method: the resonance group result agrees with MCNP-4 while the thermal and fast groups do not (although the fast group result is still within the 95% ($\pm 2\sigma$) confidence interval of MCNP-4), and the total change in axial leakage is just inside the 99.7% ($\pm 3\sigma$) confidence interval.

The results using a 250 cm and 120 cm channel are listed in (A.4), Table A.4 and Table A.5, respectively. While absolute leakage would be higher in these geometries, the relative perturbation upon voiding should remain fairly constant since it is primarily a function of material properties. This is reflected in the MCNP-4 results for all three channel lengths (Table A.3 to Table A.5), with the exception of an anomaly in the thermal group for the 250 cm channel ((A.4), Table A.4). Aside from this anomaly the results for all energy bins do increase slightly with decreasing channel length, but not by more than 3σ from the 600 cm channel case.

Note that the 120 cm channel results (Table A.5) show very good agreement between WIMS-AECL (with Benoist diffusion coefficients) and MCNP-4 in all four energy bins. The MCNP-4 statistics are, as expected, best for this case, despite the fact that 12 Mh were run instead of 24 Mh as in the other two cases. Based upon these results we can look back at the 600 cm channel results in Table A.3 and suspect that the MCNP-4 calculation, especially for total leakage, had not yet converged satisfactorily. This demonstrates the need for extraordinary long runtimes when such small perturbations are involved.

In the interest of completeness the values of k_{eff} and Δk_{eff} for the two short channel cases are included in Table A.6. The trend of overestimation in absolute criticality by WIMS-AECL continues, and in these cases the disagreement in void reactivity is pronounced. This is due to an increase in the relative

importance of leakage over absorption as a loss mechanism.

Some light can be shed upon the relative changes in axial leakage in Table A.3, by splitting the relative leakage changes into the constituents which change upon voiding — the cell diffusion coefficient, average flux and buckling in Equation (A.3). These partial contributions, R_D, R_ϕ and R_B (where $R_a \equiv (\partial a/a)$ + second-order Taylor series term), appear in Table A.7 and Table A.8 for the longest and shortest channels, respectively. For WIMS-AECL it is a trivial matter to generate the data in these tables; for MCNP-4 we must average quantities over the axial direction and, in the case of diffusion coefficient[9] and buckling[7], make some estimations based on diffusion theory:

$$\phi(z) \approx 2\left[J_Z^+(z) + J_Z^-(z)\right] \quad ; \quad \bar{\phi} = \frac{\int_Z \phi(z)}{\int_Z dz} \quad ; \quad D_Z \approx \frac{L_Z}{V B_Z^2 \bar{\phi}} \quad . \tag{A.4}$$

Accuracy estimates for MCNP-4 average flux and diffusion coefficient have been based on the MCNP-4 error for the partial currents, and on the accuracy estimate for B_Z^2 (± 0.2%).

It can be seen that all energy groups experience an increase in the cell diffusion parameter upon coolant voiding, and that the drop in thermal leakage is due to a drop in thermal cell flux. The comparison between the two codes indicates that WIMS-AECL (with Benoist option) overestimates the increase in diffusion coefficient for all energy groups, but the effect is not significant for the low-leakage cases corresponding to an operating CANDU reactor. The perturbations in cell flux predicted by WIMS-AECL have a negative bias in comparison with the corresponding MCNP-4 values, indicating that its calculation of voided flux could be too low. These trends are true for both channel lengths, although the overall leakage perturbations for the shortest channel case are similar for the two codes, as noted earlier. An earlier experimental work[11] on D_2O coolant voiding in a natural UO_2 lattice predicts a value of 9% for total $\delta D_Z / D$ based upon the ratio of void volume to cell volume (but different geometry).

A.6 CONCLUSION

In general we find reasonable agreement between MCNP-4 and WIMS-AECL in terms of estimating axial leakage perturbation upon lattice cell voiding, particularly for cases of direct interest to operating CANDU reactors. An overestimate of the WIMS-AECL change in diffusion coefficient and a negative bias in the flux change, both in comparison with MCNP-4, appear to cancel. The importance of ensuring adequate convergence of the Monte-Carlo process is demonstrated, as is the enormous dedication of CPU time that is required. For these reasons it is clear that we describe a benchmark procedure here and not a routine analysis method. The inadequacy of two-dimensional lattice codes in certain finite geometries is noted.

A.7 ACKNOWLEDGEMENTS

This work was partially funded by grants from the Natural Sciences and Engineering Council of Canada, and the CANDU Owners Group.

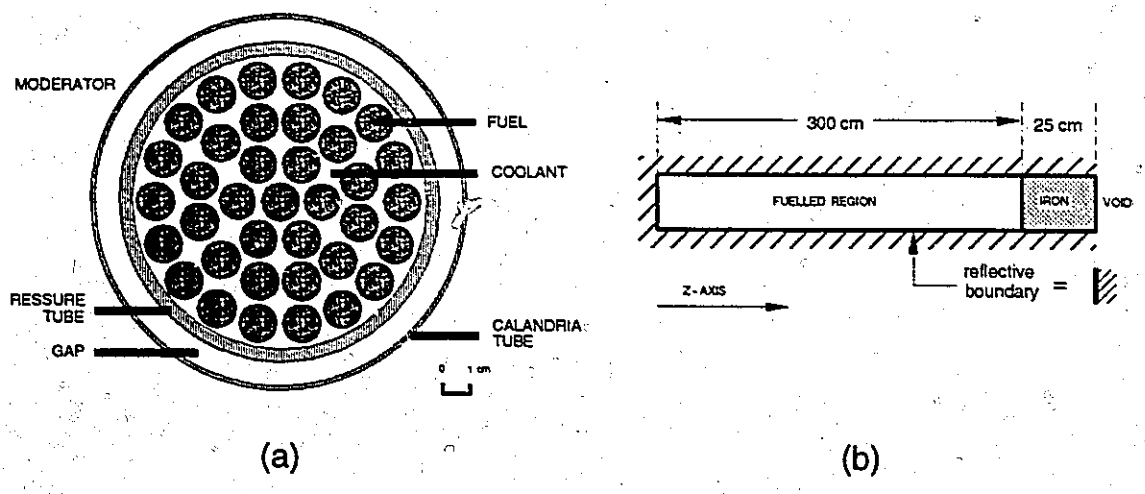

Figure A.1 (a) 37-Element CANDU Lattice Cell; (b) Axial Model Used in MCNP-4

Table A.1 Axial Bucklings Derived for WIMS-AECL (accuracy ± 0.2%)

Total Channel Length	Cooled Case (cm-2)	Voided Case (cm-2)	Theoretical Value (cm-2)
600 cm	2.59×10^{-5}	2.60×10^{-5}	2.74×10^{-5}
250 cm	1.39×10^{-4}	1.38×10^{-4}	1.58×10^{-4}
120 cm	5.59×10^{-4}	5.52×10^{-4}	6.85×10^{-4}

Table A.2 Comparison of Criticality and Void Reactivity Between MCNP-4 and WIMS-AECL for 600 cm Fuel Channel

	WIMS-AECL			MCNP-4 (error = σ)	
	k_{eff} with Benoist	k_{eff} without Benoist	k_∞	k_{eff}	k_∞
cooled	1.1223	1.1227	1.1328	1.1175 ± .0001	1.1284 ± .0001
voided	1.1441	1.1449	1.1555	1.1395 ± .0001	1.1503 ± .0001
void reactivity (Δk_{eff} or Δk_∞)	21.8 mk	22.2 mk	22.7 mk	22.0 ± .1 mk	21.9 ± .1 mk

Table A.3 Relative Change in Axial Leakage Upon Coolant Voiding for 600 cm Fuel Channel

Energy Group	WIMS-AECL		MCNP-4 (error = σ)
	with Benoist	without Benoist	
thermal (0 - 0.625 eV)	– 1.2 %	– 5.1 %	– (1.2 ± 0.3) %
resonance (0.625 eV - 0.821 MeV)	+ 12.2 %	+ 7.5 %	+ (8.0 ± 1.4) %
fast (0.821 MeV - 10 MeV)	+ 34.7 %	+ 30.3 %	+ (33.1 ± 1.8) %
total (0 - 10 MeV)	+ 6.0 %	+ 1.8 %	+ (2.6 ± 0.3) %

Table A.4 Relative Change in Axial Leakage Upon Coolant Voiding for 250 cm Fuel Channel

Energy Group	WIMS-AECL		MCNP-4
	with Benoist	without Benoist	(error = σ)
thermal (0 - 0.625 eV)	– 2.7 %	– 6.5 %	– (0.1 ± 0.2) %
resonance (0.625 eV - 0.821 MeV)	+ 10.5 %	+ 5.8 %	+ (8.9 ± 0.7) %
fast (0.821 MeV - 10 MeV)	+ 32.7 %	+ 28.2 %	+ (31.3 ± 0.8) %
total (0 - 10 MeV)	+ 4.5 %	+ 0.4 %	+ (3.7 ± 0.2) %

Table A.5 Relative Change in Axial Leakage Upon Coolant Voiding for 120 cm Fuel Channel

Energy Group	WIMS-AECL		MCNP-4
	with Benoist	without Benoist	(error = σ)
thermal (0 - 0.625 eV)	– 2.9 %	– 6.6 %	– (2.1 ± 0.2) %
resonance (0.625 eV - 0.821 MeV)	+ 10.4 %	+ 5.2 %	+ (10.4 ± 0.2) %
fast (0.821 MeV - 10 MeV)	+ 32.8 %	+ 27.6 %	+ (28.3 ± 0.5) %
total (0 - 10 MeV)	+ 4.9 %	+ 0.6 %	+ (3.5 ± 0.1) %

Table A.6 Comparison of k_{eff} Between MCNP-4 and WIMS-AECL for 250 cm and 120 cm Fuel Channel

		WIMS-AECL		MCNP-4
		with Benoist	without Benoist	(error = σ)
250 cm	cooled	1.0778	1.0796	1.0730 ± .0001
	voided	1.0966	1.1006	1.0927 ± .0001
	void reactivity (Δk_{eff})	18.8 mk	21.0 mk	19.7 ± .1 mk
120 cm	cooled	0.9336	0.9392	0.9295 ± .0002
	voided	0.9428	0.9557	0.9436 ± .0002
	void reactivity (Δk_{eff})	9.2 mk	16.5 mk	14.1 ± .3 mk

Table A.7 Contribution of Leakage Components to Relative Change in Axial Leakage for 600 cm Fuel Channel

	WIMS-AECL (With Benoist)				WIMS-AECL (Without Benoist)			
Energy Group	R_D	R_ϕ	R_B (derived from MCNP-4)	Total ($R=\Sigma R_i$)	R_D	R_ϕ	R_B (derived from MCNP-4)	Total ($R=\Sigma R_i$)
thermal (0 - .625 eV)	+ 6.0 %	– 7.6 %	+ 0.4 %	– 1.2 %	+ 1.9 %	– 7.4 %	+ 0.4 %	– 5.1 %
resonance (.625 eV - .821 MeV)	+ 9.5 %	+ 2.3 %	+ 0.4 %	+ 12.2 %	+ 4.8 %	+ 2.3 %	+ 0.4 %	+ 7.5 %
fast (.821 - 10 MeV)	+ 18.4 %	+ 15.9 %	+ 0.4 %	+ 34.7 %	+ 14.2 %	+ 15.7 %	+ 0.4 %	+ 30.3 %
total (0 - 10 MeV)	+ 9.6 %	– 4.0 %	+ 0.4 %	+ 6.0 %	+ 5.4 %	– 4.0 %	+ 0.4 %	+ 1.8 %

	MCNP-4			
Energy Group	R_D	R_ϕ	R_B	Total ($R=\Sigma R_i$)
thermal (0 - .625 eV)	+ (3.7 ± 0.3) %	– (5.3 ± 0.01) %	+ (0.4 ± 0.3) %	– (1.2 ± 0.4) %
resonance (.625 eV - .821 MeV)	+ (3.1 ± 1.4) %	+ (4.5 ± 0.02) %	+ (0.4 ± 0.3) %	+ (8.0 ± 1.4) %
fast (.821 - 10 MeV)	+ (12.7 ± 1.5) %	+ (19.5 ± 0.03) %	+ (0.4 ± 0.3) %	+ (33.1 ± 1.6) %
total (0 - 10 MeV)	+ (3.9 ± 0.3) %	– (1.8 ± 0.01) %	+ (0.4 ± 0.3) %	+ (2.6 ± 0.4) %

Table A.8 Contribution of Leakage Components to Relative Change in Axial Leakage for 120 cm Fuel Channel

	WIMS-AECL (With Benoist)				WIMS-AECL (Without Benoist)			
Energy Group	R_D	R_ϕ	R_B (derived from MCNP-4)	Total ($R=\Sigma R_i$)	R_D	R_ϕ	R_B (derived from MCNP-4)	Total ($R=\Sigma R_i$)
thermal (0 - .625 eV)	+ 5.9 %	– 7.5 %	– 1.3 %	– 2.9 %	+ 2.0 %	– 7.2 %	– 1.3 %	– 6.6 %
resonance (.625 eV - .821 MeV)	+ 9.4 %	+ 2.3 %	– 1.3 %	+ 10.4 %	+ 4.8 %	+ 1.7 %	– 1.3 %	+ 5.2 %
fast (.821 - 10 MeV)	+ 18.1 %	+ 16.0 %	– 1.3 %	+ 32.8 %	+ 13.9 %	+ 15.0 %	– 1.3 %	+ 27.6 %
total (0 - 10 MeV)	+ 9.8 %	– 3.6 %	– 1.3 %	+ 4.9 %	+ 5.7 %	– 3.8 %	– 1.3 %	+ 0.6 %

	MCNP-4			
Energy Group	R_D	R_ϕ	R_B	Total ($R=\Sigma R_i$)
thermal (0 - .625 eV)	+ (4.8 ± 0.2) %	– (5.5 ± 0.01) %	– (1.3 ± 0.3) %	– (2.1 ± 0.3) %
resonance (.625 eV - .821 MeV)	+ (7.9 ± 0.2) %	+ (3.8 ± 0.02) %	– (1.3 ± 0.3) %	+ (10.4 ± 0.3) %
fast (.821 - 10 MeV)	+ (10.4 ± 0.5) %	+ (18.9 ± 0.03) %	– (1.3 ± 0.3) %	+ (28.3 ± 0.5) %
total (0 - 10 MeV)	+ (6.6 ± 0.1) %	– (1.7 ± 0.01) %	– (1.3 ± 0.3) %	+ (3.5 ± 0.3) %

A.8 REFERENCES

1. J. GRIFFITHS, "Lattice Characteristics that Influence the Change in Reactivity with Coolant Voiding in CANDU Lattices," *Proc. 13th Ann. Sim. Symp. Can. Nucl. Soc.*, AECL-Research, Chalk River Laboratories, 1987.

2. A. R. DASTUR and D. B. BUSS, "The Influence of Lattice Structure and Composition on the Coolant Void Reactivity in CANDU," *Proc. 11th Ann. Conf. Can. Nucl. Soc.*, 1990.

3. J. V. DONNELLY, "WIMS-CRNL — A User's Manual For The Chalk River Version of WIMS", AECL Technical Report, *AECL-8955*, 1986.

4. "MCNP-4 — Monte Carlo Neutron and Photon Transport Code System", RSIC Computer Code Collection, *CCC-200A/B*, Oak Ridge National Laboratory, 1991.

5. M. S. MILGRAM, "Void Reactivity Predictions for an Infinite Lattice of 37-Element CANDU Fuel", *Proc. 4th Intl. Conf. Sim. Meth. Nucl. Eng.*, 1993.

6. M. S. MILGRAM, *Trans. Am. Nucl. Soc.*, **69**, 471, 1993.

7. P. BENOIST, *Nucl. Sci. Eng.*, 77, 1, 1981.

8. Y. RONEN, *Handbook of Nuclear Reactor Calculations*, Vol. II, CRC Press Inc., Boca Raton, Florida, 1986.

9. J. J. DUDERSTADT and L. J. HAMILTON, *Nuclear Reactor Analysis*, John Wiley and Sons, Inc., New York, 1976.

10. M. S. MILGRAM, "Determination of Axial Diffusion Coefficients by the Monte-Carlo Method", presented at the *INS/ENS Intl. Conf. React. Phys. React. Comp.*, Tel Aviv, 1994.

11. H. R. FIKE and W. E. GRAVES, *Trans. Am. Nucl. Soc.*, **6**, 245, 1963.

Appendix B

The following is the fortran source code and sample output for FACT-EFF.FOR, a tool used extensively in this dissertation for extracting approximate reactivity factors out of a WIMS-AECL output file. An explanation of the method can be found in Section 2.3.2.

B.1 Source Code

```
      PROGRAM FACT_EFF

*  Generates five(+) reactivity factors from a WIMS-AECL output file,
*  based upon the effective flux spectrum.
*  Jeremy Whitlock, Dept. Engineering Physics, McMaster University
*  93/02/26

*  Important:  Input file for WIMS-AECL case must include the printing
*  of reaction rate data for at least the fuel materials (easiest to
*  print all reaction rates, by using the REACTION ALL option).  This
*  means that, along with the presence of a REACTION card, the SUPPRESS
*  card must have entry # 15 = 0, and the PRINT card must start with
*  "1 1 1 0".  Also, the PARTITION card must be included.  Errors
*  messages are printed and execution is aborted if these requirements
*  are not met.

      CHARACTER RECORD*90,FLAG12*12,DUMMY*53,DUMMY2*17,DUMMY3*14
      CHARACTER*13 DUMMY4(6)
      CHARACTER DUMMY5*8,FLAG8*8,FLAG7*7,FLAG5*5,DUMMY6*11,DUMMY7
      REAL TOTNUFIS(2),FLUX2,ERRORP(2),STOT(2),TOTABS(2)
      REAL ETAF(2),F(2),ETA(2),EPSILON(2),P(2),KVALUE(2),ERRORK(2)
      INTEGER GRPBND(69),NGRPBND(69),FEWGROUP(69)
      REAL FLUX(2,69),ABSORB(2,69),ABSRATE(2,69),S(2,69),PFACT(69)
      REAL TOTFLUX(2,69),TOTABSR(2,69),PCONT(2,69),DELTAS(69)
      REAL ETACONT(2),FCONT(2),EPSICONT(2),EFFECT(2),SUM(2),SUMP(2)
      REAL ABSUMP(2),ABSUM(2),DIFF(2,69),LEAKAGE(2,69),TOTLEAK(2)
      REAL THABS(2),THNUFIS(2),THDIFF(2),FABS(2),FNUFIS(2),FDIFF(2)
      OPEN (UNIT=1,FILE='FOURFACT.INP',STATUS='UNKNOWN')
      OPEN (UNIT=2,FILE='FOURFACT.TMP',STATUS='SCRATCH')
      OPEN (UNIT=3,FILE='FIVEFACT.TMP',STATUS='SCRATCH')

*  Calculate eta-f,p,e:

      IFLAG=0
      NUMTH=0
      DELTAK=1.0E-3
      DELTARHO=1.0
 10   FORMAT(A90)
      DO 200 I=1,2
         READ(1,10,ERR=230) RECORD
         FLAG12 = RECORD(4:16)
         DO 11 WHILE (FLAG12 .NE. 'GROUPS..... ')
```

```
            IF (RECORD(1:11) .EQ. '> FEWGROUPS') THEN
         IFEWGR=1
3              IFKEY=0
         DO 5 IF=1,90
             IF (RECORD(IF:IF) .EQ. 'S')THEN
               IFKEY=1
               IF (IFEWGR .EQ. 1)THEN
                   IFEND=IF-1
                   WRITE(3,*) RECORD(12:IFEND)
               ELSE
                   IFEND=IF-1
                   WRITE(3,*) RECORD(2:IFEND)
               ENDIF
             ENDIF
5              CONTINUE
         IF (IFKEY .EQ. 1) THEN
             IFEWGR=IFEWGR+1
             READ(1,10,ERR=230) RECORD
             GOTO 3
         ELSE
             IF (IFEWGR .EQ. 1)THEN
               WRITE(3,*) RECORD(12:90)
             ELSE
               WRITE(3,*) RECORD(2:90)
             ENDIF
         ENDIF
         REWIND(3)
         READ(3,*,ERR=8) (FEWGROUP(IFEW),IFEW=1,69)
8              REWIND(3)
            ENDIF
            IF (RECORD(1:7) .EQ. '> PRINT' .AND.
     >       RECORD(9:15) .NE. '1 1 1 0') THEN
         WRITE(*,*) '*** ERROR ***  "PRINT" STATEMENT IN',
     >                ' EDIT SECTION OF INPUT FILE IS WRONG: '
         WRITE(*,*) ' '
         WRITE(*,*) RECORD(1:20)
         WRITE(*,*) ' '
         WRITE(*,*) 'SHOULD START WITH "1 1 1 0 ...".',
     >                '  RERUN CASE.'
         STOP
            ENDIF
            IF (RECORD(1:10) .EQ. '> BUCKLING') THEN
         WRITE(3,*) RECORD(12:90)
         REWIND(3)
         READ(3,*) BUCK1,BUCK2
         REWIND(3)
         BUCKTOT=BUCK1+BUCK2
            ENDIF
            INUMTH=0
            IF (RECORD(1:11) .EQ. '> PARTITION') THEN
         DO 14 IR=13,89
             IRR=IR+1
             IF (RECORD(IR:IR) .EQ. ' ' .AND.
     >                RECORD(IRR:IRR) .NE. ' ')THEN
               NUMTH=NUMTH+1
             ELSEIF (RECORD(IR:IRR) .EQ. '  ' .AND.
     >                INUMTH .EQ. 0)THEN
               NUMTH=NUMTH+1
               INUMTH=1
             ENDIF
14             CONTINUE
         WRITE(3,*) RECORD
         REWIND(3)
         READ(3,*) DUMMY7,DUMMY6,(GRPBND(K),K=1,NUMTH)
         REWIND(3)
            ENDIF
            READ(1,10,ERR=230) RECORD
            FLAG12 = RECORD(4:16)
11       CONTINUE
        WRITE(2,*) RECORD
        REWIND(2)
        READ(2,*) NGROUPS
        REWIND(2)
        DO 12 I1=1,3
            READ(1,10,ERR=230) RECORD
```

```
12        CONTINUE
          DO 13 I2=1,NGROUPS
              READ(1,*) DUM1,DUM2,DUM3,ABSORB(I,I2),DUM4,DUM5,
     >         FLUX(I,I2),DUM6,DUM7,DUM8,DUM9,DIFF(I,I2)
13        CONTINUE
          READ(1,10,ERR=230) RECORD
          FLAG12 = RECORD(1:12)
          DO 15 WHILE (FLAG12 .NE. ' 2 GROUPS...')
              READ(1,10,ERR=230) RECORD
              FLAG12 = RECORD(1:12)
15        CONTINUE
          WRITE(2,*) RECORD
25        CONTINUE
          REWIND (2)
          READ(2,30) DUMMY,KVALUE(I)
          READ(1,10,ERR=230) RECORD
          READ(1,10,ERR=230) RECORD
          READ(1,10,ERR=230) RECORD
          READ(1,10,ERR=230) RECORD
          REWIND (2)
          WRITE(2,*) RECORD
          REWIND (2)
          READ(2,31) DUMMY2,FDIFF(I),FABS(I),DUMMY3,FNUFIS(I),
     >         FLUX1
          FABS(I)=(FABS(I)+(FDIFF(I)*BUCKTOT))*FLUX1
          FNUFIS(I)=FNUFIS(I)*FLUX1
          READ(1,10,ERR=230) RECORD
          REWIND (2)
          WRITE(2,*) RECORD
          REWIND (2)
          READ(2,31) DUMMY2,THDIFF(I),THABS(I),DUMMY3,THNUFIS(I),
     >         FLUX2
          THABS(I)=(THABS(I)+(THDIFF(I)*BUCKTOT))*FLUX2
          THNUFIS(I)=THNUFIS(I)*FLUX2
          TOTNUFIS(I)=FNUFIS(I)+THNUFIS(I)
30        FORMAT(A53,F7.5)
31        FORMAT(A17,F5.3,2X,E10.4,A14,E10.4,2X,E10.4)
40        FORMAT(A15,F4.1,A3)
          ETAF(I)=THNUFIS(I)/THABS(I)
          EPSILON(I)=TOTNUFIS(I)/THNUFIS(I)
          P(I)=THABS(I)/(THABS(I)+FABS(I))
          REWIND (2)

*  Calculate S(N):

          DO 702 K1=1,2
              DO 703 K2=1,69
           TOTABSR(K1,K2)=0.
           TOTFLUX(K1,K2)=0.
           LEAKAGE(K1,K2)=0.
703           CONTINUE
702       CONTINUE

          DO 700 IFEW=1,NUMTH
              DO 701 IMANY=1,NGROUPS
           IF (GRPBND(IFEW) .EQ. FEWGROUP(IMANY))THEN
               NGRPBND(IFEW)=IMANY
           ENDIF
701           CONTINUE

              IF (IFEW .EQ. 1) THEN
           NSTART=1
              ELSE
           NSTART=NGRPBND(IFEW-1)+1
              ENDIF
              DO 710 IMANY=NSTART,NGRPBND(IFEW)
           TOTABSR(I,IFEW)=(ABSORB(I,IMANY)*FLUX(I,IMANY))+
     >                (BUCKTOT*DIFF(I,IMANY)*FLUX(I,IMANY))+
     >                TOTABSR(I,IFEW)
           TOTFLUX(I,IFEW)=FLUX(I,IMANY)+TOTFLUX(I,IFEW)
           LEAKAGE(I,IFEW)=BUCKTOT*DIFF(I,IMANY)*
     >                FLUX(I,IMANY)+LEAKAGE(I,IFEW)
710           CONTINUE
              ABSRATE(I,IFEW) = TOTABSR(I,IFEW)
              TOTABS(I) = TOTABS(I) + TOTABSR(I,IFEW)
```

```
            TOTLEAK(I) = TOTLEAK(I) +LEAKAGE(I,IFEW)
700       CONTINUE

          DO 720 IFEW=2,NUMTH
            ABSUM1=0.
            ABSUM2=0.
            IBEFORE=IFEW-1
            DO 730 I2FEW=IBEFORE,NUMTH
         ABSUM2=ABSUM2+ABSRATE(I,I2FEW)
730           CONTINUE
            ABSUM1=ABSUM2-ABSRATE(I,IBEFORE)
            S(I,IFEW)=ABSUM1/ABSUM2
720       CONTINUE

200   CONTINUE

*  Calculate eta, f:

230   REWIND(1)
      REWIND(2)
      DO 210 I=1,2
         READ(1,10,ERR=70) RECORD
         FLAG7 = RECORD(1:7)
         FLAG8 = RECORD(1:8)
70        DO 80 WHILE ((FLAG7 .NE. 'NUCLIDE') .AND.
     >            (FLAG8 .NE. '> READ 1'))
            READ(1,10,ERR=220) RECORD
            FLAG7 = RECORD(1:7)
            FLAG8 = RECORD(1:8)
80        CONTINUE
         IF (FLAG8 .EQ. '> READ 1')THEN
            GOTO 220
         ELSE
            FLAG5 = RECORD(11:15)
            IF (FLAG5 .NE. 'U235 ' .AND. FLAG5 .NE. 'U238 ' .AND.
     >        FLAG5 .NE. 'PU239' .AND. FLAG5 .NE. 'TH232' .AND.
     >        FLAG5 .NE. 'U233 ' .AND. FLAG5 .NE. 'U234 ' .AND.
     >        FLAG5 .NE. 'U236 ' .AND. FLAG5 .NE. 'NP239' .AND.
     >        FLAG5 .NE. 'PU240' .AND. FLAG5 .NE. 'TH241' .AND.
     >        FLAG5 .NE. 'AM242' .AND. FLAG5 .NE. 'PA233') THEN
          GOTO 92
            ELSE
          IFLAG=1
          DO 82 N=1,9
             READ(1,10,ERR=240) RECORD
82              CONTINUE
          IF (RECORD(1:7) .EQ. 'FISSION') THEN
             GOTO 92
          ENDIF
          WRITE(2,*) RECORD
          READ(1,10,ERR=240) RECORD
          DO 83 N=1,NUMTH
             READ(1,10,ERR=240) RECORD
83              CONTINUE
          WRITE(2,*) RECORD
          REWIND(2)
          READ(2,90) DUMMY5,(DUMMY4(J),J=1,6)
          JTOT=1
85              IF (DUMMY4(JTOT) .EQ. 'TOTAL        ')THEN
             JTOTFLAG=JTOT-1
          ELSE
             JTOT=JTOT+1
             GOTO 85
          ENDIF
90              FORMAT(A8,2X,6A13)
          READ(2,*) DUMMY5,(DUMMY4(J),J=1,JTOTFLAG),VALUE
          THFUABS=THFUABS+VALUE
            ENDIF
         ENDIF
         IF (IFLAG .EQ. 0) THEN
            WRITE(*,*) 'OUTPUT FILE DOES NOT CONTAIN REACTION',
     >        ' RATE DATA.  RERUN CASE.'
            STOP
         ENDIF
92        READ(1,10,ERR=240) RECORD
```

```
         FLAG7 = RECORD(1:7)
         FLAG8 = RECORD(1:8)
         REWIND(2)
         GOTO 70
 220      IF (IFLAG .EQ. 0) THEN
             WRITE(*,*) '*** ERROR ***  OUTPUT FILE DOES NOT',
     >         ' CONTAIN REACTION RATE DATA.  RERUN CASE.'
             STOP
         ENDIF
         F(I) = THFUABS/THABS(I)
         ETA(I) = ETAF(I)/F(I)
         THFUABS=0.
 210  CONTINUE

*  Calculate change in reactivity factors:

      DELTAET=ETA(2)-ETA(1)
      DELTAEP=EPSILON(2)-EPSILON(1)
      DELTAF=F(2)-F(1)
      DO 900 IFEW=2,NUMTH
         DELTAS(IFEW)=S(2,IFEW)-S(1,IFEW)
 900  CONTINUE
      DELTAP=P(2)-P(1)

*  Generate Method 1 void effect values:

      PMULT=1.
 240  DO 800 IFEW=2,NUMTH
         PMULT=PMULT*S(1,IFEW)
 800  CONTINUE
      DO 810 IFEW=2,NUMTH
         PFACT(IFEW)=ETAF(1)*EPSILON(1)*PMULT/S(1,IFEW)
 810  CONTINUE

      EFFECT(1)=(KVALUE(2)-KVALUE(1))*1000

      ETAFACT=P(1)*EPSILON(1)*F(1)
      FFACT=P(1)*EPSILON(1)*ETA(1)
      EPSIFACT=P(1)*ETAF(1)

      DO 820 IFEW=2,NUMTH
         PCONT(1,IFEW)=DELTAS(IFEW)*PFACT(IFEW)*1000
 820  CONTINUE
      ETACONT(1)=DELTAET*ETAFACT*1000
      FCONT(1)=DELTAF*FFACT*1000
      EPSICONT(1)=DELTAEP*EPSIFACT*1000
      DO 825 IFEW=2,NUMTH
         ABSUMP(1)=ABSUMP(1)+ABS(PCONT(1,IFEW))
 825  CONTINUE

      TAYLOR1=DELTAP*DELTAEP*ETA(1)*F(1)
     >         + DELTAP*DELTAF*ETA(1)*EPSILON(1)
     >         + DELTAP*DELTAET*EPSILON(1)*F(1)
     >         + DELTAEP*DELTAF*ETA(1)*P(1)
     >         + DELTAEP*DELTAET*F(1)*P(1)
     >         + DELTAF*DELTAEP*ETA(1)*P(1)
      TAYLOR1=1000.*TAYLOR1

      ABSUM(1)=ABS(ETACONT(1))+ABS(FCONT(1))+ABS(EPSICONT(1))
     >          +ABSUMP(1)
      ETACONT(1)=ETACONT(1)+((ABS(ETACONT(1))/ABSUM(1))*TAYLOR1)
      FCONT(1)=FCONT(1)+((ABS(FCONT(1))/ABSUM(1))*TAYLOR1)
      EPSICONT(1)=EPSICONT(1)+((ABS(EPSICONT(1))/ABSUM(1))*TAYLOR1)
      DO 920 IFEW=2,NUMTH
         PCONT(1,IFEW)=PCONT(1,IFEW)+((ABS(PCONT(1,IFEW))/ABSUM(1))
     >                    *TAYLOR1)
 920  CONTINUE

      DO 925 IFEW=2,NUMTH
         SUMP(1)=SUMP(1)+PCONT(1,IFEW)
 925  CONTINUE
      SUM(1)=SUMP(1)+ETACONT(1)+EPSICONT(1)+FCONT(1)

*  Generate Method 2 void effect values:
```

```
      EFFECT(2)=EFFECT(1)/(KVALUE(2)*KVALUE(1))
      FACTOR1=1.-((KVALUE(1)-1.)/KVALUE(1))
      FACTOR2=1.-((KVALUE(2)-KVALUE(1))/KVALUE(1))

      DO 826 IFEW=2,NUMTH
         PCONT(2,IFEW)=DELTAS(IFEW)/S(1,IFEW)*1000*FACTOR1
826   CONTINUE
      ETACONT(2)=DELTAET/ETA(1)*1000*FACTOR1
      FCONT(2)=DELTAF/F(1)*1000*FACTOR1
      EPSICONT(2)=DELTAEP/EPSILON(1)*1000*FACTOR1
      DO 827 IFEW=2,NUMTH
         ABSUMP(2)=ABSUMP(2)+ABS(PCONT(2,IFEW))
827   CONTINUE

      TAYLOR2=(DELTAP*DELTAEP)/(P(1)*EPSILON(1))
     >         + (DELTAP*DELTAF)/(P(1)*F(1))
     >         + (DELTAP*DELTAET)/(P(1)*ETA(1))
     >         + (DELTAEP*DELTAF)/(EPSILON(1)*F(1))
     >         + (DELTAEP*DELTAET)/(EPSILON(1)*ETA(1))
     >         + (DELTAF*DELTAET)/(F(1)*ETA(1))
      TAYLOR2=TAYLOR2*1000.*FACTOR1

      ABSUM(2)=ABS(ETACONT(2))+ABS(FCONT(2))+ABS(EPSICONT(2))
     >          +ABSUMP(2)
      ETACONT(2)=(ETACONT(2)+((ABS(ETACONT(2))/ABSUM(2))*TAYLOR2))
     >            *FACTOR2
      FCONT(2)=(FCONT(2)+((ABS(FCONT(2))/ABSUM(2))*TAYLOR2))
     >            *FACTOR2
      EPSICONT(2)=(EPSICONT(2)+((ABS(EPSICONT(2))/ABSUM(2))*TAYLOR2))
     >            *FACTOR2
      DO 940 IFEW=2,NUMTH
         PCONT(2,IFEW)=(PCONT(2,IFEW)+((ABS(PCONT(2,IFEW))/ABSUM(2))
     >                  *TAYLOR2))*FACTOR2
940   CONTINUE
      DO 945 IFEW=2,NUMTH
         SUMP(2)=SUMP(2)+PCONT(2,IFEW)
945   CONTINUE
      SUM(2)=SUMP(2)+ETACONT(2)+EPSICONT(2)+FCONT(2)

*  Write output, Methods 1 and 2:

      WRITE(*,250) 'VOID EFFECT 1 = ',EFFECT(1),'(DELTA-K)   ',
     >  'VOID EFFECT 2 = ',EFFECT(2),'(DELTA-RHO)'
      WRITE(*,*) ' '
      WRITE(*,300) '     DELTA ETA = ',ETACONT(1),ETACONT(1)/
     > SUM(1)*100,'     DELTA ETA = ',ETACONT(2),ETACONT(2)/
     >  SUM(2)*100
      WRITE(*,300) '       DELTA F = ',FCONT(1),FCONT(1)/SUM(1)*100,
     >  '       DELTA F = ',FCONT(2),FCONT(2)/SUM(2)*100
      DO 830 IFEW=2,NUMTH
         WRITE(*,330) '    DELTA P(',IFEW-1,') = ',PCONT(1,IFEW),
     >      PCONT(1,IFEW)/SUM(1)*100,'    DELTA P(',IFEW-1,') = ',
     >      PCONT(2,IFEW),PCONT(2,IFEW)/SUM(2)*100
830   CONTINUE
      WRITE(*,300) 'DELTA EPSILON = ',EPSICONT(1),EPSICONT(1)/
     >   SUM(1)*100,'DELTA EPSILON = ',EPSICONT(2),EPSICONT(2)/
     >   SUM(2)*100

*  Write output, general:

      WRITE(*,500)
      WRITE(*,350) 'COOLED','VOIDED'
      WRITE(*,400) '     ETA:',ETA(1),ETA(2),
     >  '(Neutrons per thermal fuel absorption)'
      WRITE(*,400) '       F:',F(1),F(2),
     > '(Thermal utilization)'
      DO 840 IFEW=2,NUMTH
         IF (IFEW .EQ. 2)THEN
            ISTART=1
         ELSE
            ISTART=GRPBND(IFEW-2)+1
         ENDIF
         IEND=GRPBND(IFEW-1)
         WRITE(*,450) '    P(',IFEW-1,'):',S(1,IFEW),S(2,IFEW),
     >      ISTART,IEND
```

```
840   CONTINUE
      WRITE(*,400) 'EPSILON:',EPSILON(1),EPSILON(2),
     > '(Fast fission)                          '
      WRITE(*,*) ' '
      WRITE(*,400) '  K-INF:',KVALUE(1),KVALUE(2)

*  Check K-values by multiplying five factors together:

      STOT(1)=1.
      STOT(2)=1.
      DO 850 IFEW=2,NUMTH
         STOT(1)=S(1,IFEW)*STOT(1)
         STOT(2)=S(2,IFEW)*STOT(2)
850   CONTINUE
      ERRORK(1)=KVALUE(1)-(ETA(1)*F(1)*EPSILON(1)*STOT(1))
      ERRORK(2)=KVALUE(2)-(ETA(2)*F(2)*EPSILON(2)*STOT(2))
      IF (ABS(ERRORK(1)) .GT. DELTAK .OR.
     >  ABS(ERRORK(2)) .GT. DELTAK)THEN
         WRITE(*,*) ' *** ERROR ***  DIFFERENCE IN K-VALUES',
     >     ' BETWEEN WIMS AND THIS CODE > 1 mk.'
      ENDIF

*  Check void effect values by adding five factors together:

      ERRORP(1)=EFFECT(1)-SUM(1)
      ERRORP(2)=EFFECT(2)-SUM(2)
      IF (ABS(ERRORP(1)) .GT. DELTARHO .OR.
     >  ABS(ERRORP(2)) .GT. DELTARHO)THEN
         WRITE(*,*) ' *** ERROR ***  DIFFERENCE IN VOID EFFECTS',
     >     ' BETWEEN WIMS AND THIS CODE > 1 mk.'
      ENDIF

250   FORMAT(1X,A16,F6.1,' mk',1X,A11,2X,A16,F6.1,' mk',1X,A11)
300   FORMAT(1X,A16,F6.1,' mk',1X,'(',F6.1,'%)',4X,
     >         A16,F6.1,' mk',1X,'(',F6.1,'%)')
330   FORMAT(1X,A11,I1,A4,F6.1,' mk',1X,'(',F6.1,'%)',4X,
     >           A11,I1,A4,F6.1,' mk',1X,'(',F6.1,'%)')
350   FORMAT(1X,9X,A6,2X,A6)
400   FORMAT(1X,A8,2X,F5.3,3X,F5.3,3X,A38)
450   FORMAT(1X,A5,I1,A2,2X,F5.3,3X,F5.3,3X,
     >  '(Escape from groups ',I2,' to ',I2,')')
500   FORMAT(1X,'-----------------------------------------------',
     >    '---------------------------')
      END
```

B.2 Sample Output

```
VOID EFFECT 1 =   21.4 mk (DELTA-K)    VOID EFFECT 2 =   17.1 mk (DELTA-RHO)

    DELTA ETA =    2.2 mk (  10.4%)        DELTA ETA =    1.8 mk (  10.4%)
      DELTA F =    4.2 mk (  19.6%)          DELTA F =    3.4 mk (  19.6%)
   DELTA P(1) =   -3.2 mk ( -14.8%)       DELTA P(1) =   -2.5 mk ( -14.9%)
   DELTA P(2) =   13.1 mk (  60.9%)       DELTA P(2) =   10.4 mk (  60.9%)
DELTA EPSILON =    5.1 mk (  24.0%)    DELTA EPSILON =    4.1 mk (  24.0%)

-------------------------------------------------------------------------

          COOLED  VOIDED
    ETA:  1.307   1.310   (Neutrons per thermal fuel absorption)
      F:  0.937   0.940   (Thermal utilization)
   P(1):  0.974   0.971   (Escape from groups  1 to  5)
   P(2):  0.857   0.867   (Escape from groups  6 to 45)
EPSILON:  1.085   1.090   (Fast fission)

  K-INF:  1.109   1.130
```

Appendix C

The following is adapted from a paper presented at the 1992 ANS Winter Meeting, November 15-20, Chicago (*Trans. Am. Nucl. Soc.*, **66**, 525).

DEPENDENCE OF CALCULATED VOID REACTIVITY ON FILM BOILING REPRESENTATION IN A CANDU LATTICE

by

J.J. Whitlock and Wm.J. Garland

Department of Engineering Physics
McMaster University, Hamilton, Ontario, Canada

The distribution dependence of void reactivity in a CANDU (CANada Deuterium Uranium) lattice is studied, specifically in the regime of film boiling. A heterogeneous model of this phenomenon predicts a 4% increase in void reactivity over a homogeneous model for fresh fuel, and 11% at discharge. An explanation for this difference is offered, with regard to differing changes in neutron mean free path upon voiding.

C.1 INTRODUCTION

Partial voiding of a fuel channel can lead to complicated neutronic analysis due to highly non-uniform spatial distributions. Total void reactivity is usually calculated by modelling a lattice cell with and without coolant and defining either an absolute quantity (Equation (C.1)), based on deviation in multiplication factor (k), or a relative quantity (Equation (C.2)), based on deviation in reactivity (ρ).

$$\Delta k \equiv \left[k_\infty(\text{voided}) - k_\infty(\text{cooled})\right] \times 1000 \quad \text{mk} \tag{C.1}$$

$$\Delta \rho \equiv \rho(\text{voided}) - \rho(\text{cooled}) = \left[\frac{\Delta k}{k_\infty(\text{voided})\, k_\infty(\text{cooled})}\right] \times 1000 \quad \text{mk} \tag{C.2}$$

Such calculations of void reactivity in a CANDU lattice agree favourably with both experiments[1] in a small test reactor, and Monte-Carlo neutron transport simulation[2]. In practice there is only slight deviation in the predictions of Equations (C.1) and (C.2), the latter having more direct relevance to kinetics calculations. For simplicity, however, Equation (C.1) for reactivity differences will be used in this paper.

Partial voids can be modelled in a similar manner after determining an effective coolant density based on void fraction. This study was initiated by curiosity over the legitimacy of such a homogeneous treatment of partial voiding, given that voiding processes generally lead to highly heterogeneous partial void distributions. In boiling phenomena, for example, there are several different spatial distributions between initial and full boiling[3]. Although one could argue in favour of homogenous modelling in the regime of turbulence, it is not clear that this approach is valid in more spatially distinct regimes such as film boiling.

Film boiling begins when heat is no longer transported efficiently from the fuel sheath by nucleate boiling. Bubbles coalesce and a period of fuel sheath "dry-out" begins, during which coolant no longer wets the sheath surface. In a critical CANDU fuel lattice this condition is significant since it removes scattering material from a location (between fuel elements) of relatively high neutron importance. It should be noted that this boiling regime represents a radical departure from operating conditions, and therefore the core is

not expected to remain critical. However, a study of this nature does augment current knowledge of void reactivity in the CANDU lattice. It should also be noted that concurrent physical phenomena such as thermal expansion and fuel temperature rise have not been included in this analysis, in order to isolate the film boiling effect.

The effect on reactivity of coolant voiding in this lattice has been well-documented[4,5]. Upon coolant voiding, loss of moderation near the fuel causes a shift of the neutron energy spectrum. Less down-scattering from the fast region (> 1 MeV) increases both fast fission and leakage, while decreasing resonance absorption. Less up-scattering in the thermal region (< 0.625 eV) increases the yield in U^{235} by softening the spectrum, while decreasing the yield in Pu^{239} by shifting thermal flux away from the 0.3 eV resonance. Additionally, thermal neutron flux increases near the centre pins and decreases in the outer region and moderator. The net reactivity effect (see Equation (C.1)) is on the order of +20 mk for complete voiding from operating conditions, decreasing with burnup but always positive.

C.2 DETAILS OF STUDY

A description of the CANDU reactor system can be found elsewhere[6]. The lattice cell used in this study, shown in Figure C.1, is typical of contemporary CANDU designs. A cylindrical array of 37 natural Uranium fuel pins (each O.D. 1.3 cm) at 882°C sits in a Zircalloy pressure tube (O.D. 10.3 cm) filled with D_2O coolant at 290°C. This is surrounded by a Zircalloy calandria tube and D_2O moderator at 71°C, with an overall square pitch of 28.6 cm.

The lattice code WIMS-AECL[7] and Winfrith 69-group library were used in this study of the partial voiding phenomenon. Two approaches were employed: a "homogeneous model" averaged partial void over area, and a "heterogeneous model" used actual void distribution. Film boiling was represented as a voided annulus around each fuel pin, with thicknesses up to the "geometric limit" of 0.9 mm, where neighbouring annuli intersect (void fraction 0.43) and further partial void expansion can no longer be simply modelled in the heterogeneous case.

The effect was studied first at zero burnup, followed by an analysis over fuel burnup. Since CANDU cores are continuously refuelled, conclusions about total core reactivity have most relevance when considering mid-burnup results, which best approximate equilibrium core behaviour[5].

C.3 RESULTS AND DISCUSSION

Figure C.2 shows the two reactivity effects, defined here using Equation (C.1). The results show a small but distinct difference in the predictions of the two models, with a maximum deviation (heterogeneous — homogeneous) of +0.37 mk, or approximately 4% of the predicted effect.

To investigate concerns that this small difference might be an artifact of the numerical treatment in WIMS-AECL, a second geometry with a single, central pin was studied (coolant and fuel temperatures: 600K and 300K, respectively). This amplified the effect by increasing the coolant-to-fuel ratio, which in turn permitted verification of the results using MCNP 4[8], a Monte-Carlo neutron transport code (it was impossible to detect the effect in the 37-element fuel array using MCNP 4 due to the large statistical error in k_∞ for practical run times). The results in Figure C.3 show a maximum deviation of about +10 mk around 50% voiding, with good agreement between WIMS-AECL and MCNP 4. This exercise helps to confirm the existence of a physical effect, as well as instill confidence in the methodology.

Figure C.4 illustrates the fast flux spectral change in the inner fuel pin of the 37-element fuel array, with 0.9 mm annular void formation. Average fast flux (> 0.821 MeV) increased by 5.5 % for the

heterogeneous case, and 4.5 % for the homogeneous case. A comparison of flux change throughout the fuel in three different spectral ranges is given in Table C.1. Note that the heterogenous model predicts a greater change in most fuel rings and spectral ranges; the exception is the non-fast flux (< 0.821 MeV) in the outer (fourth) fuel ring. The last column in Table C.1 summarizes the spectral effect alone, obtained by taking a weighted sum of all fuel rings.

The origin of the effect is geometrical. A collection of discrete voids in the heterogeneous case allows a greater increase in neutron mean free path length within the fuel array, despite conservation of average coolant density. This is attributable to the proximity of fuel elements with the array, causing the slightest film voiding to lead to both a larger increase in streaming between elements, and a larger reduction in coolant moderation. The effect on the flux, evident in Table C.1, can be summarized using three groups:

(1) *Thermal Flux* arises from the moderator. Upon voiding, an increase in mean free path length leads to a spatial flux shift towards the centre of the fuel array. The heterogeneous model, therefore, predicts an increase in this shift relative to the homogeneous model, although cancellation between the outer and inner regions causes the net effect on thermal flux throughout the fuel to be very small in both cases (about 0.2 – 0.3 %). Additionally, upon voiding, the spectral shift towards a lower average neutron temperature is observed to be greater in the heterogeneous case, although this information is not presented in Table C.1.

(2) *Fast Flux* arises from the fuel. Upon voiding, this component is increased by loss of coolant moderation and decreased by greater leakage to the bulk moderator. The loss of moderation is the dominant effect, and the heterogeneous model predicts a greater increase in fast flux across the fuel array.

(3) *Resonance Flux* arises partly from coolant moderation within the fuel array. Upon voiding, reduction of this moderation leads to a corresponding reduction in resonance flux across the fuel array, with a smaller effect in the outer rings. Accordingly, the heterogeneous model predicts a greater reduction in resonance flux across the array, with a smaller effect in the outer rings.

Such differences in flux response will be manifested in nuclide reaction rates. Table C.2 lists the partial reactivity (isotopic yield / total cell absorption) for U^{235} and U^{238} in the cooled and 0.9 mm annular void (0.43 void fraction) cases. Since fresh fuel was modelled, these partial reactivities are the only components of fissile reactivity in the fuel. A total increase of 0.52 mk for U^{238} is observed between the heterogeneous and homogeneous results, while a slight decrease (–0.17 mk) is observed for U^{235}, indicating that the effect is not significantly related to thermal flux (for this geometry and for fresh fuel). Rather, the difference between the two models appears mostly related to differences in predicted U^{238} reactivity across the fuel, while a greater difference in U^{235} reactivity in the inner three rings of fuel is almost cancelled by a decrease in the outer ring.

The results for single-pin geometry, on the other hand, show entirely opposite behaviour. A comparison of the cooled and 1.85 cm annular void (void fraction 0.24) cases in Table C.3 shows the important component here to be the doubling of U^{235} reactivity, since the U^{238} contribution is small. This is to be expected, since the absence of surrounding fuel pins decreases the effects of fast fission and resonance absorption.

Figure C.5 shows the effect on reactivity of burnup in the 37-element, 0.9 mm film void case, as predicted by the two models. The time-dependent discrepancy is shown in Figure C.6 in terms of both absolute reactivity and a percentage of the total effect. At discharge burnup (7500 MWd/Mg-initial U) the difference is 0.70 mk, or about 11 %. At mid-burnup the difference is 0.56 mk, or about 8 %.

Figure C.5 is another listing of partial reactivities (isotopic yield / total cell absorption), this time at discharge burnup, and includes both Pu^{239} and Pu^{241}. Since U^{238} is fairly insensitive to burnup its contribution to both total reactivity and the film void model discrepancy does not change significantly. U^{235} contributes less to both total reactivity and the discrepancy, due to depletion. Pu^{239} is affected by the same opposing shifts in thermal flux across the fuel array as is U^{235}, although its net contribution is less negative in the heterogeneous case than in the homogeneous case, adding +0.13 mk to the observed discrepancy. The effect of burnup, therefore, is to increase the difference in predictions of the homogeneous and heterogeneous models due to the depletion of U^{235}, which has a reducing effect on the discrepancy, and the creation of Pu^{239}, which has an enlarging effect.

C.4 CONCLUSION

A reactivity difference is found when film boiling is modelled heterogeneously and homogeneously. An increase in fast flux, due to a greater increase in mean free path length, is the explanation. The effect increases with burnup due to depletion of U^{235} and creation of Pu^{239}. In contemporary designs the effect is minor (about 4 % and 11 % at zero and full burnup, respectively), but a small effect could still be significant in postulated low void reactivity CANDU fuel bundles[9].

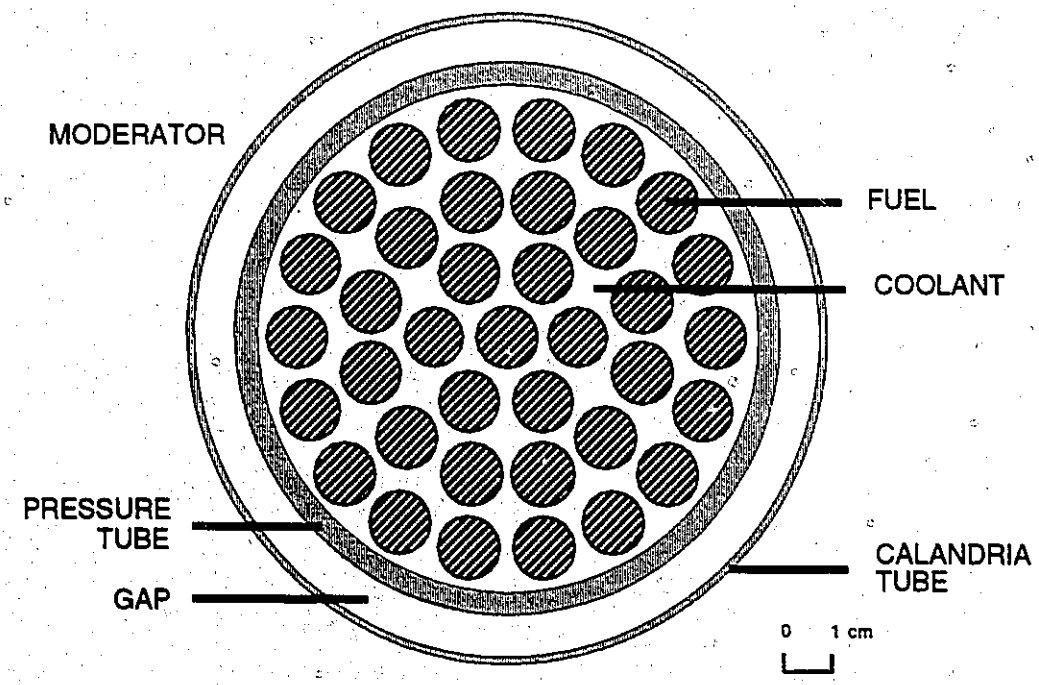

Figure C.1 Geometry of 37-element lattice cell.

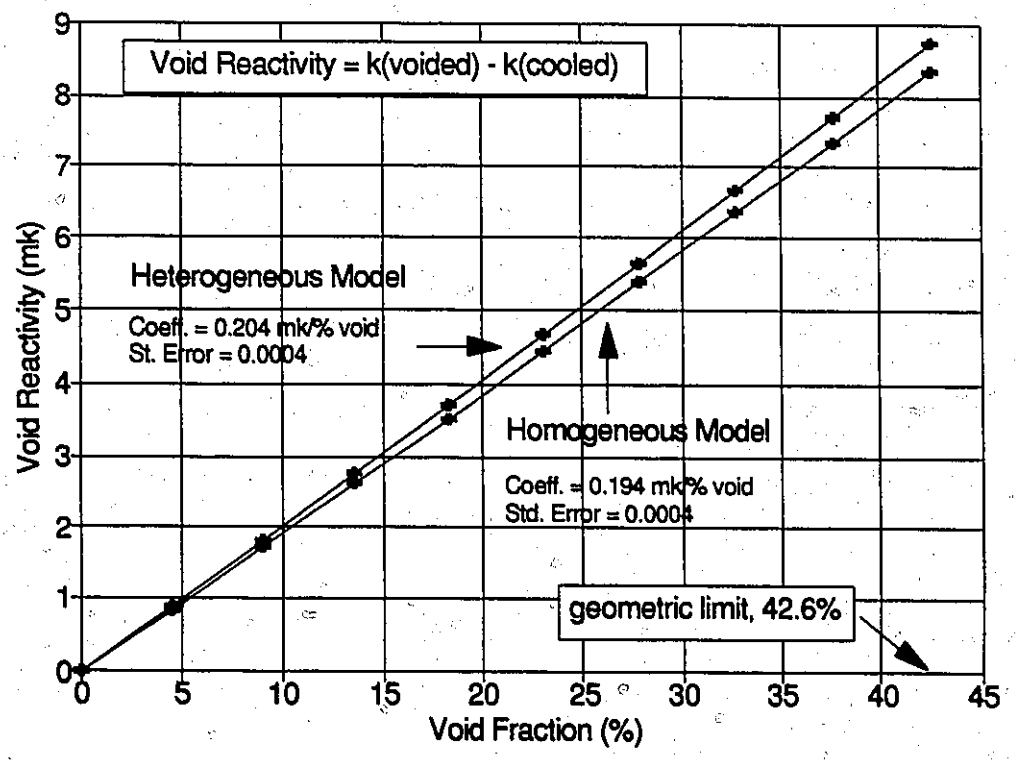

Figure C.2 **Void reactivity due to film boiling in 37-element cell, as a function of void fraction: Comparison of predictions using heterogeneous and homogeneous models.**

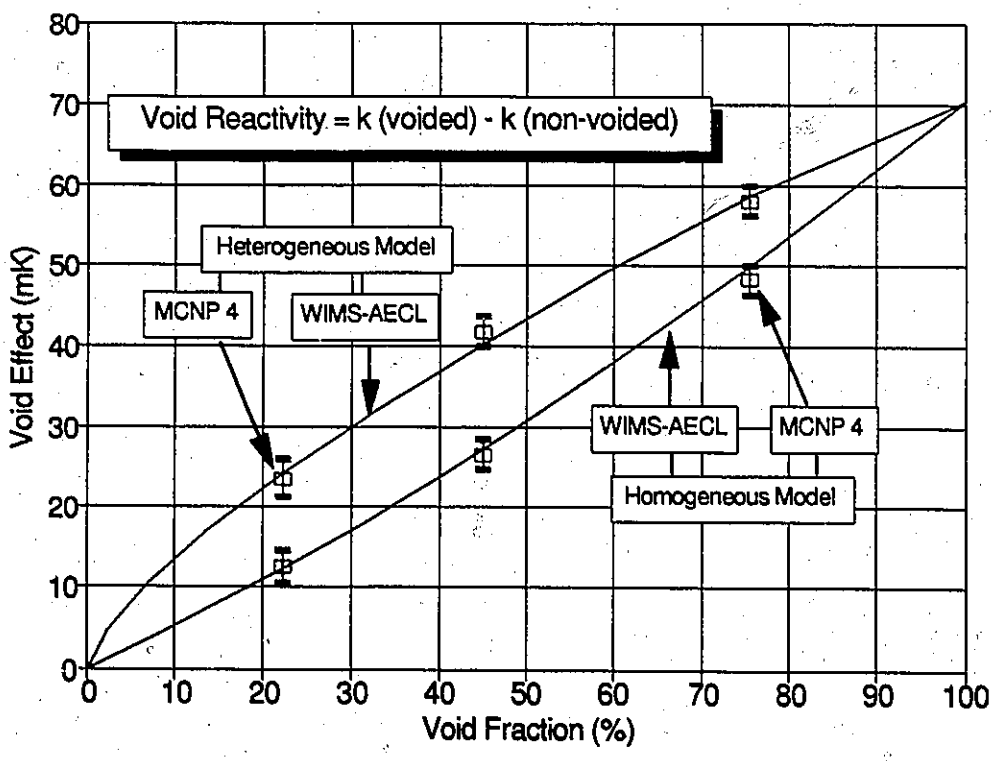

Figure C.3 **Void reactivity due to annular voids in single pin cell, as a function of void fraction: Comparison of WIMS-AECL and MCNP-4 predictions.**

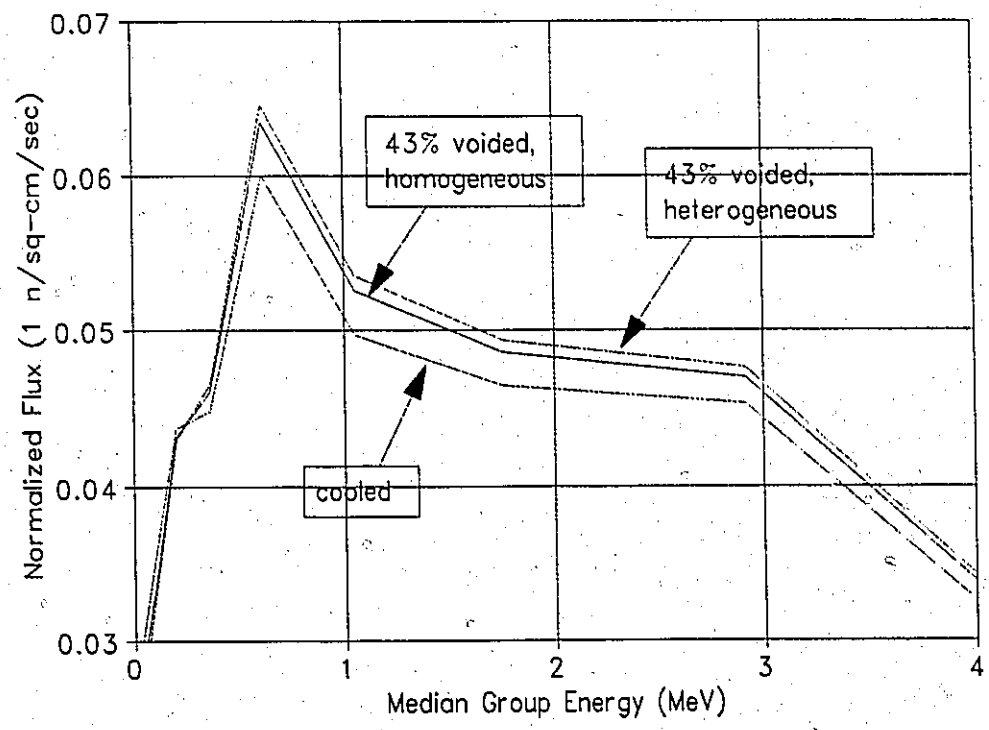

Figure C.4 **Fast neutron spectrum in inner fuel pin of 37-element cell, before and after 0.9 mm annular void formation (43% void fraction): Comparison of predictions using heterogeneous and homogeneous models.**

Table C.1 Change (%) in average fuel flux spectrual distribution with 0.9 mm annular void formation (43% void fraction) in 37-element cell.

Spectrum Range	Model Used	Fuel Ring 1 (%)	Fuel Ring 2 (%)	Fuel Ring 3 (%)	Fuel Ring 4 (%)	Total Fuel (%)
Fast (> .821 MeV)	heterogeneous	6.70	6.26	5.59	5.17	5.52
	homogeneous	4.81	4.85	4.58	4.32	4.50
	het. / hom.	1.39	1.05	1.22	1.20	1.23
Resonance (.625 eV - .821 MeV)	heterogeneous	−2.66	−2.28	−1.47	−0.15	−0.99
	homogenous	−2.21	−1.96	−1.38	−0.29	−0.97
	het. / hom.	1.21	1.50	1.06	0.53	1.03
Thermal (< .625 eV)	heterogeneous	1.50	1.05	0.16	−0.88	−0.17
	homogeneous	1.17	0.70	−0.03	−0.93	−0.32
	het. / hom.	1.29	1.50	4.66	0.95	0.52

Table C.2 Change in reactivity ($\Delta^{Yield}/_{Total\ Absorption}$) of U-235 and U-238 with 0.9 mm annular void formation (43% void fraction) in 37-element cell.

	Model Used	Fuel Ring 1 (mk)	Fuel Ring 2 (mk)	Fuel Ring 3 (mk)	Fuel Ring 4 (mk)	Total (mk)
U^{238}	heterogeneous	0.11	0.52	0.99	1.17	2.85
	homogeneous	0.08	0.45	0.82	0.98	2.33
	het. – hom.	0.03	0.13	0.17	0.19	0.52
	% difference	39.2 %	28.6 %	21.2 %	19.1 %	22.3 %
U^{235}	heterogeneous	0.65	3.28	3.78	−1.68	6.03
	homogeneous	0.59	2.83	3.50	−0.72	6.20
	het. – hom.	0.07	0.45	0.27	−0.96	−0.17
	% difference	11.2 %	16.0 %	7.8 %	132.9 %	−2.7 %

Table C.3 Change in reactivity ($\Delta^{Yield}/_{Total\ Absorption}$) of U-235 and U-238 with 1.85 cm annular void formation (24% void fraction) in single element cell.

	Model Used	Fuel Pin (mk)
U^{238}	heterogeneous	−0.16
	homogeneous	−0.03
	het. – hom.	−0.13
	% difference	433.3 %
U^{235}	heterogeneous	19.37
	homogeneous	9.76
	het. – hom.	9.61
	% difference	98.5 %

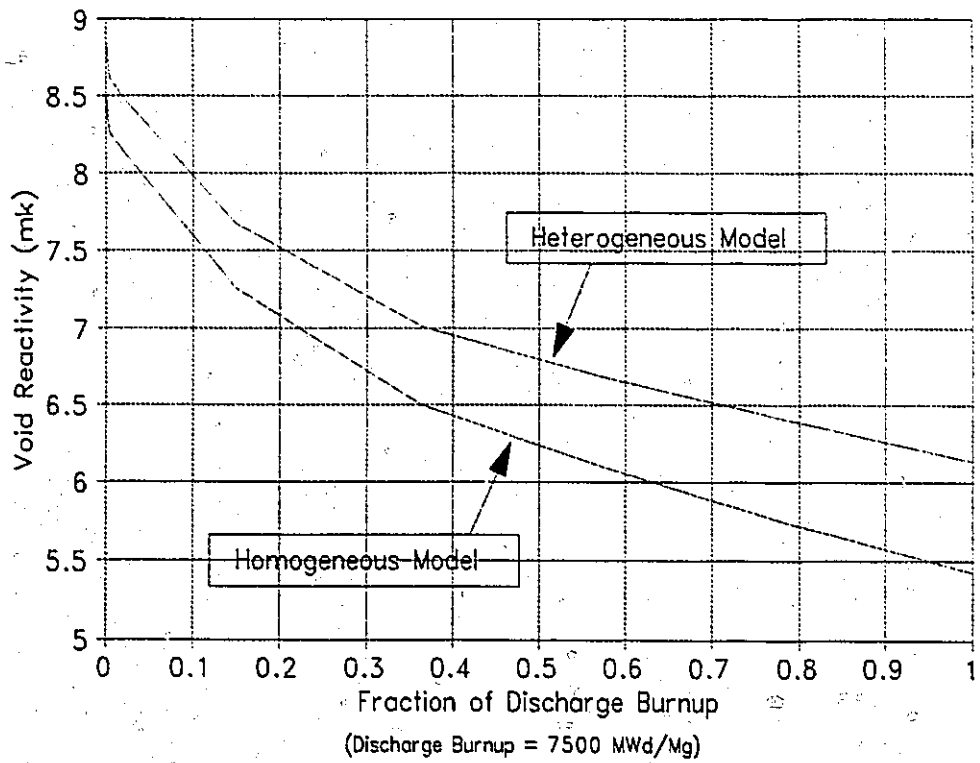

Figure C.5 **Effect of burnup on void reactivity with 0.9 mm annular void formation (43% void fraction): Comparison of predictions using heterogeneous and homogeneous models.**

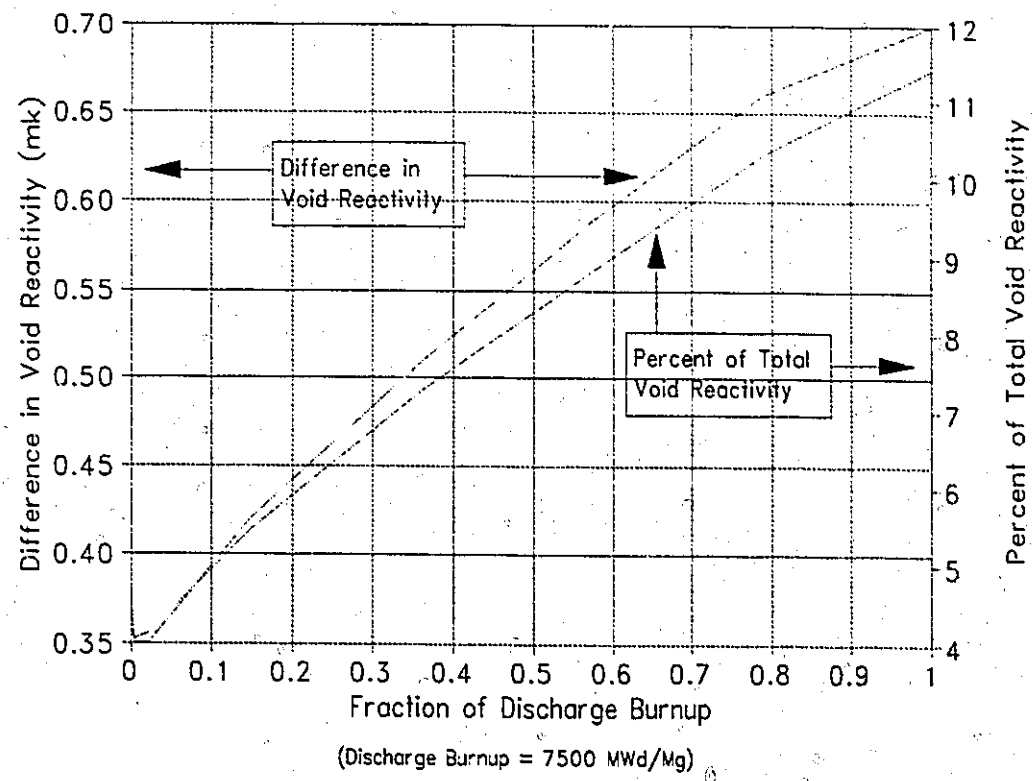

Figure C.6 **Effect of burnup on discrepancy between predictions of heterogeneous and homogeneous models for void reactivity with 0.9 mm annular void formation (43% void fraction).**

Table C.4 Change in reactivity ($\Delta^{Void}/_{Total\ Absorption}$) of U-235, U-238, Pu-239, and Pu-241 with 0.9 mm annular void formation (43% void fraction) in 37-element cell at discharge burnup (7500 MWd/Mg-U).

	Model Used	Fuel Ring 1 (mk)	Fuel Ring 2 (mk)	Fuel Ring 3 (mk)	Fuel Ring 4 (mk)	Total (mk)
U^{238}	heterogeneous	0.11	0.61	1.03	1.22	2.98
	homogeneous	0.08	0.48	0.85	1.02	2.43
	het. – hom.	0.03	0.13	0.18	0.20	0.55
	% difference	38.1 %	27.9 %	21.3 %	19.9 %	22.6 %
U^{235}	heterogeneous	0.30	1.49	1.75	0.25	3.79
	homogeneous	0.28	1.35	1.67	0.46	3.75
	het. – hom.	0.03	0.14	0.08	–0.21	0.04
	% difference	9.4 %	10.7 %	4.7 %	–45.8 %	1.0 %
Pu^{239}	heterogeneous	0.23	1.01	0.63	–2.50	–0.64
	homogeneous	0.21	0.87	0.50	–2.35	–0.77
	het. – hom.	0.02	0.13	0.13	–0.15	0.13
	% difference	7.7 %	15.4 %	26.0 %	–6.3 %	17.0 %
Pu^{241}	heterogeneous	0.03	0.14	0.17	–0.15	0.19
	homogeneous	0.02	0.12	0.16	–0.12	0.19
	het. – hom.	0.00	0.02	0.02	–0.03	0.00
	% difference	9.9 %	13.5 %	10.2 %	–29.5 %	0.3 %

C.5 ACKNOWLEDGEMENT

The authors wish to thank Mike Milgram, AECL – Chalk River Laboratories, for his invaluable assistance and guidance throughout this study.

C.6 REFERENCES

1. Kay, R.E., "Lattice Measurements With 37-Element Bruce Reactor Fuel in Heavy Water Moderator: Detailed Lattice Cell Parameters," AECL Technical Report, *AECL-5307*, 1976.

2. Craig, D.S., "A Comparison of Lattice Parameters for CANDU-type Lattices Obtained Using MCNP, WIMS, and WIMS With Resonance Reaction Rates From MCNP," AECL Technical Report, *AECL-9778*, 1989.

3. Collier, J.G., *Convective Boiling and Condensation*, 2nd ed., McGraw-Hill Inc., 1981.

4. Dastur, A.R., and Buss, D.B., "The Influence of Lattice Structure and Composition on the Coolant Void Reactivity in CANDU", *Proc. 11th Ann. Conf. CNS*, Toronto, 1990.

5. Griffiths, J., "Lattice Characteristics that Influence the Change in Reactivity with Coolant Voiding in CANDU Lattices," *Proc. 13th Ann. Sim. Symp. Can. Nucl. Soc.*, Chalk River Laboratories, 1987.

6. Griffiths, J., "Reactor Physics and Economic Aspects of the CANDU Reactor System," AECL Technical Report, *AECL-7615*, 1983.

7. Donnelly, J.V., "WIMS-CRNL. A User's Manual for the Chalk River Version of WIMS," AECL Technical Report, *AECL-8955*, 1986.

8. "MCNP 4 — Monte Carlo Neutron and Photon Transport Code System", *CCC-200A/B*, RSIC Computer Code Collection, Oak Ridge National Laboratory, 1991.

9. Dastur, A.R., Chan, P.S.W., Bowslaugh, D., "The Use of Depleted Uranium for the Reduction of Void Reactivity in CANDU Reactors," *Proc. 13th Ann. Conf. Can. Nucl. Soc.*, 1992.

Appendix D

The following is the WIMS-AECL input file for the reference 37-element CANDU lattice cell without burnup.

```
TITLE "WIMS 37-PIN NORMAL DESIGN, 92-08-19, J.WHITLOCK"
SEQUENCE PIJ
SCAN
NRODS 37 -12 0 0 4 2 1
PREOUT
ANNULUS 1 1.431 COOLANT
ANNULUS 2 2.179 COOLANT
ANNULUS 3 2.926 COOLANT
ANNULUS 4 3.674 COOLANT
ANNULUS 5 4.421 COOLANT
ANNULUS 6 5.1689 COOLANT
ANNULUS 7 5.6210 PT
ANNULUS 8 6.4478 VOID
ANNULUS 9 6.6002 CT
NPIJAN #
POLYGON 10 4 MODER 14.2875
ARRAY 1 1 1 0 0
RODSUB 1 1 0.6075 FUEL_1
RODSUB 1 2 0.654 CLAD
ARRAY 2 1 6 1.48845 0
RODSUB 2 1 0.6075 FUEL_2
RODSUB 2 2 0.654 CLAD
ARRAY 3 1 12 2.8753 0.261798
RODSUB 3 1 0.6075 FUEL_3
RODSUB 3 2 0.654 CLAD
ARRAY 4 1 18 4.3307 0
RODSUB 4 1 0.6075 FUEL_4
RODSUB 4 2 0.654 CLAD
MESH #
NEWRES
FEWGROUPS 1 2 3 4 5 6 7 8 9 10 11 12 13 14 15 16 17 18 19 20 21 S
22 23 24 25 26 27 28 29 30 31 32 33 34 35 36 37 38 39 40 41 42 S
43 44 45 46 47 48 49 50 51 52 53 54 55 56 57 58 59 60 61 62 63 64 S
65 66 67 68 69
TOLERANCE 1E-5
SUPPRESS 1 0 1 1 1  1 1 1 1 1  1 0 1 0 0 -1
MATERIAL COOLANT 0.80406 563.16 COOL H1=.028 D2=20.063 O16=79.909
MATERIAL MODER  1.0835 344.16 MODE  H1=.017 D2=20.083 O16=79.9
MATERIAL PT 6.57 563.16 MODER  ZR91=97.5 NB93=2.5 B10B=3.8E-5
MATERIAL VOID 0.0014 341.16 MODER  HE4=100.
MATERIAL CT 6.44 341.16 MODER ZR91=99.67 FE56=.16 CR52=.11 NI58=.06 S
     B10B=5.34E-5
MATERIAL CLAD 6.23 293.16 CLAD ZR91=99.67 FE56=.16 CR52=.11 NI58=.06 S
     B10B=5.34E-5
MATERIAL FUEL_1 10.358 1155.16 FUEL U235= 0.6267 U238=87.526 O16=11.8472
MATERIAL FUEL_2 10.358 1155.16 FUEL U235= 0.6267 U238=87.526 O16=11.8472
MATERIAL FUEL_3 10.358 1155.16 FUEL U235= 0.6267 U238=87.526 O16=11.8472
MATERIAL FUEL_4 10.358 1155.16 FUEL U235= 0.6267 U238=87.526 O16=11.8472
WRITE 1
BUCKLING .4826E-4 .2794E-4
BEGIN
BUCKLING .4826E-4 .2794E-4
NOBUCK
BENOIST 1
PRINT 1 1 1 0 1 0
REACTION ALL
PARTITION 5 45 69
BEGIN
READ 1
DENSITY 0.0001
BEGIN
BEGIN
STOP
```

Appendix E

The following is the fortran source code for FPT.FOR, a code used to search for successful two-ring nested annular geometries based on a balance of coolant flow rate and power deposition between the three flow subchannels, checking also for centreline fuel temperature acceptability. A similar algorithm was used to search for three-ring and four-ring geometries. Output is printed in WIMS-AECL input format. An explanation of the method can be found in Section 5.2.7.

```
      PROGRAM FPT7

*  Calculates several two-ring nested annular fuel geometries, incl.
*  cladding, which satisfy subchannel flow/power balance, centreline
*  temp. condition, delta-p condition, total flow area condition, and
*  heat flux approx.condition. All dimensions in cm.
*
*  Jeremy Whitlock, 94/08/16

      DATA GAP1ST,GAP2ST,T1ST,GAP3MIN/0.08,0.29,0.0,0.1/
      DATA VOLST,VOLMAX,ICOUNTST/40.0,60.0,500/
      DATA GAP1INC,GAP2INC,T1INC,VOLINC/0.02,0.02,0.1,0.3/
      DATA CLAD,RADOUT,RADIN,RADINC/0.05,5.1689,0.5889,0.1/
      DATA PI,BUNDLEP,MAXTEMP,FUELK/3.1415927,640,2000,0.025/
      DATA COOLT,CLADT,RATMIN,T2MIN,PFRAC1/310,100,0.98,0.3,0.45/
      DATA PDROPREF,SREF,AREF,VREF/2.4704E-3,152.0,34.2,42.9/
      DATA AMIN,DELPMAX,SVMAX1,SVMAX2/0.02,1.1,100.,100./
      DATA FOM1MAX,FOM2MAX/0.,0./
      CHARACTER NAME*3,FILENAME*8,MULTINAM*4
      OPEN (UNIT=1,FILE='FPT7.OUT')
      OPEN (UNIT=4,FILE='FPT.TMP',STATUS='SCRATCH')
      OPEN (UNIT=5,FILE='SVMAX.OUT')
      OPEN (UNIT=6,FILE='SVCOMP.OUT')
      OPEN (UNIT=7,FILE='C:\JEREMY\WIMSAECL\MULTI.BAT')

*  Start loops

      PFRAC2=1-PFRAC1
      ICOUNT=ICOUNTST
      VOL=VOLST
      DO 50 IRADIN=1,20
        RADIN=RADIN+RADINC
        VOL=VOLST
        DO 100 WHILE (VOL .LE. VOLMAX)
          GAP1=GAP1ST
          DO 200 IGAP1=1,100
            GAP1=GAP1+GAP1INC
            T1=T1ST
            DO 400 IT1=1,100
```

```
          T1=T1+T1INC
          GAP2=GAP2ST
          DO 500 IGAP2=1,100
      GAP2=GAP2+GAP2INC

*  Calculate dimensions, volumes, flow areas and hydraulic diameters.

      R1=RADIN+GAP1+CLAD
      R2=R1+T1
      R3=R2+(2*CLAD)+GAP2
      AREAF1=PI*(R2**2-R1**2)
      AREAF2=VOL-AREAF1
      VOL1=AREAF1*49.5
      VOL2=AREAF2*49.5
      R4=SQRT(AREAF2/PI + R3**2)
      T2=R4-R3
      GAP3=RADOUT-(R4+CLAD)
      AREA1=PI*((R1-CLAD)**2-RADIN**2)
      AREA2=PI*((R3-CLAD)**2-(R2+CLAD)**2)
      AREA3=PI*(RADOUT**2-(R4+CLAD)**2)
      TOTAREA=AREA1+AREA2+AREA3
      S=2*PI*(R1+R2+R3+R4)
      S1=2*PI*(R1+R2)
      S2=2*PI*(R3+R4)
      D1=4*AREA1/(2*PI*((R1-CLAD)+RADIN))
      D2=4*AREA2/(2*PI*((R3-CLAD)+(R2+CLAD)))
      D3=4*AREA3/(2*PI*(RADOUT+(R4+CLAD)))

*  Check for impossible geometry.

      IF (GAP3 .LT. GAP3MIN) THEN
        GOTO 400
      ENDIF
      IF (T2 .LT. T2MIN) THEN
        GOTO 500
      ENDIF

*  Calculate delta-T across each ring.

      PDENS1=BUNDLEP*1000*PFRAC1/VOL1
      PDENS2=BUNDLEP*1000*PFRAC2/VOL2
      RMAX1=SQRT((R2**2-R1**2)/(2*LOG(R2/R1)))
      RMAX2=SQRT((R4**2-R3**2)/(2*LOG(R4/R3)))
      ALPHA1=(RMAX1/R1)**2
      ALPHA2=(RMAX2/R3)**2
      DELT1=PDENS1*R1**2*(1-ALPHA1+ALPHA1*LOG(ALPHA1))/(4*FUELK)
      DELT2=PDENS2*R3**2*(1-ALPHA2+ALPHA2*LOG(ALPHA2))/(4*FUELK)

*  Check for unacceptable max. fuel temp.; try next IGAP2 on fail.

      FUELT1=COOLT+CLADT+DELT1
      FUELT2=COOLT+CLADT+DELT2
      IF (FUELT1 .GT. MAXTEMP .OR. FUELT2 .GT. MAXTEMP) THEN
        GOTO 500
      ENDIF

*  Calculate fractional power load in each flow channel.

      FRAC12=(1+((1-(R1**2/R2**2))/(2*LOG(R1/R2))))/(1-(R1**2/R2**2))
      FRAC11=1.0-FRAC12
      FRAC23=(1+((1-(R3**2/R4**2))/(2*LOG(R3/R4))))/(1-(R3**2/R4**2))
      FRAC22=1.0-FRAC23
      PLOAD1=FRAC11*PFRAC1
      PLOAD2=((FRAC12*PFRAC1)+(FRAC22*PFRAC2))
      PLOAD3=FRAC23*PFRAC2

*  Calculate fractional flow rate in each flow channel.

      EXP=2./3.
      AD1=AREA1*D1**EXP
      AD2=AREA2*D2**EXP
      AD3=AREA3*D3**EXP
      TOTALAD=AD1+AD2+AD3
      WFRAC1=AD1/TOTALAD
      WFRAC2=AD2/TOTALAD
```

```
      WFRAC3=AD3/TOTALAD

*  Check for equal flow area and delta-P ratio less than 1.1.

      AREAERR=(ABS(TOTAREA-AREF))/AREF
      EXP2=-1.6
      DELP=(AD1+AD2+AD3)**EXP2
      PDROP=DELP/PDROPREF
      DELPRAT=DELP/PDROPREF

      IF (AREAERR .GT. AMIN .OR. DELPRAT .GT. DELPMAX) THEN
        GOTO 500
      ENDIF

*  Compare fractional power loads and flow rates; try new IGAP2 on fail.

      RATIO1=WFRAC1/PLOAD1
      RATIO2=WFRAC2/PLOAD2
      RATIO3=WFRAC3/PLOAD3
      IF (RATIO1 .LT. RATMIN .OR. RATIO2 .LT. RATMIN .OR. RATIO3 .LT. RATMIN) THEN
        GOTO 500
      ELSE IF (1/RATIO1 .LT. RATMIN .OR. 1/RATIO2 .LT.
     >                        RATMIN .OR. 1/RATIO3 .LT. RATMIN) THEN
        GOTO 500
      ENDIF

*  Write results if acceptable.

      ICOUNT=ICOUNT+1
      WRITE(1,*) ICOUNT
      WRITE(1,*) ' VOLUME= ',VOL,'   RADIN= ',RADIN
      WRITE(1,*) ' R1= ',R1,' R2= ',R2,' R3= ',R3,' R4= ',R4
      WRITE(1,*) ' FUELT1= ',FUELT1,' FUELT2= ',FUELT2
      WRITE(1,*) ' PLOAD: ',PLOAD1,PLOAD2,PLOAD3
      WRITE(1,*) ' WFRAC: ',WFRAC1,WFRAC2,WFRAC3
      WRITE(1,*) ' GAPS: ',GAP1,GAP2,GAP3

*  Sort surface-to-volume ratios.

      SVRAT1=S1/AREAF1
      SVRAT2=S2/AREAF2
      SVREF=SREF/VREF
      SVERR1=ABS(SVRAT1/SVREF-1.)
      SVERR2=ABS(SVRAT2/SVREF-1.)
      IF (SVERR1 .LT. SVMAX1 .AND. SVERR2 .LT. SVMAX2) THEN
        WRITE(5,*) ICOUNT,' SVERR1= ',SVERR1,' SVERR2= ',SVERR2
        SVMAX1=SVERR1
        SVMAX2=SVERR2
      ENDIF
      FOM1=SVERR1/DELPRAT
      FOM2=SVERR2/DELPRAT
      IF (FOM1 .GT. FOM1MAX .AND. FOM2 .GT. FOM2MAX) THEN
        WRITE(6,*) ICOUNT,' FOM1= ',FOM1,' FOM2= ',FOM2
        FOM1MAX=FOM1
        FOM2MAX=FOM2
      ENDIF

      WRITE(1,*) ' AREA= ',TOTAREA/AREF, ' DEL-P=',
     >                        PDROP,' S1= ',SVERR1,' S2= ',SVERR2
      WRITE(1,*) ' '

*  Write entire WIMS-AECL input file.

      REWIND(4)
      WRITE(4,*) ICOUNT
      REWIND(4)
      READ(4,*) NAME
      FILENAME='X'//NAME//'.INP'
      MULTINAM='X'//NAME
      OPEN(UNIT=3,FILE=FILENAME)
      WRITE(7,700) 'CALL RUNCASED',MULTINAM
700         FORMAT(A13,1X,A4)

    WRITE(3,*) 'TITLE "TWO FUEL RINGS, GRAPHITE SPACER, BALANCED',' FLOW/POWER"'
    WRITE(3,*) 'SEQUENCE 2.3'
```

```
      WRITE(3,*) 'SCAN'
      WRITE(3,*) 'PREOUT'
      WRITE(3,10) 'ANNULUS 1 ',RADIN-CLAD,'CORE'
      WRITE(3,10) 'ANNULUS 2 ',RADIN,'CLAD'
      WRITE(3,10) 'ANNULUS 3 ',RADIN+GAP1,'COOLANT'
      WRITE(3,10) 'ANNULUS 4 ',R1,'CLAD'
      WRITE(3,10) 'ANNULUS 5 ',R2,'FUEL_1'
      WRITE(3,10) 'ANNULUS 6 ',R2+CLAD,'CLAD'
      WRITE(3,10) 'ANNULUS 7 ',R2+CLAD+GAP2,'COOLANT'
      WRITE(3,10) 'ANNULUS 8 ',R3,'CLAD'
      WRITE(3,10) 'ANNULUS 9 ',R4,'FUEL_2'
      WRITE(3,10) 'ANNULUS 10',R4+CLAD,'CLAD'
 10   FORMAT(A10,1X,F6.4,1X,A10)
      WRITE(3,*) 'ANNULUS 11 5.1689 COOLANT'
      WRITE(3,*) 'ANNULUS 12 5.6210 PT'
      WRITE(3,*) 'ANNULUS 13 6.4478 VOID'
      WRITE(3,*) 'ANNULUS 14 6.6002 CT'
      WRITE(3,*) 'POLYGON 15 4 MODER 14.2875'
      WRITE(3,*) '*'
      WRITE(3,*) 'MESH #'
      WRITE(3,*) 'NEWRES'
      WRITE(3,*) '*'
      WRITE(3,*) 'FEWGROUPS 1 2 3 4 5 6 7 8 9 10 11 12 13 14 15 16 17 18 19 20 21 $'
      WRITE(3,*) '22 23 24 25 26 27 28 29 30 31 32 33 34 35 36 37 38 39 40 41 42 $'
      WRITE(3,*) '43 44 45 46 47 48 49 50 51 52 53 54 55 56 57 58 59 60 61 62 63 64 $'
      WRITE(3,*) '65 66 67 68 69'
      WRITE(3,*) 'TOLERANCE 1E-5'
      WRITE(3,*) 'SUPPRESS 1 0 1 1 1  1 1 1 1 1  1 0 1 0 0 -1'
      WRITE(3,*) 'MATERIAL COOLANT 0.80406 563.16 COOL H1 =.028 D2=20.063 O16=79.909'
      WRITE(3,*) 'MATERIAL MODER  1.0835 344.26 MODE   H1 =.017 D2 20.083 O16=79.9'
      WRITE(3,*) 'MATERIAL PT 6.57 563.16 MODER  ZR91=97.5 NB93=2.5 B10B=3.8E-5'
      WRITE(3,*) 'MATERIAL VOID 0.0014 341.16 MODER  HE4=100.'
      WRITE(3,*) 'MATERIAL CT 6.44 341.16 MODER ZR91=99.67 FE56=.16 CR52=.11 NI58=.06 $'
      WRITE(3,*) '       B10B=5.34E-5'
      WRITE(3,*) 'MATERIAL CLAD 6.23 293.16 CLAD ZR91=99.67 FE56=.16 CR52=.11 NI58=.06 $'
      WRITE(3,*) '       B10B=5.34E-5'
      WRITE(3,*) 'MATERIAL FUEL_1 10.358 1155.16 FUEL U235=0.6267 U238=87.526 O16=11.847'
      WRITE(3,*) 'MATERIAL FUEL_2 10.358 1155.16 FUEL U235=0.6267 U238=87.526 O16=11.847'
      WRITE(3,*) 'MATERIAL CORE 1.6 563.16 COOL C12 1.0 '
      WRITE(3,*) 'WRITE 1'
      WRITE(3,*) 'BEGIN '
      WRITE(3,*) 'BUCKLING .4826E-4 .2794E-4 '
      WRITE(3,*) 'NOBUCK                     '
      WRITE(3,*) 'normalize loss             '
      WRITE(3,*) 'BENOIST 1                  '
      WRITE(3,*) 'PRINT 1 1 1 0 1 0          '
      WRITE(3,*) 'REACTION ALL               '
      WRITE(3,*) 'PARTITION 5 45 69          '
      WRITE(3,*) 'BEGIN                      '
      WRITE(3,*) 'READ 1                     '
      WRITE(3,*) 'DENSITY 1 1 0.0001         '
      WRITE(3,*) 'BEGIN                      '
      WRITE(3,*) 'BEGIN                      '
      WRITE(3,*) 'STOP                       '
        CLOSE(3)
        WRITE(*,*) ' SVERR1= ',SVERR1,' SVERR2= ',SVERR2

*  Increment counters and close loops.

 500          CONTINUE
 400        CONTINUE
 200      CONTINUE
          WRITE(*,*) ' VOL= ',VOL,' CORE R= ',RADIN,' HITS= ',ICOUNT-ICOUNTST
          VOL=VOL+VOLINC
 100    CONTINUE
 50   CONTINUE

      END
```

Appendix F

The following is the WIMS-AECL input file for Case 3E-NU-GS without burnup.

```
TITLE "3E-NU-GS: TWO FUEL RINGS, GRAPHITE SPACER, BALANCED FLOW/POWER"
SEQUENCE 2.3
SCAN
PREOUT
ANNULUS 1  0.6796 CORE
ANNULUS 2  1.3593 CORE
ANNULUS 3  2.0389 CORE
ANNULUS 4  2.0889 CLAD
ANNULUS 5  2.3989 COOLANT
ANNULUS 6  2.4489 CLAD
ANNULUS 7  2.8589 FUEL_1
ANNULUS 8  2.9089 CLAD
ANNULUS 9  3.3589 COOLANT
ANNULUS 10 3.4089 CLAD
ANNULUS 11 3.8489 FUEL_2
ANNULUS 12 3.8989 CLAD
ANNULUS 13 4.3589 COOLANT
ANNULUS 14 4.4089 CLAD
ANNULUS 15 4.8336 FUEL_3
ANNULUS 16 4.8836 CLAD
ANNULUS 17 5.1689 COOLANT
ANNULUS 18 5.6210 PT
ANNULUS 19 6.4478 VOID
ANNULUS 20 6.6002 CT
POLYGON 21 4 MODER 14.2875
*
MESH #
NEWRES
*
FEWGROUPS 1 2 3 4 5 6 7 8 9 10 11 12 13 14 15 16 17 18 19 20 21 $
22 23 24 25 26 27 28 29 30 31 32 33 34 35 36 37 38 39 40 41 42 $
43 44 45 46 47 48 49 50 51 52 53 54 55 56 57 58 59 60 61 62 63 64 $
65 66 67 68 69
TOLERANCE 1E-5
SUPPRESS 1 0 1 1 1  1 1 1 1 1  1 0 1 0 0 -1
MATERIAL COOLANT 0.80406 563.16 COOL H1 =.028 D2=20.063 O16=79.909
MATERIAL MODER  1.0835 344.26 MODE   H1 =.017 D2 20.083 O16=79.9
MATERIAL PT 6.57 563.16 MODER  ZR91=97.5 NB93=2.5 B10B=3.8E-5
MATERIAL VOID 0.0014 341.16 MODER  HE4=100.
MATERIAL CT 6.44 341.16 MODER ZR91=99.67 FE56=.16 CR52=.11 NI58=.06 $
      B10B=5.34E-5
MATERIAL CLAD 6.23 293.16 CLAD ZR91=99.67 FE56=.16 CR52=.11 NI58=.06 $
      B10B=5.34E-5
MATERIAL FUEL_1 10.358 1155.16 FUEL U235= 0.6267 U238=87.526 O16=11.8472
MATERIAL FUEL_2 10.358 1155.16 FUEL U235= 0.6267 U238=87.526 O16=11.8472
MATERIAL FUEL_3 10.358 1155.16 FUEL U235= 0.6267 U238=87.526 O16=11.8472
MATERIAL CORE 1.6 563.16 COOL C12 1.0
WRITE 1
BEGIN
BUCKLING .4826E-4 .2794E-4
NOBUCK
NORMALIZE LOSS
BENOIST 1
PRINT 1 1 1 0 1 0
REACTION ALL
PARTITION 5 45 69
BEGIN
READ 1
DENSITY 1 1 0.0001
BEGIN
BEGIN
STOP
```

Appendix G

The following are the MCNP-4 and WIMS-AECL input files for the single-lump annular fuel case used as a benchmark the calculations of WIMS-AECL.

MCNP-4 Cooled Case

```
test case, cooled
    1 3 -.80406 -1 8 9 10 -11 12   imp:n=1 vol=34.66545 $ coolant
    2 4 -10.358  1 -13 8 9 10 -11     imp:n=1 vol=42.90326 $ fuel
    3 3 -.80406  13 -2 8 9 10 -11  imp:n=1 vol=6.369768 $ coolant
    4 5 -6.57    2 -3 8 9 10 -11      imp:n=1 vol=15.32505 $ p/t
    5 6 -.0014   3 -4 8 9 10 -11      imp:n=1 vol=31.34833 $ void
    6 7 -6.44    4 -5 8 9 10 -11      imp:n=1 vol=6.247105 $ c/t
    7 8 -1.0835  5 8 9 10 -11 -6 -7   imp:n=1 vol=679.6746 $ moderator
    8 9 -1.6     -12 8 9 10 -11       imp:n=1

    1 cz 3.3218                       $ coolant
    2 cz 5.1689                       $ fuel
    3 cz 5.6210                       $ p/t
    4 cz 6.4478                       $ void
    5 cz 6.6002                       $ c/t
   *6 px 14.2875                      $ cell boundary
   *7 py 14.2875                      $ cell boundary
   *8 px 0.0                          $ cell boundary
   *9 py 0.0                          $ cell boundary
  *10 pz 0.0                          $ cell boundary
  *11 pz 50.0                         $ cell boundary
   12 cz 3.3018
   13 cz 4.9689

mode:n
kcode 2000 1.15000 20 10000 10000 0
ksrc  2.5  2.5  2.0
      3.2  3.2  2.0
totnu
m3   1001.50c 1.3405e-4 1002.55c 4.8233e-2 8016.50c 2.4190e-2 $ coolant
m8   1001.50c 1.0877e-4 1002.55c 6.5060e-2 8016.50c 3.2593e-2 $ moderator
m7   40000.57c 4.2374e-2 24000.50c 8.2021e-5 26000.55c 1.1106e-4
     28000.50c 3.9632e-5 5010.50c 2.0e-7                $ c/t
m6   8016.50c  -1.0
m5   40000.57c 4.2289e-2 41093.51c 1.0646e-3 5010.50c 1.5e-7 $ p/t
m4   8016.50c  -.1344410 92235.50c -0.00720 92238.50c -0.992800 $ ring 1
m9   6012.10c 1.0
mt3    hwtr.04t lwtr.04t
mt8    hwtr.01t lwtr.01t
phys:n    10 0
print 90 110 120 130 140 170
prdmp 3j 1
```

G.1 MCNP-4 Voided Case

```
test case, voided
    1 3 -.80406e-4 -1 8 9 10 -11 12   imp:n=1 vol=34.66545 $ coolant
    2 4 -10.358  1 -13 8 9 10 -11     imp:n=1 vol=42.90326 $ fuel
    3 3 -.80406e-4  13 -2 8 9 10 -11  imp:n=1 vol=6.369768 $ coolant
    4 5 -6.57    2 -3 8 9 10 -11      imp:n=1 vol=15.32505 $ p/t
    5 6 -.0014   3 -4 8 9 10 -11      imp:n=1 vol=31.34833 $ void
    6 7 -6.44    4 -5 8 9 10 -11      imp:n=1 vol=6.247105 $ c/t
    7 8 -1.0835  5 8 9 10 -11 -6 -7   imp:n=1 vol=679.6746 $ moderator
    8 9 -1.6     -12 8 9 10 -11       imp:n=1
```

```
   1 cz 3.3218                    $ coolant
   2 cz 5.1689                    $ fuel
   3 cz 5.6210                    $ p/t
   4 cz 6.4478                    $ void
   5 cz 6.6002                    $ c/t
  *6 px 14.2875                   $ cell boundary
  *7 py 14.2875                   $ cell boundary
  *8 px 0.0                       $ cell boundary
  *9 py 0.0                       $ cell boundary
 *10 pz 0.0                       $ cell boundary
 *11 pz 50.0                      $ cell boundary
  12 cz 3.3018
  13 cz 4.9689

mode:n
kcode 2000 1.15000 20 10000 10000 0
ksrc  2.5  2.5  2.0
      3.2  3.2  2.0
totnu
m3   1001.50c 1.3405e-4 1002.55c 4.8233e-2 8016.50c 2.4190e-2 $ coolant
m8   1001.50c 1.0877e-4 1002.55c 6.5060e-2 8016.50c 3.2593e-2 $ moderator
m7   40000.57c 4.2374e-2 24000.50c 8.2021e-5 26000.55c 1.1106e-4
     28000.50c 3.9632e-5 5010.50c 2.0e-7                $ c/t
m6   8016.50c  -1.0
m5   40000.57c 4.2289e-2 41093.51c 1.0646e-3 5010.50c 1.5e-7 $ p/t
m4   8016.50c  -.1344410 92235.50c -0.00720 92238.50c -0.992800 $ ring 1
m9   6012.10c 1.0
mt3    hwtr.04t lwtr.04t
mt8    hwtr.01t lwtr.01t
phys:n    10 0
print 90 110 120 130 140 170
prdmp 3j 1
```

G.2 WIMS-AECL Case

```
TITLE "TWO OUTER FUEL RINGS, EQUAL WIDTH, CORRECT Vc/Sf"
SEQUENCE 2.3
SCAN
PREOUT
ANNULUS 1  1.1006 C_ROD
ANNULUS 2  2.2012 C_ROD
ANNULUS 3  3.3018 C_ROD
ANNULUS 4  3.3218 COOLANT
ANNULUS 5  4.1454 FUEL
ANNULUS 6  4.9689 FUEL
ANNULUS 7  5.1689 COOLANT
ANNULUS 8  5.6210 PT
ANNULUS 9  6.4478 VOID
ANNULUS 10 6.6002 CT
POLYGON 11 4 MODER 14.2875
MESH #
NEWRES
FEWGROUPS 1 2 3 4 5 6 7 8 9 10 11 12 13 14 15 16 17 18 19 20 21 $
22 23 24 25 26 27 28 29 30 31 32 33 34 35 36 37 38 39 40 41 42 $
43 44 45 46 47 48 49 50 51 52 53 54 55 56 57 58 59 60 61 62 63 64 $
65 66 67 68 69
TOLERANCE 1E-5
SUPPRESS 1 0 1 1 1  1 1 1 1 1  1 0 1 0 0 -1
MATERIAL COOLANT 0.80406 600. COOL H1 =.028 D2=20.063 O16=79.909
MATERIAL MODER  1.0835 300. MODE   H1 =.017 D2 20.083 O16=79.9
MATERIAL PT 6.57 300. MODER  ZR91=97.5 NB93=2.5 B10B=3.8E-5
MATERIAL VOID 0.0014 300. MODER  O16=100.
MATERIAL CT 6.44 300. MODER ZR91=99.67 FE56=.16 CR52=.11 NI58=.06 $
      B10B=5.34E-5
MATERIAL CLAD 6.23 293.16 CLAD ZR91=99.67 FE56=.16 CR52=.11 NI58=.06 $
      B10B=5.34E-5
MATERIAL FUEL 10.358 300. FUEL U235= 0.6267 U238=87.526 O16=11.8472
MATERIAL C_ROD 2.5 0.0 COOL C12=100.
WRITE 1
BEGIN
PRINT 1 1 1 0 1 0
REACTION U235=0 U238=0
PARTITION 5 45 69
BEGIN
READ 1
DENSITY 1 0.0001
BEGIN
BEGIN
STOP
```